August 2018

Evaluation of Thermal Effects and Lattice Vibrations in Molecular Crystals

Adam Joseph Zaczek
Syracuse University

Recommended Citation

Zaczek, Adam Joseph, "Evaluation of Thermal Effects and Lattice Vibrations in Molecular Crystals" (2018). *Dissertations - ALL*. 946.
https://surface.syr.edu/etd/946

Abstract

The effect of temperature plays a large role in the behavior of many physical systems. While it is certainly the case that many effects of temperature can be observed macroscopically, they are often of molecular origin, and determining why these effects occur can provide insight into the nature of chemical systems as a whole. A large portion of this work is dedicated to analyzing polymorphic forms and small organic molecules with interesting thermal effects. Low-frequency spectroscopy is a very useful tool in the investigation of polymorphs, providing a method of probing a sample to investigate the possible motions and characteristics that these systems exhibit with the effect of heating or cooling. In this work, low-frequency spectroscopy is combined with X-ray diffraction to differentiate polymorphs and analyze systems that behave anharmonically with temperature. This experimental work is complemented with solid-state density functional theory calculations, enabling for the evaluation of the energetics of the studied systems, providing insight into the relative stabilities of the studied systems over a range of temperatures, and can even elucidate the mechanisms by which polymorphic transformations may occur. Overall, this is an achievement in the understanding of thermal effects in crystalline systems made possible by the combination of experimental and theoretical techniques.

EVALUATION OF THERMAL EFFECTS AND LATTICE VIBRATIONS IN MOLECULAR CRYSTALS

by

Adam Joseph Zaczek

B.S., State University of New York College at Geneseo, 2014
M.Phil., Syracuse University, 2016

Dissertation

Submitted in partial fulfillment of the requirements for the degree of

Doctor of Philosophy in Chemistry

Syracuse University

August 2018

ACKNOWLEDGEMENTS

I consider myself extremely lucky to have been able to work with Dr. Timothy Korter as my advisor. Without him, none of this work would have been possible. I cannot thank him enough. He allowed me to travel around the world to take place in many conferences to further my scientific career and was always looking out for research projects that I could contribute to. But more importantly, he was always available for daily discussions and was a great person, as well as an advisor. I can't think of anyone else I would have rather worked for in these last four years. He also put up with all of my antics, which I am truly appreciative of.

I would also like to thank previous Korter group member Michael Ruggiero for convincing me to join Dr. Korter's group and dragging me along throughout the course of my research, teaching me in and out of the lab in his own way, and providing me with great opportunities after Syracuse. I would also like to thank the other members of the Korter group I have had the pleasure of working with; Teresa Dierks, Meg Davis, Elyse Kliest, and Sara Dampf (who has truly put up with me the most throughout the course of our many journeys).

I would also like to thank both of my parents for supporting me in their own ways throughout my education. I know they have always believed in me, and this is my way of challenging myself to rise to what they know I can achieve. Finally, I wish to give a special thanks to my grandfather Al Cortese. He was always there to support me through all of my education, from driving me out to the bus stop when it was too cold out, to contributing to my college fund, to his look of shock when he realized I was going to get paid to go to school when I got my first contract with Syracuse. His support meant the world to me, and I hope that all the work I have done in my time here would have made him proud.

Table of Contents

CHAPTER 5. Isomerization of *cis-cis* to *cis-trans* Muconic Acid in Aqueous Solution…..135

List of Illustrative Materials

CHAPTER 1. Introduction and Overview

1.1 Research Motivation

The research projects presented in this work are connected by the common motif of temperature changes causing significant effects in the formation and stabilization of organic crystalline systems. Common phenomena (e.g. melting, freezing, subliming) are typically thought of when temperature changes occur. However, a more subtle example of a temperature-dependent change is a difference in molecular packing within a crystalline lattice which can result in unique spectral features and even unusual shifting of features in response to temperature variations.

This research can be broadly grouped into two temperature-dependent topics: the stabilization of polymorphs and the changes in spectra with temperature in a crystalline solid. The phenomena analyzed range from crystallizations favoring one polymorph over another (**Chapter 4**) to crystals that physically jump when they undergo a polymorph change when heated (**Chapter 6**). In this research, experimental methods such as X-ray diffraction, terahertz time-domain spectroscopy, and low-frequency Raman spectroscopy are utilized to characterize the thermal response to crystalline samples. While experimental methods can observe these changes, density functional theory calculations can determine why these changes occur and provide a detailed picture of the studied chemical systems which gives insight into their energetic and thermal properties. Without theoretical methods, explorations of temperature-induced changes would be far more difficult and critical explanations may be overlooked.

All the systems studied in this research are small crystalline organics except for the work on aqueous muconic acid (**Chapter 5**). Density functional theory calculations are especially useful in polymorph studies, making it possible to determine which polymorph will be more stable at a given temperature. All of the systems studied in this work have unique responses to temperature, and determining the mechanisms behind isomer and polymorph transformations as well as investigating how temperature can affect the vibrational motions and energetics of crystalline systems can help to guide the crystal engineering of new materials with unique properties.

1.2 Polymorphism

In nature, it is possible for crystals composed of the same molecules to pack in different ways which is known as polymorphism[1]. The topic of polymorphism is not uncommon, and has even been published in popular literature, such as Ice IX in Kurt Vonnegut's *Cat's Cradle*[2]. While a world-ending scenario is an extreme exaggeration in polymorph discovery, it does hold some truth in the significance of polymorphic stability. When multiple polymorphs exist for a crystalline sample, the form that predominates does so because it is typically more thermodynamically stable. This results in one form being favored over another depending upon the crystallization conditions, such as temperature[3-5] , pressure[6, 7], and solvent[8, 9]. Upon formation, some polymorphs can only be observed at the conditions required for crystallization[10, 11] while others remain stable when exposed to other conditions[12]. Some polymorphs have very noticeable physical differences, like β and γ quinacridone which are dark violet and red, respectively[13], and shown in **Figure 1-1** (and detailed in **Chapter 8**). However, many polymorph changes are more subtle, and are noticed only through further experimentation after their creation.

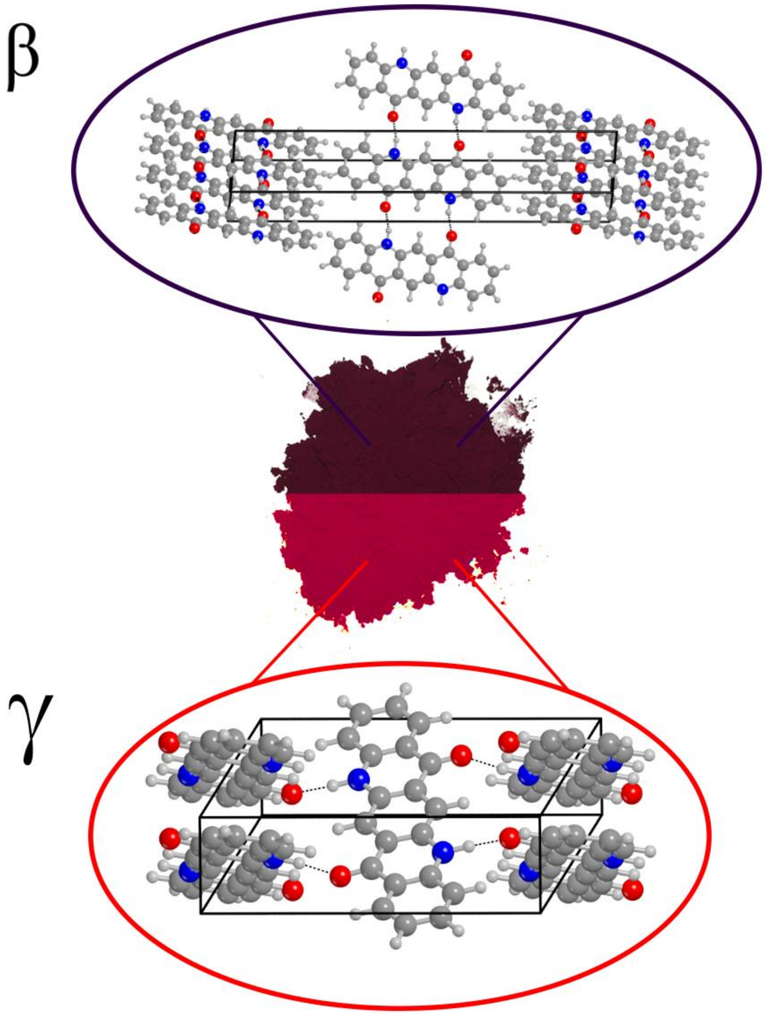

Figure 1-1. The β and γ polymorphs of quinacridone. The polymorphs each have unique colors, making them easy to differentiate.

Polymorphs contain components with different molecular conformations and unique intermolecular interactions[14], such as modified hydrogen bonding networks within a polymorphic group. Melting points[15, 16] and solubilities[17] are suggestive of different intermolecular interactions, and polymorphs with higher melting points and lower solubilities typically indicate increased stability[18]. There are many other nondestructive methods for determination and characterization of polymorphic systems that can provide more insight into their structure such as X-ray diffraction and terahertz spectroscopy, which will be discussed in the following section and in **Chapter 2.**

One of the reasons for studying polymorphism lies in the pharmaceutical industry. With polymorphs having different physical properties, the shelf-life[19, 20] or drug uptake can be directly affected, creating new patent oppotrunities[21, 22]. While patented drugs can lead to multimillion dollar ventures, the discovery of a new polymorph can result in the production of the same drug with different properties that does not break patent laws[23]. In a quest for making better and more effective drugs, understanding polymorphism is crucial.

It is generally the case that the more time that is spent studying a crystalline system, the greater the number of polymorphs that will be discovered. There are some exceptions to this, such as aspirin, one of the most studied and used drugs over the past 100 years. For almost its entire existence, only one ambient polymorph was known[24], with definitive evidence for a second polymorph discovered in 2005[25], and a possible third in 2017[26]. This is why the study of polymorphism is not an open-and-shut case and continues to have new discoveries today.

1.3 Research Methods

1.3.1 X-ray Diffraction

One of the more common methods for obtaining information from crystalline materials is through X-ray diffraction. Interest in crystallinity dates back to the 17th century, when Kepler[27] questioned why snowflakes always had six-fold symmetry. In the centuries following this observation, work was performed in order to identify how atoms could arrange in ordered planes and the various crystal faces that were possible. With the discovery of X-rays (originally called Rontgen rays) in 1895 by Wilhelm Rontgen[28] (for which he won a Nobel Prize in 1901), the study of crystal structures soon skyrocketed. In 1914, Max von Laue won the Nobel Prize for his discovery that crystals diffract X-rays[29], and the next year W.H. Bragg and W.L. Bragg won the Nobel Prize for using X-rays to determine crystal structures[30]. Since then, many more awards have been won that involve X-ray crystallography.

Over the course of this research, two types of X-ray diffraction were used. The first method is powder X-ray diffraction (PXRD), which provides a distinct fingerprint and yields the lattice dimensions and space group symmetries of the crystalline species within a bulk sample. This can be used to differentiate polymorphs, investigate crystalline mixtures, and determine if a sample is partially amorphous. An example is (+)-sucrose, which shows a different powder pattern when exposed to high pressure due to a polymorph change from phase I to phase II[31], shown in **Figure 1-2**.

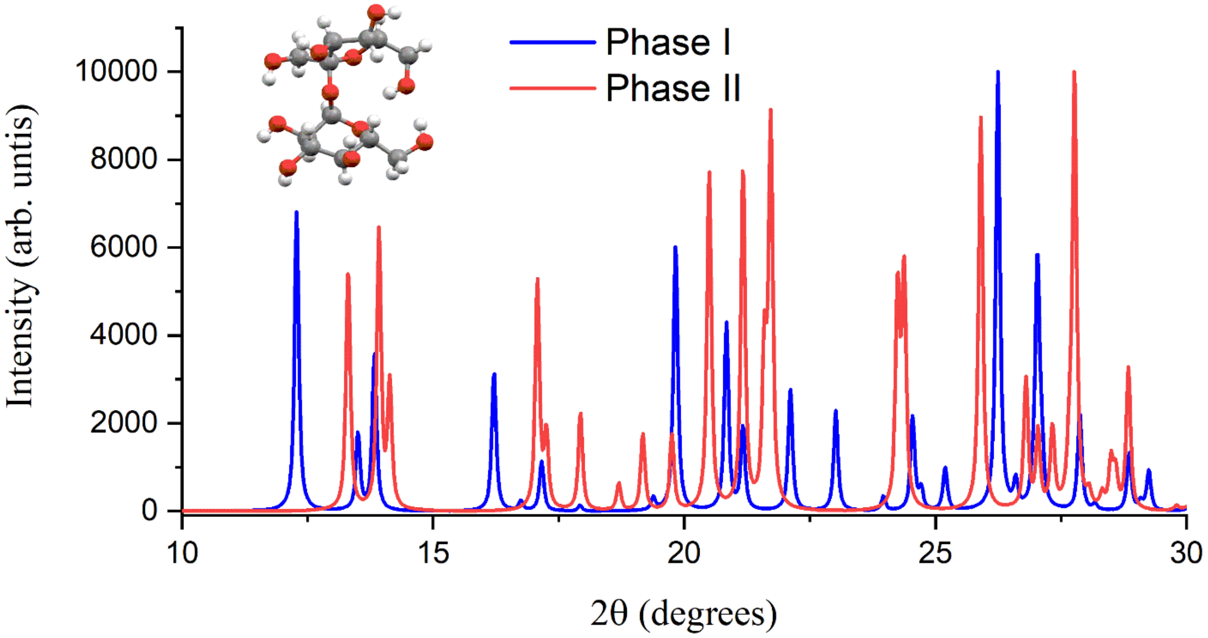

Figure 1-2. Powder patterns of form I and form II of (+)-sucrose[31], showing the different PXRD patterns that are observed between polymorphs.

The second method of X-ray diffraction that is used is single-crystal X-ray diffraction (SC-XRD). While PXRD is used for bulk crystalline samples, SC-XRD is used to accurately determine the three-dimensional atomic positions within a single crystal, as well as the lattice parameters associated with its periodicity. This technique enables the structure of a crystalline system to be solved completely. The use of SC-XRD is an extremely active area of study in the analysis of crystal systems, with databases dedicated to collecting solved structures that are continuously updated[32]. An SC-XRD analysis can also show how the unit cell dimensions of a crystal and atom positions within the cell change with temperature. The combination of PXRD and SC-XRD provides a means for determining the content of a bulk crystalline sample and the atomic structure of the crystal.

1.3.2 Low-Frequency Vibrational Spectroscopy

The difference between polymorphic systems can be very subtle, so a method that can investigate their intermolecular and intramolecular interactions is useful for distinguishing them. Terahertz (THz) spectroscopy (3–333 cm^{-1}) operates in the far-IR range of the electromagnetic spectrum, lying between microwave and mid-IR radiation (**Figure 1-3**). Benefits of THz spectroscopy include its non-ionizing, non-destructive nature that can probe through many common materials such as paintings[33-35] and coatings[36, 37] and can readily identify drugs[38, 39], explosives[40, 41], and amino acids[42]. However, THz radiation is not as easy to generate or detect as other forms of radiation, cannot penetrate metal surfaces, and is absorbed by water vapor at ambient conditions. Nevertheless, THz spectroscopy is a technique that has proven to be very useful.

While THz spectroscopy has been investigated for decades, it wasn't until 1995 that it began gaining more traction due to the use of the time-domain spectroscopy[43]. Publications that involve THz radiation have been exponentially increasing[44] since the inception of these time-domain techniques. As THz spectroscopy has become a more sought-after technique, it is now possible to obtain a commercial terahertz system which typically takes up considerably less space in a laboratory and often requires less user maintenance than a custom-built spectrometer. In this research, two THz spectrometer systems are used; a homemade system that generates and detects THz radiation through ZnTe crystals, and a commercial Toptica brand spectrometer that generates and detects THz radiation using photoconductive antennas.

With new advances in technology, low-frequency Raman spectroscopy is an emerging technique in spectroscopic studies. Although the same spectral region is analyzed as a THz system, the method by which low-frequency Raman spectra are obtained is very different. While THz spectroscopy involves absorption of light in a sample, Raman spectroscopy is performed using the scattering of light off a sample. The Ondax brand Raman spectrometer used in this work utilizes a series of volume holographic grating notch filters (VHGs) that eliminate a majority of the light at the probing laser wavelength. This allows the peaks that were previously overpowered by the Rayleigh peak to be observed in the low-frequency (5 cm^{-1} -300 cm^{-1}) range. The lack of good Rayleigh scattering rejection was the limiting step and these new filters have propelled low-frequency Raman spectroscopy forward in recent years.

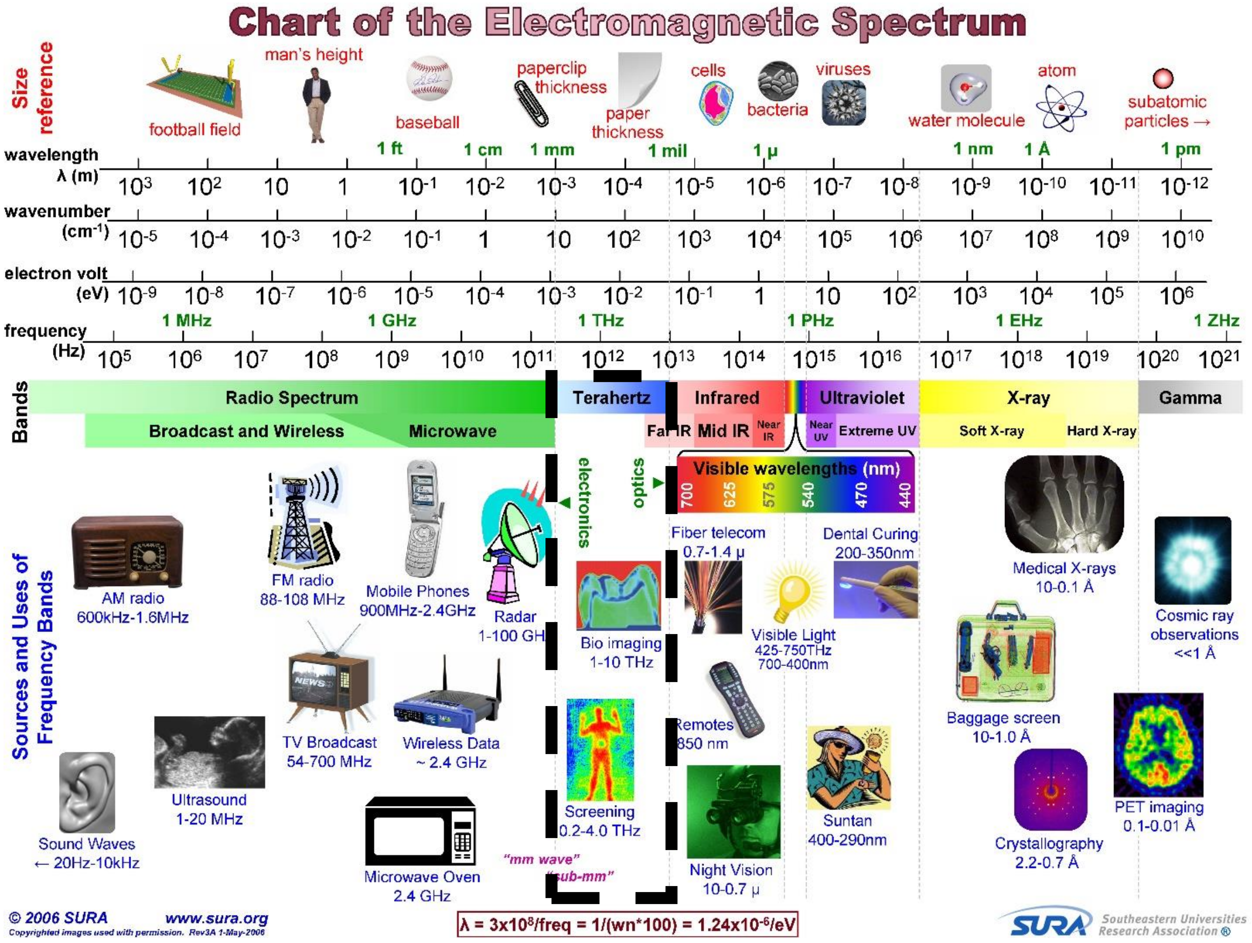

Figure 1-3. The electromagnetic spectrum, illustrating the terahertz region and its benefits outlined by the black dashed box, adapted from reference 39.

All molecules naturally exhibit vibrations at temperatures above 0 K. Based on symmetry, some vibrations change either the dipole moment or polarizability of molecules within a crystal. If these vibrations occur at the same frequency as incoming radiation, resonance occurs, and the radiation is absorbed or scattered by the sample, exhibiting peaks in the spectrum at the corresponding frequencies. Vibrations that involve the dipole moment are IR active while vibrations involving polarizability are Raman active. While it is possible that some vibrational modes in a molecular system can be both IR and Raman active (as long as there is no inversion center), there is typically a large difference in the spectra from the same sample due to the different selection rules, making these methods complementary. One example is seen in *trans-trans* muconic acid shown in **Figure 1-4** and discussed in **Chapter 4**. A more in-depth discussion of low-frequency spectroscopy and the generation of THz is discussed in **Chapter 2**.

Over the course of this research, low-frequency spectroscopy was used to investigate the vibrations in many chemical systems. By obtaining spectra at different temperatures, it is possible to observe how peaks shift. Typically, vibrational modes are considered to behave harmonically with evenly spaced energy levels in a symmetric well. In reality the well is actually asymmetric, and as temperature changes the unit cells volumes also change, causing vibrations to shift and result in anharmonic effects with unusual spectral results. While there are many instances of low-frequency vibrational spectroscopy as a method of fingerprinting and identifying a sample, in order to find significant meaning and actual motions that the vibrations correspond to, computational simulations are a necessity.

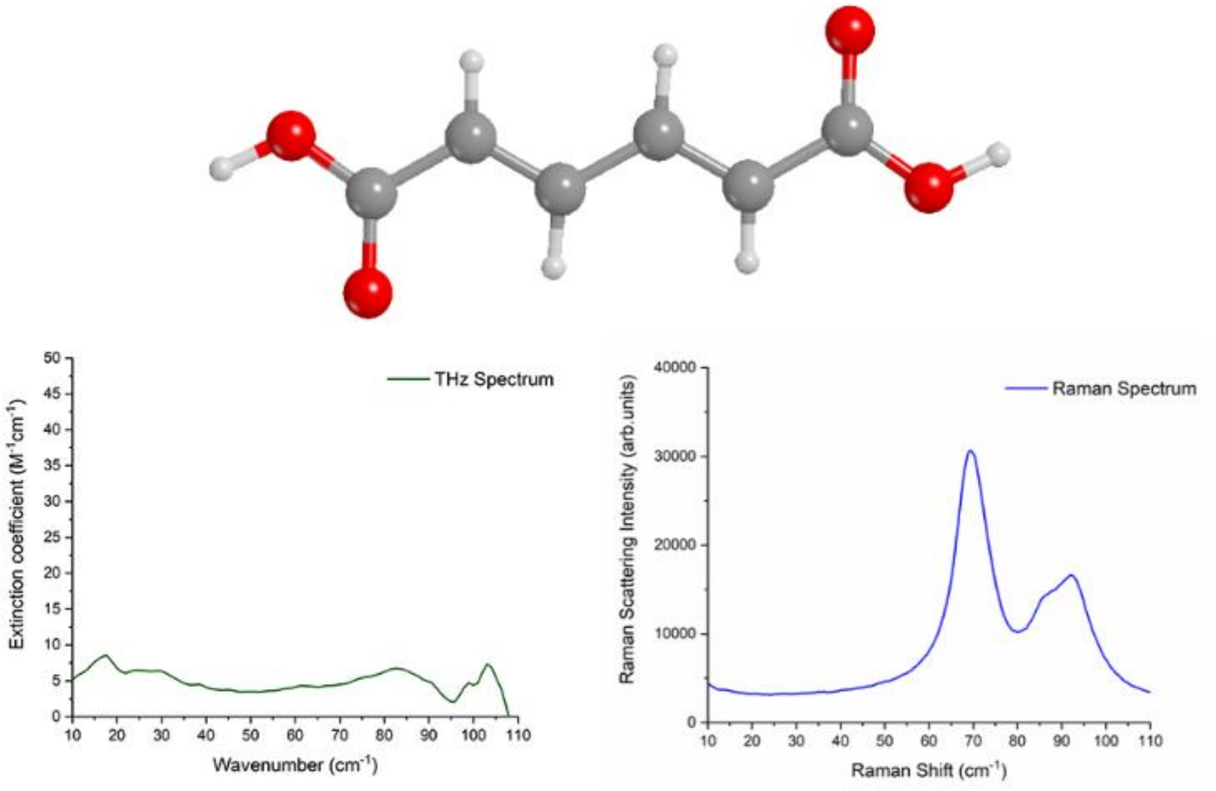

Figure 1-4. Terahertz and Raman spectra of crystalline *trans-trans* muconic acid, demonstrating how low-frequency spectra can be observed in one spectroscopic method and not the other.

1.3.3 Density Functional Theory

The combination of X-ray diffraction and low-frequency spectroscopy provides the ideal scenario for analysis with solid-state density functional theory (ss-DFT). In mid-IR spectroscopy, there are characteristic modes that correspond to specific vibrations within a chemical system, such as a narrow C=O peak at ~1700 cm^{-1} or a broad peak at ~3000 cm^{-1} representing OH stretches. However, in the low-frequency range there are no peaks that are universally defined, and ss-DFT can be used to solve this problem.

Using ss-DFT, it is possible to simulate crystalline solids using previously measured structures as a starting point. By obtaining a simulated low-frequency spectrum from an optimized structure that closely agrees with experimental results, it is possible to assign motions to the corresponding peaks. These motions would be very difficult to identify via any other method, making ss-DFT a valuable tool for further insight when interpreting low-frequency spectra.

When structural and vibrational simulations agree with experimental results, confidence is established, and the energetic properties of a system can also be reliably investigated. By calculating the total energy of crystalline unit cells, it is possible to determine the relative energies between isomers and polymorphic systems. Gibbs free energy curves can aid in the determination of polymorph stabilities at any given temperature. It is also possible to deconstruct the total electronic energy into cohesive and conformational energies, which provides insight into what keeps molecules in a crystal bound together (e.g. strength of London dispersion forces, hydrogen bonding), and the internal energy of a molecule held within a crystal.

In this work, the CRYSTAL[46, 47] software package is used for all ss-DFT calculations, utilizing periodic boundary conditions to simplify the infinitely extended three-dimensional crystal array. The use of DFT will be discussed in further detail in **Chapter 3**.

1.4 Summary of the Chapters

The experimental techniques of X-ray diffraction, THz spectroscopy, and low-frequency Raman spectroscopy used in this work are discussed in detail in **Chapter 2**. This covers how X-ray methods differ from one another in setup and analysis, as well as how THz and Raman spectrometers operate. **Chapter 3** provides a further look into the DFT methods that are used in all calculations in this work, as well as the nuances that make ss-DFT a reliable tool for the analysis of crystalline systems.

The original research portion begins in **Chapter 4,** with a polymorph study of *cis-trans* muconic acid, wherein *cis-cis* muconic acid is found to convert to two *cis-trans* muconic acid polymorphs with very different hydrogen bonding patterns depending on the heat applied and time of crystallization. All solids are examined via X-ray diffraction and THz spectroscopy. The continuation of this work is performed in **Chapter 5**, which discusses how *cis-cis* muconic acid converts to *cis-trans* muconic acid when dissolved in water, utilizing a muconate ion intermediate in the mechanism. This is the only chapter which does not use ss-DFT, although gas-phase DFT is used to simulate individual molecules.

1,2,4,5-tetrabromobenzene is discussed in **Chapter 6**, which investigates how a polymorph change can occur reversibly with temperature. This study is performed using low-frequency Raman spectroscopy and ss-DFT to determine and detect the causes of polymorphic change, leading to the discovery of the specific vibrational mode that causes the conversion from one form to another. **Chapter 7** is an investigation of the vibrational modes in glutaric acid using low-frequency spectroscopy. In the low-frequency Raman spectrum, it was possible to identify and investigate a unique mode that shifts abnormally with temperature. With ss-DFT, it was possible to determine the motion and the chemical origins of the odd behavior. The final study involves quinacridone dyes in **Chapter 8**, which are experimentally characterized via PXRD and THz spectroscopy. In the PXRD patterns, it was found that some peaks for one of the quinacridone polymorphs (β-quinacridone) shift in unusual directions in response to temperature. Using ss-DFT, it was possible to simulate this change in the PXRD pattern and determine which planes in the unit cell these peaks correspond to.

The collection of research in this work details the many effects that temperature can have on different crystalline systems. Using a combination of theoretical and experimental techniques provides further insight into the intermolecular and intramolecular forces as well as the energetics that govern chemical systems. This research has furthered the knowledge of the behavior of small organic crystals and the nature of how isomerization and polymorph transitions can be facilitated and stabilized by temperature.

1.5 References

(1) Bernstein, J.; Bernstein, J. M.; Crystallography, I. U. o.; Press, O. U., *Polymorphism in Molecular Crystals*. ed.; Clarendon Press: 2002.

(2) Vonnegut, K., *Cat's cradle*. ed.; Delacorte Press: New York, 1963.

(3) Boldyreva, E. V.; Drebushchak, V. A.; Drebushchak, T. N.; Paukov, I. E.; Kovalevskaya, Y. A.; Shutova, E. S., Polymorphism of glycine, Part I. *Journal of Thermal Analysis and Calorimetry* **2003,** 73, (2), 409-418.

(4) Siegrist, T.; Fleming, R. M.; Haddon, R. C.; Laudise, R. A.; Lovinger, A. J.; Katz, H. E.; Bridenbaugh, P.; Davis, D. D., The crystal structure of the high-temperature polymorph of α–hexathienyl (α–6T/HT). *Journal of Materials Research* **2011,** 10, (9), 2170-2173.

(5) T., S.; C., B.; S., H.; M., S.; P., P.; D., C.; B., B.; C., K., A Polymorph Lost and Found: The High-Temperature Crystal Structure of Pentacene. *Advanced Materials* **2007,** 19, (16), 2079-2082.

(6) Fabbiani, F. P. A.; Allan, D. R.; David, W. I. F.; Moggach, S. A.; Parsons, S.; Pulham, C. R., High-pressure recrystallisation-a route to new polymorphs and solvates. *CrystEngComm* **2004,** 6, (82), 505-511.

(7) G., I. H.; F., P.; A., B., Polymorphism of phenylbutazone: Properties and compressional behavior of crystals. *Journal of Pharmaceutical Sciences* **1977,** 66, (5), 669-673.

(8) Flaten, E. M.; Seiersten, M.; Andreassen, J.-P., Polymorphism and morphology of calcium carbonate precipitated in mixed solvents of ethylene glycol and water. *Journal of Crystal Growth* **2009,** 311, (13), 3533-3538.

(9) Parmar, M. M.; Khan, O.; Seton, L.; Ford, J. L., Polymorph Selection with Morphology Control Using Solvents. *Crystal Growth & Design* **2007,** 7, (9), 1635-1642.

(10) Nishimura, S.-i.; Tanibata, N.; Hayashi, A.; Tatsumisago, M.; Yamada, A., The crystal structure and sodium disorder of high-temperature polymorph β-Na3PS4. *Journal of Materials Chemistry A* **2017,** 5, (47), 25025-25030.

(11) Sclar, C. B.; Carrison, L. C.; Gager, W. B.; Stewart, O. M., Synthesis and stability of a high-pressure polymorph of sulfur. *Journal of Physics and Chemistry of Solids* **1966,** 27, (8), 1339-1343.

(12) Angus, J. C.; Wang, Y.; Sunkara, M., Metastable Growth of Diamond and Diamond-Like Phases. *Annual Review of Materials Science* **1991,** 21, (1), 221-248.

(13) Barczewski, M.; Matykiewicz, D.; Hoffmann, B., *Effect of Quinacridone Pigments on Properties and Morphology of Injection Molded Isotactic Polypropylene*. ed.; 2017; Vol. 2017, p 7043297.

(14) Sainz-Díaz, C. I.; Francisco-Márquez, M.; Soriano-Correa, C., Polymorphism, Intermolecular Interactions, and Spectroscopic Properties in Crystal Structures of Sulfonamides. *Journal of Pharmaceutical Sciences* **2018,** 107, (1), 273-285.

(15) Wille, R. L.; Lutton, E. S., Polymorphism of cocoa butter. *Journal of the American Oil Chemists Society* **1966,** 43, (8), 491-496.

(16) Vrecˇer, F.; Srcˇicˇ, S.; Sˇmid-Korbar, J., Investigation of piroxicam polymorphism. *International Journal of Pharmaceutics* **1991,** 68, (1), 35-41.

(17) Llinas, A.; Box, K. J.; Burley, J. C.; Glen, R. C.; Goodman, J. M., A new method for the reproducible generation of polymorphs: two forms of sulindac with very different solubilities. *Journal of Applied Crystallography* **2007,** 40, (2), 379-381.

(18) Llinàs, A.; Goodman, J. M., Polymorph control: past, present and future. *Drug Discovery Today* **2008,** 13, (5), 198-210.

(19) Karabas, I.; Orkoula, M. G.; Kontoyannis, C. G., Analysis and stability of polymorphs in tablets: The case of Risperidone. *Talanta* **2007,** 71, (3), 1382-1386.

(20) Brits, M.; Liebenberg, W.; de Villiers, M. M., Characterization of polymorph transformations that decrease the stability of tablets containing the WHO essential drug mebendazole. *Journal of Pharmaceutical Sciences* **2010,** 99, (3), 1138-1151.

(21) Tandon, R.; Tandon, N.; Thapar, R. K., Patenting of polymorphs. *Pharmaceutical Patent Analyst* **2018,** 7, (2), 59-63.

(22) Kapczynski, A.; Park, C.; Sampat, B., Polymorphs and Prodrugs and Salts (Oh My!): An Empirical Analysis of "Secondary" Pharmaceutical Patents. *PLoS ONE* **2012,** 7, (12), e49470.

(23) Redondo, G. L. M., Retrospective and Analytical Study of the Doctrine Related Pharmaceutical Polymorphism and Patents. *Journal of Innovations in Pharmaceuticals and Biological Sciences* **2015,** 2, (4), 579-595.

(24) Wheatley, P. J., 1163. The crystal and molecular structure of aspirin. *Journal of the Chemical Society (Resumed)* **1964**, (0), 6036-6048.

(25) Vishweshwar, P.; McMahon, J. A.; Oliveira, M.; Peterson, M. L.; Zaworotko, M. J., The Predictably Elusive Form II of Aspirin. *Journal of the American Chemical Society* **2005,** 127, (48), 16802-16803.

(26) Shtukenberg, A. G.; Hu, C. T.; Zhu, Q.; Schmidt, M. U.; Xu, W.; Tan, M.; Kahr, B., The Third Ambient Aspirin Polymorph. *Crystal Growth & Design* **2017,** 17, (6), 3562-3566.

(27) Shafranovskii, I. I., 14.10. Kepler's crystallographic ideas and his tract "The six-cornered snowflake". *Vistas in Astronomy* **1975,** 18, 861-876.

(28) xf; ntgen, W. C., On a New Kind of Rays. *Science (New York, N.Y.)* **1896,** 3, (59), 227-231.

(29) Forman, P., The Discovery of the Diffraction of X-Rays by Crystals; A Critique of the Myths. *Archive for History of Exact Sciences* **1969,** 6, (1), 38-71.

(30) Palenik, G. J.; Jensen, W. P.; Suh, I.-H., The History of Molecular Structure Determination Viewed through the Nobel Prizes. *Journal of Chemical Education* **2003,** 80, (7), 753.

(31) Patyk, E.; Skumiel, J.; Podsiadło, M.; Katrusiak, A., High-Pressure (+)-Sucrose Polymorph. *Angewandte Chemie International Edition* **2012,** 51, (9), 2146-2150.

(32) Basis Set Exchange. https://bse.pnl.gov/bse/portal

(33) Seco-Martorell, C.; López-Domínguez, V.; Arauz-Garofalo, G.; Redo-Sanchez, A.; Palacios, J.; Tejada, J., Goya's artwork imaging with Terahertz waves. *Opt. Express* **2013,** 21, (15), 17800-17805.

(34) Jackson, J. B.; Mourou, M.; Whitaker, J. F.; Duling, I. N.; Williamson, S. L.; Menu, M.; Mourou, G. A., Terahertz imaging for non-destructive evaluation of mural paintings. *Optics Communications* **2008,** 281, (4), 527-532.

(35) Janssens, K.; Dik, J.; Cotte, M.; Susini, J., Photon-Based Techniques for Nondestructive Subsurface Analysis of Painted Cultural Heritage Artifacts. *Accounts of Chemical Research* **2010,** 43, (6), 814-825.

(36) Zeitler, J. A.; Shen, Y.; Baker, C.; Taday, P. F.; Pepper, M.; Rades, T., Analysis of Coating Structures and Interfaces in Solid Oral Dosage Forms by Three Dimensional Terahertz Pulsed Imaging. *Journal of Pharmaceutical Sciences* **2007,** 96, (2), 330-340.

(37) Wagh, M. P.; Sonawane, Y. H.; Joshi, O. U., Terahertz technology: a boon to tablet analysis. *Indian J Pharm Sci* **2009,** 71, (3), 235-41.

(38) Federici, J. F.; Schulkin, B.; Huang, F.; Gary, D.; Barat, R.; Oliveira, F.; Zimdars, D., THz imaging and sensing for security applications - explosives, weapons and drugs. *Semicond. Sci. Technol.* **2005,** 20, (7), S266-S280.

(39) Zeitler, J. A.; Kogermann, K.; Rantanen, J.; Rades, T.; Taday, P. F.; Pepper, M.; Aaltonen, J.; Strachan, C. J., Drug hydrate systems and dehydration process studied by terahertz pulsed spectroscopy. *Int. J. Pharm.* **2007,** 334, (1-2), 78-84.

(40) Allis, D. G.; Prokhorova, D. A.; Korter, T. M., Solid-State Modeling of the Terahertz Spectrum of the High Explosive HMX. *The Journal of Physical Chemistry A* **2006,** 110, (5), 1951-1959.

(41) Hu, Y.; Huang, P.; Guo, L.; Wang, X.; Zhang, C., Terahertz spectroscopic investigations of explosives. *Physics Letters A* **2006,** 359, (6), 728-732.

(42) Ueno, Y.; Rungsawang, R.; Tomita, I.; Ajito, K., Quantitative Measurements of Amino Acids by Terahertz Time-Domain Transmission Spectroscopy. *Analytical Chemistry* **2006,** 78, (15), 5424-5428.

(43) Sethy, P.; Pratyush, S.; Mishra, R.; Behera, S., *An Introduction to Terahertz Technology, Its History, Properties and Application*. ed.; 2015.

(44) Lewis, R. A., A review of terahertz sources. *Journal of Physics D: Applied Physics* **2014,** 47, (37), 374001.

(45) SURA Terahertz Applications Symposium. http://www.sura.org/commercialization/terahertz.html (7/2/2018),

(46) Dovesi, R.; Erba, A.; Orlando, R.; Zicovich-Wilson, C. M.; Civalleri, B.; Maschio, L.; Rérat, M.; Casassa, S.; Baima, J.; Salustro, S.; Kirtman, B., Quantum-mechanical

condensed matter simulations with CRYSTAL. *Wiley Interdisciplinary Reviews: Computational Molecular Science* **2018,** 0, (0), e1360.

(47) Dovesi, R.; Orlando, R.; Erba, A.; Zicovich-Wilson, C. M.; Civalleri, B.; Casassa, S.; Maschio, L.; Ferrabone, M.; De La Pierre, M.; D'Arco, P.; Noel, Y.; Causa, M.; Rerat, M.; Kirtman, B., CRYSTAL14: A program for the ab initio investigation of crystalline solids. *Int. J. Quantum Chem.* **2014,** 114, (19), 1287-1317.

CHAPTER 2. Experimental Techniques

2.1 X-ray Crystallography

A crystal is a solid that has a regular repeating arrangement of atoms. Because crystals are in a neat, ordered array, there is a finite amount of ways that they can pack. There are seven crystal systems: triclinic, monoclinic, orthorhombic, tetrahedral, trigonal, hexagonal, and cubic[1, 2]. These systems are differentiated depending on the type of symmetry that is present, which results in a relationship where it is often the case that multiple unit cell dimensions or angles are equal to one another. The seven crystal systems can be further categorized into the 230 space groups[3, 4] depending on the atomic symmetry within the crystal which defines all of the possible ways that a crystalline system can possibly be arranged. In order to determine the space group and atomic structure of a crystal, X-ray crystallography is the most common tool.

The wavelength of X-rays are approximately 0.1-10 nm. The distances typically observed between atoms in a crystal are within this range, indicating that it is possible to determine the distances between atoms using X-rays. The relationship between atomic distance and the X-ray scattering angles are defined by Bragg's law[5-7]:

$$2d\sin(\theta) = n\lambda \tag{2.1}$$

where d is the distance between parallel atomic planes in the crystal lattice, θ is the angle of the incident X-rays, and λ is the wavelength of the X-rays. While in-phase X-rays scatter off of the crystal, some X-rays diffract off atoms in the top plane, while others travel through the plane and diffract off of atoms in planes further into the crystal. When the X-rays that probe into the deeper layers diffract off the atoms with an integer with a distance that is an integer of the wavelength (*n*), the interference between the X-ray layers will be constructive[8]. This is shown in **Figure 2-1.** This constructive interference is how we gather meaningful data from X-ray diffraction.

2.1.1 Powder X-ray Diffraction (PXRD)

PXRD is used as a method to determine the identity of a bulk crystalline sample. In PXRD, a polycrystalline powder is homogenized and spread evenly on a sample holder. X-rays are then shone on the sample. There are two ways to perform PXRD and obtain results: By rotating the sample while the X-ray beam remains still or rotating the X-ray beam around the sample. In this work, a Bruker D8 ADVANCE PXRD system was used which operates using the latter method.

When one of the microcrystals in the powder diffracts X-rays in accordance with Bragg's law, a reflection will be observed. Depending on the rotation of the X-ray beam over the sample, the scattering angle will change, and the reflection will disappear unless the scattering angle remains the same. With an essentially random distribution of crystal positions arranged on the sample holder, all of the unique reflections in a sample are obtained, which forms a cone centered around the X-ray beam. When the cone is projected on a detector, a series of rings are observed for each unique reflection (shown in **Figure 2-2**), which corresponds to different planes within the crystal. From these rings, it is possible to generate unique peak positions and intensities for each diffraction ring obtained, giving each crystalline sample a unique powder pattern due to different unit cell dimensions and atomic positions[9]. This also allows for the analysis of crystalline mixtures.

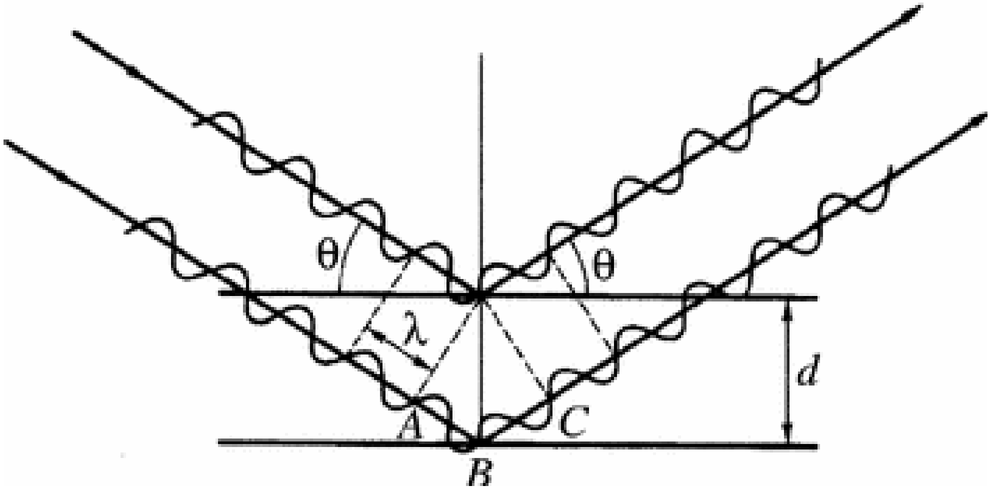

Figure 2-1. Illustration of Bragg's law diffracting off of different planes in a crystal. Adapted from reference 8.

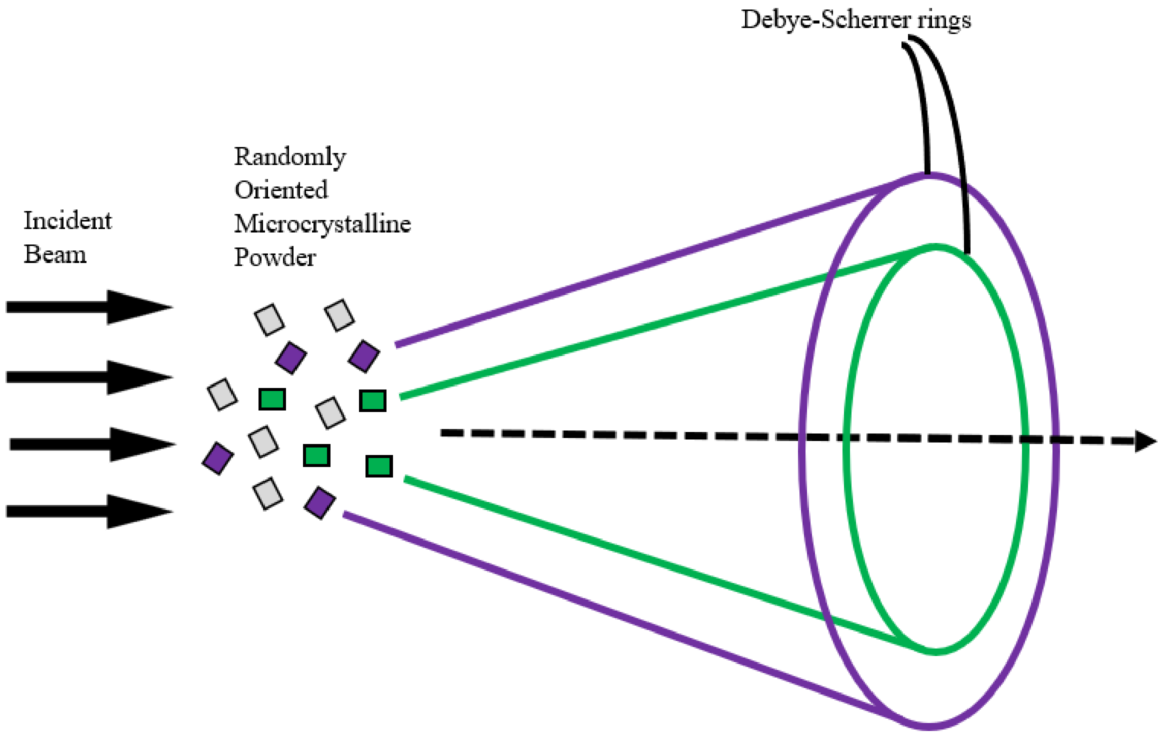

Figure 2-2. Diagram of how PXRD patterns are obtained from a bulk crystalline sample Purple and green represent different crystal arrangements in the bulk corresponding to different observed Debye-Scherrer rings. Adapted from reference 7.

A PXRD pattern has arbitrary units of intensity based on how long a time the sample is collected over, although all peaks have significant intensities to one another, with more intense peaks indicating a plane that contains more atoms along it. A way to define planes within a crystal is through Miller indices, defined by *h k l*, which have an inverse relationship to the real lattice vectors. An example is by defining the <0 2 0> plane, which corresponds to a plane halfway along the *k* index.

The positions of the peaks are measured in degrees as 2θ. Based on Braggs law, as 2θ increases, the distance between the planes decrease. There is a relationship between the interplanar spacing and the planes and the Miller indices (defined by *h k l* values) which differs depending on the crystal system. As an example, for an orthorhombic crystal, the relationship can be defined as:

$$\frac{1}{d_{hkl}^2} = \frac{h^2}{a^2} + \frac{k^2}{b^2} + \frac{l^2}{c^2} \tag{2.2}$$

where d is the distance between planes, h, k, and l are the Miller indices, and a, b, and c are the dimensions of the unit cell.

While determining the unit cell dimensions from a PXRD pattern is relatively straightforward, it is also possible to determine the atomic structure of a crystal from PXRD results. This is done through a Rietveld refinement[10, 11]. In a Rietveld refinement, a structural model is guessed, and the corresponding PXRD pattern is compared to the experimental pattern. This is done multiple times in a trial-and-error fashion until a pattern is reached that adequately matches experiment. While this refining takes place, this process takes into account the baseline as well as the observed peaks which means that if the experimental data has a rising baseline or does not have well-defined peaks, it will not be a viable method of structure solving. It is much more common to solve a structure with single-crystal X-ray diffraction.

2.1.2 Single-Crystal X-ray Diffraction (SC-XRD)

The most common way to experimentally solve a crystal structure is through SC-XRD. In SC-XRD, a single crystal is mounted from a stock of grown crystals and mounted on a MiTeGen brand Dual Thickness MicroMount using paraffin oil. In this research, crystal structures were solved using a Bruker Kappa APEX II DUO diffractometer. This system allows for samples to be taken at a temperature range of 90 K-298 K and can use both molybdenum or copper to generate X-rays at wavelengths of 0.7108 Å and 1.5418 Å, respectively. It is often the case that molybdenum is the preferred source when crystals contain large metal atoms, while copper is preferred when examining crystals that only contain small organic molecules.

Once a crystal is successfully loaded on a MicroMount, it is centered in the diffractometer so that the X-ray beam will always be hitting the crystal. The MicroMounts are highly X-ray transparent, so they do not appreciably affect a sample collection. Initially, a brief scan is performed to determine the unit cell and space group of the crystal. When the X-rays are shone on a single crystal, individual spots are observed which correspond to X-rays diffracting off evenly spaced planes within the crystal. If spots bleed into one another, it is an indication that the crystal is not good enough quality or has defects that interfere with the data collection. Conversely, if minimal to no spots are observed it indicates that the sample may not truly be crystalline, the crystal is too small, or the X-rays are not properly hitting the sample.

From the initial unit cell check, a collection of reflections are obtained which can be used to run a full scan of the crystal. The length of a full scan depends on the symmetry of the crystal, the angular increments to be scanned over, and the time spent on each angle. Collections with longer scans are typically better quality, which can be useful if there are few reflections in the crystal. Crystals with higher space group symmetry can be collected faster because certain angular positions can be omitted due to redundancy within the crystal.

The SC-XRD used in this work is connected to a liquid nitrogen Cryocool LN-3 cooling system, which allows for structures to be obtained at temperatures between 90 K and 300 K. 90 K structures are typically preferred, as there is less thermal motion and atomic positions are easier to define when solving. Also, because quantum calculations are performed at 0 K conditions (**Chapter 3**), the most accurate way to compare simulated to experimental results is with a cold structure. However, the temperature control allows for the analysis of the effect of temperature on the unit cell of a crystal which can give insight into many chemical systems, such as how the volumes and densities of polymorphs can change at different rates and effect their relative stabilities (**Chapter 4**).

After a full collection is complete, the crystal structure is solved in APEX 3 using a SHELXL[12, 13] module. In this process, the reflection spots that are found during a collection are integrated to determine the atomic positions within the crystal, allowing for the structure to be solved. A best guess of a molecular formula must be included to allow for accurate solving. Once a general structure is obtained, a series of refinements are performed which typically involves adding hydrogen atoms to the crystal structure which were not placed initially, until the desired structure is obtained. A final anisotropic refinement gives a resulting crystal structure.

The use of SC-XRD requires a certain amount of practice. The ability to pick a single crystal from a stock of crystals can be very challenging, and it is possible that multiple crystallizations and changing solvent or crystallization time is necessary to obtain crystals that are large enough and of good enough quality to adequately use. The process of solving a crystal structure presents a very different challenge. The difficulty is dependent on crystal quality and atomic makeup, and even simple crystals require chemical intuition when solving to determine proper atom placements and geometries. If a crystal is twinned or is disordered, solving is still possible, but requires more time and skill. In the case of some twinned crystals, it is possible to omit reflections from one twin and solve for only one crystal, but the reflections that this omits negatively impacts the quality of the data.

In the study of polymorphs, X-ray diffraction is overall an ideal method. Since polymorphs contain the same molecules packed differently (and often in different space group symmetries, indicating different atoms along different crystal planes), PXRD shows different powder patterns for each polymorph, easily differentiating them from one another[14-16]. SC-XRD can take this a step further and determine the atomic positions of the polymorphs. A combination of both PXRD and SC-XRD provides a much more complete analysis than either could produce alone. With this structural data known, analysis into the intermolecular forces and interactions that make polymorphs different is possible.

2.2 Low-Frequency Vibrational Spectroscopy

The way that molecules are packed in a solid greatly impacts the vibrational spectra that are observed. This is especially true below the fingerprint region (< 500 cm^{-1}) where intermolecular interactions can be observed. Because of the unique packing of solids, it is possible for solids that contain the same molecules to exhibit different intermolecular interactions based on their packing, showing markedly different spectra in the low-frequency region[17-19]. In order to access the low-frequency region, terahertz time-domain spectroscopy and low-frequency Raman spectroscopy can be utilized. A combination of both techniques allows for the complete determination of all vibrational motions in a sample. In this section, the differences between both techniques and the generation and detection of terahertz pulses will be discussed, as well as how it is possible to obtain Raman spectra in the low-frequency region.

2.2.1 Vibrational Spectroscopy

When radiation interacts with a sample, it can absorb a portion of the energy which causes different effects. Low energy microwaves cause molecular rotations, high energy ultraviolet radiation can cause electronic transitions, and IR radiation causes molecules to vibrate. The vibrations that are caused can help to define a chemical system through vibrational spectroscopy. As a basic model, vibrational spectroscopy of a bond stretching motion in a diatomic molecule can be modeled by a one-dimensional quantum harmonic oscillator[20]. In a harmonic oscillator, a molecule can only exist in discrete energy levels, which are defined as:

$$E_n = \left(n + \frac{1}{2}\right)\hbar\omega \tag{2.3}$$

where n is a positive integer value that defines the energy state (n=0 for the ground state), ħ is Planck's constant divided by 2π and ω is 2π times the frequency. Because of the simplifications that exist in a diatomic molecule, it is possible to define the frequency ω as:

$$\omega = \sqrt{\frac{k}{m_r}} \tag{2.4}$$

Where k is the force constant and m_r is the reduced mass of the system. This indicates that any chemical system with a different force constant or reduced mass will exhibit different frequencies. Unfortunately, the harmonic oscillator is not an accurate way to define vibrations in the real world, and an anharmonic oscillator is much more accurate in defining vibrational states. The shape of the anharmonic oscillator can be approximated by the Morse potential[21]:

$$V = D_e(1 - e^{-\beta(r-r_0)^2}) \tag{2.5}$$

where D_e is the depth of the well, β is the level of curvature at the bottom of the well and $(r - r_0)$ is the internuclear distance. The Morse potential can be expanded using a Taylor series which defines the energy level differences as:

$$E_n = \left(n + \frac{1}{2}\right)\omega_e - \left(n + \frac{1}{2}\right)^2 \omega_e x_e \tag{2.6}$$

where the first term is essentially the same as the harmonic oscillator and the second term is an anharmonic correction. While energy levels in a harmonic oscillator are evenly spaced, this results in energy levels getting closer together as *n* increases. This also implies that anharmonic effects become more prevalent as the amplitude of the oscillation becomes larger (i.e. at higher energy levels).

The energy levels within the well eventually become infinitely close together as the slope of the well falls off, corresponding to the dissociation energy of a molecule[22, 23]. A comparison of the harmonic and anharmonic potential energy wells are shown in **Figure 2-3**. When a sample absorbs light, it is initially in the $n=0$ ground state. When excited, the allowed vibrational mode must be $n \pm 1$. While the equations and examples given were for diatomic molecules, it is important to note that all molecules have some level of anharmonic behavior and all follow the same basic vibrational rules.

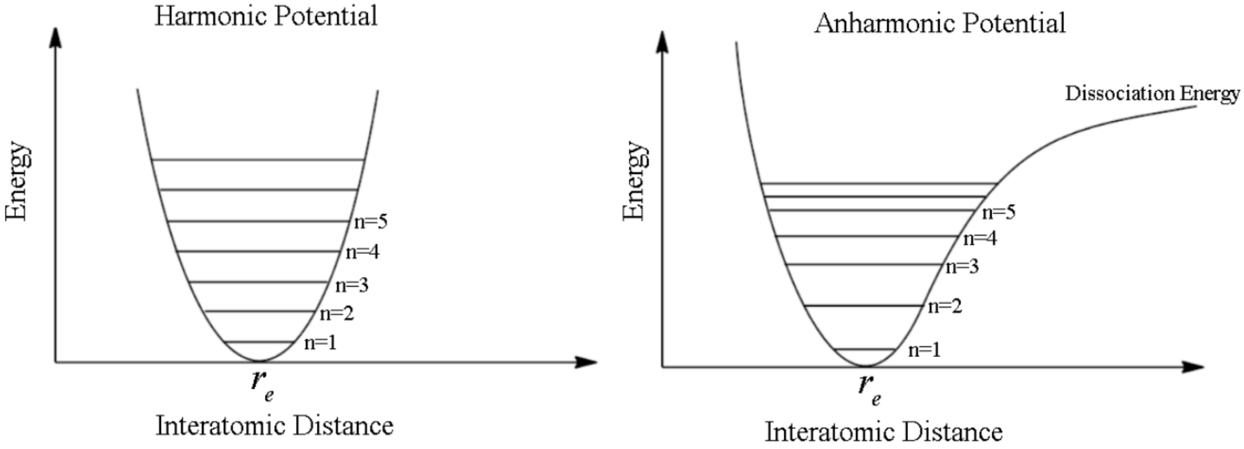

Figure 2-3. Illustration of the harmonic oscillator (left) and anharmonic oscillator (right). Adapted from reference 23.

2.2.2 Raman Scattering

When a sample is exposed to light, the sample will absorb a portion of that light. However, a small amount of that light will be scattered by the sample in all directions. The light that is scattered can have varying frequencies. If the scattered light has the same frequency as the incident light, it is known as Rayleigh scattering. A large majority of scattering that occurs is Rayleigh scattering. The probability of light undergoing Rayleigh scattering is given by the equation:

$$I \propto \frac{1}{\lambda^4} \tag{2.7}$$

where I is the scattering intensity and λ is the wavelength of light. Because intensity drops off so fast with wavelength, light with smaller wavelengths will scatter considerably more. This is the reason behind why the sky is blue, because of all the light released by the sun, blue light with a lower wavelength scatters much more than any other color in the visible spectrum.

While Rayleigh scattering accounts for a vast majority of light scattering, one in $10^6 – 10^8$ photons has a scattered frequency that is not equal to the incident light[24]. This is the basis for Raman scattering. In Raman scattering, a photon is excited to a virtual state which then falls from its virtual state to a lower energy level. There are three options for energy levels that the photon can fall to. The most common is that it returns to the energy level it was originally in as Rayleigh scattering. However, sometimes the energy level that the photon falls to is at a higher energy level than where it began. This is known as a Stokes peak. It is also possible for the electron to fall to an energy level lower than where it started, known as an anti-Stokes peak. This is illustrated in **Figure 2-4**.

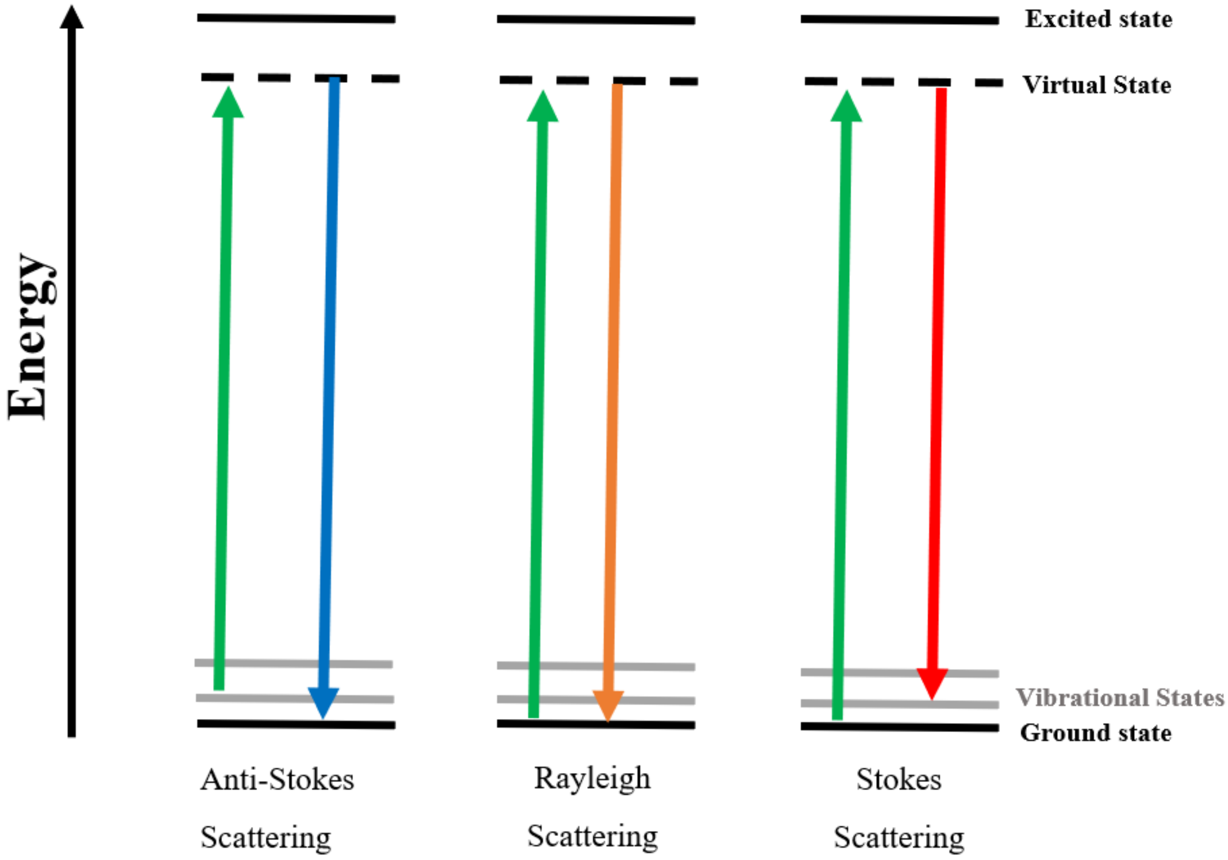

Figure 2-4. Illustration of anti-stokes shift (left), Rayleigh scattering, and Stokes scattering (right).

2.2.3 Vibrational Selection Rules

Only certain transitions are allowed in a chemical system, and all motion can be described by the total wavefunction:

$$\Psi(r,R) = \psi_e(r,R_e)\psi_v(R)\psi_r(R) \tag{2.8}$$

where *R* is the equilibrium nuclear coordinates, ψ_e is the electronic wavefunction, ψ_v is the vibrational wavefunction, and ψ_r is the rotational wavefunction. In order to simplify the transition moment, the rotational and electronic portion can be removed which can define the integral for the vibration transition moment as:

$$M = \int \psi_v'(R) \cdot \psi_v''(R) dR \tag{2.9}$$

where the prime terms represent a lower energy state and the double prime terms represent a higher energy state.

While it is possible for an atom or molecule to absorb radiation and go to another energy level, it depends if the frequency from the radiation is equal to the difference between the two eigenstates Ψ_1 and Ψ_2. If this is the case, it is known as the transition moment. The probability of this transition occurring uses the vibrational transition moment from equation 2.9, given by:

$$< u >= \int \Psi_2^* \hat{u} \Psi_1 d\tau \tag{2.10}$$

where <u> is the intensity of the absorption or emission depending on if Ψ_1 or Ψ_2 is larger, and $\hat{u}$ is the transition moment operator. This term will be non-zero if v = ± 1, which corresponds a vibrational energy level change, as shown in **Figure 2-3**. This is indicative of the vibrational selection rule, which is that the change in energy level must be ± 1, ± 2, …, and the greater the change, the lower the intensity of the observed peak. An energy level change of ± 1 is referred to as the fundamental vibration, while anything larger is called an overtone.

2.2.3.1 IR Selection Rules

A vibrational transition is considered IR active if there is a change in dipole moment of the molecule or unit cell. This implies that no homonuclear diatomic molecule can be IR active, because it is impossible to induce a dipole in it. For polyatomic molecules, there is an electric dipole component associated with the three cartesian directions. For example, along the z coordinate, this is defined as:

$$\mu_x = \sum_i e_i z_i \tag{2.11}$$

where e_i is the charge on atom i and z_i is its z coordinate. If the change in x, y, or z components are non-zero during a vibration, it will be considered IR active.

2.2.3.2 Raman Selection Rules

A vibrational transition is considered Raman active if there is a change in polarizability in the molecule or unit cell. This is defined as:

$$P = \alpha E \tag{2.12}$$

where the polarizability is α, P is the induced dipole moment, and the electric field is E. It is often the case that atoms with larger electron clouds are more susceptible to polarizability. The polarizability is defined in a 3 X 3 matrix for anisotropic systems in order to account for all of the ways that it can respond to an electric field:

$$\alpha = \begin{bmatrix} \alpha_{xx} & \alpha_{xy} & \alpha_{xz} \\ \alpha_{yx} & \alpha_{yy} & \alpha_{yz} \\ \alpha_{zx} & \alpha_{yz} & \alpha_{zz} \end{bmatrix} \tag{2.13}$$

The diagonal of the matrix (α_{xx}, α_{yy}, and α_{zz}) corresponds to an electric field applied along the x, y, and z directions. The other matrix values define how strongly a system will polarize along a certain direction. For example, if α_{zx} was found to be large, it implies that an electric field along the z direction would strongly polarize in the x direction. Although not performed in this work, it is possible to perform Raman spectroscopy along distinct crystal faces in order to induce stronger polarizability, leading to different observed intensities depending on the position of the crystal. This can help in the characterization of vibrational modes by determining what directions have strongest intensity.

2.3 Instrumentation

Over the course of this research, various instrumentation was used to obtain results. While performing THz-TDS, two systems were used which generated and detected THz radiation from crystals or antennas. Low-frequency Raman spectroscopy makes it possible to detect the active modes that THz-TDS does not.

2.3.1 Sample Preparation

2.3.1.1 THz-TDS Sample Preparation

When performing THz-TDS, samples were mixed with polytetrafluoroethylene (PTFE) at w/w concentrations typically between 3-7%. The mixtures were then ball milled to create a homogenous mixture to reduce scattering and diffraction artifacts. The powder mixture was then compressed into 13 mm pellets of 2 mm thickness with a mass of approximately 550 mg. If a pure sample pellet was analyzed, it would absorb much too strongly, and the observed peaks would be too intense to provide accurate information. Contrary to this, if a pellet is too weak, no considerable peaks would be observed.

2.3.1.2 Raman Sample Preparation

There were two methods by which samples were prepared for Raman spectroscopy. The first method uses a pure powder sample in a 10 mm glass vial. The sample is placed in the sample holder attached to the spectrometer, and as long as the sampled powder is completely in the laser's path, a reliable spectrum will be collected.

In the second method of preparation, a sample pellet was made. Because Raman spectroscopy utilizes scattering and does not rely on probing through a sample like THz-TDS, a pure sample pellet of arbitrary thickness is used. Pellets are held in a cryostat (which allows for temperature-dependent measurements) at a further distance away from the probing laser, and while a lens is used to properly focus on the pellet there is less Raman scattering collection efficiency compared to using the powder samples. Both a powder and pellet sample are shown in **Figure 2-5.**

Figure 2-5. Powder (left) and pellet sample (right) for spectroscopic measurements.

2.3.2 Terahertz Generation and Detection

2.3.2.1 Custom-Built Terahertz Spectrometer

The work discussed in **Chapter 4** utilizes a custom-built terahertz time-domain spectrometer. In this system, an initial Coherent Verdi-V5 laser (diode-pumped Nd:YVO_4 at 527 nm) is used in tandem with a Coherent Mira Ti:Sapphire laser to generate 35 fs pulses centered at 800 nm. A Coherent Evolution laser is used to pump a Ti:Sapphire Regenerative Amplifier to produce 35 fs pulses at 800 nm with a maximum energy of 2.5 mJ/pulse. The beam is then split, creating detector and generator arms for performing THz research.

The other portion of the beam that was split travels through a ZnTe crystal that generates THz radiation through optical rectification with a time duration of ~200 ps. The ZnTe crystal is what limits the bandwidth of the instrument to approximately 3 THz. The pulse of THz radiation is then passed through an optical chopper, which is then directed onto an off-axis parabolic mirror which collimates the pulse. The collimated THz radiation is then focused by a second off-axis paraboloid mirror, which focuses the THz radiation onto the sample which absorbs the THz pulse at frequencies corresponding to the vibrations they exhibit.

After the THz radiation passes through the sample, a third off-axis parabolic mirror collimates the THz radiation again, and a fourth off-axis parabolic mirror directs the pulse to another ZnTe crystal which detects the THz radiation by free-space electro-optic sampling[25-27]. At the same time THz radiation arrives at the ZnTe crystal, the detection arm also arrives. The change in birefringence that is caused by the THz radiation affects the detector arm pulse. This pulse is changed from linearly polarized to elliptically polarized. The pulse is then passed through a quarter-wave plate which further refines the elliptically polarized light. The pulse then passes through a Wollaston prism, which separates the light into its corresponding vertical and horizontal components. Both of the beams are then focused on individual photodiodes, and the difference in the signal is recorded. Because length of a THz pulse is much monger than the detector arm pulse (200 fs vs. 35 fs), the THz beam is scanned in 0.95 fs increments using a time delay stage. The result of the scan gives amplitude and phase of the THz pulse which is used in analysis. The experimental setup is shown in **Figure 2-6**.

When using the custom-built THz spectrometer, data was acquired over 32 scans with a 32 ps window consisting of 3200 points. When analyzing a sample, a pure PTFE pellet with the same dimensions as the sample is used as a blank and run under identical conditions to the sample in order to get proper absorption units. The waveforms of the sample and the blank were treated using a Hanning window and then Fourier transformed. The sample spectrum is divided by the blank spectrum, giving a absorption spectrum with an intensity of optical density units. The optical density units can be converted to units of extinction coefficients using the concentration and dimensions of the sample pellet. Using extinction coefficients as units of intensity is useful because these values are constant no matter what instrument the data is taken on and is unique to the chemical system, making reproducing results a simple task.

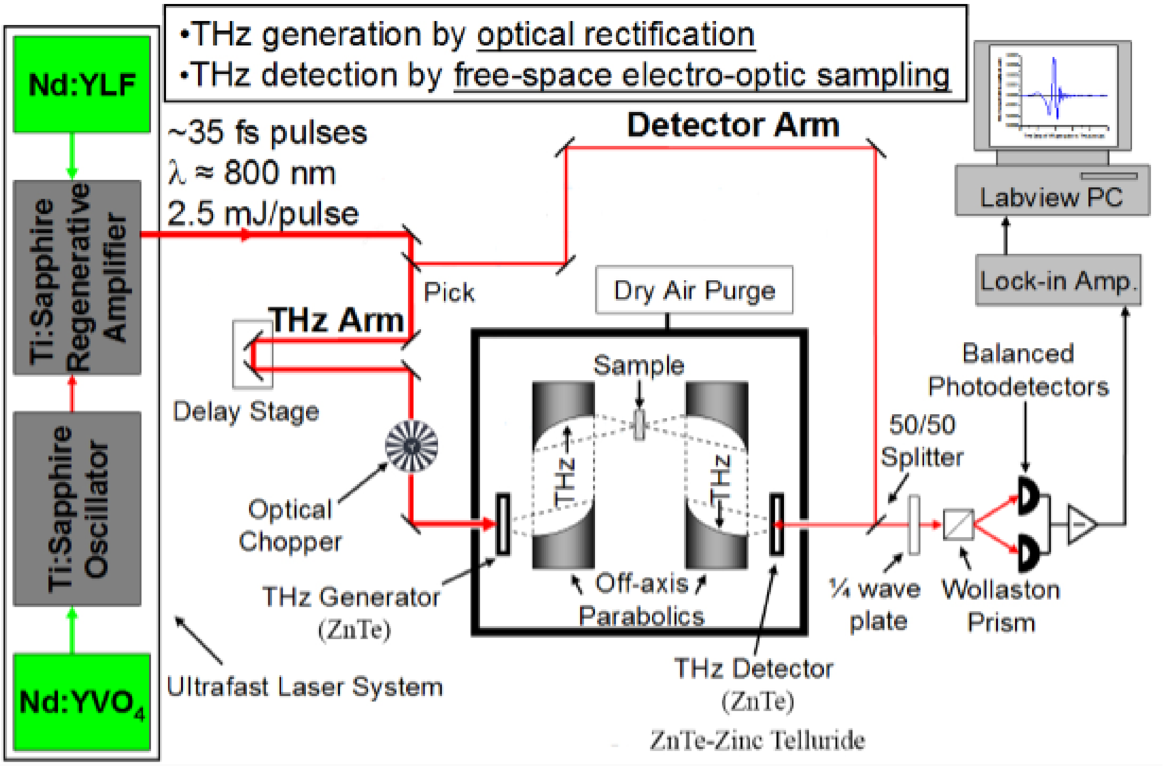

Figure 2-6. Experimental setup of the custom-built THz spectrometer.

2.3.2.2 Toptica TeraFlash Spectrometer

The second way that THz radiation was generated in the presented research (**Chapter 7**) was using a Toptica TeraFlash Spectrometer, shown in **Figure 2-7**. This is a commercial time-domain THz platform and utilizes a Toptica FemtoFiber femtosecond laser with a fiber-pigtailed InGaAs photoconductive antennas[28]. Much like ZnTe, the antennas act as both an emitter and receiver of the generated THz radiation which is induced by femtosecond near-infrared laser pulses.

In order for a photoconductive antenna to generate THz radiation, an antenna is made on a photoconductive substrate for contact with InGaAs, which is a semiconductor. At the center of the antenna structure there is a physical space gap. When voltage is applied across the gap using a power supply, electric energy is stored in the gap. When a femtosecond laser pulse illuminates the gap, it generates photo-excited carriers which create an ultra-short current pulse. The current generates pulsed THz radiation[29-31] due to the acceleration of charged species, resulting in electromagnetic radiation. The THz pulse then probes the sample. The use of an antenna for THz generation is shown in **Figure 2-8.**

When detecting THz radiation, the THz wave and femtosecond pulse are focused on another antenna's gap, which generates photo-excited carriers. This produces a current that flows with the arrival of a detection laser pulse and allows for detection. The detection pulse can be delayed, allowing for the electric field in the THz pulse to be recorded as a function of time, similarly to the scanning in the custom-built system, but in 2 fs increments.

There are distinct advantages to using the Toptica brand spectrometer over the custom-built spectrometer. The antenna setup uses considerably less space than the custom-built spectrometer and spectra can be obtained in approximately half the time. The use of antennas also allows for measurements to be recorded up to 150 cm^{-1} compared to the custom-built 100 cm^{-1} limit.

Figure 2-7. Commercial Toptica TeraFlash THz spectrometer.

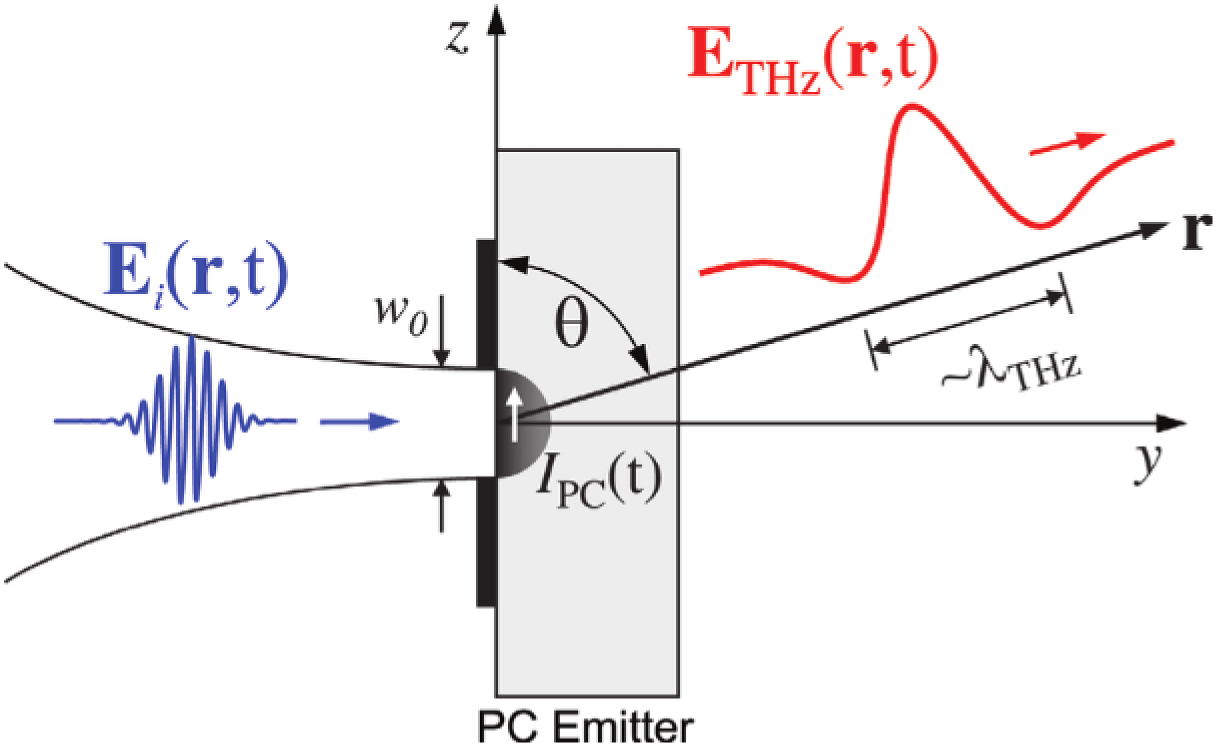

Figure 2-8. Illustration of the antenna system used to generate THz adapted from reference 28.

2.3.3 Low-Frequency Raman Spectroscopy

All Raman spectra in this work were obtained using an Ondax SureBlock XLF-CLM THz-Raman spectrometer with the laser stabilized at 784.7 nm and coupled to an Andor Shamrock 750 spectrograph with an Andor iDus 416 CCD camera. The Raman spectrometer is shown in **Figure 2-9.** Low-frequency Raman spectroscopy probes the same range as THz spectrometers, although this technique relies on light scattering instead of absorption.

As the 784.7 nm red light hits the sample, it causes Stokes and anti-Stokes inelastic scattering. Typically, scattering in the low-frequency range is difficult to obtain because they are lost within the Rayleigh peak. In order to resolve this issue, volume holographic grating notch filters (VGHs) are used, which are able to filter out the very specific wavelength corresponding to the Rayleigh peak by approximately 90%. To ensure that the Rayleigh peak is filtered out and one can clearly observe the modes that are present at very low frequencies, multiple VHG filters are used, each time filtering out 90% of the Rayleigh peak until the Rayleigh peak is diminished enough. This leads to resolvable peaks in Raman spectra as low as 5.0 cm^{-1} from the laser line, depending on how strongly the sample scatters.

When collecting a Raman spectrum, it is possible to change the number of acquisitions and exposure time. After the appropriate settings have been determined, a dark count background is taken to reduce noise in the data. In this work, it was found that 225 averaged exposures and a 3 second exposure time yielded spectra with excellent signal-to-noise ratios. In samples that scatter weakly, more averages can be taken, although this will increase the collection time, and there will eventually be a point of diminishing returns as the noise deceases as the square root of the number of averages

The Raman spectrometer allows for the power of the incident laser to be altered using a variable neutral density filter. This allows for powers between 2-113 mW to strike the sample. At lower powers, there is poorer signal-to-noise, which makes it harder to collect meaningful spectra of weakly scattering samples. However, as the laser power is increased to generate more Raman scattered photons, one has to be careful because more heat is imparted to the sample. At full power, it was determined that the temperature could reach up to 20° C higher than what was expected (**Chapter 6**). This is significant in systems where temperature induced polymorph changes or chemical degradation is possible, so there is merit in keeping the power low in these cases.

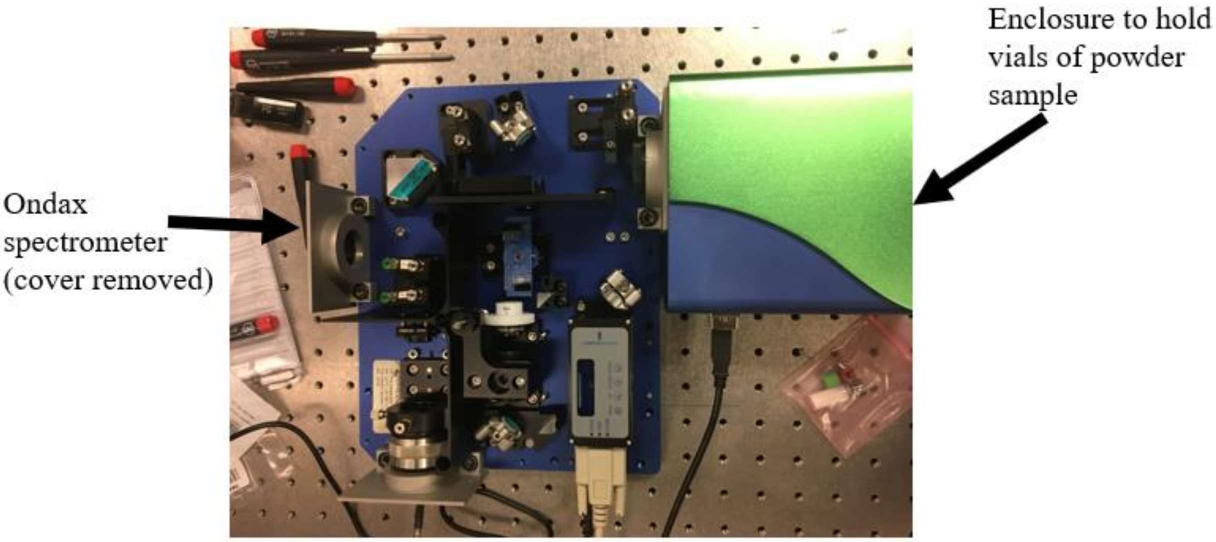

Figure 2-9. Ondax Raman spectrometer.

2.3.4 Temperature Dependent Measurements

In order to see how temperature affects the vibrational spectra of a crystalline sample and compare simulated 0 K data as accurately as possible to experimental results, spectra are often recorded at varying temperatures. In all cryogenic measurements for both THz and Raman, a Janis ST-100 cryostat is used and positioned so that the mounted pellets are perpendicular to the incoming radiation. TPX polymer windows in the cryostat are used in THz-TDS expeiments which does absrob THz radiation. In Raman measurements, the visible radiation passes through a glass window. A vacuum is applied to the sample chamber of the cryostat and then it is cooled with liquid nitrogen, allowing for spectra to be taken as low as 78 K. A Cryo-con 32 temperature controller also allows for spectra at intermediate temperatures to be taken using a combination of liquid nitrogen cooling and electrical heating.

There are expected trends from both THz and Raman spectra taken at different temperatures. In a typical low-frequency vibrational spectrum, the energy levels in the anharmonic oscillator are populated in multiple vibrational energy levels. The most populated is the fundamental $v=0 \rightarrow v=1$ transition, following the Boltzmann distribution. As the temperature decreases, less vibrational overtone transitions (transitions that are not $v=0 \rightarrow v=1$) occur due to reduced vibrational level populations. This narrows the Boltzmann distribution and results in a narrower, more intense peak. The narrowing and intensifying effect can often reveal weaker peaks that were concealed by the stronger peaks at higher temperatures, or turn what was originally observed as a single peak into multiple distinct peaks. The reason that peak narrowing is prevalent in the THz range is because energy level spacings are relatively small and higher levels can be more populated when compared to mid-IR energy differences at thousands of wavenumbers which do not narrow appreciably with temperature.

Another result of cooling is typically a contraction of crystalline unit cell dimensions. The thermal expansion and contraction of a lattice is a direct result of anharmonicity within a solid. As the unit cell contracts, atoms come closer together, which increases their force constants. The increase in force constant leads to an increase in frequency by equation 2.4, which is why a spectrum usually shifts to higher frequencies as the temperature decreases.

In a Raman spectrum it is possible to directly calculate the average temperature of a sample due to the nature of the Stokes and anti-Stokes peaks. This is done using the equation:

$$\frac{I_{anti-Stokes}}{I_{Stokes}} = \left(\frac{v_0 + v_1}{v_0 - v_1}\right)^4 e^{\frac{-hv_1}{kT}} \tag{2.14}$$

where I is the intensity of an anti-Stokes and its corresponding Stokes peaks, v_0 is the frequency of the exciting light, v_1 is the frequency of the Raman shift, h is Planck's constant, and k is the Boltzmann constant. Using this equation, it is possible to solve for the temperature (T). As previously mentioned, in Raman spectroscopic techniques, heating a sample is possible based on the power of the incident laser, and temperatures up to 320 K have been calculated when the laser is brought to full power. While an increased temperature broadens the observed features in Raman spectra, it provides a larger range for temperature analysis which is significant in the study of systems that undergo polymorph changes at warmer temperatures (**Chapter 6**).

2.4 References

(1) Suh, I. H.; Kim, K. J.; Choo, G. H.; Lee, J. H.; Choh, S. H.; Kim, M. J., The asymmetric unit of X-ray intensity data of the seven crystal systems. *Acta Crystallographica Section A* **1993,** 49, (2), 369-371.

(2) Dorset, D. L., X-ray Diffraction: A Practical Approach. *Microscopy and Microanalysis* **2005,** 4, (5), 513-515.

(3) M, H. D.; T, S. H., *Isotropy Subgroups Of The 230 Crystallographic Space Groups*. ed.; World Scientific Publishing Company: 1989.

(4) Buerger, M. J., Tables of the characteristics of the vector representations of the 230 space groups. *Acta Crystallographica* **1950,** 3, (6), 465-471.

(5) Cook, E.; Fong, R.; Horrocks, J.; Wilkinson, D.; Speller, R., Energy dispersive X-ray diffraction as a means to identify illicit materials: A preliminary optimisation study. *Applied Radiation and Isotopes* **2007,** 65, (8), 959-967.

(6) Kacher, J.; Landon, C.; Adams, B. L.; Fullwood, D., Bragg's Law diffraction simulations for electron backscatter diffraction analysis. *Ultramicroscopy* **2009,** 109, (9), 1148-1156.

(7) Barnes, P. J., Simon; Vickers, Martin Powder Diffraction. http://pd.chem.ucl.ac.uk/pdnn/diff2/kinemat2.htm (7/22/2018),

(8) Prestini, E., X-ray Crystallography: Protein Structure and DNA. In *The Evolution of Applied Harmonic Analysis: Models of the Real World*, Prestini, E., Ed. Springer New York: New York, NY, 2016; pp 151-180.

(9) Fultz, B.; Howe, J. M., *Transmission Electron Microscopy and Diffractometry of Materials*. ed.; Springer Berlin Heidelberg: 2013.

(10) McCusker, L. B.; Von Dreele, R. B.; Cox, D. E.; Louer, D.; Scardi, P., Rietveld refinement guidelines. *Journal of Applied Crystallography* **1999,** 32, (1), 36-50.

(11) Sakata, M.; Cooper, M. J., An analysis of the Rietveld refinement method. *Journal of Applied Crystallography* **1979,** 12, (6), 554-563.

(12) Sheldrick, G., A short history of SHELX. *Acta Crystallographica Section A* **2008,** 64, (1), 112-122.

(13) Sheldrick, G., Crystal structure refinement with SHELXL. *Acta Crystallographica Section C* **2015,** 71, (1), 3-8.

(14) Bellur Atici, E.; Karliga, B., Quantitative determination of two polymorphic forms of imatinib mesylate in a drug substance and tablet formulation by X-ray powder diffraction, differential scanning calorimetry and attenuated total reflectance Fourier transform infrared spectroscopy. *Journal of pharmaceutical and biomedical analysis* **2015,** 114, 330-40.

(15) Kommavarapu, P.; Maruthapillai, A.; Palanisamy, K., Identification and quantitative determination of eletriptan hydrobromide polymorphs: Thermal, diffractometric and spectrometric studies. *Journal of Taibah University for Science* **2015,** 9, (4), 586-593.

(16) Bunaciu, A. A.; Udriştioiu, E. g.; Aboul-Enein, H. Y., X-Ray Diffraction: Instrumentation and Applications. *Critical Reviews in Analytical Chemistry* **2015,** 45, (4), 289-299.

(17) Shen, Y.-C., Terahertz pulsed spectroscopy and imaging for pharmaceutical applications: A review. *International Journal of Pharmaceutics* **2011,** 417, (1), 48-60.

(18) Strachan, C. J.; Taday, P. F.; Newnham, D. A.; Gordon, K. C.; Zeitler, J. A.; Pepper, M.; Rades, T., Using terahertz pulsed spectroscopy to quantify pharmaceutical polymorphism and crystallinity. *J Pharm Sci* **2005,** 94, (4), 837-46.

(19) McIntosh, A. I.; Yang, B.; Goldup, S. M.; Watkinson, M.; Donnan, R. S., Terahertz spectroscopy: a powerful new tool for the chemical sciences? *Chemical Society Reviews* **2012,** 41, (6), 2072-2082.

(20) Atkins, P.; Atkins, P. W.; de Paula, J., *Atkins' Physical Chemistry*. ed.; OUP Oxford: 2014.

(21) Harris, D. C.; Bertolucci, M. D., *Symmetry and Spectroscopy: An Introduction to Vibrational and Electronic Spectroscopy*. ed.; Dover Publications: 1989.

(22) Pasquini, C., Near Infrared Spectroscopy: fundamentals, practical aspects and analytical applications. *Journal of the Brazilian Chemical Society* **2003,** 14, 198-219.

(23) Takahashi, M., Terahertz Vibrations and Hydrogen-Bonded Networks in Crystals. *Crystals* **2014,** 4, (2), 74.

(24) Alkire, R. C.; Bartlett, P. N.; Lipkowski, J., *Nanopatterned and Nanoparticle-Modified Electrodes*. ed.; Wiley: 2017.

(25) Rice, A.; Jin, Y.; Ma, X. F.; Zhang, X. C.; Bliss, D.; Larkin, J.; Alexander, M., Terahertz optical rectification from 〈110〉 zinc-blende crystals. *Applied Physics Letters* **1994,** 64, (11), 1324-1326.

(26) Wu, Q.; Litz, M.; Zhang, X. C., Broadband detection capability of ZnTe electro-optic field detectors. *Applied Physics Letters* **1996,** 68, (21), 2924-2926.

(27) Auston, D. H.; Cheung, K. P.; Valdmanis, J. A.; Kleinman, D. A., Cherenkov Radiation from Femtosecond Optical Pulses in Electro-Optic Media. *Physical Review Letters* **1984,** 53, (16), 1555-1558.

(28) Han, S.-P.; Kim, N.; Ko, H.; Ryu, H.-C.; Park, J.-W.; Yoon, Y.-J.; Shin, J.-H.; Lee, D. H.; Park, S.-H.; Moon, S.-H.; Choi, S.-W.; Chun, H. S.; Park, K. H., Compact fiber-pigtailed InGaAs photoconductive antenna module for terahertz-wave generation and detection. *Opt. Express* **2012,** 20, (16), 18432-18439.

(29) Georgiou, G.; Tyagi, H. K.; Mulder, P.; Bauhuis, G. J.; Schermer, J. J.; Rivas, J. G., Photo-generated THz antennas. *Scientific Reports* **2014,** 4, 3584.

(30) Zhang, X.-C.; Xu, J., Generation and Detection of THz Waves. In *Introduction to THz Wave Photonics*, Zhang, X.-C.; Xu, J., Eds. Springer US: Boston, MA, 2010; pp 27-48.

(31) Klymenko, M.; Shulika, O.; Sukhoivanov, I., *Semiconductor THz Lasers and Their Applications in Spectroscopy of Explosives*. ed.; 2017.

CHAPTER 3. Density Functional Theory

3.1 Introduction

Computational chemistry provides insight into the energetics and properties of a chemical system that are challenging to obtain experimentally. By utilizing quantum mechanics, it becomes possible to simulate experimental results, revealing the energetics, relative stabilities, and vibrational motions that are present in chemical systems.

Everything exhibits both particle and wave properties, given by the de Broglie equation[1]:

$$\lambda = \frac{h}{mv} \tag{3.1}$$

where λ is the wavelength, *h* is Planck's constant, *m* is mass, and *v* is velocity. Using this relationship, anything with a mass larger than that of a molecule will have a wavelength that can be considered negligible. This is why macroscopic objects that we interact with everyday do not exhibit wave-like properties. However, for electrons with a very small mass (9.109×10^{-31} kg), the wavelength relationship is significant for defining them as both a particle and a wave.

The motivation to model the behavior of the wave-particle duality of electrons resulted in the Schrödinger equation[2, 3], given by:

$$H\Psi = \mathrm{E}\Psi \tag{3.2}$$

where H is the Hamiltonian operator, Ψ is the wavefunction, and E is the total energy of the system relating to the eigenvalues that solve the equation[4, 5]. The Hamiltonian in the

Schrödinger equation is a set of operations that describes the total (potential plus kinetic) energy of the system[6, 7] and is dependent on the chemical system that is being analyzed. In order to accurately define the Hamiltonian, every potential and kinetic interaction that occurs between all of the nuclei and electrons must be considered, shown as:

$$H = T_N + T_e + V_{ee} + V_{NN} + V_{eN} \tag{3.3}$$

In this equation, T_N corresponds to the nuclear kinetic energy, T_e is the electron kinetic energy, V_{ee} is the electron-electron repulsion, V_{NN} is the nuclear-nuclear repulsion, and V_{eN} is the electron-nuclear attraction. In this definition, if one particle moves it induces movement onto all other particles in the system, and calculating this is not computationally feasible. Therefore, approximations must be made in order to arrive at reasonable results.

In order to simplify the Schrödinger equation, the Born-Oppenheimer approximation is used. The Born-Oppenheimer approximation states that when studying an atomic system, due to the mass of the nuclei being much larger than the mass of the electrons, it is possible to ignore nuclear kinetic energy and only consider their potential energy[5, 8]. This causes the nuclei to be treated as fixed, unmoving points. The Born-Oppenheimer approximation eliminates the T_N term from equation 3.3. While all other terms only involve one electron, the V_{ee} term is difficult to solve for because it must take into account two electrons interacting with one another, which is made even more difficult because an electron moves in relation to how the others move. The Hamiltonian (excluding the T_N term) can also be written as:

n

$$H = \overbrace{-\sum_{i}^{N}\frac{\hbar}{2m_e}}^{T_e} + \overbrace{\frac{1}{4\pi\varepsilon_0}\sum_{\substack{i,j=1\\ j>i}}^{n}\frac{e^2}{|r_i - r_j|}}^{V_{ee}} + \overbrace{\frac{1}{4\pi\varepsilon_0}\sum_{\substack{I,J=1\\ J>I}}^{N}\frac{Z_I Z_J e^2}{|R_I - R_j|}}^{V_{NN}} \overbrace{- \frac{1}{4\pi\varepsilon_0}\sum_{i=1}^{n}\sum_{J=1}^{N}\frac{Z_J e^2}{|r_i - R_J|}}^{V_{eN}} \tag{3.4}$$

where m_e is the mass of an electron, $\hbar$ is Planck's constant divided by 2π, $\frac{1}{4\pi\varepsilon_0}$ is the Coulomb's Law constant, e is the electron charge, Z_i and Z_J are the atomic numbers of nucleus I and J, r_i and r_j represent the distance between different electrons, and R_i and R_j represent the distance between different nuclear coordinates. In this equation, it is once again possible to see the difficulty that lies in the electron-electron repulsion term, as it is the only term that contains two different electrons.

Because of this extreme difficulty of describing every individual wavefunction for every electron in the system due to their interactions with one another, it is much easier to define the probability of finding all of the electrons into one term as the total electron density of the system. This simplification of defining all the electrons to a total electron density is central to density functional theory, and further theorems have been postulated in order to relate energy to the electron density.

3.2 Density Functional Theory

The initial steps in defining a chemical system using electron density began with the work of Kohn and Hohenberg. Hohenberg and Kohn proposed that the total energy of a chemical system (external potential energy) is a unique functional of the electron density[9-11]. The problem with this theorem is that there is no way to adequately know the external potential energy of the system, and it must be approximated in DFT. The second theorem solved this problem, which stated that the electron density that minimizes the total energy is the ground state energy[9-11]. This means that it is possible to accurately determine the total energy of a ground-state system, because it will be the lowest possible energy that can be calculated for the system.

The next step in making DFT possible was through the work of Kohn and Sham. They proposed that instead of having the total contribution of the individual electrons represent the wavefunction, it was better for each electron to have their own non-interacting wavefunction[12]. This single particle potential is shown as:

$$V_{eff}(r) = V(r) + e^2 \int \frac{\rho_s(r')}{|r - r'|} d^3r' + \frac{\partial E_{XC}[\rho(r)]}{\partial \rho(r)} \tag{3.6}$$

where $V(r)$ is the external potential energy, ρ_s is the ground state electron probability density, r and r' represent different points in space, and $E_{XC}[\rho(r)]$ is the exchange-correlation energy functional. The final term in this equation ($\frac{\partial E_{XC}[\rho(r)]}{\partial \rho(r)}$) contains all of the particle-particle interactions and is known as the exchange-correlation potential (V_{XC}). The challenge in quantum calculations lies in the solving the exchange-correlation potential. Many attempts to solve the exchange-correlation potential have been proposed with the creation of many functionals that produce varying results.

3.2.1 Functionals

The construction and use of functionals approximates the exchange-correlation potential. This is an area of study that is constantly being improved upon. While many different functional types have been created, no functional works perfectly for all chemical systems. However, based on the system being studied, it is possible to make logical assumptions to determine what functionals will be better for proper modeling.

Over time, many functionals have been made that make various approximations. These functionals can be ranked in terms of their complexity and are often described rather dramatically as rungs in Jacob's Ladder (**Figure 3-1**), alluding to the ladder between heaven and earth described in the Book of Genesis. At higher rungs in the ladder, the functionals become more complex. This section will compare the various types of functionals and their impact to simulating a proper exchange correlation.

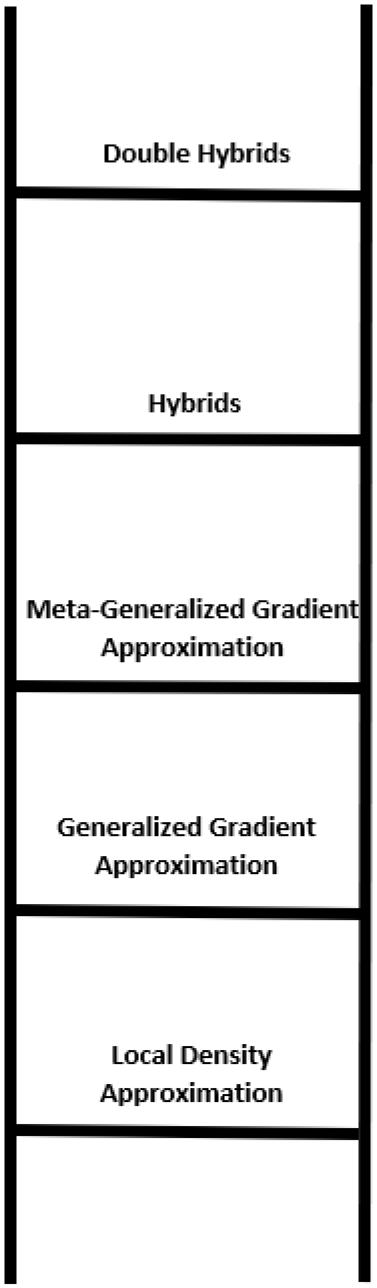

Figure 3-1. Representation of the “Jacob’s Ladder” of functionals.

3.2.1.1. Local Density Approximation (LDA) Functionals

The lowest rung in Jacob's Ladder are the LDA functionals[13, 14]. In this method, the exchange correlation is derived exactly by treating the electron density as a uniform gas. This allows for the electron density to remain constant, with integration over the electron density giving the energy of the system. This is represented by the equation:

$$V_{XC}^{LDA}(r) = V_{XC}[n(r)] \tag{3.7}$$

where $n(r)$ is the electron density and V_{XC} is the exchange-correlation energy per particle of the electron gas. Examples of some common LDA functionals are the Perdew-Wang[15] (PW92) and the Vosko-Wilk-Nusair[16] (VWN) functionals.

LDA functionals have proven to be effective in many cases, although drawbacks are evident. Oftentimes, approaching a study with an LDA functional leads to a larger calculated cohesive energy than what is expected[17], which in turn leads to contracted unit cell dimensions that affect the quality of the simulation. While the LDA functional can be used to satisfy solving the Kohn-Sham equations, due to the assumptions that are used, it is not the most accurate way to define the exact exchange-correlation functional. For this reason, it is often the case that a functional higher up on Jacob's Ladder will be more effective for modelling a chemical system.

3.2.1.2 Generalized Gradient Approximation (GGA) Functionals

The GGA functionals are one of the most common and familiar functionals used today. While the LDA functionals assume the same electron density throughout the system, the GGA functionals consider the gradients in the electron density of a system[18]. This is especially useful in polar and covalently bound solids, where uneven electron density is paramount to their chemical nature. The GGA functionals add an extra term for the gradient of the electron density[14], shown as:

$$V_{XC}^{GGA}(r) = V_{XC}[n(r), \nabla n(r)] \tag{3.8}$$

where the additional term $\nabla n(r)$ represents the gradient. As seen in equation 3.8, it is often the case that the GGA functionals use a homogenous electron density and then apply the gradient to this, essentially making the GGA functionals LDA functionals with an added correction.

The GGA functionals are widely used in computational chemistry and contain some of the most common and recognizable functionals. Two examples of commonly-used functionals are those developed by Perdew-Becke-Ernzerhof[19], known as PBE and the Becke-Lee-Yang-Parr[13, 20] (BLYP) functional. A minor caveat to these functionals is that they were originally optimized for use in the gas-phase, although this does not imply that they cannot produce valid results in the solid-state. However, some GGA functionals have been developed specifically for the solid-state, such as the PBEsol[21] functional. Finding the proper functional for a chemical system is very much trial and error, and it can still be the case that the PBE functional can better model a solid than PBEsol.

3.2.1.3 Meta-Generalized Gradient Approximation (mGGA) Functionals

One way to improve upon the GGA functional is to include the kinetic energy density to the gradient of the electron density[14, 22]. This is shown as:

$$V_{XC}^{mGGA}(r) = V_{XC}[n(r), \nabla n(r), \tau(r)] \tag{3.9}$$

where $\tau(r)$ represents the added kinetic energy. Some examples of mGGA functionals are the TPSS[23] and M06-2X[24] functionals. Compared to the GGA functionals, the mGGA functionals seem to be a much better model for certain systems, but the GGA functionals are a better general choice over a broad range of systems.

3.2.1.4 Hybrid Functionals

To further the complexity of functionals, a percentage of the Hartree-Fock exchange is added to the exchange-correlation term[25, 26]. In the definition of this functional, there are constants that have been determined from thermochemical data, defining a percentage of mixing of the LDA exchange correlation energies. An example of this is the definition of the most common hybrid, the Becke-3-Lee-Yang-Par[27] (B3LYP) functional, which is defined as:

$$E_{XC}^{B3LYP} = E_{XC}^{LDA} + \alpha_1\left(E^{exchange} - V_X^{LDA}\right) + \alpha_2\left(V_X^{GGA} - V_X^{LDA}\right) + \alpha_3\left(V_C^{GGA} - V_C^{LDA}\right) \tag{3.10}$$

where V_X^{GGA} is the exchange functional, V_C^{GGA} is the correlation functional, and α_1, α_2, and α_3 are the numerical constants, which for B3LYP are $\alpha_1 = 0.20$, $\alpha_2 = 0.72$, and $\alpha_3 = 0.81$.

Similar to the GGA functionals, there are other hybrid functionals that are *ab initio*, such as the PBE0 functional[28]. The hybrid functionals have seen a wide range of use in computational chemistry, with many reliable results[26, 29-31], and they are one of the most commonly used functional types.

3.2.1.5 Additional Functionals

The functionals previously described are sufficient for accurately modeling various chemical systems. However, there are still other functionals that have a niche use, and research is still being performed today to create new functionals. For example, the range-separated functional splits the Coulombic interaction into specific distances, leading to functionals based on PBE that include short range (HSE06[32, 33]), middle range (HISS[34, 35]), and long range (LC-ωPBE[36], ωB97-X[37, 38]) corrections.

The most modern functionals are known as the double hybrids, which are considered the current top rung in Jacob's Ladder. These functionals are still very new and still developmental, but they include explicit electron correlation to very accurately describe a chemical system, making them very promising in the coming years. A downside to the double hybrids is that they are computationally costly and may not currently be feasible for regular use.

Although there have been many different types of functionals developed, and over time more terms to better describe systems have been added, this does not mean the older functional types have become obsolete. When choosing a functional, it is important to choose one that is well known to give accurate results and is feasible based on computational time. While a double hybrid functional for all calculations is desirable, it is often the case that a GGA functional may work just as well and take considerably less time to obtain the results. There are educated guesses as to what functionals should be used based on published results, but the real way of finding the best functional for a system is to test it and see how the results compare to experiment.

3.3 Dispersion Correction

Many of the commonly used functionals in density functional theory fail to account for the presence of weak London dispersion interactions. These forces are extremely important to consider, especially in the solid-state where these interactions are often a stabilizing factor in holding crystals together. While there are multiple ways of considering dispersion, the method that is used in all of the research presented in this work is Grimme's D3 correction[39, 40]. The work of Grimme throughout the years has progressed through multiple variations, and the D3 is the most current and effective method.

The total energy of the D3 dispersion correction is given by:

$$E_{DFT-D3} = E_{KS-DFT} - E_{disp} \tag{3.11}$$

In order to calculate the energy of the dispersion correction, two-body and three-body energies are used, given by:

$$E_{disp} = E^{(2)} - E^{(3)} \tag{3.12}$$

The $E^{(2)}$ energy, the more important term of the two, is defined as:

$$E^{(2)} = \sum_{AB} \sum_{n=6,8,10,\ldots} s_n \frac{C_n^{AB}}{R_{IJ}^n} f_{dmp}(R_{AB}) \tag{3.13}$$

where s_n is a scaling factor. For cases where the order of the dispersion coefficient n is 6 (which is the case in the presented research), the scaling factor is not adjusted. C_n^{AB} is the averaged dispersion coefficient for atom pair AB determined by the averaged n^{th}-order dispersion coefficient, and R_{AB} is the internuclear distance between atoms. The f_{dmp} is a dampening function[41] which avoids issues with double counting the correction at intermediate distances and determines the range of the dispersion correction. Without a dampening function, systems would tend to collapse because there is only attraction in the dispersion correction.

Compared to previous dispersion models that were constructed by Grimme, this method requires less user input. In the previous D2 method, the s_6 value was manually changed, increasing computational cost by requiring multiple calculations to determine the proper s_6 value. Instead, D3 lets the s_6 value be included within the dampening term and calculates the dispersion as the calculation progresses at virtually no extra computational cost. This method also takes into account the chemical environment of the system as the calculation progresses based upon the atoms that are near to one another to interact, giving an iterative method of calculating the dispersion which is a great improvement over the previous D2 method that had set scaling factors throughout the entire calculation.

The $E^{(3)}$ third-body term for three atoms ABC is defined as:

$$E^{(3)} = \sum_{ABC} f_{d,(3)}(r_{ABC})E^{ABC} \tag{3.14}$$

which takes into account another dampening function to apply a short-range dampening correction, representing the nonadditive energy contribution. The combination of using a calculated scaling factor and the inclusion of the third-body term make the D3 method of dispersion more accurate and efficient at modeling dispersion than any of the previous iterations.

3.4 Basis sets

Working towards the proper modeling of a chemical system, in addition to a functional that adequately defines the exchange-correlation potential of the system and the use of a dispersion correction to properly take into account the weak London dispersion forces, a proper basis set is needed for accurate modeling. A basis set is essentially a set of functions that defines the electrons of the atoms as molecular orbitals. Technically, there is one function that can properly define a molecular orbital which is very complex and not reasonably obtainable. In order to approximate it, many simpler functions are combined to create a model for the molecular orbital. With more functions, a molecular orbital will be better defined. However, with more functions included the computational time will also increase, so a tradeoff must be made for how accurate the simulation is against how much time it will take to obtain the results.

A certain amount of leeway must be given in determining how many functions to include for each atom. If too many functions are included, it would take too much time to obtain results. Conversely, if not enough functions are included, the results would be obtained quickly but poorly model the experiment and give no chemical insight. While two types of basis sets exist, plane waves used in programs such as CP2K[42] for molecular dynamics and atom-centered used in CRYSTAL[43], all of the research performed in this work utilizes atom-centered basis sets (although Bloch waves are used in the reciprocal space description), and they will be the focus of this section.

The two types of atom-centered basis sets that are typically used in DFT calculations are the Slater-type orbitals (STOs) and Gaussian-type orbitals GTOs). A linear combination of STOs is used when defining a system[44, 45], so as the number of atoms in the system increases, the computational cost is greatly increased. STOs may be effective on very small molecular systems, but for most studies including those in this work, GTOs are used. GTOs are multiplicative[46, 47] which makes determining the overlapping of the orbitals trivial when compared to STOs. The form of GTOs are given as:

$$\gamma^{GTO}(a, r) = e^{-ar^2} \tag{3.15}$$

where *a* is the orbital exponent and *r* is the distance to the nucleus. The form of this equation shows how it can be easily integrated, helping to simply define orbital overlap. This equation also indicates that large exponent values in the basis set yield a very small orbital size. This is often observed in the first few functions of an orbital defining the area closest to the nucleus extremely well.

It is almost always the case that a minimum basis set is not sufficient to yield proper results. For example, defining a hydrogen atom with only one orbital containing its single electron is not enough. The reason is that there must be flexibility in order to allow for scenarios such as bonding that cannot be defined by a minimal basis set. There are many common ways that functions are added. One example is by increasing size of the orbital, and thus number of functions to describe the orbital, defined by a ζ value. For example, instead of having five atomic orbitals for carbon in a single-ζ basis set (1s, 2s, 2px, 2py, 2pz), two basis functions can be given for each atomic orbital as a double-ζ basis set, giving ten basis functions. It is also possible to increase the size to triple-ζ and quadruple-ζ, although this increases computational cost. The ζ value of a basis set is often denoted in its name. For example, some of the most commonly used basis sets, the Pople sets, denote the double-ζ variant as 6-31G[48-51] and triple-ζ as 6-311G[52-55]. Other basis sets, such as those developed by Ahlrich, simply denote the double-ζ as Ahlrichs VDZ[56] (valence double-ζ) and Ahlrichs VTZ[56] (valence triple-ζ).

Another method for improving a basis sets is adding polarization functions. A polarization function is an added function that adds *l* quantum numbers to the function. For example, one polarization function added to a hydrogen atom adds a *p* orbital, and one polarization function to a carbon atom adds a *d* orbital. Because more functions better define a system, it is sometimes beneficial to have more than one polarization function for each atom. A common way to add further polarization functions, seen often in the Pople basis sets, is through the half-doubling process[51, 57, 58]. Starting from one polarization function with a size x, the function is split into two polarization functions of the same type with sizes of 0.5x and 2x. This has been shown to be effective in adding polarization, and is seen in many basis sets, including the Pople sets when polarization is added.

The way that polarization functions are denoted in basis sets is different than defining increasing ζ values. For example, the basis set 6-31G* indicates that one *d* polarization function is added to all heavy atoms in the system, while 6-31G** indicates that there is a *p* polarization function on the hydrogen and an additional *d* function on all heavy atoms. Another way of describing 6-31G* and 6-31G** are 6-31G(d) and 6-31G(d,p), respectively. The asterisk method of adding polarization functions is only employed to the (d,p) level. If more polarization functions are added, all polarization additions are simply listed, such as 6-31G(3df, 3pd), which has 3 d functions and 1 f function added for the heavy atoms, and 3 p functions and one d function added for hydrogen.

In this work, different basis sets are used depending on the studied system. In the gas-phase studies (**Chapter 5**), the aug-cc-pVTZ basis set[59-63] is used, which is a very large and complete basis set which was possible to use because of the small molecular system being studied, allowing for a thorough analysis. In solid-state calculations, the triple-ζ basis set with added polarization (def2-TZVP[64]) developed by Ahlrichs is used, which has shown to produce good results. The only case that does not use def2-TZVP is in **Chapter 8**, where large conjugated ring systems are studied. In this case, Ahlrich pVTZ[56] was found to be the best basis set for these simulations, which is an earlier iteration of the def2-TZVP basis set but was found to run on these solids when def2-TZVP did not.

When selecting a basis set, the struggle lies in how accurate the results need to be while managing computational time. While it is certainly favored to be able to use a larger basis set sometimes further constraints need to be put on a calculation in doing so, which slows it down even further, and in some cases too large a basis set causes the calculation to crash and is impossible to use at all with the specific chemical system. When using a basis set, it is often best to use one that is well documented for its good results and known in the computational chemistry community. However, many basis sets exist, and more are constantly being made. Each have their positives and negatives which must be weighed when selecting the proper basis set for a calculation. A very large collection of basis sets where all of the basis sets were obtained over the course of this research is available at the Basis Set Exchange[65].

3.5 Solid-State Density Functional Theory

For all solid-sate density functional theory (ss-DFT) calculations in this work, the CRYSTAL software package[43, 66] has been used. Crystals are very large systems to perform calculations on with many atoms in the bulk of the crystal. Performing calculations that explicitly include all the atoms would take too much computational time. However, because of the periodicity of a crystal, there are approaches that can be applied and are within the CRYSTAL code that make modeling a crystalline system in the solid-state possible in a reasonable amount of time. The use of ss-DFT allows for the accurate reproduction of experimental results and the determination of energetic factors of a crystalline system.

3.5.1 The Periodic Boundary Condition

As discussed in **Chapter 2**, there are only a finite number of ways that crystals can be arranged totaling 230 different space groups, all of which belong to one of the seven crystal systems[67, 68]. Depending on the space group, each crystal will have a certain amount of symmetry associated with it in regular repeating units. These symmetrically repeating units are known as unit cells. Although there are multiple ways to define a unit cell, the smallest repeat unit, known as the asymmetric unit, can be exploited in ss-DFT calculations.

Using the asymmetric unit of a crystal greatly simplifies calculations and making them feasibly possible, as compared to attempting to calculate an infinitely large crystal strucutre. The asymmetric unit can be repeated outward in all directions to model the total crystal. This is known as the periodic boundary condition[69], schematically shown in **Figure 3-2**. Only using the asymmetric unit does not affect the accuracy of calculations, and the same results are observed if the calculation was performed on the entirety of the unit cell. In cases where part of a molecule is cut off by defining the asymmetric unit, its symmetrical equivalent is observed on the opposite side of the unit cell.

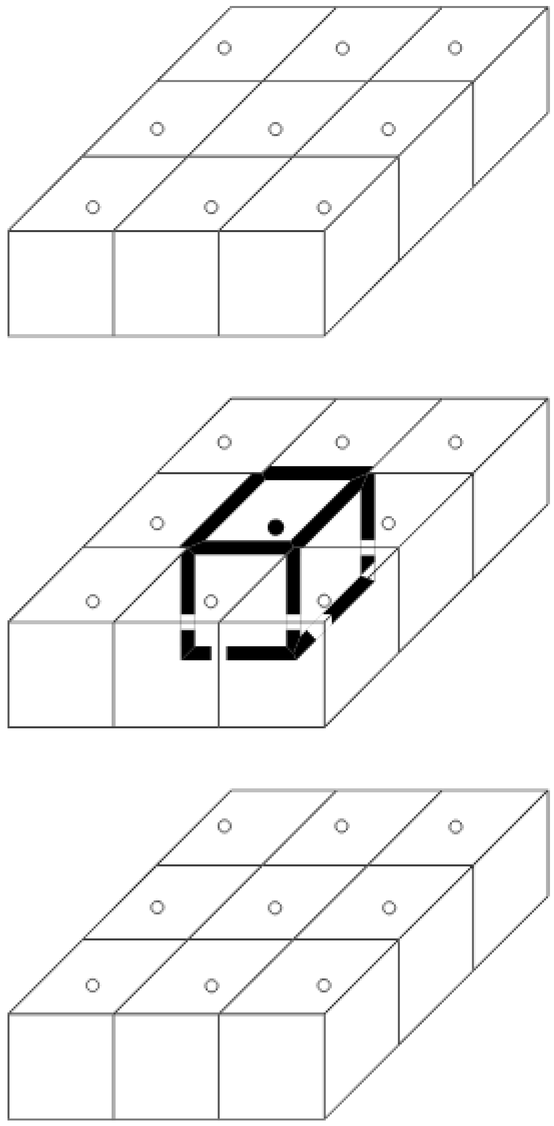

Figure 3-2. Illustration of the periodic boundary condition, adapted from reference 69.

3.5.2 Reciprocal Space

As mentioned in the previous section, the smallest unit cell defined by lattice vectors is known as a primitive cell. When the primitive cell is converted into reciprocal space, it is called the Brillouin zone[70]. The use of reciprocal space and the Brillouin zone is very useful in simplifying ss-DFT calculations. In order to convert primitive cell dimensions a,b, and c into reciprocal lattice dimensions a*, b*, and c*, the following equations are used:

$$a^* = 2\pi \frac{b\times c}{a\cdot(b\times c)}\; b^* = 2\pi \frac{c\times a}{b\cdot(c\times a)}\; c^* = 2\pi \frac{a\times b}{c\cdot(a\times b)} \tag{3.16}$$

Based on these equations, it is evident that if an axis increases in real space, it decreases in reciprocal space. This is also true when describing the volume of a system, with unit cells having a smaller volume in real space having a larger volume in reciprocal space. This has implications in ss-DFT parameters that will be discussed later in this section. Reciprocal space is the momentum space, which is defined by **k** vectors. In reciprocal space, it is possible to convert the atom-centered basis sets that are used in real space into Bloch waves, which is done via a Fourier transform[70, 71]. When a Bloch wave has a periodicity that corresponds to the crystal being studied, it takes the form:

$$\psi(r) = e^{\boldsymbol{ikr}}u(r) \tag{3.17}$$

where the function has the same value at the corresponding k points. This means the solid can be defined by the k vectors in the Brillouin zone, and as a result allowing each **k** vector to be treated independently of one another. This is the reason for converting into reciprocal space, as this significantly simplifies calculations. The use of Bloch functions also makes it is possible to observe the interactions between neighboring points, which improves the accuracy of calculations.

3.5.3 Single-Point Energies, Shrinking Factors, and Geometry Optimizations

A single-point energy calculation in the CRYSTAL software determines the electronic energy of a crystalline unit cell. This is performed via an iterative process, known as the self-consistent field (SCF) method[12, 72]. Given an initial system, a “guess” of the electron density based on atom position and type is made. The exchange-correlation is then solved using the diagonalized matrix from conversion to reciprocal space, which yields a total energy of the system. This information is then used to perturb the electron density, and the energy is then recalculated. This process is repeated over several cycles until there is essentially no difference in energy between SCF cycles. In this research, the energy convergence when performing single point energies was set to $\Delta E < 10^{-10}$ hartree.

Single point energy calculations can be used to determine the number of k points needed to properly define a system. The CRYSTAL software implements shrinking factors, which are defined by two individual integer numbers. The first shrinking factor defines the number of k points that are used to describe the system, defined by the Pack-Monkhorst method[73]. This factor is determined in all works presented by incrementally increasing the integer value, and thus number of k points, until the energy calculation changes by less than $\Delta E < 10^{-10}$ hartree. A representation of the first parameter at values of 3 and 6 for graphite are shown in **Figure 3-3**[74]. The shrinking factor defines the sampling of k-points used to calculate the density matrix and determine the Fermi energy in conductors. None of the systems studied in this work were conductors, and so the second parameter was not relevant and was set as the value of the first determined parameter. As a result of the inverse relationship between distance and volume between direct and reciprocal space, and that the shrinking factor for the entire cell is defined by a single value, the shrinking factor for the number of k points is limited by the smallest unit cell dimension. It is possible to define an asymmetric shrink in cases where there are very large unit cell axis differences, but this was not performed in any of the research presented. While the only way to know the proper shrinking factor value is by determining the convergence on energy, it is good form to know whether high or low values are expected.

After the appropriate shrinking factor has been determined, it is possible to begin optimizing the geometry of a crystalline solid. During a geometry optimization, an SCF cycle is performed, and the resulting electron density is used as a guess to perturb the atomic positions a small amount. This process repeats until the energy of the structure minimizes and converges to the set tolerance. Over the course of a geometry optimization, the only constraint is symmetry, and the atomic positions and unit cell dimensions will change as geometry steps proceed. For all geometry optimizations performed in this work, an energy convergence of $\Delta E < 10^{-8}$ was used.

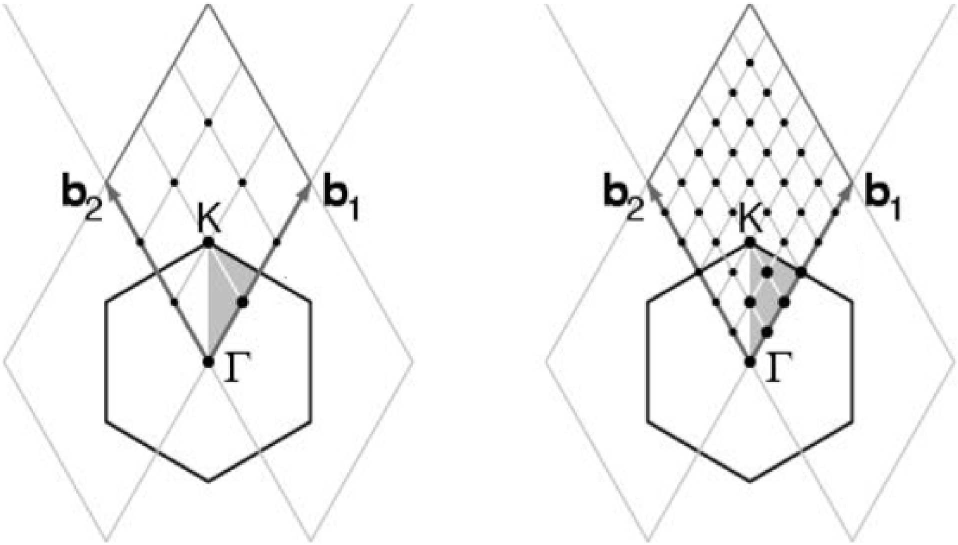

Figure 3-3. Representation of the reciprocal lattice cell of graphite, showing the grid of k vectors that define the sample. Shrinking factors of 3 (left) and 6 (right) are shown. The figure has been adapted from reference 66.

Although a full geometry optimization is the ideal method to obtain an optimized structure, some systems do not behave as expected and other optimization methods must be performed. For example, if a temperature analysis is performed experimentally, simulation of the results from a full optimization is not the most appropriate because in ss-DFT, optimizations are performed at 0 K. In order to solve this problem, lattice parameters can be set to experimental values and remain constant throughout the optimization. This allows the atoms to optimize within the defined, unchanging unit cell dimensions. While doing this puts strain on the system and prevents it from optimizing to its lowest energy value, it allows for a comparison of different temperature structures and their corresponding relative energies. This type of atoms-only optimization is performed in **Chapters 6**, **7**, and **8**.

Additionally, it is also possible to freeze the atoms and optimize only the lattice parameters of the unit cell. While this is a less common type of optimization, it is useful when displacing along vibrational eigenvectors in order to see how the unit cell responds to a specific vibration. In the same sense, it is also possible to freeze individual bond lengths, angles, or dihedral angles and allow the structure to otherwise fully optimize. Freezing specified coordinates can find transition state energies and allows for a less constrained method of freezing along a vibrational coordinate when compared to freezing all of the atoms in place. Optimizations of only the unit cell and freezing selected coordinates are performed in **Chapter 6**.

It is important to note that in order to accurately compare the results from multiple geometry many of the convergence criteria must be identical. The values here are those that are changed from the default values over the course of the presented research. The gradient on the root-mean-squared of the potential energy surface values is set to 0.000010 a.u. (keyword TOLDEG), while the root-mean-squared of the displacement is set to 0.000040 a.u. (keyword TOLDEX). Truncation tolerances for the Coulombic and Hartree-Fock exchange integrals are also defined for each calculation (keyword TOLINTEG), but this value is determined based on the system. The general form of these values is 10^{-X}, 10^{-X}, 10^{-X}, 10^{-X}, 10^{-Y}, where Y is typically a value twice that of X. Occasionally optimizations have trouble with SCF cycle convergence and increasing the TOLINTEG values is typically the first thing changed to allow for proper convergence.

Geometry optimizations are used to allow for a comparison to the experimental structures and judge the validity of a simulation. Typically, an excellent agreement of a full geometry optimization requires all errors in the unit cell dimensions and volume to be below 1%. It is also possible to compare optimized bond lengths and angles to experimental values. If the differences between experimental and calculated are too large, it is possible that a more complete basis set or a different functional will yield better results. The total solid-state electronic energy of the system is also determined during an optimization, which can be used to compare the relative energies of chemical systems (e.g polymorphs) that are optimized with the same criteria.

3.5.4 Frequency Calculations

Optimized crystal structures can be used to simulate IR and Raman normal mode vibrational frequencies and intensities. Although the energy convergence tolerance in optimizations is set at $\Delta E < 10^{-8}$, frequency calculations are more sensitive to small energy differences, so a convergence tolerance of $\Delta E < 10^{-10}$ is used. In a frequency calculation, a central point is defined by which all of the vibrational displacements will be determined. Based on the harmonic approximation, the Born-Oppenheimer potential energy surface of N nuclei can be given by:

$$V(0) = \frac{1}{2} u_i H_{ij} u_j \tag{3.18}$$

where u_i represents the displacement of the corresponding Cartesian coordinate from its equilibrium position and H is the Hessian matrix of the second derivatives of V(x) at equilibrium compared to the displaced coordinates, given by

$$H_{ij} = \frac{1}{2} \left[\frac{\partial^2 V(x)}{\partial u_i u_j} \right] \tag{3.19}$$

The CRYSTAL software calculates the energy first derivatives analytically, while the second derivatives are calculated numerically. Because the calculations of a crystal can be reduced in reciprocal space, this reduces the system to be 3N dimensional, meaning that frequency positions can be calculated by performing 3N + 1 SCF energy calculations, based on displacement of each atom along each Cartesian coordinate (X, Y, and Z), and the central point. Because the frequencies are all based on displacement compared to the central point, it is imperative that the correct initial geometry is used before performing a frequency analysis.

While the frequencies of IR and Raman vibrations are performed in the same way, the method by which the intensities are determined are very different from one another. In the calculation of IR frequencies, the Berry phase method[75] is employed which uses the polarization differences between the equilibrium geometry and corresponding displacements. For IR simulations, it is also important to ensure that the simulated intensities represent the total number of molecules within the unit cell, or else the intensities may be offset by a factor of Z.

For Raman intensities, a Raman tensor is calculated utilizing a Coupled-Perturbed Hartree-Fock/Kohn Sham approach[76, 77]. This calculation computes the Raman polarizability tensors based on an applied electric field in all Cartesian directions (X, Y, X, XX, XY, XZ, YY, YZ, ZZ). In all Raman intensity calculations in this work, a Fock matrix mixing combined with a mixing of Fock and Kohn Sham matrix second derivatives[78] were used. It is also possible to take experimental conditions into account when performing a Raman frequency analysis. For all Raman simulations, a laser excitation of 784.7 nm was used (matching the experimental setup described in **Chapter 2**), as well as the temperature at which the experiment was conducted. In all situations, using experimental parameters in the calculations caused the relative peak intensities to match significantly better than if they were excluded. Raman intensities have an arbitrary absolute intensity based on how much scattering occurs, but the relative intensities are still significant to accurate modeling.

The results of frequency simulations calculate peak positions, but the peak widths used to facilitate comparison with experiment must be fit to experimental results. The experimental frequencies were fit to Lorentzian line shapes and the full-width at half-maximum values were determined. The full-width-half-maximum values are used to properly determine the width of the simulated spectra peaks.

3.5.5 Energy Calculations and Gibbs Free Energy Curves

By accurately modeling the vibrational spectra of a chemical system, it ensures that the theory has accurately modeled the intermolecular forces. This indicates that the energies calculated from the structure are reliable which can be broken down and used to provide further insight into the chemical systems.

The energy that is given at the end of a geometry optimization is the total solid energy. This total solid energy can also be obtained from an energy calculation of any arrangement of atoms. From this energy alone, it is possible to determine relative energy trends in similar chemical systems (e.g. polymorphs, isomers) with the more stable form having lower energy. Because the Z value differs between crystalline systems, it is best to divide the total energy by the Z value in order to make sure energies are realistically comparable. Because the Z value is typically the number of molecules in the unit cell, the total energy is often represented as the total electronic energy corresponding to one molecule within the unit cell.

The total electronic energy can be decomposed into parts, shown as:

$$E_{Total\ Electronic} = E_{Conformational} + E_{Cohesive} \tag{3.20}$$

The conformational energy is determined by simply running an energy calculation for a single molecule within the unit cell being studied. This energy corresponds to the amount of intramolecular energy that keeps the molecule together. The cohesive energy corresponds to the intermolecular energy that holds molecules within the crystal structure together. It is obtained by subtracting the electronic energy (per molecule) from the conformational energy because the intermolecular forces are non-covalent in nature. Typically, the cohesive energy is much less than the conformational energy. By comparing the conformational and cohesive energies of polymorphic systems, it is possible to determine what the stabilizing factors are in each form, and whether it is due to its conformation or the way it is interacting within the crystal.

All energy calculations mentioned previously have calculated the internal energy (enthalpy), but in order to completely define the energy of a system, the contribution of entropy, temperature, and the thermal contribution of the vibrational energies must be taken into account via Gibbs free energy curves. The relationship is given by:

$$\Delta G = \Delta H - T\Delta S \tag{3.21}$$

where G is the Gibbs free energy, H is the enthalpy, S is the entropy, and T is temperature. By examining the energy over a range of temperatures, which is an inexpensive calculation to perform within CRYSTAL after a frequency job, it is possible to accurately determine the thermodynamic data of a system at varying temperatures. This is extremely helpful in the study of polymorphs, where the more stable polymorph can be dependent upon the temperature. If Gibbs free energy curves are constructed for both polymorphs, and there is a crossing point that corresponds to the temperature at which conversion occurs experimentally, it only emphasizes the quality of the simulations.

The zero-point energy is also included in the calculation of a Gibbs free energy curve. However, in order to know the value of the zero-point energy or factor it into other calculations, it is given at the end of a frequency calculation. This can simply be added to the total electronic energy calculations to take it into account. The inclusion of zero-point energy can have a large impact on results and the electronic energy trends that are observed.

3.5.5.1 Basis Set Superposition Error (BSSE)

One of the largest sources of error in solid-state density functional theory (and all calculations that use atom-centered basis sets) is basis set superposition error (BSSE). BSSE is a purely artificial lowering of the energy within a system due to the incompleteness of the basis set being used. The larger and more defined a basis set is, the less BSSE will be present, which is another reason to use the largest basis set possible when performing calculations. Removing BSSE from energetic calculations makes the results more accurate, and not doing so can lead to incorrect interpretation of results.

BSSE is corrected in CRYSTAL through the counterpoise method[79]. This method is a BSSE correction for each molecule within the unit cell. The BSSE corrected energy can be subtracted from the conformational energy to yield the amount of BSSE per molecule. From the BSSE calculation, it is possible to obtain corrected solid and cohesive energies to give a more computationally meaningful result for all the energies shown in equation 3.20. It is also important to correct the Gibbs free energy curves for BSSE, as the amount of BSSE is different for each system, even between similar polymorphs. This means that correction could greatly shift crossing points in Gibbs curves, cause them not to cross, or change the ordering that is observed.

3.6 References

(1) de Broglie, L., *The reinterpretation of wave mechanics*. ed.; 1970; Vol. 1, p 5-15.

(2) Schrödinger, E., Quantisierung als Eigenwertproblem. *Ann. Phys.* **1926,** 384, (6), 489-527.

(3) Schrödinger, E., Quantisierung als Eigenwertproblem. *Ann. Phys.* **1926,** 384, (4), 361-376.

(4) Angelow, A. a. B., M C, About Heisenberg Uncertainty Relation (by E. Schrödinger). *Bulg. J. Phys.* **1999,** 26, (5-6), 193-203.

(5) Atkins, P.; Atkins, P. W.; de Paula, J., *Atkins' Physical Chemistry*. ed.; OUP Oxford: 2014.

(6) Strauss, H. L.; Pickett, H. M., Conformational structure, energy, and inversion rates of cyclohexane and some related oxanes. *Journal of the American Chemical Society* **1970,** 92, (25), 7281-7290.

(7) Maschke, B. M.; Schaft, A. J. v. d. In *A Hamiltonian approach to stabilization of nonholonomic mechanical systems*, Proceedings of 1994 33rd IEEE Conference on Decision and Control, 14-16 Dec 1994, 1994; 1994; pp 2950-2954 vol.3.

(8) Pilar, F. L., *Elementary quantum chemistry*. ed.; McGraw-Hill: 1968.

(9) Sahni, V., The Hohenberg-Kohn Theorems and Kohn-Sham Density Functional Theory. In *Quantal Density Functional Theory*, Springer Berlin Heidelberg: Berlin, Heidelberg, 2004; pp 99-123.

(10) S., K. E., Hohenberg-Kohn theorem. *International Journal of Quantum Chemistry* **1980,** 18, (4), 1029-1035.

(11) Epstein, S. T.; Rosenthal, C. M., The Hohenberg–Kohn theorem. *The Journal of Chemical Physics* **1976,** 64, (1), 247-249.

(12) Kohn, W.; Sham, L. J., Self-Consistent Equations Including Exchange and Correlation Effects. *Physical Review* **1965,** 140, (4A), A1133-A1138.

(13) Lee, C.; Yang, W.; Parr, R. G., Development of the Colle-Salvetti correlation-energy formula into a functional of the electron density. *Physical Review B* **1988,** 37, (2), 785-789.

(14) Sholl, D.; Steckel, J. A., *Density Functional Theory: A Practical Introduction*. ed.; Wiley: 2011.

(15) Perdew, J. P.; Wang, Y., Accurate and simple analytic representation of the electron-gas correlation energy. *Physical Review B* **1992,** 45, (23), 13244-13249.

(16) Vosko S. H, L.; Wilk, L. H.; Nusair, M., *Accurate Spin-Dependent Electron Liquid Correlation Energies for Local Spin Density Calculations: A Critical Analysis*. ed.; 1980; Vol. 58, p 1200-1211.

(17) Zhao, Y.; Truhlar, D. G., Density Functionals with Broad Applicability in Chemistry. *Accounts of Chemical Research* **2008,** 41, (2), 157-167.

(18) Perdew, J. P.; Chevary, J. A.; Vosko, S. H.; Jackson, K. A.; Pederson, M. R.; Singh, D. J.; Fiolhais, C., Atoms, molecules, solids, and surfaces: Applications of the generalized gradient approximation for exchange and correlation. *Physical Review B* **1992,** 46, (11), 6671-6687.

(19) Perdew, J. P.; Burke, K.; Ernzerhof, M., Generalized gradient approximation made simple. *Phys. Rev. Lett.* **1996,** 77, (18), 3865-3868.

(20) Becke, A. D., Density-functional exchange-energy approximation with correct asymptotic behavior. *Physical review. A, General physics* **1988,** 38, (6), 3098-3100.

(21) Perdew, J. P.; Ruzsinszky, A.; Csonka, G. I.; Vydrov, O. A.; Scuseria, G. E.; Constantin, L. A.; Zhou, X.; Burke, K., Restoring the density-gradient expansion for exchange in solids and surfaces. *Phys Rev Lett* **2008,** 100, (13), 136406.

(22) Tao, J., An accurate MGGA-based hybrid exchange-correlation functional. *The Journal of Chemical Physics* **2002,** 116, (6), 2335-2337.

(23) Tao, J.; Perdew, J. P.; Staroverov, V. N.; Scuseria, G. E., Climbing the Density Functional Ladder: Nonempirical Meta--Generalized Gradient Approximation Designed for Molecules and Solids. *Physical Review Letters* **2003,** 91, (14), 146401.

(24) Zhao, Y.; Truhlar, D. G., The M06 suite of density functionals for main group thermochemistry, thermochemical kinetics, noncovalent interactions, excited states, and transition elements: two new functionals and systematic testing of four M06-class functionals and 12 other functionals. *Theoretical Chemistry Accounts* **2008,** 120, (1), 215-241.

(25) Becke, A. D., Density-functional thermochemistry. III. The role of exact exchange. *The Journal of Chemical Physics* **1993,** 98, (7), 5648-5652.

(26) Becke, A. D., A new mixing of Hartree–Fock and local density-functional theories. *The Journal of Chemical Physics* **1993,** 98, (2), 1372-1377.

(27) Becke, A. D., A new mixing of Hartree-Fock and local-density-functional theories. *J. Chem. Phys.* **1993,** 98, (2), 1372-7.

(28) P. Perdew, J.; Ernzerhof, M.; Burke, K., *Rationale for Mixing Exact Exchange with Density Functional Approximations*. ed.; 1996; Vol. 105.

(29) Gerber, I. C.; Ángyán, J. G., Hybrid functional with separated range. *Chemical Physics Letters* **2005,** 415, (1), 100-105.

(30) Stanton, J. F., A Chemist's Guide to Density Functional Theory By Wolfram Koch (German Chemical Society, Frankfurt am Main) and Max C. Holthausen (Humbolt University Berlin). Wiley-VCH: Weinheim. 2000. xiv + 294 pp. $79.95. ISBN 3-527-29918-1. *Journal of the American Chemical Society* **2001,** 123, (11), 2701-2701.

(31) Arbuznikov, A. V., Hybrid exchange correlation functionals and potentials: Concept elaboration. *Journal of Structural Chemistry* **2007,** 48, (1), S1-S31.

(32) Krukau, A. V.; Vydrov, O. A.; Izmaylov, A. F.; Scuseria, G. E., Influence of the exchange screening parameter on the performance of screened hybrid functionals. *J Chem Phys* **2006,** 125, (22), 224106.

(33) Perdew, J. P.; Ruzsinszky, A.; Csonka, G. I.; Vydrov, O. A.; Scuseria, G. E.; Constantin, L. A.; Zhou, X.; Burke, K., Restoring the Density-Gradient Expansion for Exchange in Solids and Surfaces. *Physical Review Letters* **2008,** 100, (13), 136406.

(34) Henderson, T. M.; Izmaylov, A. F.; Scuseria, G. E.; Savin, A., The importance of middle-range Hartree-Fock-type exchange for hybrid density functionals. *J Chem Phys* **2007,** 127, (22), 221103.

(35) Henderson, T. M.; Izmaylov, A. F.; Scuseria, G. E.; Savin, A., Assessment of a Middle-Range Hybrid Functional. *Journal of Chemical Theory and Computation* **2008,** 4, (8), 1254-1262.

(36) Weintraub, E.; Henderson, T. M.; Scuseria, G. E., Long-Range-Corrected Hybrids Based on a New Model Exchange Hole. *Journal of Chemical Theory and Computation* **2009,** 5, (4), 754-762.

(37) Chai, J. D.; Head-Gordon, M., Systematic optimization of long-range corrected hybrid density functionals. *J Chem Phys* **2008,** 128, (8), 084106.

(38) D. Becke, A., *Density functional thermochemistry. V. Systematic optimization of exchange-correlation functionals*. ed.; 1997; Vol. 107, p 8554-8560.

(39) Grimme, S.; Hansen, A.; Brandenburg, J. G.; Bannwarth, C., Dispersion-Corrected Mean-Field Electronic Structure Methods. *Chemical Reviews* **2016,** 116, (9), 5105-5154.

(40) Grimme, S.; Antony, J.; Ehrlich, S.; Krieg, H., A consistent and accurate ab initio parametrization of density functional dispersion correction (DFT-D) for the 94 elements H-Pu. *J Chem Phys* **2010,** 132, (15), 154104.

(41) Grimme, S.; Ehrlich, S.; Goerigk, L., *Effect of the Damping Function in Dispersion Corrected Density Functional Theory*. ed.; 2011; Vol. 32, p 1456-65.

(42) Hutter, J.; Iannuzzi, M.; Schiffmann, F.; VandeVondele, J., cp2k: atomistic simulations of condensed matter systems. *Wiley Interdisciplinary Reviews: Computational Molecular Science* **2013,** 4, (1), 15-25.

(43) Dovesi, R.; Erba, A.; Orlando, R.; Zicovich-Wilson, C. M.; Civalleri, B.; Maschio, L.; Rérat, M.; Casassa, S.; Baima, J.; Salustro, S.; Kirtman, B., Quantum-mechanical condensed matter simulations with CRYSTAL. *Wiley Interdisciplinary Reviews: Computational Molecular Science* **2018,** 0, (0), e1360.

(44) Hehre, W. J.; Stewart, R. F.; Pople, J. A., Self-Consistent Molecular-Orbital Methods. I. Use of Gaussian Expansions of Slater-Type Atomic Orbitals. *The Journal of Chemical Physics* **1969,** 51, (6), 2657-2664.

(45) Chong Delano, P.; Van Lenthe, E.; Van Gisbergen, S.; Baerends Evert, J., Even-tempered slater-type orbitals revisited: From hydrogen to krypton. *Journal of Computational Chemistry* **2004,** 25, (8), 1030-1036.

(46) Edited Board. In *Advances in Quantum Chemistry*, Löwdin, P.-O., Ed. Academic Press: 1990; Vol. 21, p ii.

(47) Dunlap, B. I.; Rosch, N., The Gaussian-Type Orbitals Density-Functional Approach to Finite Systems. In *Advances in Quantum Chemistry*, Löwdin, P.-O., Ed. Academic Press: 1990; Vol. 21, pp 317-339.

(48) Hehre, W. J.; Ditchfield, R.; Pople, J. A., Self—Consistent Molecular Orbital Methods. XII. Further Extensions of Gaussian—Type Basis Sets for Use in Molecular Orbital Studies of Organic Molecules. *The Journal of Chemical Physics* **1972,** 56, (5), 2257-2261.

(49) Dill, J. D.; Pople, J. A., Self-consistent molecular orbital methods. XV. Extended Gaussian-type basis sets for lithium, beryllium, and boron. *The Journal of Chemical Physics* **1975,** 62, (7), 2921-2923.

(50) Francl, M. M.; Pietro, W. J.; Hehre, W. J.; Binkley, J. S.; Gordon, M. S.; DeFrees, D. J.; Pople, J. A., Self-consistent molecular orbital methods. XXIII. A polarization-type basis set for second-row elements. *The Journal of Chemical Physics* **1982,** 77, (7), 3654-3665.

(51) Rassolov, V. A.; Pople, J. A.; Ratner, M. A.; Windus, T. L., 6-31G* basis set for atoms K through Zn. *The Journal of Chemical Physics* **1998,** 109, (4), 1223-1229.

(52) Krishnan, R.; Binkley, J. S.; Seeger, R.; Pople, J. A., Self-consistent molecular orbital methods. XX. A basis set for correlated wave functions. *The Journal of Chemical Physics* **1980,** 72, (1), 650-654.

(53) McLean, A. D.; Chandler, G. S., Contracted Gaussian basis sets for molecular calculations. I. Second row atoms, Z=11–18. *The Journal of Chemical Physics* **1980,** 72, (10), 5639-5648.

(54) Blaudeau, J.-P.; McGrath, M. P.; Curtiss, L. A.; Radom, L., Extension of Gaussian-2 (G2) theory to molecules containing third-row atoms K and Ca. *The Journal of Chemical Physics* **1997,** 107, (13), 5016-5021.

(55) Curtiss, L. A.; McGrath, M. P.; Blaudeau, J. P.; Davis, N. E.; Binning, R. C.; Radom, L., Extension of Gaussian-2 theory to molecules containing third-row atoms Ga–Kr. *The Journal of Chemical Physics* **1995,** 103, (14), 6104-6113.

(56) Schäfer, A.; Horn, H.; Ahlrichs, R., Fully optimized contracted Gaussian basis sets for atoms Li to Kr. *The Journal of Chemical Physics* **1992,** 97, (4), 2571-2577.

(57) Mitin, A. V., Polarization functions for the modified m6-31G basis sets for atoms Ga through Kr. *J Comput Chem* **2013,** 34, (23), 2014-9.

(58) A., R. V.; A., R. M.; A., P. J.; C., R. P.; A., C. L., 6-31G* basis set for third-row atoms. *Journal of Computational Chemistry* **2001,** 22, (9), 976-984.

(59) Dunning, T. H., Gaussian basis sets for use in correlated molecular calculations. I. The atoms boron through neon and hydrogen. *The Journal of Chemical Physics* **1989,** 90, (2), 1007-1023.

(60) Woon, D. E.; Dunning, T. H., Gaussian basis sets for use in correlated molecular calculations. IV. Calculation of static electrical response properties. *The Journal of Chemical Physics* **1994,** 100, (4), 2975-2988.

(61) Woon, D. E.; Dunning, T. H., Gaussian basis sets for use in correlated molecular calculations. III. The atoms aluminum through argon. *The Journal of Chemical Physics* **1993,** 98, (2), 1358-1371.

(62) Balabanov, N. B.; Peterson, K. A., Systematically convergent basis sets for transition metals. I. All-electron correlation consistent basis sets for the 3d elements Sc-Zn. *J Chem Phys* **2005,** 123, (6), 64107.

(63) Wilson, A. K.; Woon, D. E.; Peterson, K. A.; Dunning, T. H., Gaussian basis sets for use in correlated molecular calculations. IX. The atoms gallium through krypton. *The Journal of Chemical Physics* **1999,** 110, (16), 7667-7676.

(64) Weigend, F.; Ahlrichs, R., Balanced basis sets of split valence, triple zeta valence and quadruple zeta valence quality for H to Rn: Design and assessment of accuracy. *Physical Chemistry Chemical Physics* **2005,** 7, (18), 3297-3305.

(65) Basis Set Exchange. https://bse.pnl.gov/bse/portal

(66) Dovesi, R.; Orlando, R.; Erba, A.; Zicovich-Wilson, C. M.; Civalleri, B.; Casassa, S.; Maschio, L.; Ferrabone, M.; De La Pierre, M.; D'Arco, P.; Noel, Y.; Causa, M.; Rerat, M.; Kirtman, B., CRYSTAL14: A program for the ab initio investigation of crystalline solids. *Int. J. Quantum Chem.* **2014,** 114, (19), 1287-1317.

(67) Bradley, C.; Cracknell, A., *The Mathematical Theory of Symmetry in Solids: Representation Theory for Point Groups and Space Groups*. ed.; OUP Oxford: 2010.

(68) Suryanarayana, C.; Norton, M. G., *X-Ray Diffraction: A Practical Approach*. ed.; Springer US: 1998.

(69) Cramer, C. J., *Essentials of Computational Chemistry: Theories and Models*. Second ed.; Wiley: Southern Gate, Chichester,West Sussex PO19 8SQ, England, 2005; p 607.

(70) *INTRODUCTION TO SOLID STATE PHYSICS, 7TH ED*. ed.; Wiley India Pvt. Limited: 2007.

(71) Felbacq, D., Bloch waves. In *Advanced Numerical and Theoretical Methods for Photonic Crystals and Metamaterials*, ed.; Morgan & Claypool Publishers: 2016; pp 2-1-2-21.

(72) Blinder, S. M., Basic Concepts of Self-Consistent-Field Theory. *American Journal of Physics* **1965,** 33, (6), 431-443.

(73) Monkhorst, H. J.; Pack, J. D., Special points for Brillouin-zone integrations. *Physical Review B* **1976,** 13, (12), 5188-5192.

(74) R. Dovesi, V. R. S., C. Roetti, R. Orlando, C. M. Zicovich-Wilson, F. Pascale, B. Civalleri, K. Doll, N. M. Harrison, I. J. Bush, P. D'Arco, M. Llunell, M. Causà, Y. Noël, L. Maschio, A. Erba, M. Rerat and S. Casassa, *CRYSTAL17 User's Manual*. ed.; University of Torino, Torino, 2017, 2017.

(75) Noel, Y.; Zicovich-Wilson, C. M.; Civalleri, B.; D'Arco, P.; Dovesi, R., Polarization properties of ZnO and BeO: An *ab-initio* study through the Berry phase and Wannier functions approaches. *Physical Review B* **2001,** 65, (1), 014111.

(76) Maschio, L.; Kirtman, B.; Rerat, M.; Orlando, R.; Dovesi, R., Ab initio analytical Raman intensities for periodic systems through a coupled perturbed Hartree-Fock/Kohn-Sham method in an atomic orbital basis. I. Theory. *J. Chem. Phys.* **2013,** 139, (16), 164101/1-164101/13.

(77) Maschio, L.; Kirtman, B.; Rerat, M.; Orlando, R.; Dovesi, R., Ab initio analytical Raman intensities for periodic systems through a coupled perturbed Hartree-Fock/Kohn-Sham method in an atomic orbital basis. II. Validation and comparison with experiments. *J. Chem. Phys.* **2013,** 139, (16), 164102/1-164102/9.

(78) Anderson, D. G., Iterative Procedures for Nonlinear Integral Equations. *Journal of the American Chemical Society* **1965,** 12, (4), 547-560.

(79) Boys, S. F.; Bernardi, F., The calculation of small molecular interactions by the differences of separate total energies. Some procedures with reduced errors. *Mol. Phys.* **1970,** 19, (4), 553-566.

CHAPTER 4: Polymorphism in *cis-trans* Muconic Acid Crystals and the Role of C-H···O Hydrogen Bonds

The material contained within this chapter is published in *Crystal Growth and Design* (Zaczek, A. J.; Korter, T. M. *Cryst. Growth Des.* **2017,** 17, (8), 4458-4466)

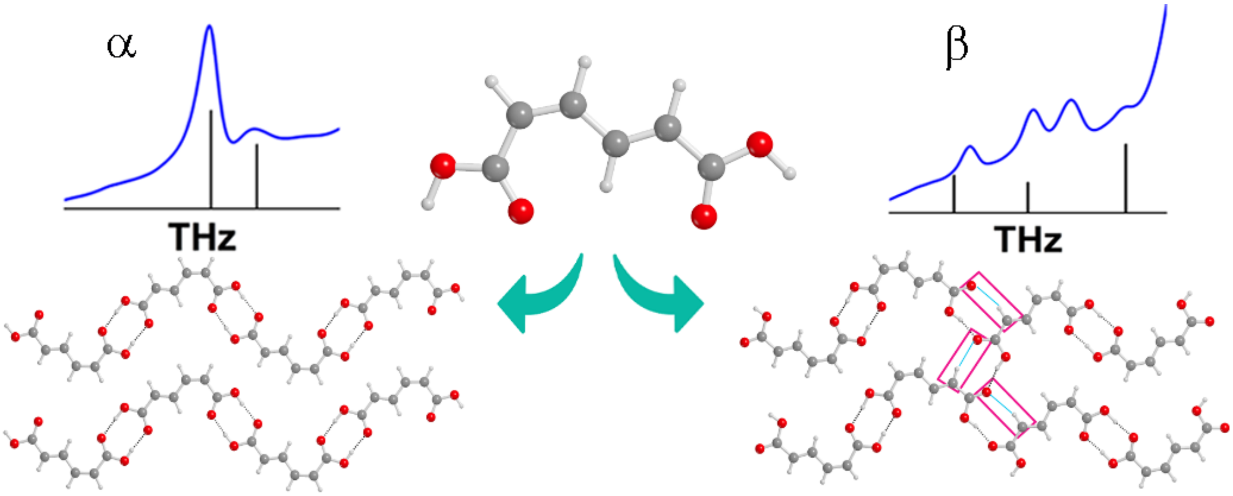

Abstract

Cis-trans isomerization of muconic acid is an important component of various chemical syntheses. Despite the existence of three geometric muconic acid isomers, little atomically-precise information is actually known of their structures. In this work, the complete crystal structures of *cis-cis, cis-trans,* and *trans-trans* muconic acid were determined via single-crystal X-ray diffraction and then further analyzed using terahertz vibrational spectroscopy and solid-state density functional theory. In addition to being the first reported crystal structure for *cis-trans* muconic acid, two polymorphs of this species were discovered, with one exhibiting a two-dimensional hydrogen-bonding pattern stabilized through C-H···O interactions. Terahertz spectroscopy aided in polymorph characterization and also provided clear evidence of a hydrated crystalline species that grows only from one of the *cis-trans* muconic acid polymorphs. *Ab initio* simulations showed that while the typical end-to-end hydrogen-bonding motif found in dicarboxylic acid crystals dominates at room temperature for *cis-trans* muconic acid, the two-dimensional hydrogen-bonding network with C-H···O hydrogen bonding is energetically favored at very low temperatures.

4.1 Introduction

Muconic acid ($C_6H_6O_4$) is a dicarboxylic acid alkene that has been used industrially for decades. It exists primarily in two isomeric forms determined by the conformations about the double bonds in the carbon chain **(Figure 4-1)**. *Trans-trans* muconic acid (*tt*MA) is used to form terephthalic acid through a Diels-Alder reaction with acetylene[1], which is a precursor for polyethylene terephthalate production[2]. The *tt*MA isomer is generally considered to be the most stable conformation due to reduced steric effects. In muconic acid biosyntheses[1,3], the *cis-cis* (*cc*MA) isomer is often reported to be produced from molecules such as glucose[4], and then typically used for conversion to adipic acid[5,6]. Transformation between the two isomers in solution is possible, with *cc*MA converted to *tt*MA upon exposure to ultraviolet light in solutions of alcohol with trace iodine[7], although the reverse reaction has not been reported. Solid-state *cis*-to-*trans* photoisomerizations of muconic acid derivatives (though not muconic acid itself) have been reported several times[8,9,10] and are relevant to the current work. However, the findings are of limited utility here because the mechanisms[11] detailed in those instances are not directly transferrable to pure muconic acid since it exhibits a unique spontaneous isomerization from *cc*MA to *cis-trans* muconic acid (*ct*MA) in water[12].

The *cis-trans* isomerization flexibility that exists within the muconic acid alkene chain is important to consider given its influence on reaction mechanisms and kinetics, and potential role in crystal engineering[13,14] . The complete isomerization pathway between *cc*MA and *tt*MA is not clear, since the *ct*MA isomer complicates the mechanism and possibly represents a first order approximation of the midway point between the two. The existence of *ct*MA was originally determined by ultraviolet and infrared spectroscopies[12], and then verified by ^{1}H NMR experiments[15]. The rate of *ct*MA formation has recently been shown to be sensitive to pH, with very acidic solutions (pH < 2.5) slowing *ct*MA growth, and multiple mechanisms for this observation have been proposed[16].

Despite the relevance of the structure and flexibility of muconic acid to synthetic methodologies, little atomically-precise structural information has been reported in the literature. Of the three MA isomers, a single-crystal X-ray diffraction (SCXRD) study has appeared only for *tt*MA[17], although the hydroxylic hydrogens were excluded. Data limited to only unit cell dimensions from powder X-ray diffraction (PXRD) are available for *cc*MA[18], while no crystallographic studies have been reported for the *ct*MA isomer.

In order to address the lack of solid-state data, SCXRD and terahertz time-domain spectroscopy (THz-TDS) were used to characterize crystalline samples of all three MA isomers. The SCXRD study confirmed the crystal structure of *tt*MA and yielded the full structures of both *cc*MA and *ct*MA for the first time. The THz-TDS measurements in the low-frequency (10-90 cm^{-1}) range revealed the torsional and intermolecular vibrations that are a direct product of the molecular conformations and crystal packing. Most interesting is that these vibrational measurements helped reveal the existence of two *ct*MA polymorphs, with one of the polymorphs exhibiting an unexpected two-dimensional hydrogen bonding scheme that deviates from the typical behavior of solid dicarboxylic acids. The experimental results were complemented with solid-state density functional theory (ss-DFT) simulations to evaluate the energetic factors governing the relative stabilities of all three MA isomers in their crystalline forms.

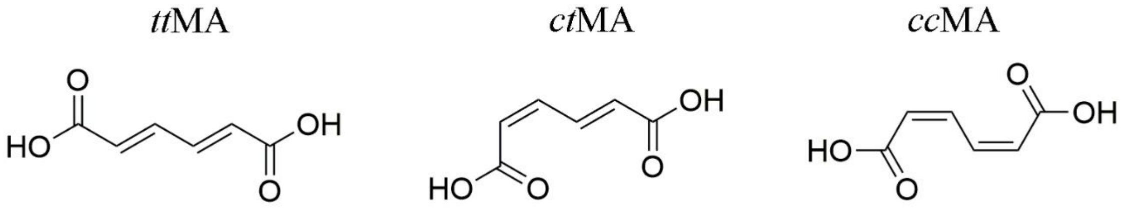

Figure 4-1. ***Trans-trans*** **(ttMA),** ***cis-trans*** **(ctMA), and** ***cis-cis*** **(*cc*MA) isomers of muconic acid.**

4.2 Methods

4.2.1 Experimental

Samples of *cc*MA (97% purity) and *tt*MA (98% purity) were purchased from Sigma Aldrich. *Cc*MA was recrystallized from heated methanol yielding tan block-shaped crystals, while *tt*MA was recrystallized from water at room temperature as white needles. PXRD at 95K was used to confirm their bulk identities both before and after recrystallization and these remained unchanged after two months of material storage. The recrystallized samples contained individual single crystals of sufficient size to be used for SCXRD.

The crystallization of *ct*MA was performed by dissolving *cc*MA to saturation in approximately 30 mL of boiling water. The solution was left to evaporate under ambient conditions for approximately one week, yielding clusters of planar crystals in rosette formations. This *ct*MA form has been designated as α-*ct*MA. Several test solutions of *ct*MA were made by varying the heat applied during dissolution and amount of solvent used, with solvent evaporation times as short as 20 minutes investigated at boiling temperatures. It was found that creating a saturated solution (~90mL) at 80º C and limiting evaporation by covering the solution to result in a four-week crystallization, produced a different *ct*MA polymorph. This second form was detected first by its distinct PXRD pattern and has been designated as β-*ct*MA. PXRD patterns of the two *ct*MA polymorphs taken months apart showed no detectable interconversion between the forms stored under laboratory conditions.

SCXRD studies were conducted using a Bruker KAPPA APEX DUO diffractometer with an APEX II CCD and monochromatic Cu Kα radiation ($\lambda = 1.5418$ Å). Liquid nitrogen boil-off gas was run over the crystal to maintain a temperature of 95 K throughout the data collection. Samples were run with a frame angle of 1 degree and a time of at least 20 seconds per angle. The structures were solved using the SHELXL-2014/7[19] software and difference vectors refinement. After the heavy atom positions were identified, hydrogens were positioned based on electron density within the refined solved structure. An anisotropic refinement was performed to yield a final structure.

Terahertz vibrational spectra were obtained from 10 to 90 cm^{-1} at both 292K (room temperature) and 78K (liquid nitrogen). Near-infrared pulses from an amplified Ti:Sapphire femtosecond laser were used to generate terahertz radiation through optical rectification[20,21] and detected via free-space electro-optic sampling[22] in zinc telluride crystals. The terahertz beam path was purged with dry air to prevent atmospheric water absorption interference. Samples were mixed with polytetrafluoroethylene (PTFE) at approximately 3% concentrations and pressed into 550 mg pellets (13 mm diameter, 2 mm thickness). A pellet of pure PTFE of similar mass was used as a blank. Samples and blanks were each scanned 32 times over a 32 ps window consisting of 3200 points. The results of four sample spectra were averaged together to yield the final spectra. Spectral intensities are reported as extinction coefficients (M^{-1} cm^{-1}), with molarity expressed as concentration of unit cells.

4.2.2 Computational

All ss-DFT calculations were performed using a developmental version of the CRYSTAL14[23] software package. The Perdew-Burke-Ernzerhof (PBE)[24] exchange and correlation functional was used with the def2-TZVP[25] basis set. This large basis set (346 functions per MA molecule) was used for its chemical accuracy and to minimize basis set superposition errors (BSSE) in the simulations. The mixture of strong hydrogen bonding within the molecular layers and weak London dispersion forces between layers can be a challenging environment for DFT modeling. A correction to the long-range non-covalent interaction energies was necessary to properly reproduce the experimentally obtained structures and was accomplished using Grimme's DFT-D3[26] approach which dynamically calculates the DFT energy corrections.

Geometry optimizations were performed using the structures obtained by SCXRD as initial starting points and allowing them to fully relax to energetic minima within the limits of the applied space group symmetries. An energy convergence of $\Delta E < 10^{-8}$ hartree was used for all geometry optimizations. Once optimized, the structures were used for harmonic normal mode frequency analyses with IR intensities calculated by the Berry phase method[27]. The energy convergence was set to a stricter threshold of $\Delta E < 10^{-10}$ hartree for frequency calculations, and a central-difference formula was used to compute the numerical first derivatives (program keyword NUMDERIV = 2). Truncation tolerances for the Coulomb and Hartree-Fock exchange integrals (program keyword TOLINTEG) were set to 10^{-9} 10^{-9} 10^{-9} 10^{-14} 10^{-28} hartree for all calculations.

Molecular conformational energies were calculated by extracting a single fixed molecule from each optimized crystal structure and evaluating its isolated-molecule energy. Cohesive energies were determined by subtracting the conformational energy of all the molecules within the unit cell from the total electronic energy of the unit cell. These energies were corrected for basis set superposition error (BSSE) using the counterpoise method[28] with periodic solid calculation cutoffs enabling > 97% of the BSSE to be accounted for.

4.3 Results and Discussion

In the crystalline state, dicarboxylic acids tend to have similar packing arrangements. The typical intermolecular bonding motif of end-to-end doubly hydrogen-bonded dicarboxylic acids is seen in most of the MA solids, and has been shown to exist for many other linear dicarboxylic acids[29,30,31]. This leads to molecules that pack in layered crystal structures, which is true for all of the MA isomer solids considered here. The unit cell structures of *cc*MA and *tt*MA are detailed in **Figure 4-2**, and the newly discovered α-*ct*MA and β-*ct*MA polymorphs are shown in **Figure 4-3.**

4.3.1 X-ray Diffraction Results

4.3.1.1 ttMA

The crystal structure of *tt*MA is arranged in the *P*-1 space group, with unit cell dimensions of *a* = 3.7380(3) Å, *b* =8.7080(7) Å, *c* = 9.6976(7) Å, α = 79.127(4)º, β = 81.978(4)º, γ = 78.546(4)º, and *V* = 302.11(4) $Å^3$, with a derived density of 1.562 g/cm^3. The crystal structure has two *tt*MA molecules per unit cell (*Z* = 2) with one molecule in the asymmetric unit. Based on the packing and hydrogen bonding pattern, only one symmetrically-unique hydrogen bond exists with an O···O separation of 2.620 Å.

4.3.1.2 ccMA

*cc*MA crystallizes in the *P*21/c space group, with two *cc*MA molecules per unit cell (*Z* = 2) and 0.5 in the asymmetric unit. Lattice dimensions were determined to be *a* = 3.6947(3) Å, *b* = 8.8679(6) Å, *c* = 9.4440(7) Å, β = 98.515(4)º, and *V* = 306.01(4) $Å^3$, with a derived density of 1.542 g/cm^3. These values agree with previously published dimensions[18], with contraction of the unit cell due to the lower temperature in the current work. The unit cell contains one symmetrically-unique hydrogen bond with an O···O separation of 2.637 Å, slightly longer than that observed in *tt*MA.

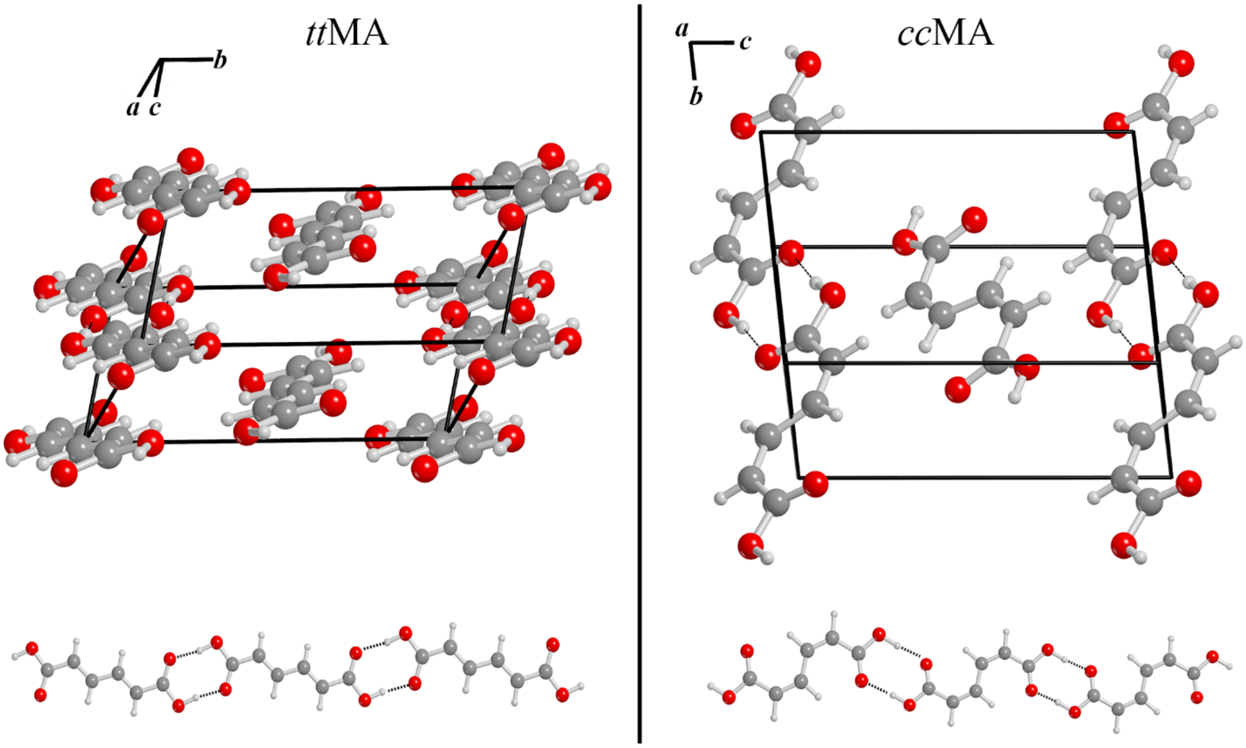

Figure 4-2. Crystallographic unit cell structures of *tt*MA and *cc*MA and representative hydrogen bonding arrangements for each solid.

4.3.1.3 α-ctMA

The α-*ct*MA polymorph contains four molecules per unit cell (*Z* = 4) with *P*nma space group symmetry (**Figure 4-3**). The measured lattice dimensions were *a* = 15.685(3) Å, *b* = 5.862(2) Å, *c* = 7.061(2) Å, and *V* = 649.3(3) Å^3, yielding a density of 1.454 g/cm^3. The hydrogen bonding scheme of α-*ct*MA is similar to *cc*MA and *tt*MA, but with two symmetry-unique bonds having O···O distances of 2.617 Å and 2.635 Å. Interestingly, one of the hydrogen bond lengths is very similar to that measured for *tt*MA and the other very similar to *cc*MA. This is likely related to the MA chains being composed of *trans* to *cis* intermolecular linkages, as shown in **Figure 4-4**.

4.3.1.4 β-ctMA

β-*ct*MA exhibited *P*21/n crystalline symmetry with four molecules per unit cell (Z=4) and lattice dimensions of *a* = 9.202(7) Å, *b* = 6.950(6) Å, *c* = 10.213(10) Å, β = 102.34(3)º, and *V* = 638.2(10) Å^3 resulting in a derived density of 1.469 g/cm^3. The molecules in β-*ct*MA connect in [···*trans-cis*···*cis-trans*···*trans-cis*···] chain sequences, while those in α-*ct*MA form [···*trans-cis*···*trans-cis*···*trans-cis*···] chains.

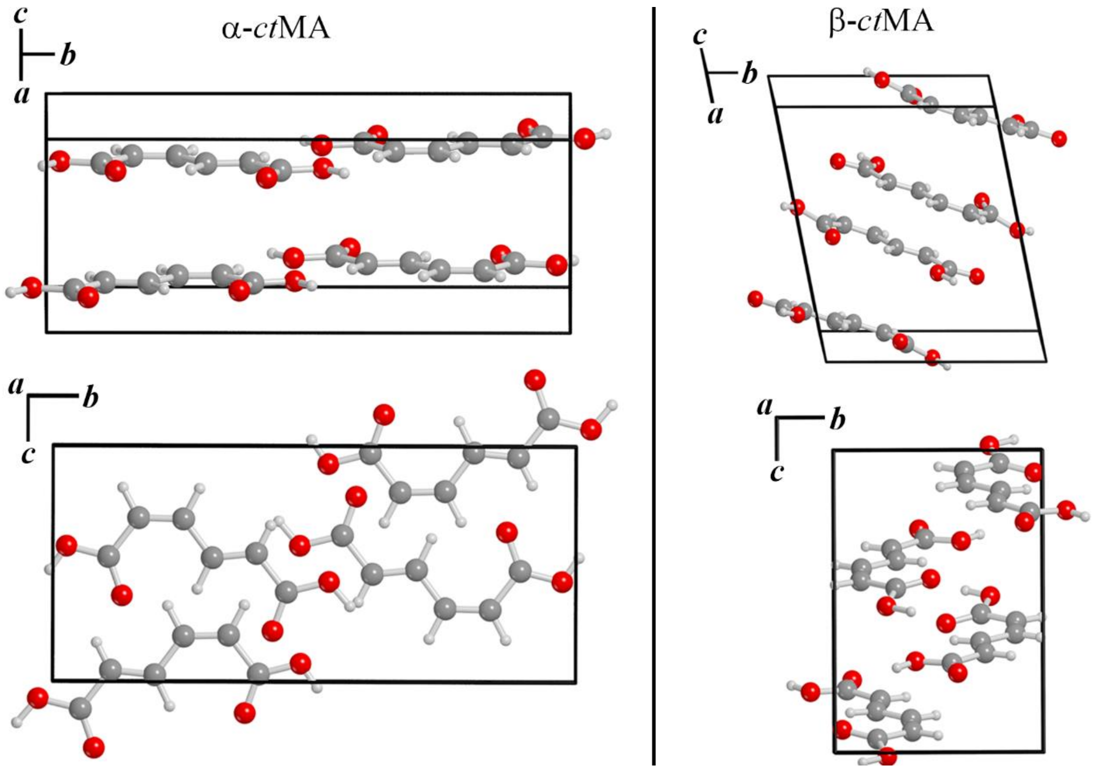

Figure 4-3. Crystallographic unit cell structures of α-*ct*MA and β-*ct*MA.

β-*ct*MA exhibited a notably different hydrogen bonding scheme than the other MA solids, with interactions that extended in two dimensions linking adjacent MA chains as illustrated in **Figure 4-4**. The intra-chain O-H···O hydrogen bonds that are equivalent to the other MA species (yellow highlights in **Figure 4-4)** have O···O distances of 2.566 Å. The contrasting hydrogen bonds that contain connections to neighboring chains (orange highlights in **Figure 4-4**) have O···O distances of 2.589 Å. The two-dimensional hydrogen bonding scheme in β-*ct*MA has been observed occasionally in other dicarboxylic acids, such as phenylpyruvic acid[32] and more notably cubane-1,4-dicarboxylic acid[33] where the influence of C-H···O hydrogen bonding is important.

Similarly, short C-H···O separations are observed in the β-*ct*MA crystal. The C···O distance at the *trans···trans* connection of the MA chain (blue highlights in **Figure 4-4)** within the β-*ct*MA polymorph was found to be 3.302 Å. It is the smallest C···O intermolecular distance in the studied MA solids by at least 0.113 Å. This short C-H···O hydrogen bonding distance clearly indicates[34, 35] that it is a stabilizing factor in this polymorph. A similar C···O interaction can be found at the *cis···cis* chain interfaces, but with a longer length of 3.415 Å indicating weaker C-H···O hydrogen bonding. The α-*ct*MA and *tt*MA crystal structures also both contain C···O bond lengths that may correspond to even weaker C-H···O hydrogen bonding with distances of 3.428 Å and 3.481 Å, respectively. The long C···O separations in *cc*MA of 3.720 Å suggest they have little importance for crystal packing.

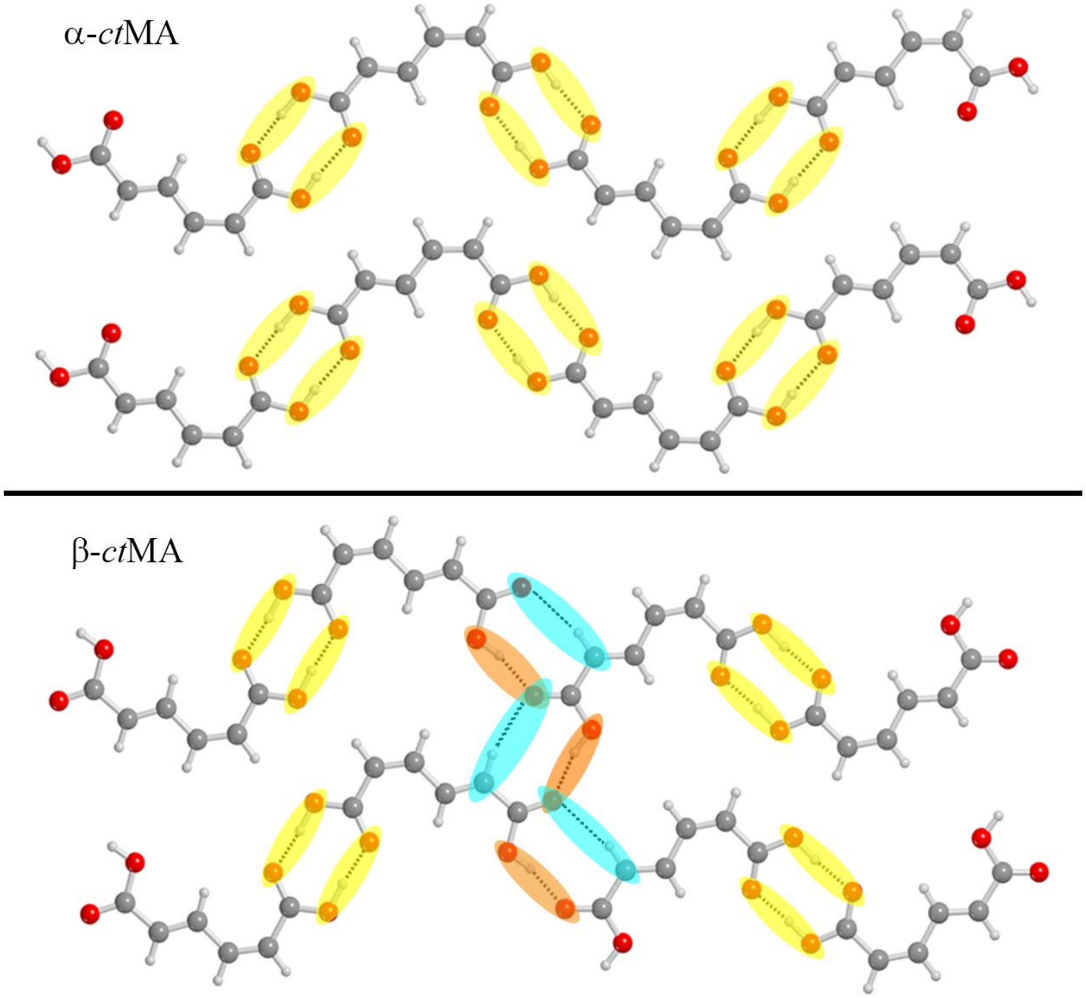

Figure 4-4. Single-layer one-dimensional hydrogen bonding scheme present in α-*ct*MA compared to the two-dimensional network of β-*ct*MA. Intra-chain hydrogen bonding is highlighted in yellow, hydrogen bonds along the inter-chain coordinate in orange, and atypical short C-H···O hydrogen bonding in blue.

In addition to crystal packing differences, the molecules within the *ct*MA polymorphs have differing hydrogen atom positions on the *trans*-end carboxylic acid groups. These two positions are shown as Hα (as found α-*ct*MA) and Hβ (as found in β-*ct*MA) in **Figure 4-5**. The Hα and Hβ structures are related to each other by a 180º torsion about the C1-C2 bond. Intermolecular hydrogen transfer is prohibited in the geometry of the β-*ct*MA hydrogen bonding network and intramolecular hydrogen rearrangement is energetically expensive. A single-molecule simulation of a relaxed potential energy scan along the C1-C2 coordinate using *Gaussian09*[36] (PBE/def2-TZVP) revealed a modest barrier of approximately 25 kJ/mol. The α-*ct*MA (Hα) molecular conformation possessed a slightly lower energy than β-*ct*MA (Hβ) by 0.36 kJ/mol, which is supported by NMR data indicating that O1-Hα is the arrangement present in solution[15,37]

While Hα and Hβ structures have similar calculated dipole moment magnitudes (2.75 D and 2.33 D, respectively), the hydrogen position significantly affects the orientation of the dipole moment in the molecular frame **(Figure 4-5)**. The Hα structure has a dipole moment oriented towards the perpendicular from the carbon chain, which leads to favorable interactions between nearby chains within a single plane (**Figure 4-4)**. The Hβ structure has a dipole moment essentially parallel to the carbon chain, which causes favorable interactions between stacked layers in the β-*ct*MA crystals.

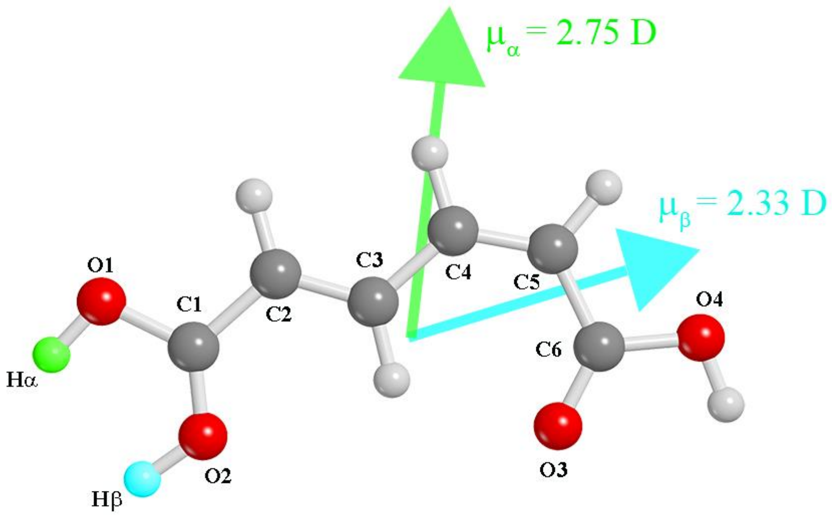

Figure 4-5. Model of *ct*MA indicating the two different hydrogen positions found in the α (green) and β (blue) crystalline polymorphs, and their corresponding calculated molecular dipole moments.

4.3.2 Polymorph Stabilities and Solid-State Energy Factors

Various experimental methods can be used to deduce the relative stabilities of crystalline polymorphs and include melting points, solubility tests, and density measurements[38]. Within a polymorphic family, the more stable crystal melts at a higher temperature, is less soluble, and has a greater density[39]. Melting points were measured for each *ct*MA polymorph, revealing α-*ct*MA to be completely melted by 438 K and β-*ct*MA by 429 K. Solubility tests using water as a solvent were also performed at room temperature, showing β-*ct*MA was approximately 1.6 times more soluble than α-*ct*MA. By both solubility and melting point indicators, the α-*ct*MA form is the more stable of the two. However, this is contradicted by the crystallographic densities of the polymorphs at 95 K, with α-*ct*MA having a density of 1.454 g/cm^3 and β-*ct*MA having a density of 1.487 g/cm^3. To account for temperature effects, the unit cell dimensions were re-evaluated at room temperature and yielded unit cell volumes of 665.19 Å^3 (1.418 g/cm^3) and 671.38 Å^3 (1.405 g/cm^3) for α-*ct*MA and β-*ct*MA, respectively. The room-temperature densities are consistent with the stability rankings found in the melting and solubility experiments. These experiments collectively indicate α-*ct*MA to be the more stable polymorph at room temperature, but that β-*ct*MA may be more stable at lower temperatures. To explore these experimental results, ss-DFT was used for a detailed analysis of the energetic factors contributing to the relative stabilities of these solids.

The ss-DFT optimized unit cells were compared to X-ray diffraction data with the results shown in **Table 4-1** (bond length and angle analyses are available in **APPENDIX A**). Although the theory replicates the experimental observations very well, it is worth noting that the larger lattice errors are along the crystalline dimensions corresponding to the spacing between MA layers which are largely governed by London dispersion forces. The expansion of the calculated lattice along these coordinates indicates that although accurate (maximum error of 1.04% in any solid), the applied model is more limited in treating weak London dispersion forces as compared to stronger hydrogen bonding.

The total electronic energy of each crystalline solid is listed in **Table 4-2**. The overall ranking of the MA isomer solids is perhaps not surprising based on expectations derived from *cis* vs. *trans* conformational arguments. The *tt*MA crystal had the lowest electronic energy and the *cc*MA the highest, with both *ct*MA polymorphs exhibiting intermediate energies. Far greater insight can be gained by decomposing the total electronic energies into conformational and cohesive energies to arrive at the origins of these rankings.

Table 4-1. Comparison of measured muconic acid X-ray crystallographic data (Exp, 95K) and results from ss-DFT structural simulations (Calc, PBE-D3/def2-TZVP).

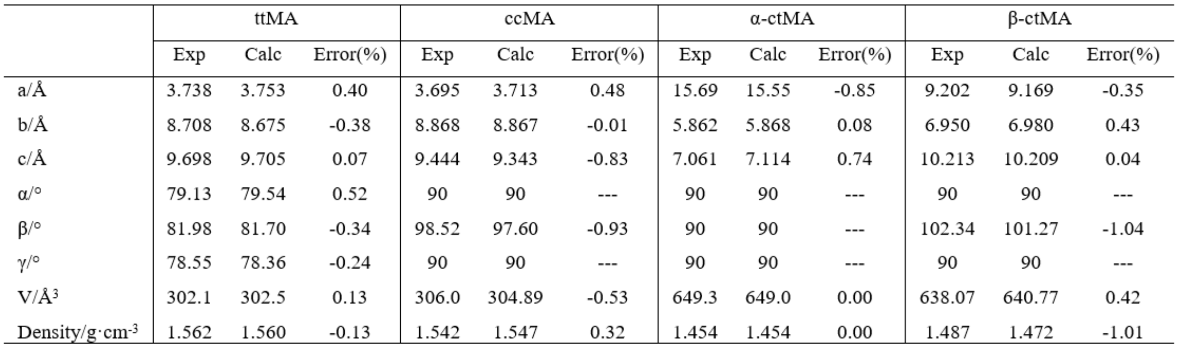

	ttMA			ccMA			α-ctMA			β-ctMA		
	Exp	Calc	Error(%)	Exp	Calc	Error(%)	Exp	Calc	Error(%)	Exp	Calc	Error(%)
a/Å	3.738	3.753	0.40	3.695	3.713	0.48	15.69	15.55	-0.85	9.202	9.169	-0.35
b/Å	8.708	8.675	-0.38	8.868	8.867	-0.01	5.862	5.868	0.08	6.950	6.980	0.43
c/Å	9.698	9.705	0.07	9.444	9.343	-0.83	7.061	7.114	0.74	10.213	10.209	0.04
α/°	79.13	79.54	0.52	90	90	---	90	90	---	90	90	---
β/°	81.98	81.70	-0.34	98.52	97.60	-0.93	90	90	---	102.34	101.27	-1.04
γ/°	78.55	78.36	-0.24	90	90	---	90	90	---	90	90	---
V/Å^3	302.1	302.5	0.13	306.0	304.89	-0.53	649.3	649.0	0.00	638.07	640.77	0.42
Density/g·cm^{-3}	1.562	1.560	-0.13	1.542	1.547	0.32	1.454	1.454	0.00	1.487	1.472	-1.01

Table 4-2. Calculated total electronic, conformational, and cohesive energies of the tested muconic acid solids. Values are listed on a per molecule basis and in hartrees unless noted otherwise. All have been corrected for BSSE.

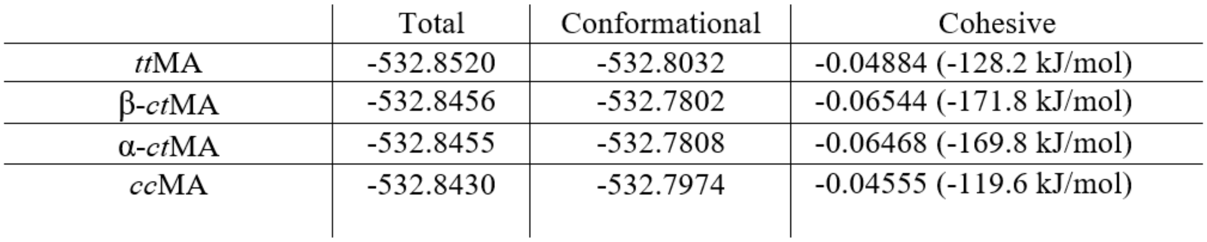

	Total	Conformational	Cohesive
*tt*MA	-532.8520	-532.8032	-0.04884 (-128.2 kJ/mol)
β-*ct*MA	-532.8456	-532.7802	-0.06544 (-171.8 kJ/mol)
α-*ct*MA	-532.8455	-532.7808	-0.06468 (-169.8 kJ/mol)
*cc*MA	-532.8430	-532.7974	-0.04555 (-119.6 kJ/mol)

As anticipated, *tt*MA is the preferred MA conformation being 60.4 kJ/mol lower in energy than the least stable conformer found in β-*ct*MA. Of the two *ct*MA polymorphs, α-*ct*MA (containing O1-Hα) had a more favorable conformational energy by 1.57 kJ/mol, an energy ordering consistent with the isolated-molecule calculations discussed earlier. Due to the reduced molecular symmetry of its components compared to *tt*MA and *cc*MA, *ct*MA crystals are stabilized by dipole-dipole interactions that are absent from the other isomers. This leads to both *ct*MA isomers having significantly greater amounts of solid-state cohesive energy than either *cc*MA or *tt*MA, by an average of 38%. The favorable dipole-dipole interactions in β-*ct*MA between the crystal layers, in combination with its specific hydrogen bonding network that incorporates short C-H···O hydrogen bonds, are the primary reasons for it possessing the greatest cohesive energy in these crystals.

Temperature-dependent Gibbs free energy curves were calculated based on the simulated crystal structures and solid-state vibrations of the *ct*MA polymorphs (Gibbs energies for all isomers are provided in the **APPENDIX A**). These curves showed virtually indistinguishable energies, with β-*ct*MA being marginally lower in energy by 0.29 kJ/mol per molecule at 0K (electronic + zero-point energies). The curves cross at 55 K as the temperature increases, with α-*ct*MA being the more stable at 298 K by 1.60 kJ/mol. Although the calculated crossing point may not be absolutely correct, the general features of the Gibbs curves do agree with the experimental density results suggesting α-*ct*MA has a higher stability at room temperature, but β-*ct*MA is preferred at lower temperatures.

4.3.3 Terahertz Spectroscopy of Muconic Acid Crystals

Terahertz spectroscopy readily differentiates crystalline polymorphs[40, 41,42,43] and is used here to establish the unique spectral signatures for each MA solid while also serving as a probe of the intermolecular forces within the crystals. The investigation of *tt*MA and *cc*MA revealed no significant terahertz features below 90 cm^{-1} (see **APPENDIX A**), but distinct absorptions were apparent in both *ct*MA polymorphs. The terahertz spectra of α-*ct*MA and β-*ct*MA shown in **Figure 4-6** were obtained at 78 K and contain several features in the 40-80 cm^{-1} range.

From the ss-DFT vibrational simulations, it was possible to assign specific molecular motions to each of the observed peaks. The simulated terahertz spectra were convolved with a 4.3 cm^{-1} (full width at half maximum) Lorentzian line shape based on the experimental data to facilitate comparison. A complete list of the calculated infrared-active vibrations for all MA isomers is provided in **APPENDIX A**. In α-*ct*MA, the most intense peak at 58.5 cm^{-1} (calc. 59.5 cm^{-1}) corresponds to an intermolecular rotation about the crystallographic *a*-axis. The second mode at 67.5 cm^{-1} (calc. 67.8 cm^{-1}) arises from an intramolecular twisting out of the molecular plane. For β-*ct*MA, the experimental peak at 47.8 cm^{-1} (calc. 45.8 cm^{-1}) originates from an intramolecular rocking within the molecular plane, the feature at 59.3 cm^{-1} (calc. 60.4 cm^{-1}) is an out-of-plane twisting, and the 76.2 cm^{-1} (calc. 74.6 cm^{-1}) peak results from an out-of-plane wagging. Visual representations of the vibrations are shown in **Figure 4-7.** The experimental peak observed in the β-*ct*MA spectrum at 66.0 cm^{-1} is not from pure muconic acid and is discussed in detail in the following section.

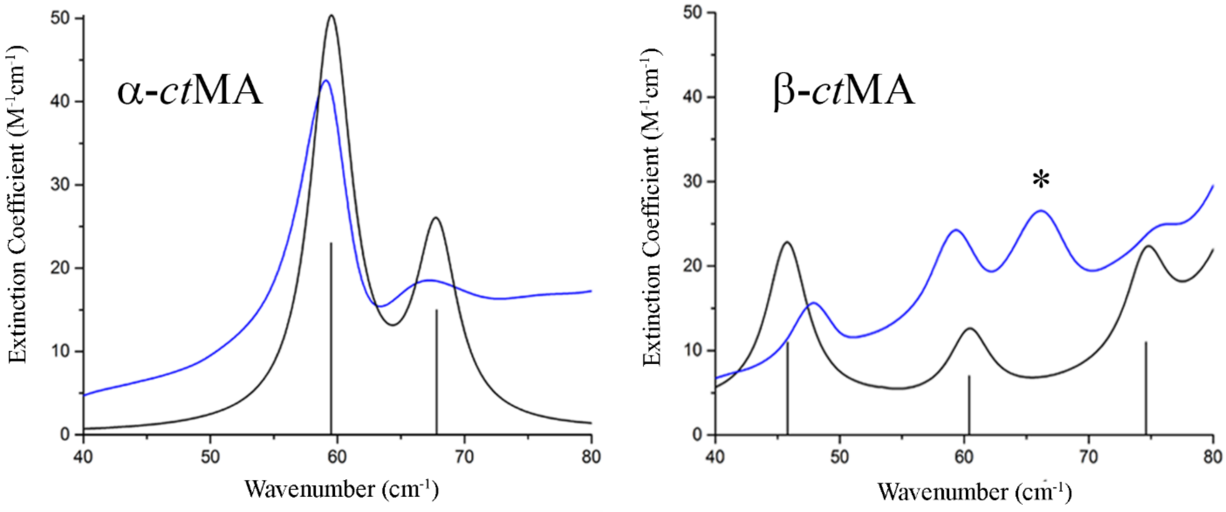

Figure 4-6. Experimental (blue) and simulated (black) terahertz spectra of α-*ct*MA and β-*ct*MA crystalline polymorphs. A possible hydrate peak is indicated with an asterisk (*).

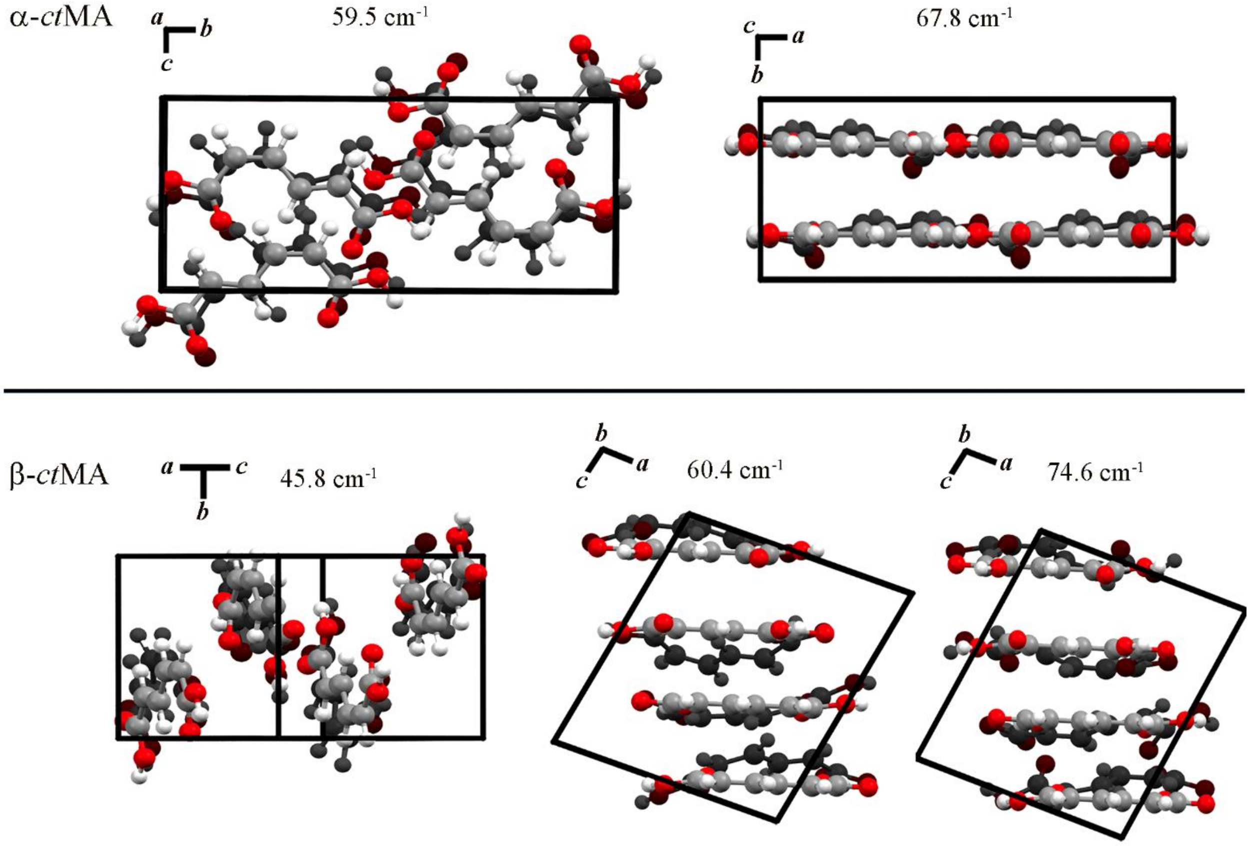

Figure 4-7. Vibrational mode character in *ct*MA polymorphs of specific terahertz frequency motions. Equilibrium structures are shown in full color and eigenvector-displaced structures are shown in black.

4.3.4 Evidence of a ctMA Hydrate

The existence of an unaccounted for narrow absorption in the terahertz spectrum of β-*ct*MA indicated that a small amount of another crystalline species was present. This anomaly prompted a reinvestigation of the terahertz spectrum of β-*ct*MA, but with a sample that had been stored in a desiccator for two weeks. The terahertz spectral data showed the peak at 66.0 cm^{-1} to be greatly reduced after drying (**Figure 4-8**), strongly suggesting a hydrate to be the cause of the absorption.

PXRD patterns taken within two days after β-*ct*MA crystallization exhibited multiple low-intensity peaks not observed in the PXRD pattern generated from SCXRD data of the pure β-*ct*MA crystal (**Figure 4-9)**. PXRD data obtained using desiccator-dried samples showed greatly reduced intensity among the unexplained peaks. Therefore, it is reasonable to assume these features arise from a crystalline hydrate of muconic acid, although the weak intensity and low number of discernable features prevents determination of the crystalline parameters (~10% contamination). Dicarboxylic acids with linear structures similar to muconic acid have been shown to form hydrates, such as pyrimidine-4,6-dicarboxylic acid dihydrate[44], acetylenedicarboxylic acid dihydrate[45], and oxalic acid dihydrate[46], but are not common. It is noteworthy that the hydrated muconic acid species was only found as a contaminant in β-*ct*MA samples, with no evidence of hydrate formation detected in any α-*ct*MA, *cc*MA, or *tt*MA studies. This observation is consistent with the already discussed relative stabilities of the *ct*MA polymorphs and the greater affinity for water shown by β-*ct*MA.

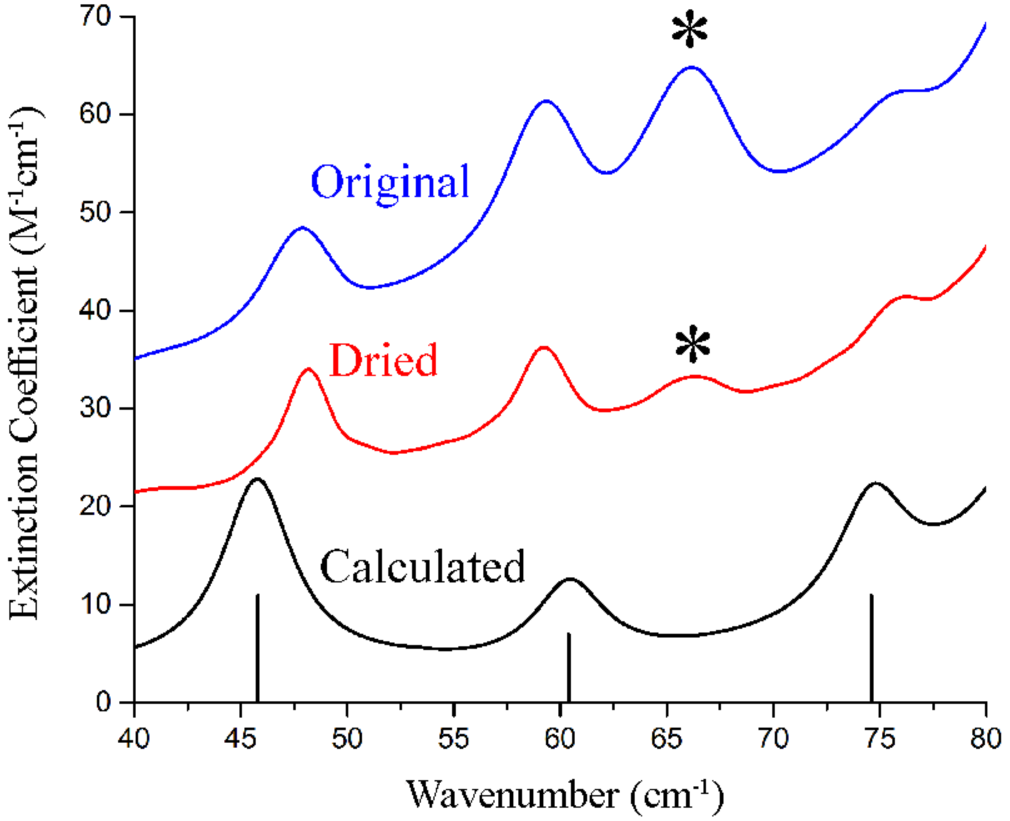

Figure 4-8. Terahertz spectra of β-*ct*MA samples (offset for clarity) soon after crystallization (blue), and after two weeks of drying (red). The ss-DFT simulated spectrum of pure β-*ct*MA is shown in black.

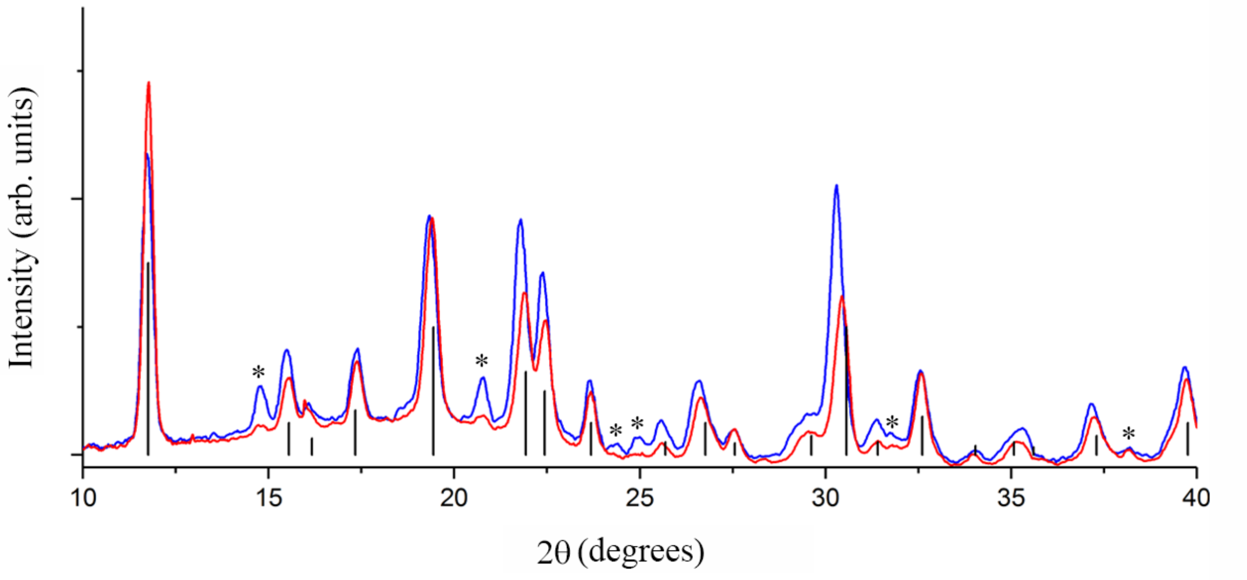

Figure 4-9. PXRD patterns of β-*ct*MA collected from a sample within two days of crystallization (blue), and after drying (red). The powder pattern predicted from single-crystal X-ray data is shown in black. Asterisks (*) mark likely hydrate features.

4.4 Conclusions

The crystalline structures of all known muconic acid isomeric species were studied using a combination of X-ray diffraction techniques, terahertz spectroscopy, and ss-DFT. While both *cc*MA and *tt*MA were found to exist in only one crystal form each, a *ct*MA structural analysis revealed two distinct polymorphs differing in both their molecular conformations and hydrogen bonding patterns. While the expected end-to-end intermolecular hydrogen bonding scheme was present in α-*ct*MA, β-*ct*MA exhibited a unique two-dimensional pattern, which resulted from significant stabilization through short C-H···O interactions not present in other muconic acid solids. The investigations also found a crystalline muconic acid hydrate with unique terahertz and X-ray diffraction characteristics that was only observed in the presence of the β-*ct*MA polymorph. The ss-DFT simulations showed that the *ct*MA crystal formation is driven by greatly enhanced cohesion forces as compared to the other isomers (+38% average cohesion energy), that overcomes the relatively poor conformational energy of the *ct*MA isomer. The determination of the contributing energy factors in these solids, in addition to the first reports of their complete crystal structures, should be helpful in elucidating the isomerization mechanisms between the various muconic acid species that are important to numerous fundamental reactions.

Supporting Information (see APPENDIX A)

Included in the supporting information is the complete PXRD patterns for all muconic acid isomers, the complete terahertz spectra for muconic acid isomers, a detailed bond length and angle analyses for the muconic acid isomers, a list of all active terahertz IR modes, and Gibbs curves for all muconic acid isomers.

4.5 Accession Codes

CCDC 1555230-1555233 contain the supplementary crystallographic data for this paper. These data can be obtained free of charge via www.ccdc.cam.ac.uk/data_request/cif, or by emailing data_request@ccdc.cam.ac.uk, or by contacting The Cambridge Crystallographic Data Centre, 12 Union Road, Cambridge CB2 1EZ, UK; fax: +44 1223 336033

4.6 Acknowledgements

The authors acknowledge the support of a grant from the National Science Foundation (CHE-1301068) and computational resources provided by Syracuse University.

4.7 References

(1) Curran, K. A.; Leavitt, J. M.; Karim, A. S.; Alper, H. S., Metabolic engineering of muconic acid production in Saccharomyces cerevisiae. *Metabolic engineering* **2013,** 15, 55-66.

(2) Lu, R.; Lu, F.; Chen, J.; Yu, W.; Huang, Q.; Zhang, J.; Xu, J., Production of Diethyl Terephthalate from Biomass-Derived Muconic Acid. *Angewandte Chemie* **2016,** 128, (1), 257-261.

(3) Vardon, D. R.; Rorrer, N. A.; Salvachua, D.; Settle, A. E.; Johnson, C. W.; Menart, M. J.; Cleveland, N. S.; Ciesielski, P. N.; Steirer, K. X.; Dorgan, J. R.; Beckham, G. T., cis,cis-Muconic acid: separation and catalysis to bio-adipic acid for nylon-6,6 polymerization. *Green Chemistry* **2016,** 18, (11), 3397-3413.

(4) Johnson, C. W.; Salvachúa, D.; Khanna, P.; Smith, H.; Peterson, D. J.; Beckham, G. T., Enhancing muconic acid production from glucose and lignin-derived aromatic compounds via increased protocatechuate decarboxylase activity. *Metabolic Engineering Communications* **2016,** 3, 111-119.

(5) Niu, W.; Draths, K. M.; Frost, J. W., Benzene-free synthesis of adipic acid. *Biotechnology progress* **2002,** 18, (2), 201-11.

(6) Weber, C.; Bruckner, C.; Weinreb, S.; Lehr, C.; Essl, C.; Boles, E., Biosynthesis of cis,cis-muconic acid and its aromatic precursors, catechol and protocatechuic acid, from renewable feedstocks by Saccharomyces cerevisiae. *Applied and environmental microbiology* **2012,** 78, (23), 8421-30.

(7) Elvidge, J. A.; Linstead, R. P.; Orkin, B. A.; Sims, P.; Baer, H.; Pattison, D. B., Unsaturated lactones and related substances. Introduction. IV. Lactonic products derived from muconic acid. *J. Chem. Soc.* **1950**, 2228-35.

(8) Matsumoto, A.; Odani, T.; Aoki, S., Stereoregular Photopolymerization of Di(benzylammonium) Muconate in the Crystalline State. *Polym J* **1998,** 30, (4), 358-360.

(9) Odani, T.; Matsumoto, A.; Sada, K.; Miyata, M., One-way EZ-isomerization of bis(n-butylammonium) (Z,Z)-muconate under photoirradiation in the crystalline state. *Chemical Communications* **2001**, (19), 2004-2005.

(10) Nishizawa, N.; Nakamura, J.; Matsumoto, A., Single-Crystal-to-Single-Crystal Transformation of Di(isopropylammonium) (Z,Z)-Muconate into the (E,E)-Muconate during One-Way Photoisomerization in the Solid State. *Cryst. Growth Des.* **2011,** 11, (8), 3442-3447.

(11) Warshel, A., Bicycle-pedal model for the first step in the vision process. *Nature* **1976,** 260, (5553), 679-683.

(12) Elvidge, J. A.; Linstead, R. P.; Sims, P.; Orkin, B. A., Third isomeric (cis-trans) muconic acid. *J. Chem. Soc.* **1950**, 2235-41.

(13) Dugave, C.; Demange, L., Cis−Trans Isomerization of Organic Molecules and Biomolecules: Implications and Applications. *Chemical Reviews* **2003,** 103, (7), 2475-2532.

(14) Biradha, K.; Santra, R., Crystal engineering of topochemical solid state reactions. *Chem. Soc. Rev.* **2013,** 42, (3), 950-967.

(15) Matthiesen, J. E.; Carraher, J. M.; Vasiliu, M.; Dixon, D. A.; Tessonnier, J.-P., Electrochemical Conversion of Muconic Acid to Biobased Diacid Monomers. *ACS Sustainable Chem. Eng.* **2016,** 4, (6), 3575-3585.

(16) Carraher, J. M.; Pfennig, T.; Rao, R. G.; Shanks, B. H.; Tessonnier, J.-P., cis,cis-Muconic acid isomerization and catalytic conversion to biobased cyclic-C6-1,4-diacid monomers. *Green Chem.* **2017**, Ahead of Print.

(17) Bernstein, J.; Leiserowitz, L., Molecular packing modes. X. Crystal and molecular structures of trans,trans-muconic acid. *Isr. J. Chem.* **1972,** 10, (2), 601-12.

(18) Bregman, J.; Schmidt, G. M. J., The Conformation of cis,cis-Muconic Acid. *Journal of the American Chemical Society* **1962,** 84, (19), 3785-3786.

(19) Sheldrick, G. M., A short history of SHELX. *Acta Crystallogr., Sect. A: Found. Crystallogr.* **2008,** 64, (1), 112-122.

(20) Rice, A.; Jin, Y.; Ma, X. F.; Zhang, X. C.; Bliss, D.; Larkin, J.; Alexander, M., Terahertz optical rectification from 〈110〉 zinc-blende crystals. *Applied Physics Letters* **1994,** 64, (11), 1324-1326.

(21) Zhang, X. C.; Ma, X. F.; Jin, Y.; Lu, T. M.; Boden, E. P.; Phelps, P. D.; Stewart, K. R.; Yakymyshyn, C. P., Terahertz optical rectification from a nonlinear organic crystal. *Applied Physics Letters* **1992,** 61, (26), 3080-3082.

(22) Wu, Q.; Litz, M.; Zhang, X. C., Broadband detection capability of ZnTe electro-optic field detectors. *Applied Physics Letters* **1996,** 68, (21), 2924-2926.

(23) Dovesi, R.; Orlando, R.; Erba, A.; Zicovich-Wilson, C. M.; Civalleri, B.; Casassa, S.; Maschio, L.; Ferrabone, M.; De La Pierre, M.; D'Arco, P.; Noel, Y.; Causa, M.; Rerat,

M.; Kirtman, B., CRYSTAL14: A program for the ab initio investigation of crystalline solids. *Int. J. Quantum Chem.* **2014,** 114, (19), 1287-1317.

(24) Perdew, J. P.; Burke, K.; Ernzerhof, M., Generalized gradient approximation made simple. *Phys. Rev. Lett.* **1996,** 77, (18), 3865-3868.

(25) Weigend, F.; Ahlrichs, R., Balanced basis sets of split valence, triple zeta valence and quadruple zeta valence quality for H to Rn: Design and assessment of accuracy. *Phys. Chem. Chem. Phys.* **2005,** 7, (18), 3297-3305.

(26) Grimme, S.; Antony, J.; Ehrlich, S.; Krieg, H., A consistent and accurate ab initio parametrization of density functional dispersion correction (DFT-D) for the 94 elements H-Pu. *J. Chem. Phys.* **2010,** 132, (15), 154104/1-154104/19.

(27) Noel, Y.; Zicovich-Wilson, C. M.; Civalleri, B.; D'Arco, P.; Dovesi, R., Polarization properties of ZnO and BeO: An *ab-initio* study through the Berry phase and Wannier functions approaches. *Physical Review B* **2001,** 65, (1), 014111.

(28) Boys, S. F.; Bernardi, F., The calculation of small molecular interactions by the differences of separate total energies. Some procedures with reduced errors. *Molecular Physics* **1970,** 19, (4), 553-566.

(29) Leiserowitz, L., Molecular packing modes. Carboxylic acids. *Acta Crystallographica Section B* **1976,** 32, (3), 775-802.

(30) Benghiat, V.; Leiserowitz, L.; Schmidt, G. M. J., Molecular packing modes. Part VII. Crystal and molecular structures of anhydrous acetylenedicarboxylic acid. *Journal of the Chemical Society, Perkin Transactions 2* **1972**, (12), 1769-1772.

(31) Brown, C., The crystal structure of fumaric acid. *Acta Crystallographica* **1966,** 21, (1), 1-5.

(32) Das, D.; Desiraju, G. R., Packing Modes in Some Mono- and Disubstituted Phenylpropiolic Acids: Repeated Occurrence of the Rare syn,anti Catemer. *Chemistry – An Asian Journal* **2006,** 1, (1-2), 231-244.

(33) Ermer, O.; Lex, J., Shortened C-C Bonds and Antiplanar O-C-O-H Torsion Angles in 1,4-Cubanedicarboxylic Acid. *Angewandte Chemie International Edition in English* **1987,** 26, (5), 447-449.

(34) Desiraju, G. R., The C-H···O hydrogen bond in crystals: what is it? *Accounts of Chemical Research* **1991,** 24, (10), 290-296.

(35) Olenik, B.; Smolka, T.; Boese, R.; Sustmann, R., Supramolecular Synthesis by Cocrystallization of Oxalic and Fumaric Acid with Diazanaphthalenes. *Crystal Growth & Design* **2003,** 3, (2), 183-188.

(36) M. J. Frisch, G. W. T., H. B. Schlegel, G. E. Scuseria, M. A. Robb, J. R. Cheeseman, G. Scalmani, V. Barone, G. A. Petersson, H. Nakatsuji, et al. Gaussian, Inc., Wallingford CT, 2016. *Gaussian 09, Revision A.02,* Gaussian, Inc.: Wallingford CT, 2016.

(37) Matthiesen, J. E.; Suástegui, M.; Wu, Y.; Viswanathan, M.; Qu, Y.; Cao, M.; Rodriguez-Quiroz, N.; Okerlund, A.; Kraus, G.; Raman, D. R.; Shao, Z.; Tessonnier, J.-P., Electrochemical Conversion of Biologically Produced Muconic Acid: Key Considerations for Scale-Up and Corresponding Technoeconomic Analysis. *ACS Sustainable Chemistry & Engineering* **2016,** 4, (12), 7098-7109.

(38) Haleblian, J.; McCrone, W., Pharmaceutical Applications of Polymorphism. *Journal of Pharmaceutical Sciences* 58, (8), 911-929.

(39) Lee, E. H., A practical guide to pharmaceutical polymorph screening & selection. *Asian Journal of Pharmaceutical Sciences* **2014,** 9, (4), 163-175.

(40) Taday, P. F.; Bradley, I. V.; Arnone, D. D.; Pepper, M., Using terahertz pulse spectroscopy to study the crystalline structure of a drug: A case study of the polymorphs of ranitidine hydrochloride. *Journal of Pharmaceutical Sciences* **2003,** 92, (4), 831-838.

(41) Strachan, C. J.; Rades, T.; Newnham, D. A.; Gordon, K. C.; Pepper, M.; Taday, P. F., Using terahertz pulsed spectroscopy to study crystallinity of pharmaceutical materials. *Chemical Physics Letters* **2004,** 390, (1–3), 20-24.

(42) Strachan, C. J.; Taday, P. F.; Newnham, D. A.; Gordon, K. C.; Zeitler, J. A.; Pepper, M.; Rades, T., Using terahertz pulsed spectroscopy to quantify pharmaceutical polymorphism and crystallinity. *J Pharm Sci* **2005,** 94, (4), 837-46.

(43) King, M. D.; Buchanan, W. D.; Korter, T. M., Identification and Quantification of Polymorphism in the Pharmaceutical Compound Diclofenac Acid by Terahertz Spectroscopy and Solid-State Density Functional Theory. *Anal. Chem. (Washington, DC, U. S.)* **2011,** 83, (10), 3786-3792.

(44) Beobide, G.; Castillo, O.; Luque, A.; Garcia-Couceiro, U.; Garcia-Teran, J. P.; Roman, P., Rational design of 1-D metal-organic frameworks based on the novel pyrimidine-4,6-dicarboxylate ligand. New insights into pyrimidine through magnetic interaction. *Dalton Transactions* **2007**, (25), 2669-2680.

(45) Dunitz, J. D.; Robertson, J. M., 37. The crystal and molecular structure of certain dicarboxylic acids. Part II. Acetylenedicarboxylic acid dihydrate. *Journal of the Chemical Society (Resumed)* **1947**, (0), 148-154.

(46) Martin, A.; Pinkerton, A. A., Charge Density Studies Using CCD Detectors: Oxalic Acid at 100 K Revisited. *Acta Crystallographica Section B* **1998,** 54, (4), 471-477.

CHAPTER 5: Isomerization of *cis-cis* to *cis-trans* Muconic Acid in Aqueous Solution

Abstract

Muconic acid is a dicarboxylic acid that can be produced biosynthetically and is widely used in manufacturing. However, the applications of muconic acid vary depending on which geometric isomer is available. In an aqueous solution, naturally produced *cis-cis* muconic acid has been shown to spontaneously convert to *cis-trans* muconic acid under specific pH conditions. While the isomerization mechanisms of similar molecules have been determined to involve lactone intermediates, the mechanism of the muconic acid transformation has not been elucidated. In this work, density functional theory has been applied in the study of the isomerization pathway, revealing that a lactone intermediate results in a significant lowering of the energy barrier to the *cis-trans* form. These same simulations show the strong pH dependence of the *cis-trans* isomer formation is tied to the protonation state of the *cis-cis* form, with only the single deprotonated state leading to isomerization.

5.1 Introduction

Muconic acid ($C_6H_6O_4$) is a dicarboxylic acid with an unsaturated carbon chain that exists in three isomeric forms; *cis-cis* muconic acid (*cc*MA), *cis-trans* (*ct*MA) muconic acid, and *trans-trans* muconic acid (*tt*MA). The difference in these isomers is based upon the orientation of the double bonds within the carbon chain. *cc*MA is easily produced from bioengineered bacteria[1-3], but has few industrial uses. Conversion to *tt*MA is possible under ultraviolet light in alcoholic solutions with trace iodine[4]. *tt*MA is much more versatile than the other isomers, being able to be hydrogenated to adipic acid[5, 6] and more notably used in a Diels-Alder reaction to generate terephthalic acid[1, 7]. Terephthalic acid is produced in millions of metric tons per year[7] and is used in polyethylene terephthalate (PET) production. Originally noted decades ago, aqueous *cc*MA has been shown to readily and completely convert to *ct*MA[8], a structure that represents a probable midway point between *cc*MA and *tt*MA. Water as a solvent has been shown to be central to this isomerization, while other solvents like methanol and ethanol have only been reported to maintain pure *cc*MA[8]. Despite the knowledge that *cc*MA in water forms *ct*MA, the structure of crystalline *ct*MA was not fully determined until recently[9].

The *cis-cis* to *cis-trans* mechanisms for muconic acid derivatives, such as 3-chloro-*cis-cis*-muconate[10] and 4-methyl-*cis-cis*-muconate[11] involve the formation of a lactone. These reactions are catalyzed by cycloisomerases, which is also true in many other cases of lactone formation[12-14]. Due to the abundance of *cis-cis* to *cis-trans* mechanisms that involve lactone formation, it is logical to investigate whether lactone formation is feasible for the pure *cc*MA to *ct*MA muconic acid mechanism which only involves water in its conversion.

Recent work performed by Carraher et. al[15] showed that the pH of a solution plays a large role in *ct*MA formation, with the level of deprotonation of *cc*MA being a key factor. The HNMR measurements in their work revealed that a singly-deprotonated muconolactone (ML^{1-}) is present in aqueous solutions, and although the means of transformation was not definitive it was concluded that ML^{1-} stabilized over time in dilute acetic acid solutions. However, in recent solid-state studies[9], it has been observed that *cc*MA dissolved in water yields pure *ct*MA upon crystallization with no lactone present which seemingly contradicts the observed stability of the

ML^{1-} in the solution-phase work. It is possible that this difference may be due to the solution-phase study being performed in the presence of acetic acid while the solid-state study crystallizations were performed in water, leading to distinct pH differences between experiments. It was originally published by Elvidge[4] that an acidic solution crystallizes ML^{1-}, suggesting a relation between lower pH and ML^{1-} stabilization. The increased acidity from acetic acid may stabilize ML^{1-}, while in an aqueous solution *ct*MA is preferred leading to a proposed mechanism shown in **Figure 5-1**.

In contrast to a stabilized ML^{1-} at lower pH levels, it has further been reported that the fully deprotonated *cc*MA^{2-} muconate ion that exists at higher pH does not lactonize or isomerize to *ct*MA. The exact reasons for this are currently unknown. It has been proposed that it may have to do with stabilization due to resonance structures[15], although no work has been done to prove or disprove this.

Density functional theory (DFT) can be used to determine the energetic stabilities of both muconic isomers and the ML^{1-} intermediate, providing useful insight into the seemingly conflicting experimental results. The calculation of potential energy surfaces by scanning along proposed mechanism coordinates provides detailed information concerning the various barriers that exist in the isomerization process and how they are related to the protonation state of muconic acid. Additionally, finding the reason for the non-isomerization of doubly deprotonated *cc*MA^{2-} is possible through energetic and spatial analyses of the molecular orbitals in these species.

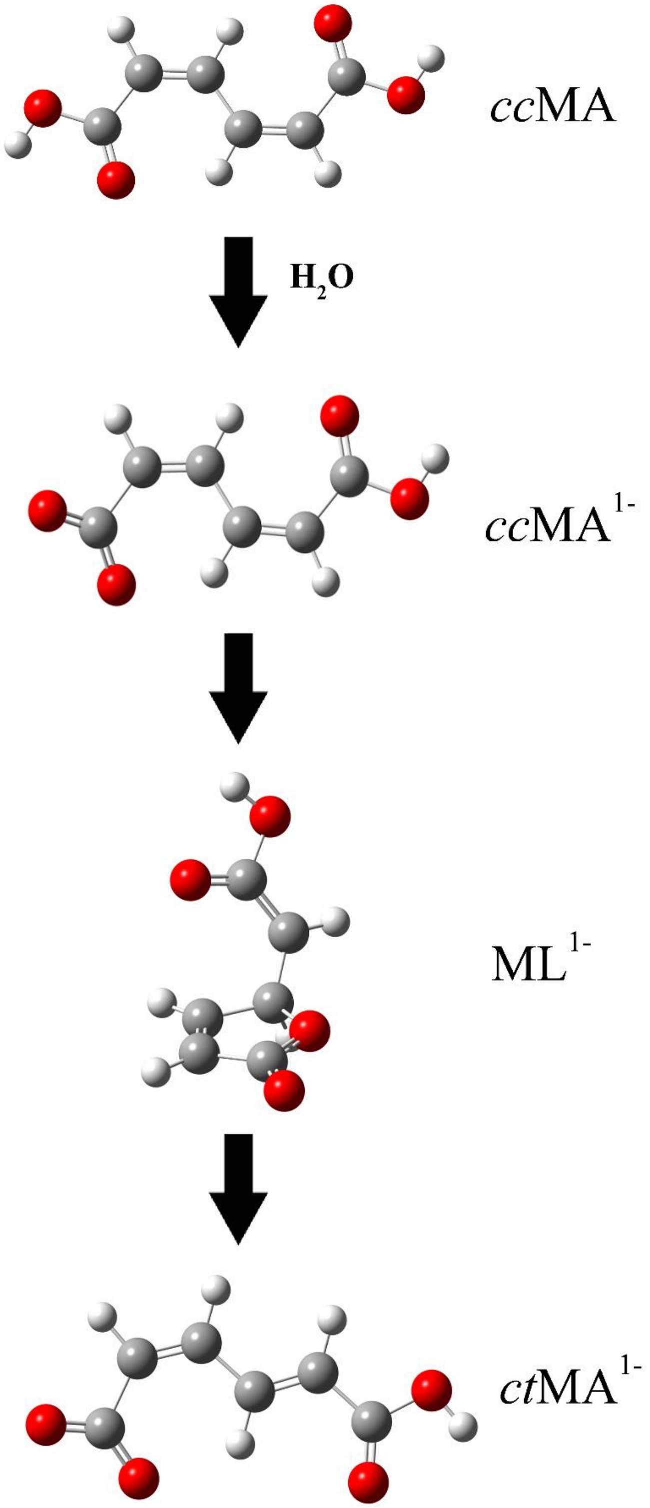

Figure 5-1. The proposed conversion of *cc*MA to *ct*MA in water, involving a single deprotonation and a lactone intermediate.

5.2 Methods

Gas-phase computational simulations on all muconic acid species were performed using the *Gaussian16* software package[16] with no symmetry constraints. The long-range corrected wB97X functional[17] was used with the aug-ccPVTZ[18-20] basis set. Other functionals that included a long-range correction term such as LC-wPBE[21] and M062X[22] showed similar results. Functionals without long range correction yielded results that did not reliably show continuity of the potential energy surfaces investigated along the isomerization coordinate. Geometry scanning calculations were performed to simulate the conversion of *cc*MA and deprotonated *cc*MA ions to *ct*MA, by incrementally changing the angles and dihedrals within the molecular structure in an attempt to facilitate muconoloactone formation. 1-degree increments were found to be sufficient in all scanning calculations to accurately define the potential energy surface. To test the effect of solvation, the conductor-like polarizable continuum model (CPCM)[23, 24] was employed in some calculations which yielded no considerable energy or structural differences.

5.3 Results

5.3.1 Structural Optimizations

For clarity, atom labels for the muconic structure are shown in **Figure 5-2.** Optimizations were performed on *cc*MA, *cc*MA^{1-} (removal of H1) and *ct*MA^{2-} (removal of H1 and H6). Both *cc*MA and *ct*MA are naturally planar molecules, but after optimization the carboxylic group on *cc*MA^{-1} became non-planar while *cc*MA^{2-} remained planar (**Figure 5-3**). A list of the bond lengths for the various protonated *cc*MA forms are detailed in **Table 5-1.**

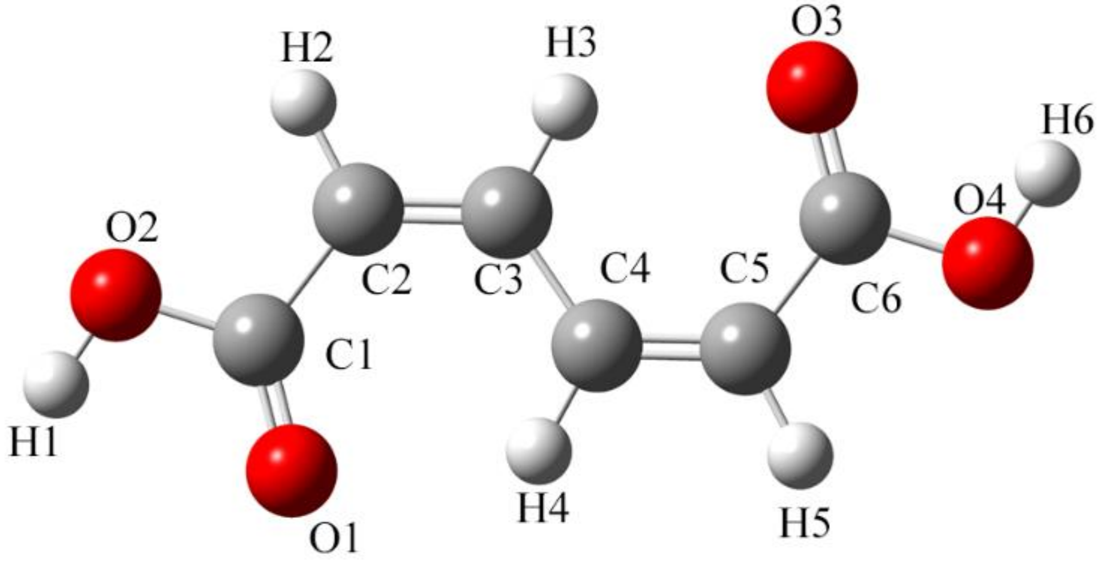

Figure 5-2. Atom labeling scheme for muconic acid.

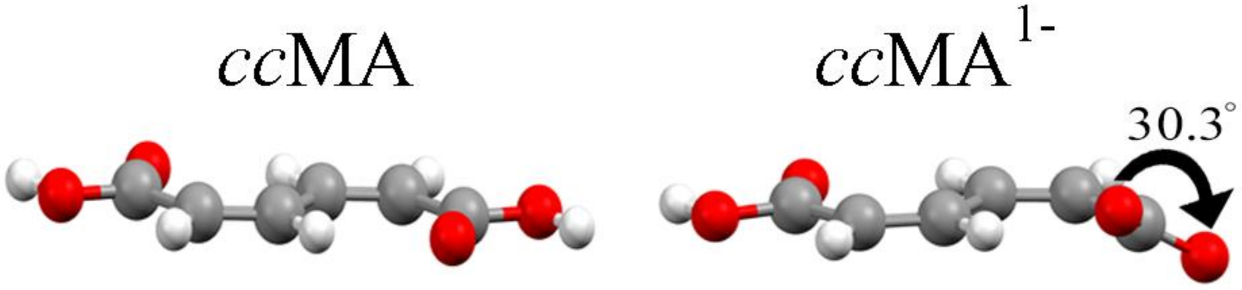

Figure 5-3. The planarity of *cc*MA (left) and non-planarity of *cc*MA^{-1} (right).

Table 5-1. Calculated bond lengths for *cc*MA at differing levels of deprotonation and ML^{1-}. Lengths are given in Angstroms.

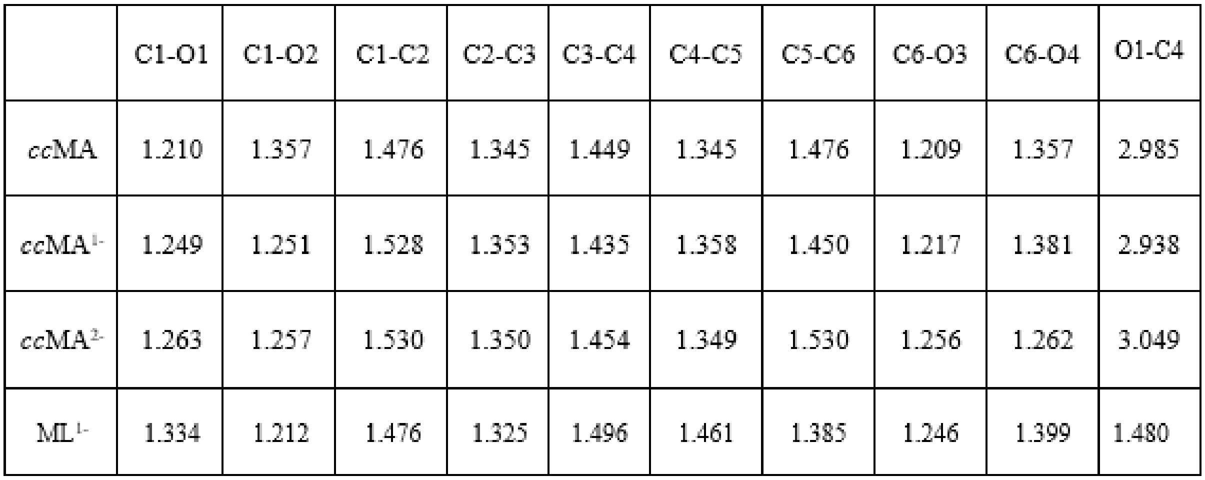

	C1-O1	C1-O2	C1-C2	C2-C3	C3-C4	C4-C5	C5-C6	C6-O3	C6-O4	O1-C4
*cc*MA	1.210	1.357	1.476	1.345	1.449	1.345	1.476	1.209	1.357	2.985
*cc*MA^{1-}	1.249	1.251	1.528	1.353	1.435	1.358	1.450	1.217	1.381	2.938
*cc*MA^{2-}	1.263	1.257	1.530	1.350	1.454	1.349	1.530	1.256	1.262	3.049
ML^{1-}	1.334	1.212	1.476	1.325	1.496	1.461	1.385	1.246	1.399	1.480

Interestingly, *cc*MA^{1-} had the longest C2-C3 and C4-C5 double bonds allowing for more freedom of movement about these bonds, implying these bond distances may help to facilitate ML^{1-} formation.

Attempts to obtain an ML^{1-} structure were first performed by simply decreasing the C1-C2-C3 angle (originally 128.76º) in *cc*MA^{1-}, bringing the deprotonated O1 oxygen atom closer to C4 carbon. This was not successful due to H4 sterically hindering O1-C4 binding. To resolve this, the C2-C3-C4-C5 dihedral angle was changed (which rotates about the C3-C4 single bond) which shifted the H4 hydrogen out of the molecular plane in conjunction with decreasing the C1-C2-C3 angle which resulted in the formation of a ring. Upon full optimization of the cyclized molecule, the angle and dihedral became 108.6º and -129.2º, respectively.

The structure of the ML^{1-} is shown in **Figure 5-4**. Compared to the corresponding *cc*MA^{1-} ion, the ML^{1-} has shorter C-O bonds, and a considerably shorter C2-C3 double bond distance which is now a part of the ring. The newly formed O1-C4 bond that is present upon ring formation has a length of 1.48Å. A frequency analysis was performed on the ML^{1-} structure which showed no imaginary modes, providing evidence for its role as an intermediate rather than a transition state. The ML^{1-} intermediate was 28.7 kJ/mol higher in energy than *cc*MA^{1-}, with *ct*MA being the most energetically favorable by 1.64 kJ/mol.

If *cc*MA^{2-} is positioned with the same angle and dihedral that causes muconolactone formation in the singly-deprotonated species, it simply optimizes back to planar *cc*MA^{2-}. To further investigate this, an optimization was performed on ML^{1-} with a removed H6 hydrogen, starting from an ML^{2-} structure. Doing so caused the ring to break, and the molecule optimized back to the *cc*MA^{2-} geometry indicating that the singly-deprotonated nature of *cc*MA^{1-} is significant. In order to determine if ring formation is the most energetically favorable way to form *ct*MA from *cc*MA, and is thus a part of the mechanism, multiple potential energy scans were performed.

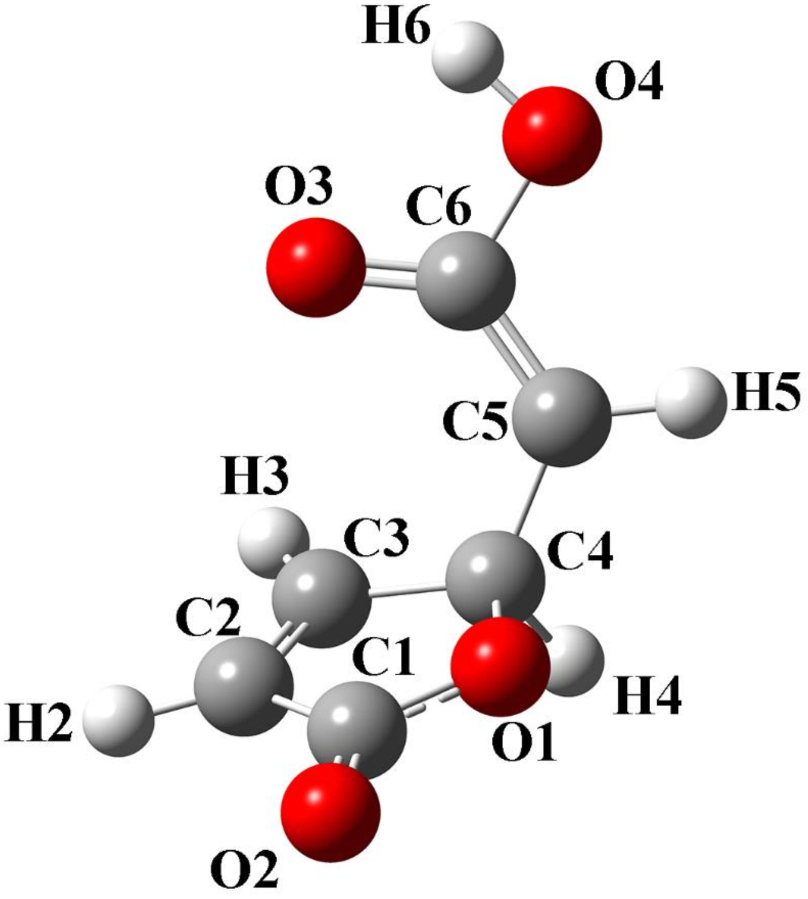

Figure 5-4. The structure of optimized ML^{1-}.

5.3.2 Potential Energy Scans (ccMA^{1-} to ML^{1-})

Energy scans were performed to map the conversion of *cc*MA^{1-} to the ML^{1-} in 1-degree increments by simultaneously changing the C1-C2-C3 angle and the C2-C3-C4-C5 dihedral angle. This provided a potential energy surface of the transition, shown in **Figure 5-5.** As the dihedral angle is changed, the H4 hydrogen tilts back, allowing O1 to bond to the C4 carbon and form the ring. The energy immediately drops upon ring formation. Without H4 tilting, no ML^{1-} formation occurs, which is why the simultaneous angle and dihedral change is significant. The lowest point in this scan, and thus the most stable, is at a dihedral angle of -129.1° and an angle of 108.6°, which agrees with the optimized ML^{1-} structure.

5.3.3 Transition State Determination

With an ML^{1-} intermediate determined, further calculations were performed to determine the transition states between the stable isomeric and ring forms. In *Gaussian16*, the Synchronous Transit-Guided Quasi Newton (STQN) Method[25] is used for transition state determination from either two or three input structures (keyword QST2 and QST3, respectively). Two QST2 calculations were performed; one using the *cc*MA and ML^{1-} optimized structures and the second using the ML^{1-} and *ct*MA optimized structures, which provided an estimation of the transition state between their respective forms

The QST2 transition state results were used as a third point in QST3 calculations, which resulted in more reliable transition state energy barrier from *cc*MA to ML^{1-} and ML^{1-} to *ct*MA. The resulting structures each had one imaginary mode, indicating their validity as a transition state. The energy barrier from *cc*MA to the transition state was 58.1 kJ/mol. The barrier of the transition state from the ML^{1-} to *ct*MA was 6.5 kJ/mol. This is shown in **Table 5-4** and in **Figure 5-6**. These barrier heights are an indication that the limiting step in *cc*MA to *ct*MA formation is in ML^{1-} formation.

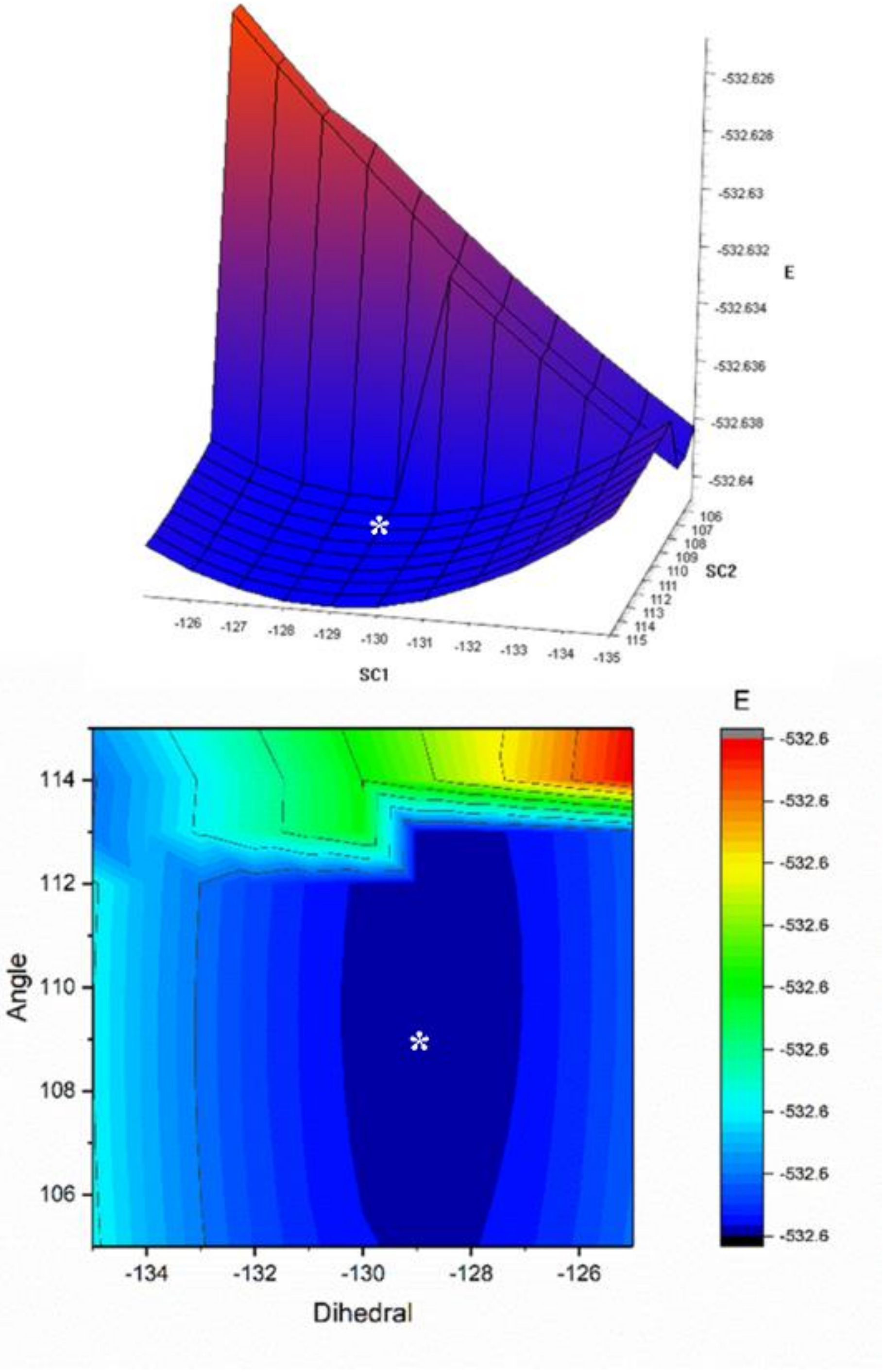

Figure 5-5. Potential energy surface of scanning over the angle and dihedral of ccMA to mlac^{1-} formation. The steep drop off is indicative of ring formation and the '*' symbol marks the optimized ring structure. A side view (upper) and top view (lower) of the surface are provided.

Table 5-4. Relative energy of the singly protonated muconic acid species and the transition state energies between their conversion states.

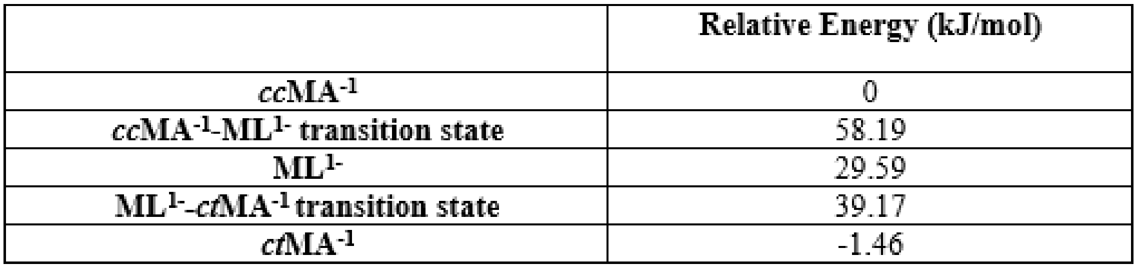

	Relative Energy (kJ/mol)
***cc*MA^{-1}**	0
***cc*MA^{-1}-ML^{1-} transition state**	58.19
ML^{1-}	29.59
ML^{1-}-*ct*MA^{-1} transition state	39.17
***ct*MA^{-1}**	-1.46

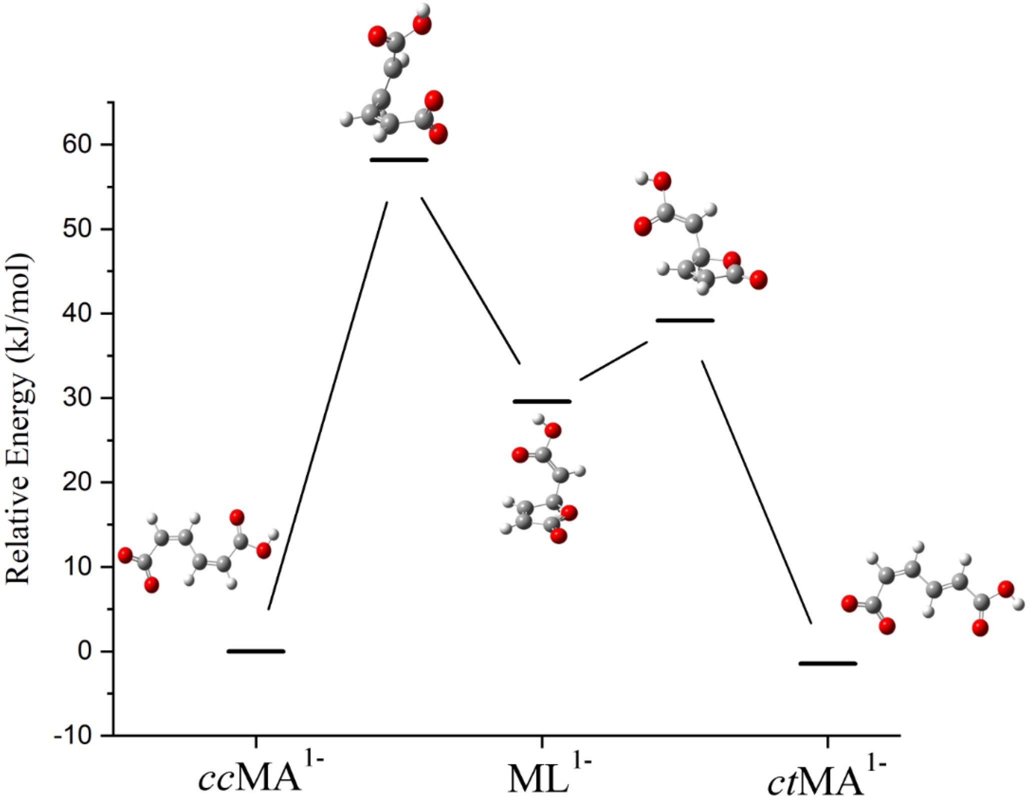

Figure 5-6. Relative energies across the transformation coordinate of *cc*MA^{1-} to *ct*MA^{1-} utilizing a lactone intermediate

5.3.4 Molecular Orbital Analysis

5.3.4.1 ccMA^{1-} HOMO Evaluation

To further consider what is occurring upon ring formation and why a sudden energy drop is observed in the scanning calculations, the HOMO electron densities were evaluated at the C1-C2-C3 angle just before ring formation (109.6º) and keeping the C2-C3-C4-C5 dihedral constant at -129º, with an energy 45.2 kJ/mol higher than that of *cc*MA^{1-}. This is shown in **Figure 5-7**. One degree before ring formation, the electron density spreads up the carbon chain with little electron density present at the -COOH group, while less electron density is present around the C2-C3 double bond. Upon ring formation, a large amount of the electron density surrounds the carbon chain and the carboxylic acid end, while less is found at the ring. It is possible that the large amount of electron delocalization along the carbon chain in the ML^{1-} structure leads to stabilization of its structure.

5.4.5.2 ccMA^{2-} HOMO Evaluation

By observing the HOMO electron density in ccMA^{2-} at the same near-ring angles as ccMA^{-1}, it can be visualized as to why the ring does not form. Detailed in **Figure 5-8**, the ring has delocalized electron density along the carbon chain but does not form a ring because the carboxylate groups symmetrically tilt away from the carbon chain as they are brought closer to it. The increased resonance[15] of the *cc*MA^{2-} because of no carboxylic hydrogens corresponds with the higher symmetry observed in its structure and makes lactonization unfavorable.

Near ring formation

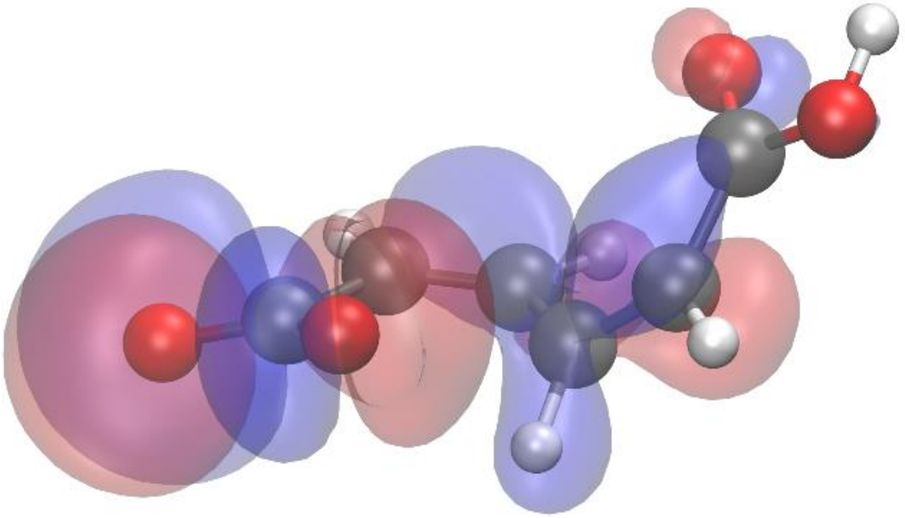

Ring formed

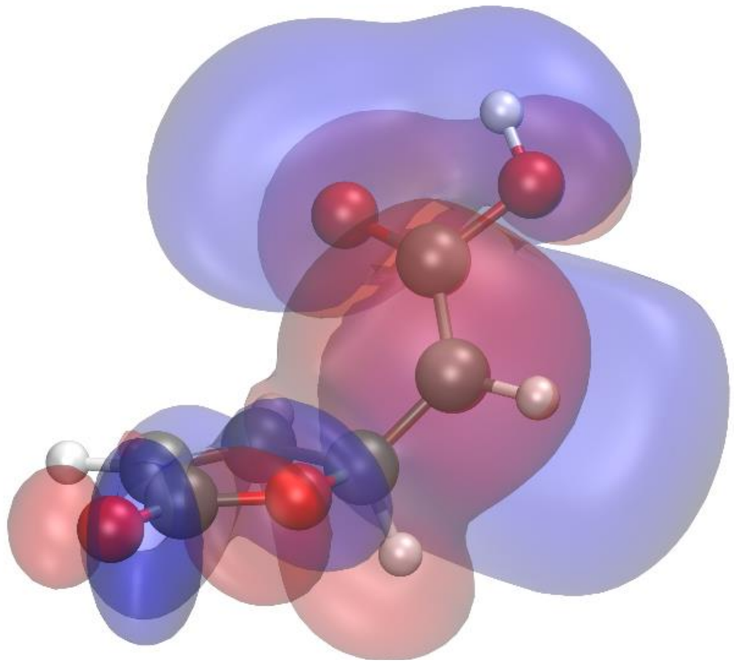

Figure 5-7. The HOMO for ccMA^{1-} as it approaches ring formation with an C1-C2-C3 angle of 110.6^{o} (above) and upon ring formation at an angle of 109.6^{o} (below), with the C2-C3-C4-C5 dihedral kept at a constant -129^{o}.

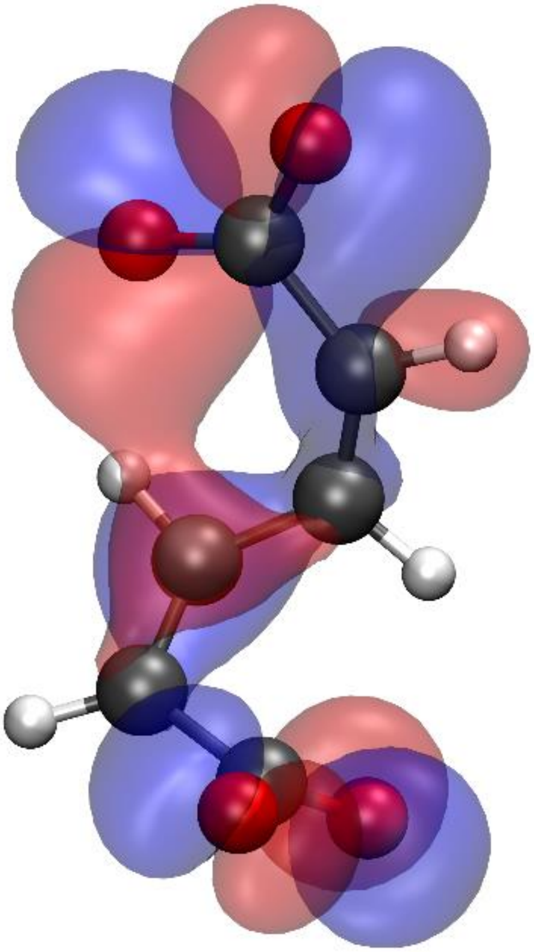

Figure 5-8. HOMO for ccMA^{2-}, set at a C1-C2-C3 angle of 108.6^{o} and C2-C3-C4-C5 dihedral angle of -129^{o} that would form ML^{1-} from *cc*MA^{1-}.

5.3.5 Potential Energy Scans (ML^{1-} to ctMA^{1-})

Once the ring is formed from *cc*MA^{1-}, the conversion of ML^{1-}to *ct*MA only requires twisting about the C3-C4-C5-C6 dihedral angle. Before ring formation, the C4-C5 bond distance was 1.358 Å, which is the typical length of a C-C double bond and makes the torsion very unfavorable. However, after lactone formation the bond length is 1.461 Å, which corresponds to a C-C single bond and allows the torsion to occur. As shown in **Figure 5-9**, past -120°, the ring breaks leading to *ct*MA stabilization at -180°.

5.3.6 Fully Protonated ccMA

In all simulations no ML^{1-} was found to form from fully protonated *cc*MA. This contradicts the previous experimental observation that ML^{1-} occurs at low pH levels from fully protonated *cc*MA. However, it was reported that the rate of ML^{1-} formation was much slower than from *cc*MA^{-1}. Since ring formation is impossible in the case of *cc*MA, a proposed method[15] of transformation of *cc*MA to *ct*MA was a twisting of *cc*MA along the C3-C4 carbon bond. Conducting a scan along this coordinate shows that the potential energy reaches as high as 300 kJ/mol, which would be too large a barrier to overcome experimentally. It is more likely that the mechanism is far more complex and perhaps solvent mediated, which is beyond the scope of this work, although a technique such as molecular dynamics may prove to be useful in this endeavor.

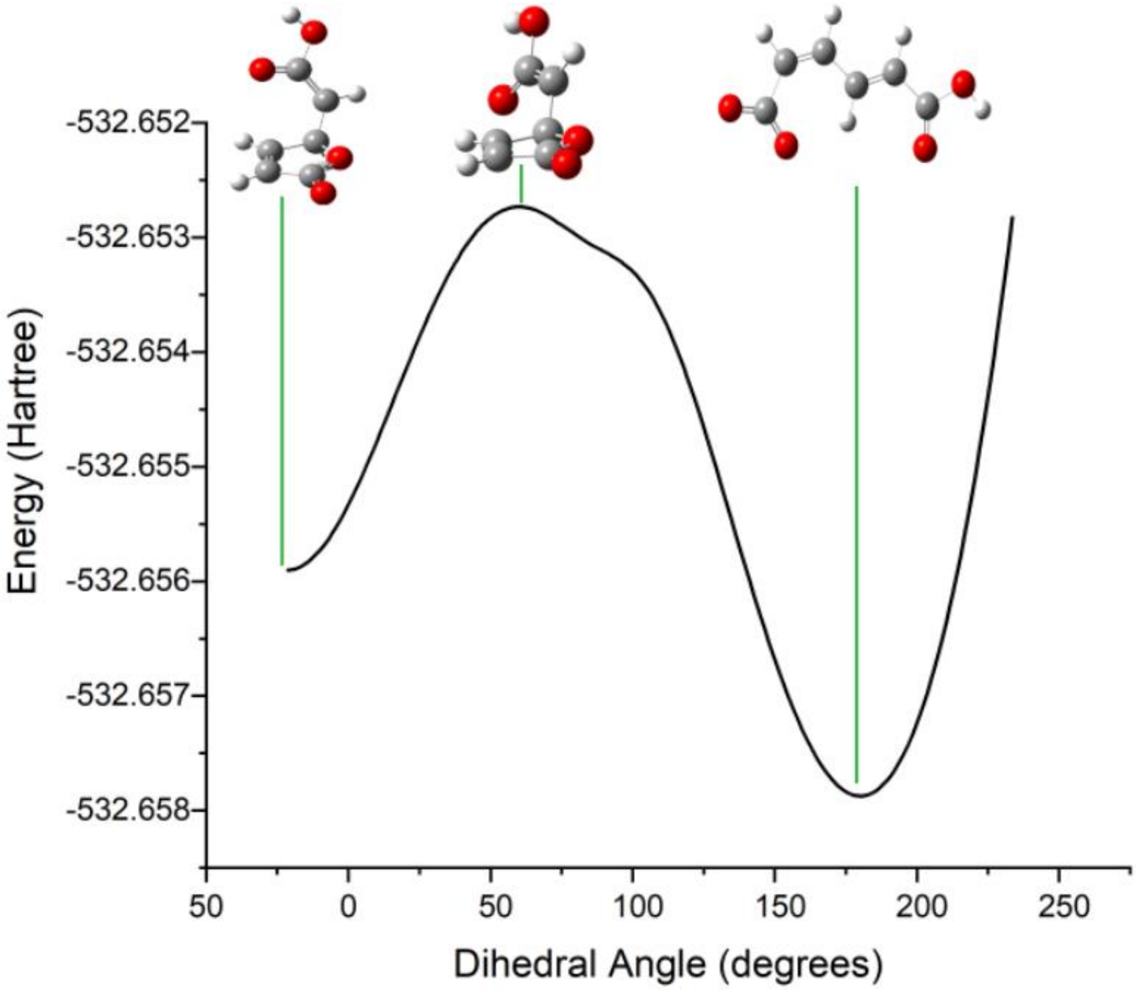

Figure 5-9. Graph of the dihedral change from the mlac^{1-} to *ct*MA^{1-}. The ring breaks at approximately -120 degrees and stabilizes to -180 degrees.

5.4 Conclusions

The isomerization of *cc*MA to *ct*MA in aqueous solution is accomplished through a cyclized ML^{1-} intermediate structure. In order for a muconolactone to form, and thus aid in *ct*MA formation, it is necessary for the *cc*MA to be singly deprotonated. Calculations performed with *cc*MA and *cc*MA^{2-} showed no evidence of muconolactone formation. Other methods of *ct*MA formation that do not involve ML^{1-} formation, such as a twisting along the carbon chain, are too energetically unfavorable to be a viable method of *ct*MA formation. The results of the DFT calculations show that it is energetically feasible for *cc*MA to convert to *ct*MA through a lactone intermediate. The role of pH may be an understudied factor in lactone formation, and these findings can may be applicable to the isomerization mechanisms in related chemical systems.

5.5 References

(1) Curran, K. A.; Leavitt, J. M.; Karim, A. S.; Alper, H. S., Metabolic engineering of muconic acid production in Saccharomyces cerevisiae. *Metabolic engineering* **2013,** 15, 55-66.

(2) Johnson, C. W.; Salvachúa, D.; Khanna, P.; Smith, H.; Peterson, D. J.; Beckham, G. T., Enhancing muconic acid production from glucose and lignin-derived aromatic compounds via increased protocatechuate decarboxylase activity. *Metabolic Engineering Communications* **2016,** 3, 111-119.

(3) Vardon, D. R.; Rorrer, N. A.; Salvachua, D.; Settle, A. E.; Johnson, C. W.; Menart, M. J.; Cleveland, N. S.; Ciesielski, P. N.; Steirer, K. X.; Dorgan, J. R.; Beckham, G. T., cis,cis-Muconic acid: separation and catalysis to bio-adipic acid for nylon-6,6 polymerization. *Green Chemistry* **2016,** 18, (11), 3397-3413.

(4) Elvidge, J. A.; Linstead, R. P.; Orkin, B. A.; Sims, P.; Baer, H.; Pattison, D. B., Unsaturated lactones and related substances. Introduction. IV. Lactonic products derived from muconic acid. *J. Chem. Soc.* **1950**, 2228-35.

(5) Niu, W.; Draths, K. M.; Frost, J. W., Benzene-free synthesis of adipic acid. *Biotechnology progress* **2002,** 18, (2), 201-11.

(6) Weber, C.; Bruckner, C.; Weinreb, S.; Lehr, C.; Essl, C.; Boles, E., Biosynthesis of cis,cis-muconic acid and its aromatic precursors, catechol and protocatechuic acid, from renewable feedstocks by Saccharomyces cerevisiae. *Applied and environmental microbiology* **2012,** 78, (23), 8421-30.

(7) Lu, R.; Lu, F.; Chen, J.; Yu, W.; Huang, Q.; Zhang, J.; Xu, J., Production of Diethyl Terephthalate from Biomass-Derived Muconic Acid. *Angewandte Chemie* **2016,** 128, (1), 257-261.

(8) Elvidge, J. A.; Linstead, R. P.; Sims, P.; Orkin, B. A., Third isomeric (cis-trans) muconic acid. *J. Chem. Soc.* **1950**, 2235-41.

(9) Zaczek, A. J.; Korter, T. M., Polymorphism in cis-trans Muconic Acid Crystals and the Role of C-H···O Hydrogen Bonds. *Cryst. Growth Des.* **2017,** 17, (8), 4458-4466.

(10) Kaulmann, U.; Kaschabek, S. R.; Schlomann, M., Mechanism of chloride elimination from 3-chloro- and 2,4-dichloro-cis,cis-muconate: new insight obtained from analysis of muconate cycloisomerase variant CatB-K169A. *J Bacteriol* **2001,** 183, (15), 4551-61.

(11) Prucha, M.; Peterseim, A.; Pieper, D. H., Evidence for an isomeric muconolactone isomerase involved in the metabolism of 4-methylmuconolactone by Alcaligenes eutrophus JMP134. *Arch Microbiol* **1997,** 168, (1), 33-8.

(12) Vollmer, M. D.; Fischer, P.; Knackmuss, H. J.; Schlömann, M., Inability of muconate cycloisomerases to cause dehalogenation during conversion of 2-chloro-cis,cis-muconate. *Journal of Bacteriology* **1994,** 176, (14), 4366-4375.

(13) Pollmann, K.; Wray, V.; H Pieper, D., *Chloromethylmuconolactones as Critical Metabolites in the Degradation of Chloromethylcatechols: Recalcitrance of 2-Chlorotoluene*. ed.; 2005; Vol. 187, p 2332-40.

(14) Prucha, M.; Peterseim, A.; Pieper, D. H., Evidence for an isomeric muconolactone isomerase involved in the metabolism of 4-methylmuconolactone by Alcaligenes eutrophus JMP134. *Archives of Microbiology* **1997,** 168, (1), 33-38.

(15) Carraher, J. M.; Pfennig, T.; Rao, R. G.; Shanks, B. H.; Tessonnier, J.-P., cis,cis-Muconic acid isomerization and catalytic conversion to biobased cyclic-C6-1,4-diacid monomers. *Green Chem.* **2017**, Ahead of Print.

(16) Frisch, M. J.; Trucks, G. W.; Schlegel, H. B.; Scuseria, G. E.; Robb, M. A.; Cheeseman, J. R.; Scalmani, G.; Barone, V.; Petersson, G. A.; Nakatsuji, et al, *Gaussian 16 Rev. B.01*, Wallingford, CT, 2016.

(17) Chai, J. D.; Head-Gordon, M., Systematic optimization of long-range corrected hybrid density functionals. *J Chem Phys* **2008,** 128, (8), 084106.

(18) Dunning, T. H., Gaussian basis sets for use in correlated molecular calculations. I. The atoms boron through neon and hydrogen. *The Journal of Chemical Physics* **1989,** 90, (2), 1007-1023.

(19) Woon, D. E.; Dunning, T. H., Gaussian basis sets for use in correlated molecular calculations. III. The atoms aluminum through argon. *The Journal of Chemical Physics* **1993,** 98, (2), 1358-1371.

(20) Woon, D. E.; Dunning, T. H., Gaussian basis sets for use in correlated molecular calculations. IV. Calculation of static electrical response properties. *The Journal of Chemical Physics* **1994,** 100, (4), 2975-2988.

(21) Weintraub, E.; Henderson, T. M.; Scuseria, G. E., Long-Range-Corrected Hybrids Based on a New Model Exchange Hole. *Journal of Chemical Theory and Computation* **2009,** 5, (4), 754-762.

(22) Zhao, Y.; Truhlar, D. G., The M06 suite of density functionals for main group thermochemistry, thermochemical kinetics, noncovalent interactions, excited states, and transition elements: two new functionals and systematic testing of four M06-class

functionals and 12 other functionals. *Theoretical Chemistry Accounts* **2008,** 120, (1), 215-241.

(23) Klamt, A.; Schüürmann, G., COSMO: a new approach to dielectric screening in solvents with explicit expressions for the screening energy and its gradient. *Journal of the Chemical Society, Perkin Transactions 2* **1993**, (5), 799-805.

(24) Takano, Y.; Houk, K. N., Benchmarking the Conductor-like Polarizable Continuum Model (CPCM) for Aqueous Solvation Free Energies of Neutral and Ionic Organic Molecules. *Journal of Chemical Theory and Computation* **2005,** 1, (1), 70-77.

(25) Peng, C.; Bernhard Schlegel, H., Combining Synchronous Transit and Quasi-Newton Methods to Find Transition States. *Israel Journal of Chemistry* **1993,** 33, (4), 449-454.

CHAPTER 6: Mapping of the Polymorph Transformation Gateway Vibration in Crystalline 1,2,4,5-Tetrabromobenzene

Abstract

The thermosalient behavior of 1,2,4,5-tetrabromobenzene (TBB) is related to a temperature-induced polymorphic structural change. The mechanism behind the phase transition has been investigated in this work using low-frequency (5-250 cm^{-1}) Raman spectroscopy and solid-state density functional theory simulations. Careful adjustments of the probing laser power permitted thermal control of the polymorph populations and enabled high-quality Raman vibrational spectra to be obtained for both the β (low temperature) and γ (high temperature) forms of TBB. Numerous well-defined vibrational features appear in the Raman spectra of both polymorphs which could be assigned to specific motions of the solid-state TBB molecules. It was discovered that the lowest-frequency vibration at 15.5 cm^{-1} in β-TBB at 291 K is a rotational mode that serves as a gateway for inducing the polymorphic phase transition to γ-TBB. Computationally mapping the potential energy surface along this vibrational coordinate reveals that the two TBB polymorphs are separated by a 2.4 kJ/mol barrier and that γ-TBB exhibits an enhanced cohesion energy that stabilizes its structure.

6.1 Introduction

The thermosalient effect is a phenomenon where a crystal undergoes a structural transformation due to changes in temperature, and this produces a physical “jumping” of the crystal[1]. From an atom-level perspective, the physical motion corresponds with sudden changes of the molecular structures and packing arrangements of the components comprising the crystalline solid. This unusual behavior has been attributed to material changes such as molecular dimerization[2] and polymorph tranformations[3, 4]. Given that this is often a reversible process[2, 5] controlled by varying sample temperature, the effect has attracted interest in the development of new energy transducing materials used in electronics[6, 7].

One of the more well-studied thermosalient materials is 1,2,4,5-tetrabromobenzene (TBB)[8-11]. TBB is often used as a starting material in the organic syntheses of liquid crystals[12] and photoconductive polymers[13]. Below 307 K[10] (previously reported at 319 K[14]), crystalline TBB naturally exists in its β polymorph, with the γ polymorph forming at higher temperatures. Single crystals of TBB are often twinned[15, 16], and the crystals jump or split upon polymorph transformation, propelling themselves several centimeters. The jumping distances are largely dependent on the crystal size, with large crystals having more pronounced jumping[8].

The structures of both TBB polymorphs have been previously determined through single-crystal X-ray diffraction[17, 18], revealing that both exist in the same space group (*P*21/n) with similar unit cell dimensions, differing primarily through an intermolecular tilting of the TBB rings with respect to one another in the unit cell, as shown in **Figure 6-1.** Because the polymorph structures are quite similar to one another and do not intuitively correspond to the significant changes that might be associated with thermosalient behavior, it warrants further analysis of the crystal structures, the intermolecular lattice vibrations, and the underlying mechanism responsible for the conversion between solid forms.

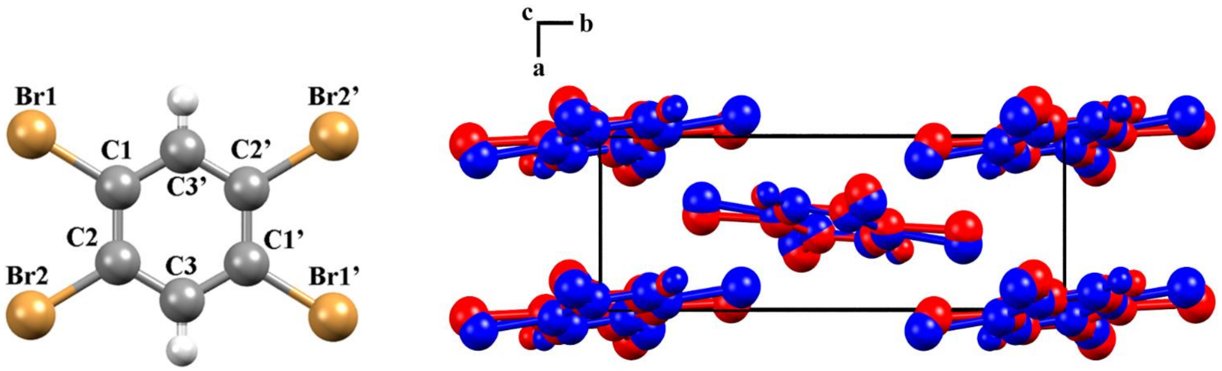

Figure 6-1. Molecular structure of a TBB molecule (left) and the polymorph packing differences between β-TBB (blue) and γ-TBB (red).

Recent work has investigated the structural strain associated with the polymorph change that contributes to TBB's thermosalient nature, and suggested that low-frequency vibrational modes near 43 cm^{-1} and 47 cm^{-1} are integral to the conversion[10]. In the current study, experimental low-frequency Raman spectral data (10-250 cm^{-1}) was collected at various temperatures and combined with solid-state density functional theory (ss-DFT) simulations to provide clear assignments of the vibrational motions in this region. This granted the ability to uniquely identify a single mode as being the gateway vibration for β-TBB to γ-TBB conversion. An in-depth computational study of the vibrational energies, motions, and potential energy surfaces of six rotational modes present in the β-TBB crystals revealed that only the vibration observed at 15.5 cm^{-1} (at 291 K) is able to initiate the $\beta \rightarrow \gamma$ transformation. The combination of experimental Raman data and *ab initio* computational analyses enables the mechanism of the polymorph transformation to be understood and quantified in terms of relative energies and barriers to conversion.

6.2 Methods

6.2.1 Experimental Details

TBB was obtained as a fine powder from New York University Abu Dhabi. Sample composition was confirmed via powder X-ray diffraction, showing β-TBB. Raman spectra were obtained with an Ondax (Monrovia, CA, USA) THz-Raman spectrometer with a laser centered at 784.7 nm and coupled to an Andor (Concord, MA, USA) Shamrock 750 spectrograph with an

Andor iDus 416 CCD. The data spanned ± 250 cm^{-1} from the Rayleigh peak with an effective spectral resolution of 0.6 cm^{-1}. For room temperature studies, the TBB sample was kept as a loose powder in a 10 mm diameter glass vial. The spectra shown here were averaged over 225 acquisitions, each with a 3 second exposure time. A range of laser power levels was used (2.5 mW, 5.2 mW, 13.1 mW, 17.7 mW, 74 mW, and 115 mW) and controlled by a variable neutral density filter.

For cooled studies, the powder samples were compressed into free-standing pellets (13 mm diameter, ~1 mm thick) and mounted in a liquid-nitrogen-cooled cryostat. With an applied pelleting pressure of 0.07 GPa, the sample disc showed β-TBB to be the major substituent, but with 0.14 GPa applied, γ-TBB was the major product. Raman spectra were obtained at set temperatures (78 K, 125 K, 150 K, 175 K, 200 K, 290 K) for each sample. Additional pellets were made at increased pressures (0.20 and 0.28 GPa) to evaluate the effect on TBB stabilization and were examined only at 290 K. The laser power was kept to a minimum (13.1 mW) for all cooled pellet experiments in order to avoid unwanted polymorph conversion while maximizing the scattering signal.

6.2.2 Computational Details

All solid-state density functional theory (ss-DFT) calculations were performed using the CRYSTAL17[19] software package. The Perdew-Burke-Ernzerhof (PBE) exchange and correlation functional[20] was used with the def2-TZVP[21] basis set. Grimme's D3 dispersion correction[22, 23] with an included Becke-Johnson dampening parameter[24] was employed to treat weak long-range London dispersion forces between molecules.

Geometry optimizations were begun using previously published crystal structures for β-TBB[17] and γ-TBB[18] as initial starting points. To account for the effects of non-zero experimental temperatures on the unit cell dimensions in the calculations, atomic positions were allowed to optimize to their energetic minima within fixed lattice dimensions and space group symmetries determined by the reported single-crystal X-ray diffraction measurements. For β-TBB, the low-temperature form, a free optimization that did not constrain lattice dimensions was also run for comparison. An energetic convergence of $\Delta E < 10^{-8}$ hartree was used for all optimizations. Separate single-point energy calculations were performed on the optimized structures in order to determine the energy stability rankings of the polymorphs, and these were corrected for basis set superposition errors using the counterpoise method[25].

Harmonic normal mode frequency analyses were executed on the structurally optimized TBB solids with a stricter energy convergence of $\Delta E < 10^{-10}$ hartree. Raman intensities were calculated by computing the Raman tensor utilizing a coupled-perturbed Hartree-Fock/Kohn Sham approach[26, 27]. To accelerate convergence, a mixing of Fock/KS matrix derivatives[28] was used. The experimental temperatures and laser excitation wavelength were also accounted for in the simulated intensities. Normal mode analyses formed the basis for constrained unit cell optimizations, using eigenvector-displaced molecular positions to determine the influence of specific lattice vibrations on the polymorphic stabilities.

6.3 Results and Discussion

6.3.1 Raman Spectroscopy of Powder Samples

Raman spectra of TBB powder were taken at varied laser power levels, with the spectrum at the lowest power (3mW) showing β-TBB, and the maximum power (115 mW) revealing γ-TBB to be present (**Figure 6-2**). The spectral features of both forms were consistent with prior reports[29, 30], aiding in their identification. The samples at the laser power extremes were found to be at least 96% polymorphically pure within the limits of detection. Polymorph changes occurred due to laser heating of the sample, with greater powers imparting more heat and causing γ-TBB formation. At intermediate powers, a mix of both polymorphs was observed, which may be attributed to uneven sample heating leading to localized partial polymorph conversion in the beam path. No thermosalient crystal movement was observed in the powder sample during heating (likely due to the very small particle size), indicating that the spectra were representative of the same probed area each time.

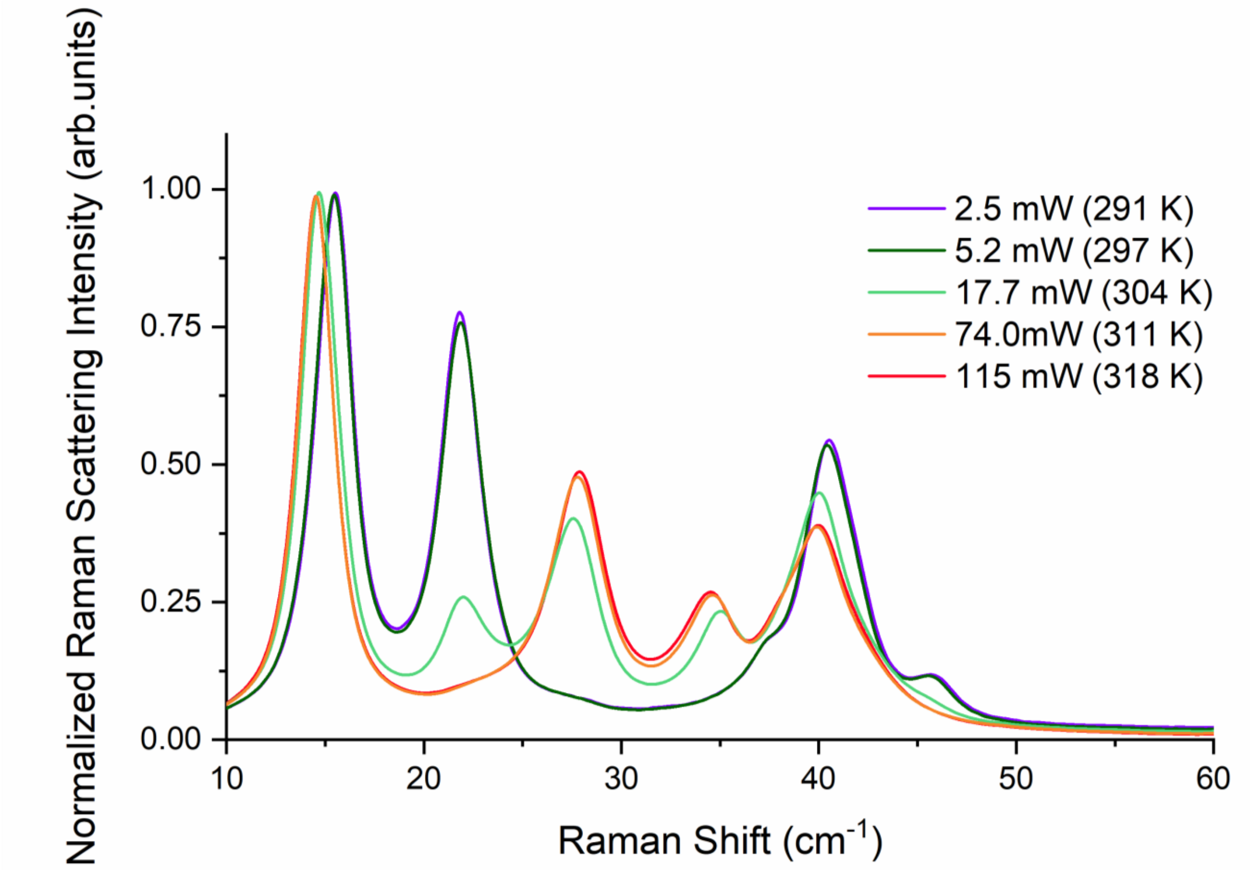

Figure 6-2. Low-frequency Raman spectra for TBB at varying applied laser powers.

It is possible to calculate the average temperature of a sample at the laser focus directly from the Raman spectral data by utilizing the relative intensities of the anti-Stokes/Stokes scattering features and the following equation:

$$\frac{I_{anti-Stokes}}{I_{Stokes}} = \left(\frac{v_0 + v_1}{v_0 - v_1}\right)^4 e^{\frac{-hv_1}{kT}} \tag{6.1}$$

where I is the intensity of an anti-Stokes and its corresponding Stokes peaks, v_0 is the frequency of the exciting light, v_1 is the frequency of the Raman shift, h is Planck's constant, and k is the Boltzmann constant. Temperatures were calculated using the peak 126.4 cm^{-1} from the Rayleigh peak, as it is a single narrow feature that is present in both TBB polymorphs, as shown in **Figure 6-3**. The peaks were fit with a Lorentzian line shape, and the areas under the best fit curves were used in the anti-Stokes/Stokes ratio. All sample temperatures reported in this work have been determined in this way. The lowest applied power of 2.5 mW was found to produce a sample temperature of 291 K ± 3 K, which is in agreement with the laboratory temperature of 290 K and represented the spectrum of β-TBB. The highest laser power (115 mW) showed that the sample had been heated to 318 ± 7 K and represented the Raman spectrum of γ-TBB, in agreement with the previous reports noting dominance above 307 K[10].

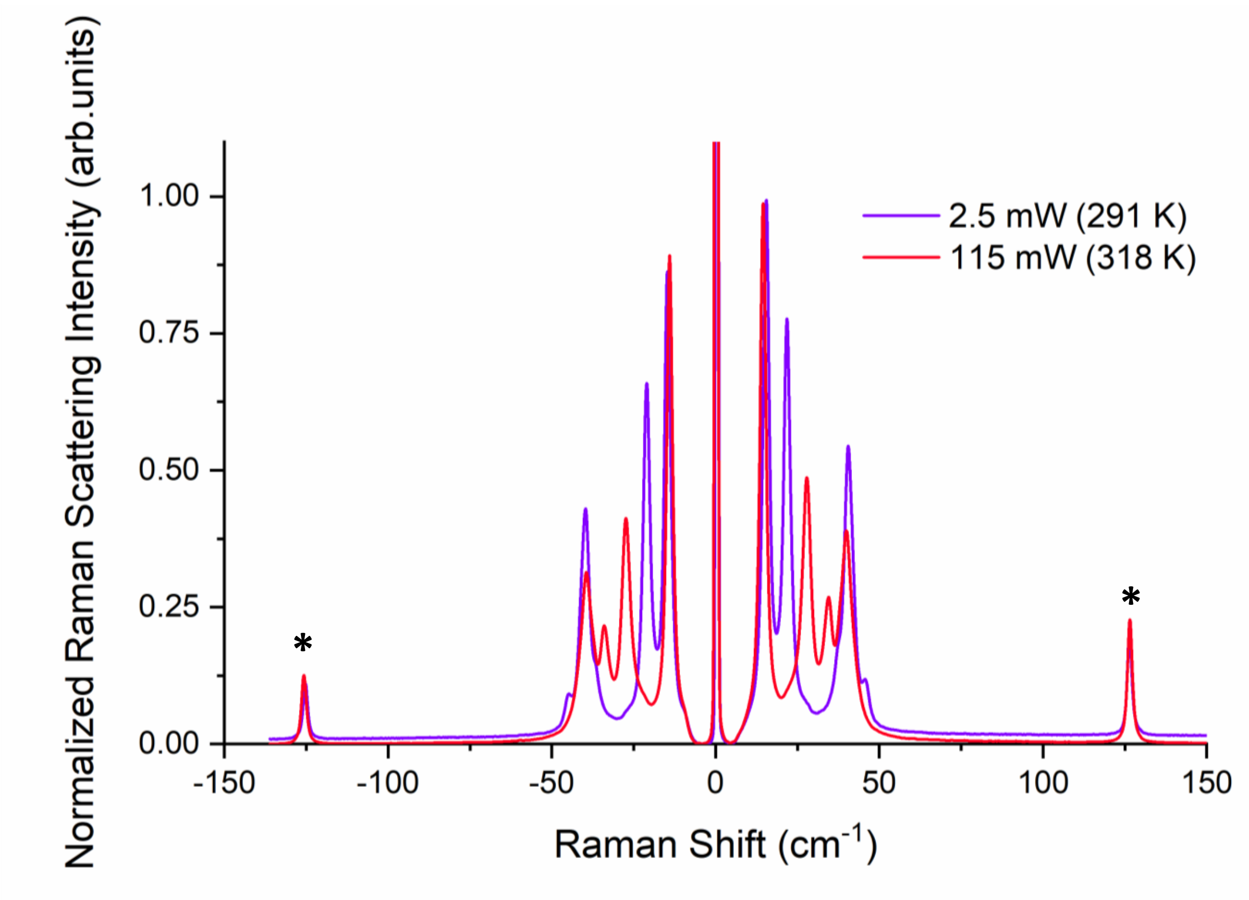

Figure 6-3. Raman spectra of β-TBB (purple) and γ-TBB (red) obtained from powder samples indicating the peaks used for temperature analysis (marked by *).

6.3.2 Raman Spectroscopy of Pelleted Samples

6.3.2.1 β-TBB

A β-TBB pellet made from the application of 0.07 GPa was studied at a low laser power (13.1 mW) with at-sample temperatures of 317 K ± 6 K and 105 K ± 4 K and is shown in **Figure 6-4**. The pellet spectra match with the corresponding Raman spectra of the powder samples, with the only differences (referring to the 105 K data) being a shoulder feature at 14.8 cm^{-1} and a peak at 32.2 cm^{-1} originating from a small amount of γ-TBB contamination. The existence of γ-TBB is likely due to transient heating upon pressure application when the pellet was created, but the low-temperature persistence of the γ polymorph is unexpected. Similarly, the observation of the clear Raman features from β-TBB at 317 K is inconsistent with the reported transition temperature of 307 K, but it is apparently stabilized by the applied pelleting pressure. Using a linear combination of the powder spectra, it was determined that the sample pellet created at 0.07 GPa contained approximately 90% β-TBB and 10% γ-TBB. While the presence of γ-TBB was initially undesirable, this result presented an opportunity since this demonstrated it could be stabilized and studied at low temperatures.

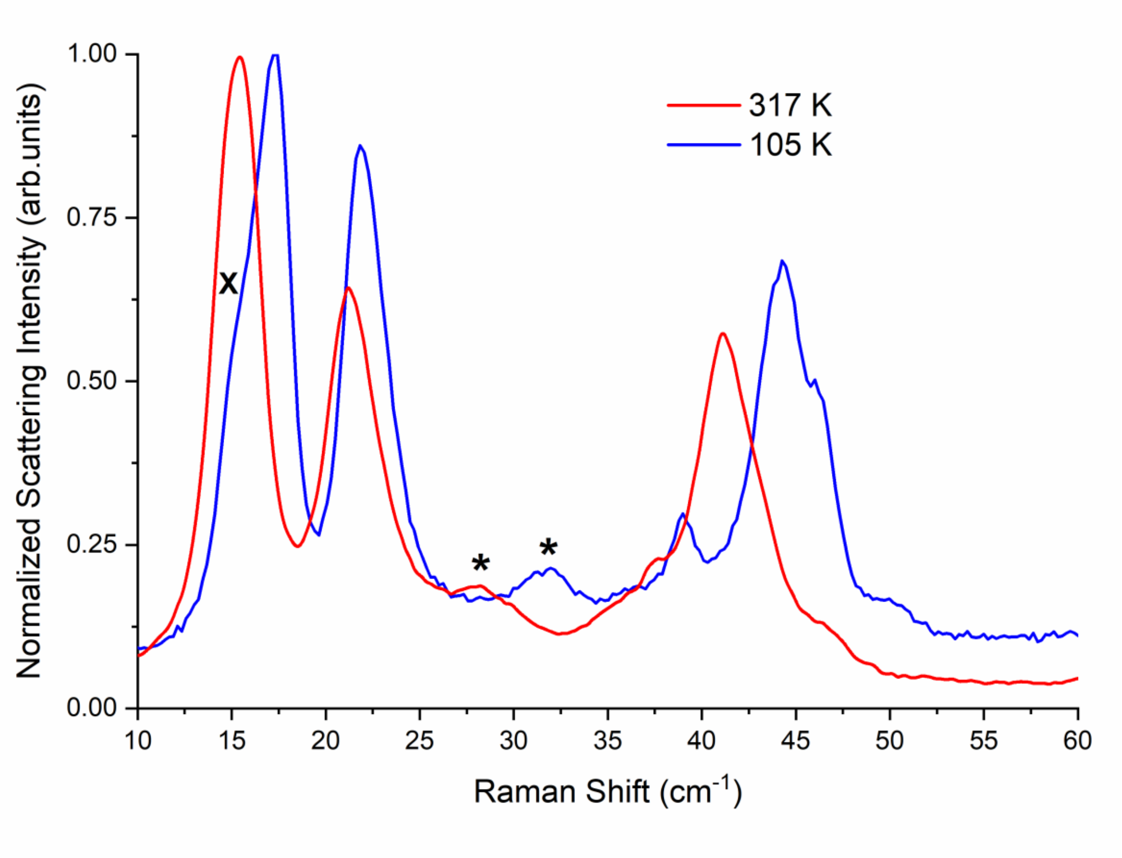

Figure 6-4. Raman spectrum of β-TBB at 319 K and 107 K. Contamination from γ-TBB is marked in the 105 K spectrum with an X and asterisks (*), corresponding to different observed peaks.

6.3.2.2 γ-TBB

To further test the stabilization of γ-TBB with pressure, another pellet was made by compressing to 0.14 GPa in an attempt to create a pellet with a higher γ-TBB concentration. The resulting sample was found to contain 80% γ-TBB, with the remainder being β-TBB. Remarkably, when this pellet was cooled to cryogenic temperatures, well below the temperature that γ-TBB should be stable, the spectral features indicated that no conversion to β-TBB had occurred. The temperature-dependent spectra for γ-TBB at 320 K and 118 K are shown in **Figure 6-5.** This is the first time that γ-TBB has been stabilized at this low a temperature, although recent work has shown that γ-TBB nanocrystals have been stabilized in anodic aluminum oxide nanopores to 183 K[8].

Pressure clearly plays a role in TBB polymorph stabilization. To investigate this, additional pellets were made at varying pressures (0.03, 0.10, 0.20, and 0.28 GPa). While very little changes were observed in the room-temperature Raman spectra at intermediate pressures, the 0.28 GPa pellet was found to contain an additional 5% γ-TBB (85% in total). Although this did not eliminate the β-TBB form completely, it showed that pressure increases do promote γ-TBB stabilization. It is worth noting that higher pressures (0.7 GPa) can cause formation of α-TBB[31], although the pressures used in the present study were not great enough to observe any trace of this polymorph.

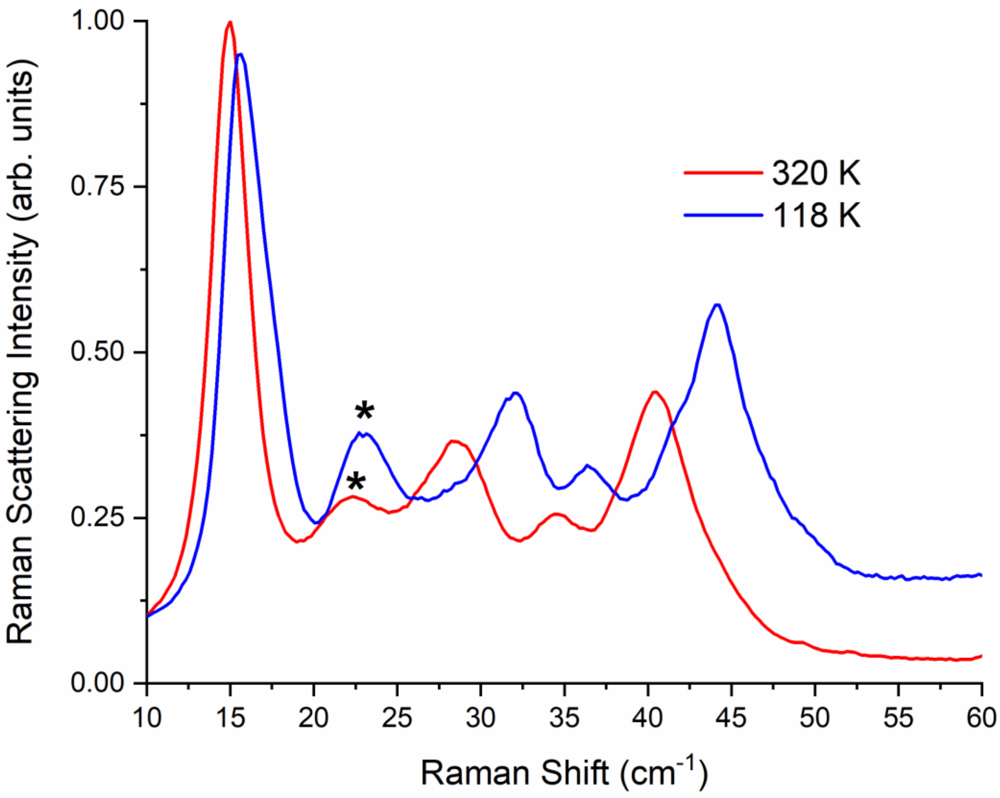

Figure 6-5. Raman spectra of γ-TBB at 320 K and 118 K. Contamination from β-TBB is marked in the 118 K spectrum with an asterisk (*).

6.3.3 Solid-State Density Functional Theory Simulations

6.3.3.1 Structural Optimizations

ss-DFT simulations were initially performed on the β-TBB polymorph. A full optimization of the unit cell dimensions and atomic positions produced excellent results (**Table 6-1**), with errors ≤ 0.15% in all cell parameters. However, when full optimizations were performed on γ-TBB, the structure immediately relaxed to the β-TBB form. This is not surprising since ss-DFT simulations are performed at 0 K, and β-TBB is the more stable polymorph at low temperatures.

To accomplish an optimization of γ-TBB, the crystal lattice parameters were held at experimentally observed values (332 K[18]) and the atoms were allowed to relax to an energetic minimum within these constraints. While no problems were encountered in the full optimization of the β-TBB structure, for a fair comparison to the fixed lattice γ-TBB calculations, a fixed-lattice (100 K[17]) optimization was also performed on β-TBB. All energy and vibrational analyses presented in this work are based on the fixed lattice calculations. Regardless of the constraints on the geometry optimizations, the molecular structures produced in the simulations agreed very well with experimental data, as shown by the root-mean-square-deviations in **Table 6-2.**

Table 6-1. Comparison of the measured β-TBB crystalline dimensions and results from a fully optimized PBE-D3/def2-TZVP structure.

	a (Å)	*b* (Å)	*c* (Å)	β (º)	Volume ($Å^3$)
Experimental[17](100K)	3.9235	10.4885	10.3675	100.367	419.675
Calculated	3.9241	10.5012	10.3559	100.516	419.580
Error (%)	0.02	0.12	-0.11	0.15	-0.02

Table 6-2. Comparison of the experimental and calculated bond lengths (Å) involving non-hydrogen atoms for β-TBB and γ-TBB.

β-TBB	C1-C2	C1-C3′	C2-C3	C1-Br1	C2-Br2	**rmsd**
Experimental	1.397	1.401	1.387	1.884	1.883	
Calculated	1.402	1.396	1.395	1.895	1.896	**0.008**

γ-TBB	C1-C2	C1-C3′	C2-C3	C1-Br1	C2-Br2	**rmsd**
Experimental	1.358	1.420	1.372	1.844	1.917	
Calculated	1.371	1.406	1.399	1.8733	1.904	**0.020**

6.3.3.2 Vibrational Analysis

Simulations of the Raman spectra of both TBB polymorphs were in excellent agreement with experimental observations (**Figure 6-6**). The β-TBB and γ-TBB simulations were compared to their corresponding 105 K and 320 K spectra, respectively, as these were closest to the reported crystallographic data temperatures. All Raman-active modes below 100 cm^{-1} represent rigid rotations of the TBB molecules in their lattice positions. This was determined through analysis of the normal mode eigenvector displaced structures, which yielded no changes in the intramolecular structure of TBB. The peak at 126.4 cm^{-1} which had negligible shifting experimentally (calculated at 125.6 cm^{-1} and 124.7 cm^{-1} in β-TBB and γ-TBB, respectively) corresponds to an in-plane intramolecular bromine wagging, while the peaks in the 190-250 cm^{-1} region originate from intramolecular ring torsions.

A complete list of the experimental and calculated Raman active modes for both TBB polymorphs below 250 cm^{-1} is shown in **Table 6-3** and **Table 6-4**. The β-TBB vibrational simulations are in excellent agreement with the current experimental results, with the only peaks not modeled arising from the aforementioned γ-TBB contamination. A recent study has presented a similar vibrational analysis of β-TBB[10], but it did not experimentally access the significant sub-40 cm^{-1} range. The peaks calculated for γ-TBB are also in excellent agreement with experimental results, with all features accounted for.

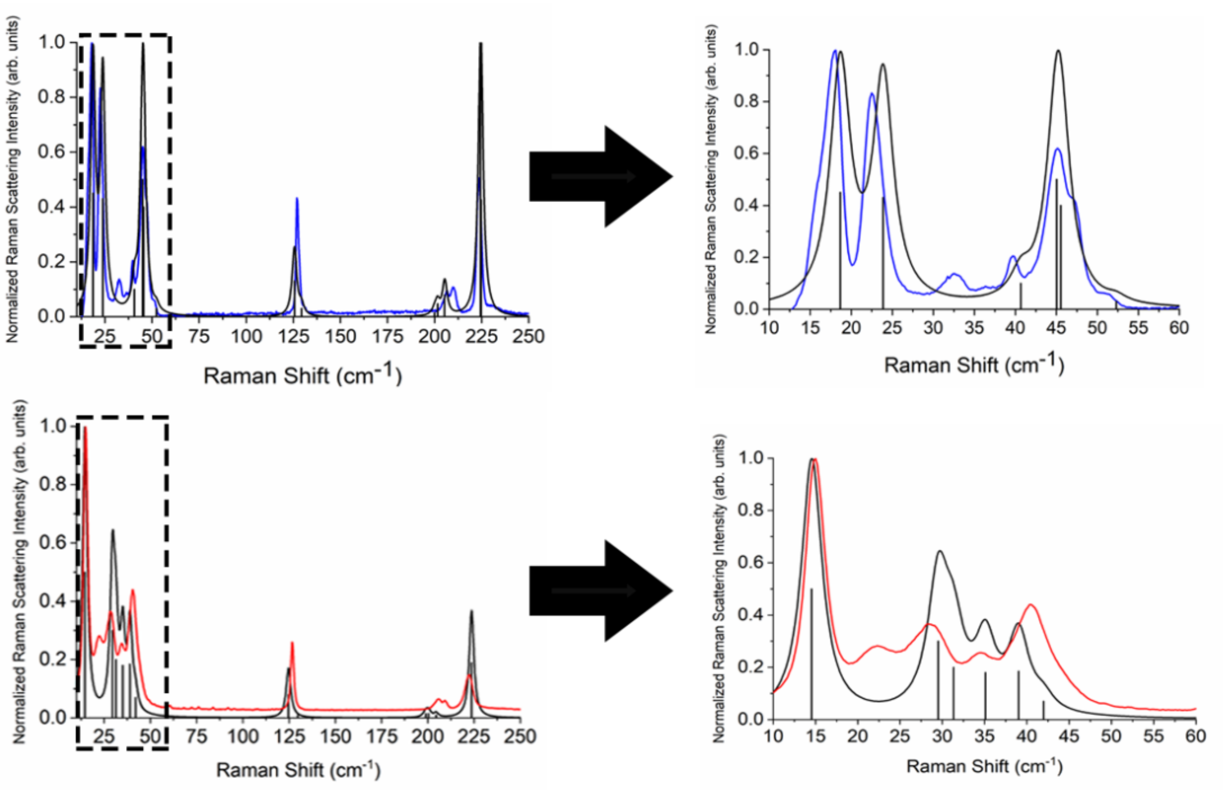

Figure 6-6. Experimental Raman spectra for β-TBB (blue) at 107 K and γ (red) at 318 K with their corresponding simulated (black) Raman spectra. The boxed areas in the lower frequency range (left) are shown expanded on the right.

Table 6-3. Experimental and simulated Raman spectral features of β-TBB with comparison to published observations. Shoulder features are indicted with “sh”.

White, et al.[29]	Zakharov, et al.[10]	Burgos & Bonadeo[30]	Current Work			
Experimental (ambient)	Experimental (ambient)	Experimental (100 K)	Experimental (291 K)	Experimental (105 K)	Calculated (100 K lattice)	Calculated Intensities
--	--	17.5	15.5	17.1	18.7	0.969
--	--	21.5	21.8	22.1	23.9	0.923
--	--	38.5	--	39.0	40.7	0.105
--	42	44.5	40.6	44.4	45.0	0.637
--	--	46	--	46.2 (sh)	45.5	0.480
--	45.5	50.5	46.2	50.1	52.3	0.025
--	--	52	--	--	--	--
--	54	--	--	--	--	--
	--	62.0	--	--	--	--
--	87	--	--	--	--	--
125	126.4	--	126.4	126.6	125.6	0.312
--	--	--	--	128.5 (sh)	129.4	0.043
--	--	--	--	204 (sh)	200.0	0.024
203	203.6	--	203.6	206.7	201.6	0.062
--	--	--	209.0	209.3	205.2	0.039
208	209	--			205.5	0.127
220	221	--	221.4	223.4	224.4	1.000
--	--	--	--	224.5(sh)	224.7	0.427
--	234	--	--	--	--	--

Table 6-4. Experimental and simulated Raman spectral features of γ-TBB with comparison to published observations.

Bugos & Bonadeo[30]	Current Work			
Experimental (330 K)	Experimental (320 K)	Experimental (118 K)	Calculated (332 K Lattice)	Normalized Intensities
14.5	14.5	14.8	14.6	1.000
28.0	27.8	28.2	29.5	0.502
			31.3	0.266
34.0	34.5	34.9	35.1	0.270
40.0	39.9	41.7	39.0	0.301
			42.0	0.054
--	126.5	126.8	124.7	0.171
--	--	--	129.1	0.001
--	205.8	205.4	198.8	0.018
--			200.4	0.001
--	208.9	209.7	204.4	0.023
--			204.5	0.014
--	222.1	222.3	223.6	0.280
--			223.9	0.093

6.3.3.3 Polymorph Stabilities

The results of energetic calculations revealed that β-TBB is 0.79 kJ/mol (per molecule) lower in total electronic energy than γ-TBB. Inclusion of zero-point energies from the vibrational simulations did not change this rank, with β-TBB remaining the more stable polymorph by 0.75 kJ/mol at 0 K. This result is consistent with β-TBB's observed dominance at temperatures below 307 K. Additional insight into the relative stabilities can be gained by decomposing the total energy into its conformational and cohesive components, which are listed in **Table 6-5**. β-TBB was found to have a more stable conformational energy, while γ-TBB had a more favorable cohesive energy.

Temperature-dependent Gibbs free energy curves (also corrected for BSSE) were constructed for both polymorphs. β-TBB is more stable at 0 K by 0.75 kJ/mol, but the curves cross at 76 K and γ-TBB becomes the more stable polymorph. While the transition temperature is quantitatively incorrect, it qualitatively agrees with experimental observations of γ-TBB being favored at higher temperatures.

Table 6-5. Calculated total electronic, conformational, and cohesive energies of the TBB polymorphs. All energies are in kJ/mol per molecule and corrected for BSSE.

	Total Energy (Relative)	**Conformational Energy (Relative)**	**Cohesive Energy**
β-TBB	0	0	-144.854
γ-TBB	0.791	2.111	-146.174

6.3.3.4 Normal Mode Eigenvector Analysis

To examine the behavior of individual vibrations, the sub-100 cm^{-1} modes in the Raman spectra were further analyzed using ss-DFT to construct potential energy surfaces associated with their motions. The modes from the simulated spectra at 18.7 cm^{-1}, 40.7 cm^{-1}, and 45.0 cm^{-1} represent three different molecular rigid rotations within the β-TBB crystal about the crystallographic *a*, *b*, and *c* axes. The modes at 23.9 cm^{-1}, 52.3 cm^{-1}, and 45.5 cm^{-1} represent the same type of molecular motions, but with out-of-phase relationships between the members of the Z=2 crystallographic unit cell, instead of the in-phase relationship found in the previous modes.

In order to test which (if any) of the modes were responsible for polymorph conversion, the atoms in the optimized β-TBB structure were incrementally displaced along the rotational mode eigenvectors and the unit cell was optimized around the new structure. The results of these eigenvector scans are shown in **Figure 6-7** and reveal that both the 18.7 cm^{-1} mode and the 23.9 cm^{-1} mode optimized towards γ-TBB unit cell dimensions, with the 18.7 cm^{-1} mode results noticeably closer to the known γ-TBB values.

By examining the eigenvector displaced crystal, it was found that the structure resulting from displacement along the 18.7 cm^{-1} eigenvector coordinate correlated very well with the atomic positions found in γ-TBB. This was not true for the out-of-phase 23.9 cm^{-1} mode, which forced TBB to an unstable high energy arrangement that did not correspond to either TBB polymorph. Although it appears from **Figure 6-7** that the 23.9 cm^{-1} mode goes towards γ-TBB formation, the actual atomic positioning contradicts this, and only the 18.7 cm^{-1} mode yields both unit cell dimensions and atomic positions that match those of γ-TBB. The vibrational motion of the 18.7 cm^{-1} mode is represented in **Figure 6-8.**

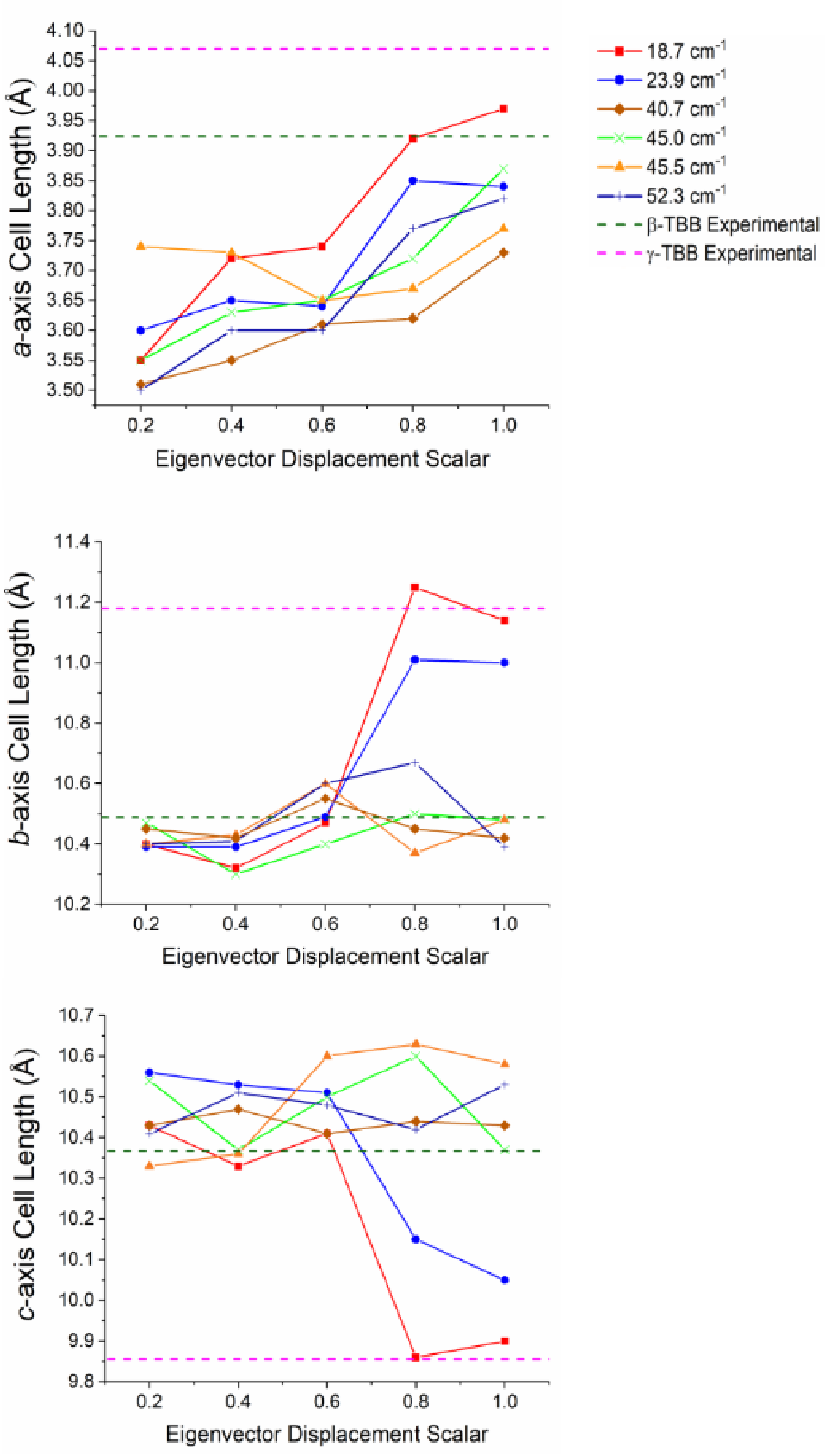

Figure 6-7. Changes in the lattice dimensions of β-TBB resulting from displacement along rotational-type lattice vibrations.

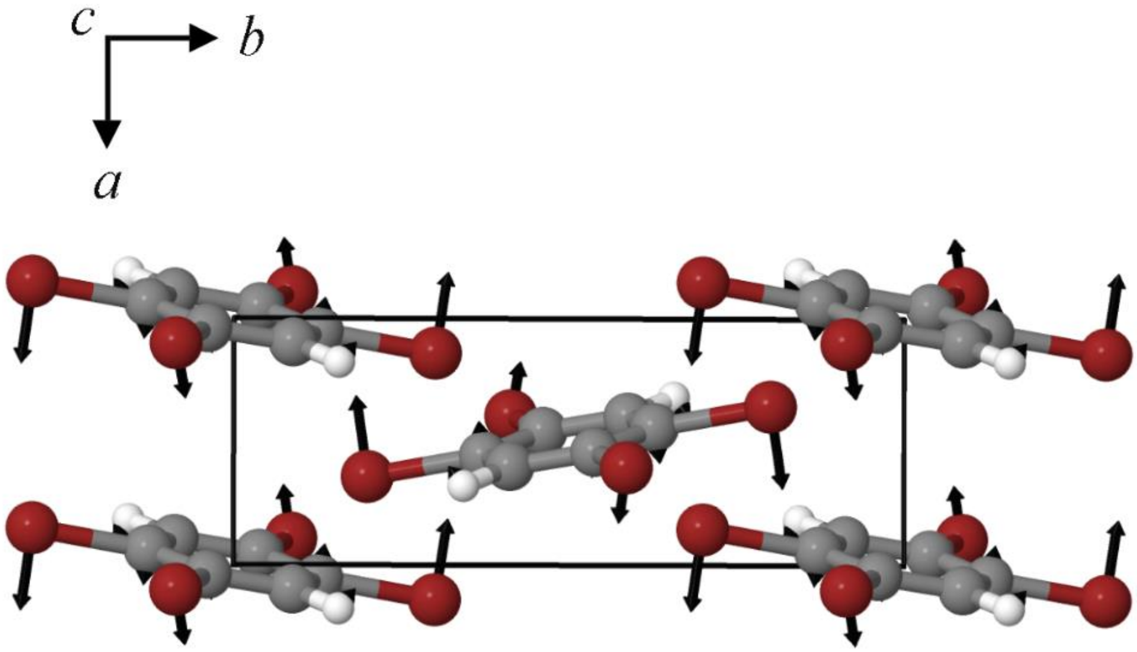

Figure 6-8. Calculated eigenvector representation of the 18.7 cm^{-1} vibrational mode in β-TBB.

A less strained and therefore more realistic approach for mapping the potential energy surface of the polymorph transformation coordinate is to freeze a single coordinate and then step along it, allowing the rest of the system to fully relax around it. A change in the intermolecular C2-Br2···C3´-C1 dihedral angle mimics the TBB ring tilting differences between the polymorphs that can be seen in **Figure 6-1** and this dihedral angle also largely corresponds to the rotational motion that forms the basis of the 18.7 cm^{-1} vibration.

Optimizations were performed by initially freezing the dihedral value at 10.5º, corresponding to the angle observed in a full optimization of β-TBB, and incrementally increasing the angle towards the γ-TBB polymorph. All other atomic positions and lattice parameters were allowed to energetically relax. A second energy minimum was found for the structure at a dihedral angle of 25.3º, which is identical to the dihedral angle observed in γ-TBB. Although the unit cell dimensions and atomic positions are in good agreement with the γ-TBB structure at this dihedral angle, there was a 4.6% contraction of the cell volume. However, contraction is expected in a 0 K structural simulation (especially versus the 332 K experimental data[18]) and the volume reduction is not unlike that reported for β-TBB when comparing room temperature to 100 K[17], which is about 5.0 %.

The energy values determined over the course of the dihedral scanning are shown in **Figure 6-9**. This revealed a barrier height of 2.40 kJ/mol, which is a reasonable energy for the β → γ polymorph transformation considering the reported transition temperature of 307 K[10] (2.55 kJ/mol). Performing a similar analysis on the dihedral angle changes that corresponded to the 23.9 cm^{-1} mode only resulted in an increase in energy along the potential energy scan, with no indication of γ-TBB formation.

As a final check to ensure that the dihedral constraint placed on the γ-TBB did not cause chemically unrealistic approximations, a frequency analysis was performed and yielded no imaginary modes. These results collectively validate the dihedral-locked γ-TBB model solid to be a physically reasonable structure, and that the 18.7 cm^{-1} mode (observed experimentally at 17.1 cm^{-1} at 105 K) is the sole gateway lattice vibration responsible for polymorph conversion.

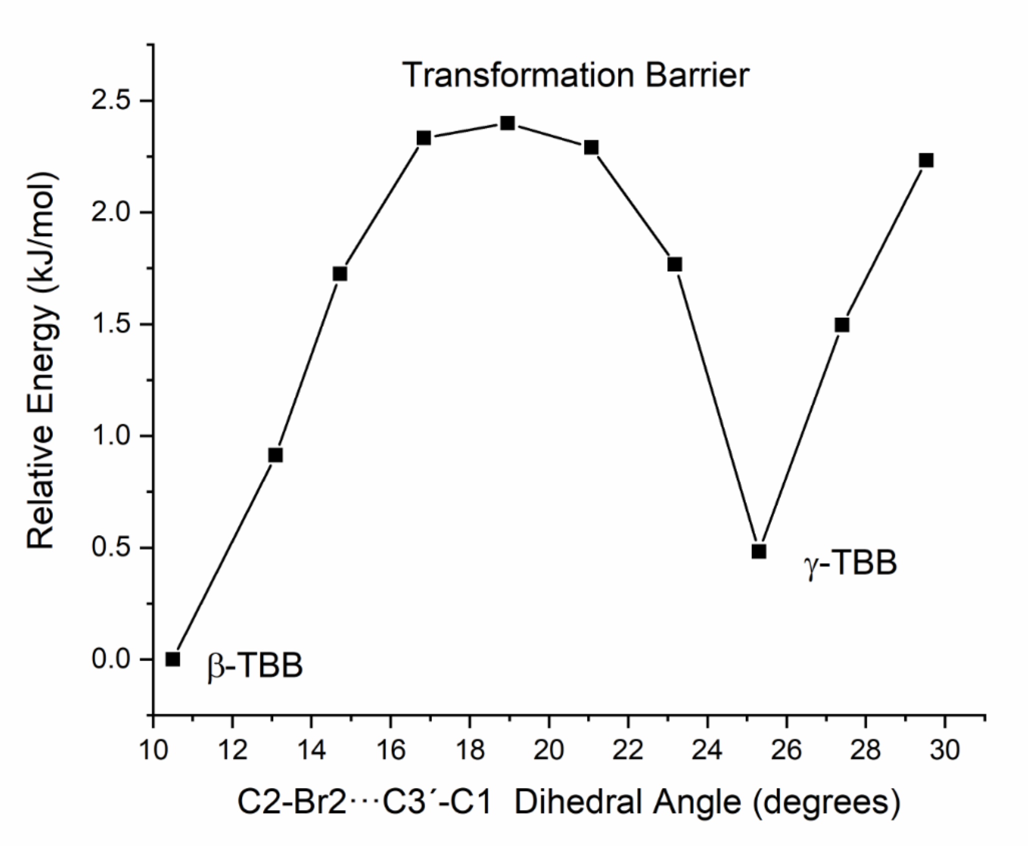

Figure 6-9. Potential energy surface for a frozen dihedral scan corresponding to the calculated 18.7 cm^{-1} mode.

6.4 Conclusions

A combined experimental and computational investigation of the Raman spectra and solid-state vibrational modes of crystalline TBB has revealed the specific vibrational mode responsible for polymorph conversion between the β and γ polymorphs. The solid-state DFT simulations were in excellent agreement with the experimental measurements, allowing for a very accurate assessment of the vibrational modes. By considering the rotational-type molecular motions and scanning along their eigenvectors in β-TBB, it was found that the 17.1 cm^{-1} mode in the 105 K Raman spectrum (calculated at 18.7 cm^{-1}) was able to act as a gateway vibration and induce the transformation of the β-form to the γ-form. This investigation also determined the barrier to conversion to be 2.40 kJ/mol, which is consistent with the mild thermal energy required to form the γ-TBB polymorph. The discovery and characterization of the gateway vibration that is the foundation of polymorphic change in crystalline TBB offers new insights into its unusual thermosalient behavior and presents a compelling target of study in other materials that undergo temperature-induced polymorph changes.

6.5 References

(1) Sahoo, S. C.; Panda, M. K.; Nath, N. K.; Naumov, P., Biomimetic Crystalline Actuators: Structure-Kinematic Aspects of the Self-Actuation and Motility of Thermosalient Crystals. *J. Am. Chem. Soc.* **2013,** 135, (33), 12241-12251.

(2) Karothu, D. P.; Weston, J.; Desta, I. T.; Naumov, P., Shape-Memory and Self-Healing Effects in Mechanosalient Molecular Crystals. *Journal of the American Chemical Society* **2016,** 138, (40), 13298-13306.

(3) Mittapalli, S.; Sravanakumar Perumalla, D.; Nangia, A., Mechanochemical synthesis of N-salicylideneaniline: thermosalient effect of polymorphic crystals. *IUCrJ* **2017,** 4, (3), 243-250.

(4) Skoko, Ž.; Zamir, S.; Naumov, P.; Bernstein, J., The Thermosalient Phenomenon. "Jumping Crystals" and Crystal Chemistry of the Anticholinergic Agent Oxitropium Bromide. *Journal of the American Chemical Society* **2010,** 132, (40), 14191-14202.

(5) Loncaric, I.; Popovic, J.; Despoja, V.; Burazer, S.; Grgicevic, I.; Popovic, D.; Skoko, Z., Reversible Thermosalient Effect of N'-2-Propylidene-4-hydroxybenzohydrazide Accompanied by an Immense Negative Compressibility: Structural and Theoretical Arguments Aiming toward the Elucidation of Jumping Phenomenon. *Cryst. Growth Des.* **2017,** 17, (8), 4445-4453.

(6) Panda Manas, K.; Etter, M.; Dinnebier Robert, E.; Naumov, P., Acoustic Emission from Organic Martensites. *Angewandte Chemie International Edition* **2017,** 56, (28), 8104-8109.

(7) Klaser, T.; Popović, J.; Fernandes, J.; Tarantino, S.; Zema, M.; Skoko, Ž., Does Thermosalient Effect Have to Concur with a Polymorphic Phase Transition? The Case of Methscopolamine Bromide. *Crystals* **2018,** 8, (7), 301.

(8) Khalil, A.; Hu, C. T.; Naumov, P., Nanoscale crystallization and thermal behaviour of 1,2,4,5-tetrabromobenzene. *CrystEngComm* **2018,** 20, (5), 636-642.

(9) Ko, J.-H.; Lee, K.-S.; Chandra Sahoo, S.; Naumov, P., Isomorphous phase transition of 1,2,4,5-tetrabromobenzene jumping crystals studied by Brillouin light scattering. *Solid State Communications* **2013,** 173, 46-50.

(10) Zakharov, B. A.; Michalchuk, A. A. L.; Morrison, C. A.; Boldyreva, E. V., Anisotropic lattice softening near the structural phase transition in the thermosalient crystal 1,2,4,5-tetrabromobenzene. *Phys. Chem. Chem. Phys.* **2018,** 20, (13), 8523-8532.

(11) Sahoo, S. C.; Sinha, S. B.; Kiran, M. S. R. N.; Ramamurty, U.; Dericioglu, A. F.; Reddy, C. M.; Naumov, P., Kinematic and Mechanical Profile of the Self-Actuation of Thermosalient Crystal Twins of 1,2,4,5-Tetrabromobenzene: A Molecular Crystalline Analogue of a Bimetallic Strip. *J. Am. Chem. Soc.* **2013,** 135, (37), 13843-13850.

(12) Ng, D. K. P.; Yeung, Y.-O.; Chan, W. K.; Yu, S.-C., Columnar Liquid Crystals Based on 2,3-Naphthalocyanine Core. *Tetrahedron Letters* **1997,** 38, (38), 6701-6704.

(13) Chen, L.; Honsho, Y.; Seki, S.; Jiang, D., Light-Harvesting Conjugated Microporous Polymers: Rapid and Highly Efficient Flow of Light Energy with a Porous Polyphenylene Framework as Antenna. *Journal of the American Chemical Society* **2010,** 132, (19), 6742-6748.

(14) Gafner, G., The crystal and molecular structures of overcrowded halogenated compounds. II. [beta]-1:2-4:5-Tetrabromobenzene. *Acta Crystallographica* **1960,** 13, (9), 706-716.

(15) Krafczyk, S.; Jacobi, H.; Follner, H., Twinning of crystals as a result of differences between symmetrical and energetical most favorable structure arrangements. *Cryst. Res. Technol.* **1994,** 29, (5), 623-31.

(16) Lieberman, H. F.; Davey, R. J.; Newsham, D. M. T., Br···Br and Br···H Interactions in Action: Polymorphism, Hopping, and Twinning in 1,2,4,5-Tetrabromobenzene. *Chem. Mater.* **2000,** 12, (2), 490-494.

(17) Mrse, A. A.; Lee, Y.; Bryant, P. L.; Fronczek, F. R.; Butler, L. G.; Simeral, L. S., Pulsed 81Br Nuclear Quadrupole Resonance Spectroscopy of Brominated Flame Retardants and Associated Polymer Blends. *Chemistry of Materials* **1998,** 10, (5), 1291-1300.

(18) Gafner, G., The crystal and molecular structures of overcrowded halogenated compounds. V. [gamma]-1,2:4,5-Tetrabromobenzene. *Acta Crystallographica* **1964,** 17, (8), 982-985.

(19) Dovesi, R.; Erba, A.; Orlando, R.; Zicovich-Wilson, C. M.; Civalleri, B.; Maschio, L.; Rérat, M.; Casassa, S.; Baima, J.; Salustro, S.; Kirtman, B., Quantum-mechanical condensed matter simulations with CRYSTAL. *Wiley Interdisciplinary Reviews: Computational Molecular Science* **2018,** 0, (0), e1360.

(20) Perdew, J. P.; Burke, K.; Ernzerhof, M., Generalized gradient approximation made simple. *Phys. Rev. Lett.* **1996,** 77, (18), 3865-3868.

(21) Weigend, F.; Ahlrichs, R., Balanced basis sets of split valence, triple zeta valence and quadruple zeta valence quality for H to Rn: Design and assessment of accuracy. *Phys Chem Chem Phys* **2005,** 7, (18), 3297-305.

(22) Grimme, S.; Antony, J.; Ehrlich, S.; Krieg, H., A consistent and accurate ab initio parametrization of density functional dispersion correction (DFT-D) for the 94 elements H-Pu. *J Chem Phys* **2010,** 132, (15), 154104.

(23) Grimme, S.; Hansen, A.; Brandenburg, J. G.; Bannwarth, C., Dispersion-Corrected Mean-Field Electronic Structure Methods. *Chemical Reviews* **2016,** 116, (9), 5105-5154.

(24) Grimme, S.; Ehrlich, S.; Goerigk, L., *Effect of the Damping Function in Dispersion Corrected Density Functional Theory*. ed.; 2011; Vol. 32, p 1456-65.

(25) Boys, S. F.; Bernardi, F., The calculation of small molecular interactions by the differences of separate total energies. Some procedures with reduced errors. *Molecular Physics* **1970,** 19, (4), 553-566.

(26) Maschio, L.; Kirtman, B.; Rerat, M.; Orlando, R.; Dovesi, R., Ab initio analytical Raman intensities for periodic systems through a coupled perturbed Hartree-Fock/Kohn-Sham method in an atomic orbital basis. I. Theory. *J. Chem. Phys.* **2013,** 139, (16), 164101/1-164101/13.

(27) Maschio, L.; Kirtman, B.; Rerat, M.; Orlando, R.; Dovesi, R., Ab initio analytical Raman intensities for periodic systems through a coupled perturbed Hartree-Fock/Kohn-Sham method in an atomic orbital basis. II. Validation and comparison with experiments. *J. Chem. Phys.* **2013,** 139, (16), 164102/1-164102/9.

(28) Anderson, D. G., Iterative Procedures for Nonlinear Integral Equations. *J. ACM* **1965,** 12, (4), 547-560.

(29) White, K. M.; Eckhardt, C. J., Single crystal Raman spectra of 1,2,4,5-tetrabromobenzene: Calculational and experimental assignment of the internal modes. *The Journal of Chemical Physics* **1998,** 109, (1), 208-213.

(30) Burgos, E.; Bonadeo, H., *The lattice vibrations of 1,2,4,5-tetrabromobenzene*. ed.; 1978; Vol. 57, p 125-127.

(31) Shimizu, F.; Suzuki, Y.; Mitarai, K.; Fujino, M.; Kawano, H.; Nibu, Y.; Shimada, H.; Shimada, R., *Pressure-Induced Phase Transition in the 1,2,4,5-Tetrabromobenzene Crystal*. ed.; 1995; Vol. 68, p 1883-1888.

CHAPTER 7. The Anomalous Temperature Dependence of Lattice Vibrations in Crystalline Glutaric Acid

Abstract

The low-frequency Raman spectrum of glutaric acid has been shown to have a mode that shifts anomalously with temperature. In order to confirm the uniqueness of the vibrational mode, THz and Raman spectra were evaluated at varying temperatures to determine spectral shifting. The single abnormal mode in the Raman spectrum has been thoroughly investigated using solid-state density functional theory calculations, providing an accurate description of the mode character which can be tied to the crystalline nature of β-GA and how its lattice dimensions change with temperature.

7.1 Introduction

Glutaric acid ($C_5H_8O_4$) is a water-soluble dicarboxylic acid (**Figure 7-1**) that is naturally produced during the metabolism of tryptophan[1] and lysine[2]. Industrially, glutaric acid (GA) is used in the production of ester plasticizers[3], corrosion inhibitors[4], and decreasing polymer elasticity[5]. Despite its many applications and prevalence biologically, there are still aspects of GA that have not been thoroughly investigated, such as the intermolecular forces that dictate its physical properties.

In the solid state, two crystalline polymorphs of GA (α[6] and β[7]) have been documented. β-GA is the form that is thermodynamically stable at ambient conditions, while α-GA is metastable and favored at higher temperatures[6] (> 75º C) and crystallizes from rapid drying of solution droplets[8]. Both GA polymorphs belong to the C2/c space group and are arranged end-to-end in hydrogen-bonded chains through their carboxylic acid groups. α-GA is composed of chains are perpendicular to one another between layers with a Z value of 8, while β-GA arranges in parallel chains with a Z value of 4. The solid-state structure of β-GA is shown in **Figure 7-2**. In order to further investigate the GA polymorphs, Raman studies have been performed[8, 9]. Cooling a spectrum causes a contraction of the unit cell which increases the force constants between atoms in a crystal that in turn increases the observed frequencies. However, a single peak in β-glutaric at approximately 86 cm^{-1} was observed to shift to lower frequencies with cooling[9]. While this spectral shift has been noticed, the implications behind this shifting and the vibrational motions that it corresponds to has yet to be analyzed.

In this work, temperature-dependent low-frequency (10-300 cm^{-1}) Raman spectroscopy was performed to confirm the reported peak shifting for β-GA. Additionally, terahertz time-domain spectroscopy (THz-TDS) from 10-140 cm^{-1} was performed to investigate the possibility of anomalous shifting in the IR active vibrations of GA. The combination of both techniques provides a complete analysis of all the active modes in the low-frequency range.

In order to fully analyze the β-GA vibrational spectra, solid-state density functional theory (ss-DFT) is employed. By properly modeling the internal and external structure of β-GA, it is possible to accurately simulate both the IR and Raman spectra and discern the motions that correspond to each vibrational mode. By characterizing the motion that corresponds to the anomalous-shifting peak, it is possible to gain further insight into its strange behavior and how this relates to the crystalline packing of β-GA.

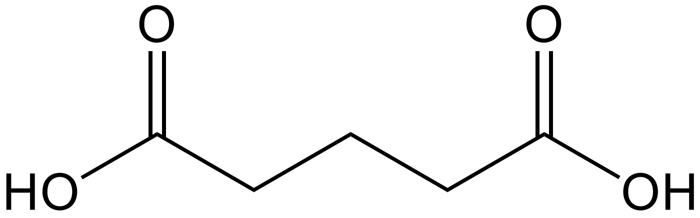

Figure 7-1. Molecular structure of GA.

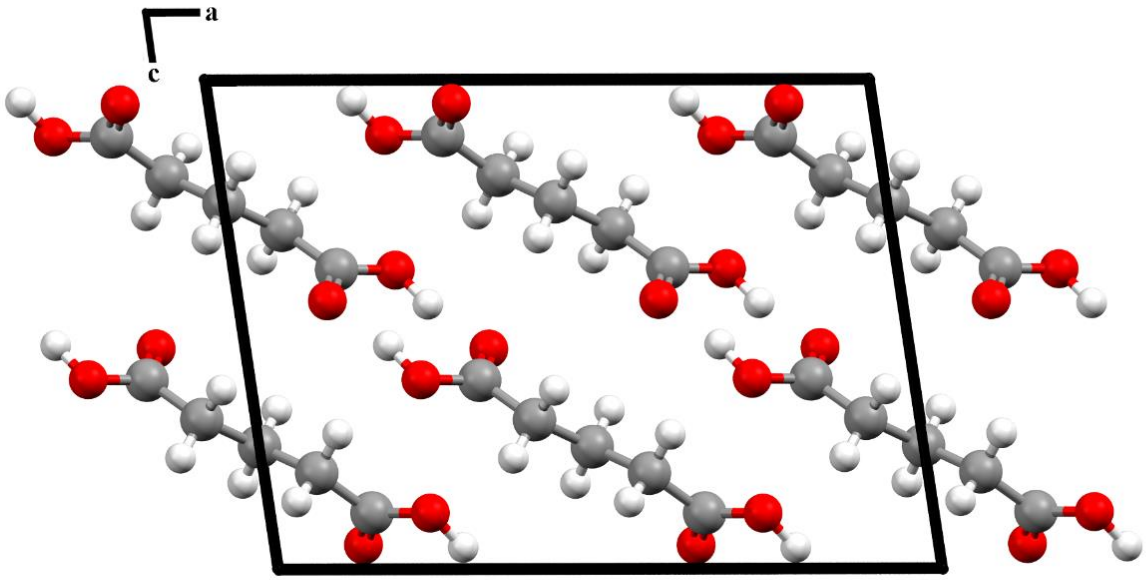

Figure 7-2. Unit cell packing structure of β-GA.

7.2. Methods

7.2.1. Experimental Methods

GA (99%) was purchased from Sigma Aldrich. A powder X-ray diffraction (PXRD) pattern (**Figure 7-3**) was obtained at 90 K using a Kappa APEX Duo by combining the average four 180º phi scans and integrating the observed diffraction rings. The results were compared to the powder patterns of previously published α[6] and β[7]-GA structures. While intensities differed, likely due to preferred orientations of the crystalline sample, the PXRD pattern had matching positions at every peak when compared to β-GA, indicating its polymorphic purity.

Raman spectra were obtained using an Ondax THz-Raman spectrometer with a laser centered at 784.7 nm. The spectrometer was coupled to an Andor Shamrock 750 spectrograph with an Andor iDus 416 CCD. Room temperature spectra were taken using a powder sample of β-GA using an enclosed apparatus on the Raman unit. For temperature analyses (78 K, 125 K, 150 K, 175 K), β-GA was pressed into a pure pellet of approximately 1 mm thickness and held in a cryostat. All spectra were averaged over 225 acquisitions with a 3 second exposure time per collection.

THz-TDS spectra were obtained using a commercial Toptica TeraFlash spectrometer from 10-140 cm^{-1} at both room temperature (290 K) and at liquid nitrogen temperature (78 K). Photoconductive antennas were utilized for both THz generation and detection. The sample chamber was evacuated in order to prevent the interference of atmospheric water. Samples of β-GA were prepared by mixing the sample with polytetrafluoroethylene to approximately 4.7 %

w/w concentrations and pressed into 550 mg pellets with 13 mm pellets with 2 mm thickness. Spectra were obtained at both 78 K and 290 K using 20000 averages and a 100 ps range. The results were Fourier transformed to yield a final spectrum that was reported with spectral intensities in terms of extinction coefficient ($M^{-1}cm^{-1}$) per unit cell.

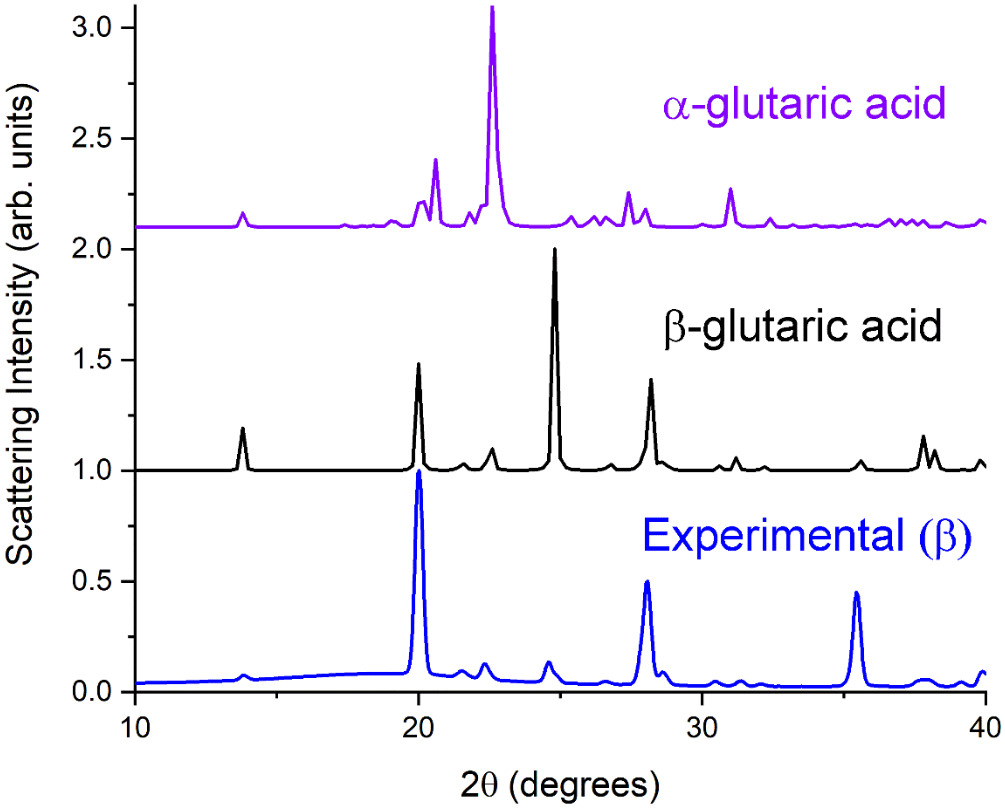

Figure 7-3. PXRD for α-GA (purple), β-GA (black), and the experimental GA powder (blue), which corresponds to β-GA.

7.2.2. Computational Methods

All ss-DFT calculations were performed using the CRYSTAL17[10, 11] software package. The PBE[12] functional was used with the def2-TZVP basis set[13]. In order to properly correct for the long-range dispersion terms, Grimme's D3 dispersion correction[14] was used with a Becke-Johnson dampening parameter[15] to dynamically correct for non-covalent London forces throughout calculations. When optimizing the geometry of β-GA, a full optimization was performed that allowed the lattice dimensions and atomic positions to relax to an energetic minimum. In order to properly model temperature effects on β-GA, further optimizations were performed using published 120 K[16] and 373 K[6] structures as starting points and fixing their lattice dimensions, allowing the atomic positions to relax within these constraints. An energy convergence of $\Delta E < 10^{-8}$ hartree was used for all optimizations. Truncation tolerances for the Coulomb and Hartree-Fock exchange integrals were set to 10^{-9} 10^{-9} 10^{-9} 10^{-9} 10^{-18} hartree. In all calculations, bielectronic integrals were computed exactly (keyword NOBIPOLA).

The optimized structures were used for frequency calculations set to a stricter convergence criterion of $\Delta E < 10^{-10}$ hartree. All frequency calculations used a central-difference formula, indicating two displacements in the cartesian directions for each atom, when computing the numerical first derivatives of the energy gradient (keyword NUMDERIV=2). Infrared intensities were calculated by the Berry phase method[17]. Raman intensities were calculated by using a Hartree-Fock/Kohn-Sham approach to compute the Raman polarizability tensor[18, 19]. Convergence was accelerated by using a Fock matrix mixing combined with Fock/Kohn Sham matrix second derivatives[20]. The experimental temperature and laser excitation wavelength

(784.7 nm) were also accounted for to ease the comparison of the Raman simulations to the experiment.

7.3. Results

7.3.1. Experimental Spectra

Raman spectra of β-GA were taken at room temperature (298 K) and cooled by liquid nitrogen (78 K). However, the feature of interest at 85 cm^{-1} in the 78 K spectrum was not resolvable at 290 K, shown in **Figure 7-4**. For this reason, and to show the effect of temperature on the vibrational features, spectra were taken at 78 K, 125 K, 150 K, and 175 K, shown in **Figure 7-5**. While the experimental range in the Raman spectra was from 10-300 cm^{-1}, the observable features are concentrated between 50 cm^{-1} and 165 cm^{-1}. As previously reported, the mode present at 85.5 cm^{-1} at 78 K shifted to higher frequencies upon heating[9], contrary to all other observed peaks. At temperatures above 175 K, it was no longer possible to resolve the spectral feature. While the shifting is bizarre, in order to investigate if this is the only spectral feature that behaves in this manner, THz spectra were also recorded to examine the IR-active modes (**Figure 7-6**). The THz spectra revealed that all peaks in the sub-150 cm^{-1} region shift to higher frequencies as the sample is cooled from 298 K to 78 K.

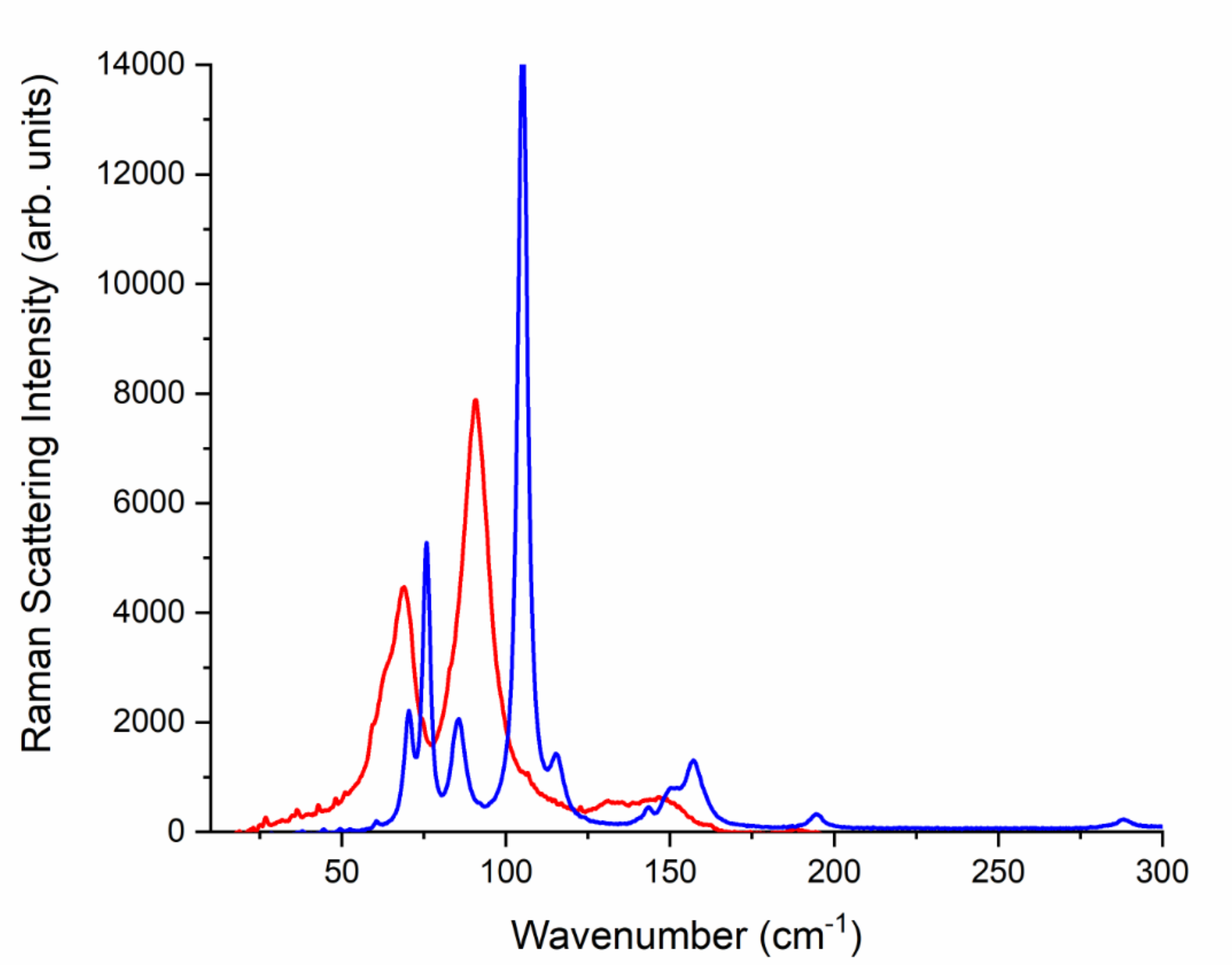

Figure 7-4. Raman spectra for β-GA at 290 K (red) and 78 K (blue).

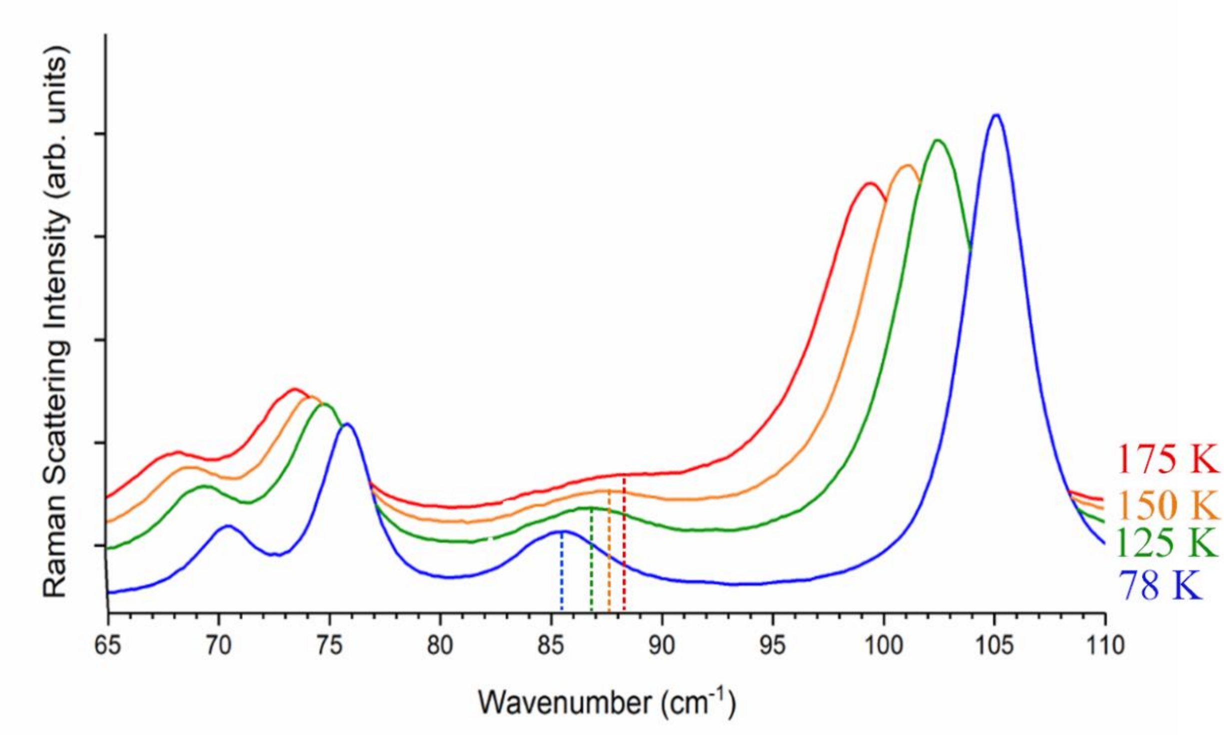

Figure 7-5. Raman spectra of β-GA between 78 K and 175 K. The spectra displayed from 65-110 cm^{-1} to better show the shifting of the peak to higher frequencies between 85 cm^{-1} and 90 cm^{-1}, emphasized by dashed lines. Spectra have been offset for clarity.

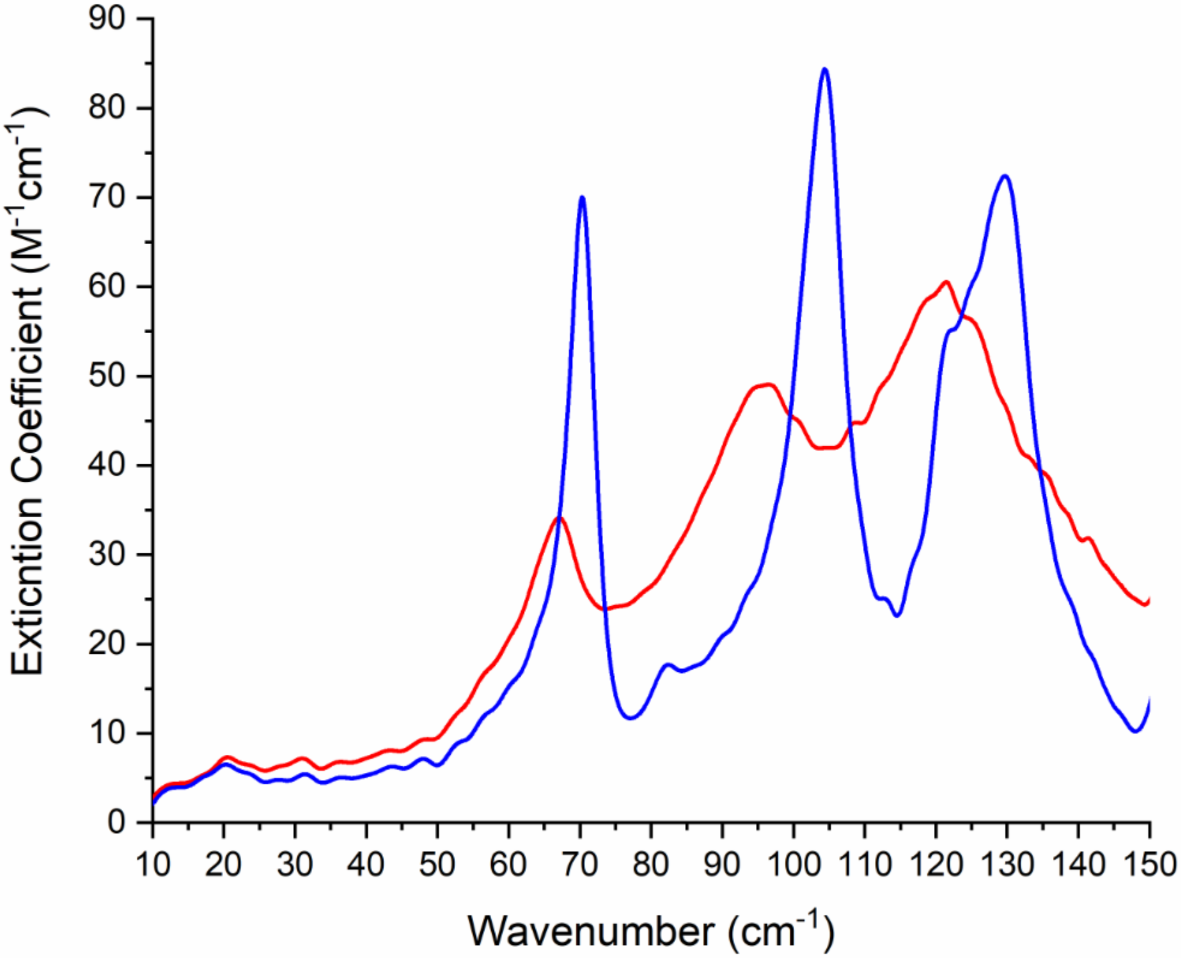

Figure 7-6. THz-TDS spectra of β-GA at 78 K (blue) and 290 K (red).

7.3.2 Computational Results

The results of a fully optimized β-GA had excellent agreement with experimental results, as shown in **Table 7-1**. Spectral simulations were also in good agreement with the experimental results. It is important that an unconstrained optimization yields accurate results because it is a benchmark to ensure that modeling is being performed properly with the given criteria, and provides more reliability to the lattice-constrained calculations.

The results of the spectral simulations from the lattice-constrained optimizations revealed the same shifting that was observed experimentally in the Raman spectra. A comparison of the 78 K and 298 K Raman spectra and the simulated spectra from the 120 K[16] and 373 K[6] lattice parameters are shown in **Figure 7-7**. The simulated data matched very well with the experimental data. While some calculated peak positions shifted slightly from experimental spectra, they were consistant throughout the simulations and the relative peak intensities were excellent. The simulated results showed a mode shifting from 87.7 cm^{-1} to 88.8 cm^{-1} in the 120 K and 373 K spectra, respectively. All other modes shifted in the to lower frequencies, in agreement with a single anomalous mode in the Raman spectra. In the simulated IR spectra no modes shifted anomalously, shown in **Figure 7-8**.

Table 7-1. Unit cell analysis of the fully optimized β-GA

	a (Å)	*b* (Å)	*c* (Å)	β (^{0})	Volume (Å^3)
Experimental[16]	12.96	4.72	9.65	98.30	584.32
Calculated	12.98	4.68	9.73	96.32	590.25
Error (%)	0.16	-0.83	0.84	-2.01	1.01

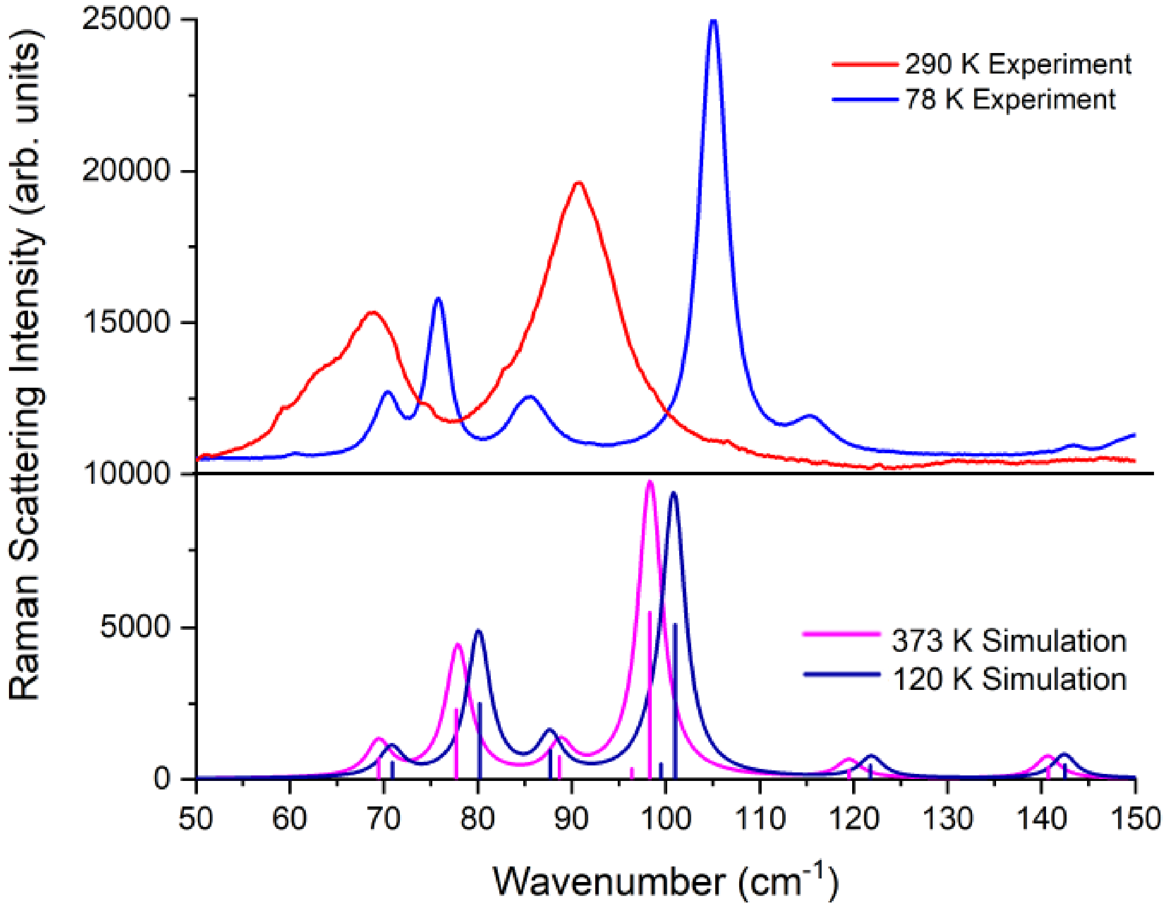

Figure 7-7. Experimental (above) and simulated (below) Raman spectra for GA. Spectra have been offset for clarity.

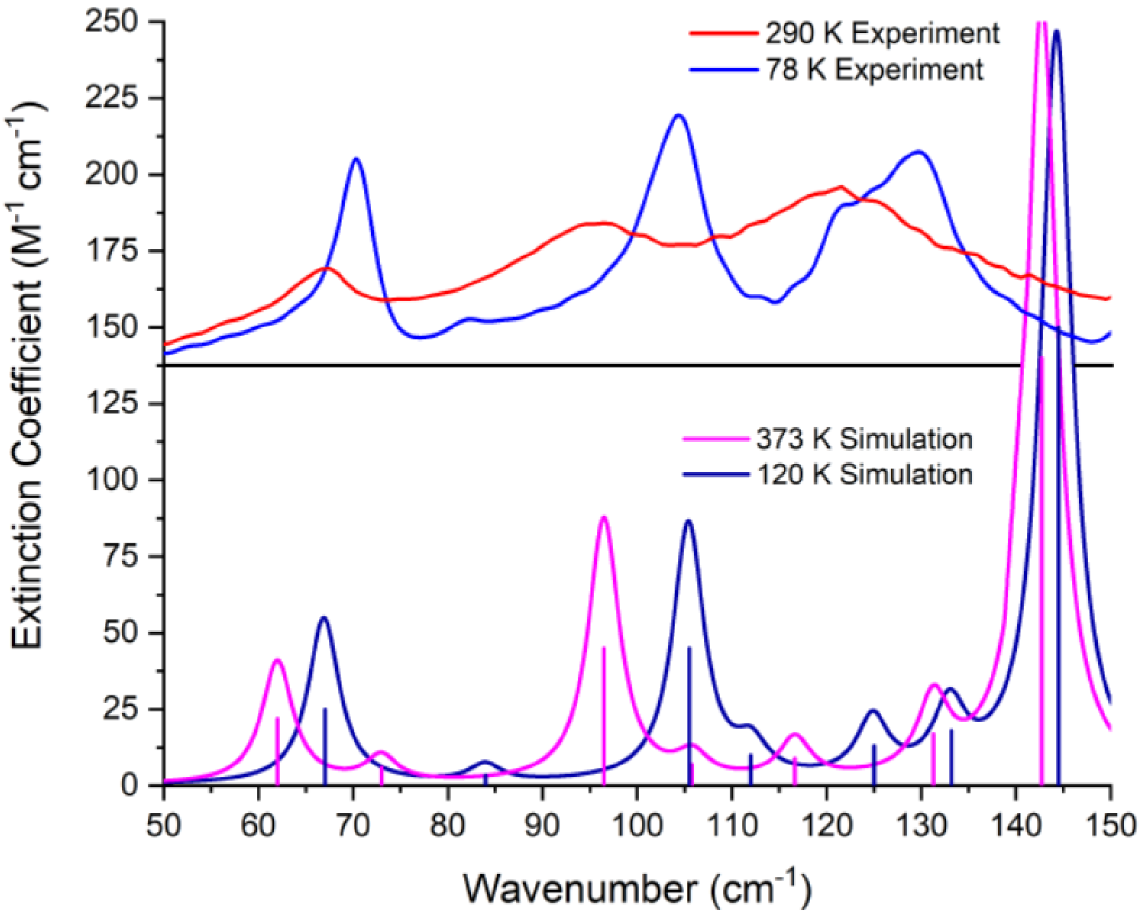

Figure 7-8. Experimental (above) and simulated (below) THz spectra for GA. Experimental spectra have been offset by 130 M^{-1} cm^{-1} for clarity.

With the vibrational spectra well modeled, it is possible to determine the motions corresponding to each molecular mode. All of the modes below 140 cm^{-1} correspond to either torsions of the carboxylic acid groups or torsions in the carbon. The anomalous shifting mode in the Raman spectrum corresponds to a torsion about the carbon chain of the molecule largely about the *a*-axis of the unit cell that evenly rotates the carbon atoms while the carboxylic groups are locked in place via intermolceular hydrogen bonding and remain largley unpertrubed.

A mode with a nearly identical molecular motion can be found in the IR active vibrations, calculated at 97.5 cm^{-1} in the 120 K simulated spectrum. It differs from the 88.8 cm^{-1} Raman-active vibration only by an in-phase intermolecular motion relationship with regard to the other GA molecules of the unit cell, while the Raman-active mode is out-of-phase. This indicates that while the molecular motion of the molecule if central importance for understanding the observed shifting, the direction of the shift is also related to the more subtle influence of phase in the collective vibrations of the molecular crystal. The difference in these vibratins is shown in **Figure 7-9**.

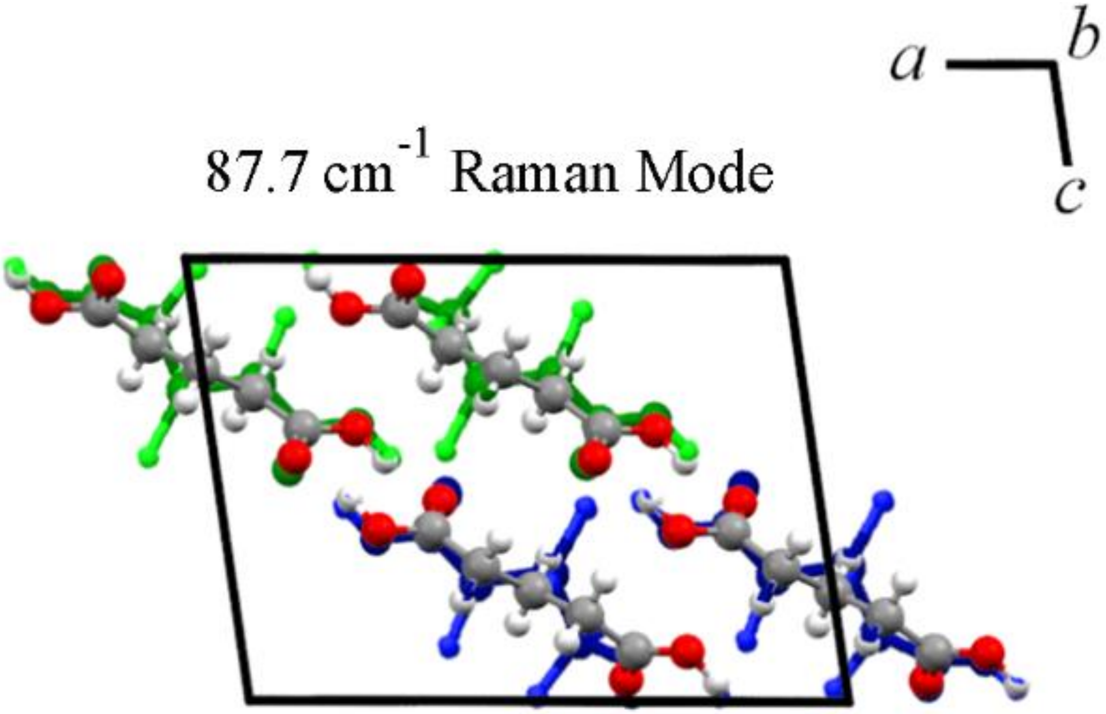

87.7 cm^{-1} Raman Mode

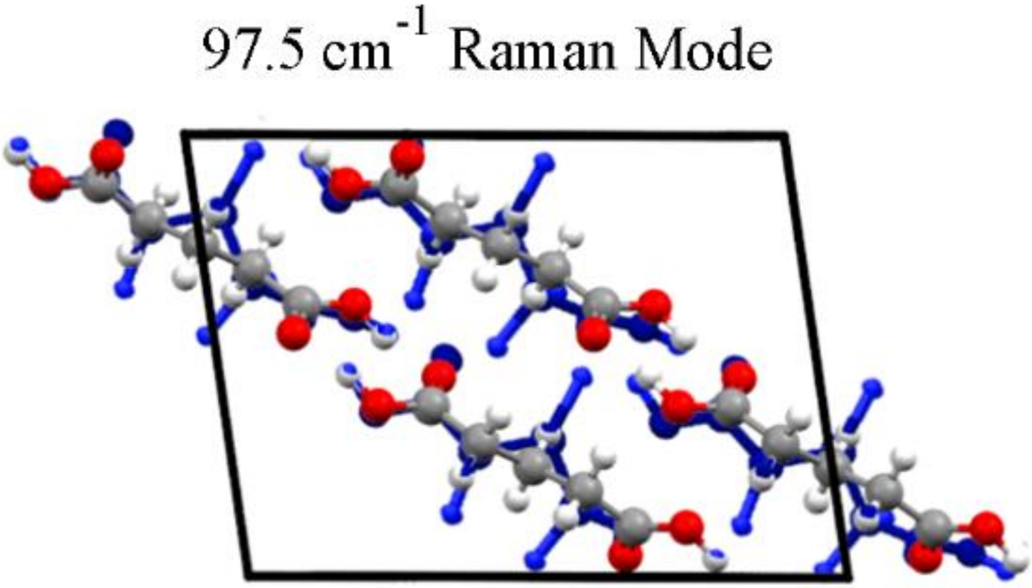

97.5 cm^{-1} Raman Mode

Figure 7-9. Vibrations of the Raman (above) and IR (below) modes with their differing phase vibrations in the carbon chain. The two directional rotations of motion are represented in blue and green.

Based on the experimental cell parameters that were used, at colder temperatures, the *a*-axis of the unit cell increases in size, which is contrary to what is typically expected. It is possible that the unit cell expansion in the *a*-axis with cooling is what causes the Raman mode to shift to lower frequencies. As the unit cell cools and the *a*-axis expands, the out-of-phase nature of the vibration would be under less strain within the unit cell which would cause the vibration to have less energy and shift to lower frequencies. Although it is not currently clear why only the Raman mode is anomylous compraed to its equivalent in-pahse IR active mode, there is ample evidence to suggest that a relationship exists between the shift in the mode and the unit cell expansion with cooling in the β-GA crystal.

7.4 Conclusions

β-GA has one mode in its Raman spectrum that shifts anomylously to lower frequencies when it is cooled. By utilizing ss-DFT calculations, it was possible to simulate IR and Raman temperature-dependent spectra. Charterizing the vibrational modes revealed that both the intermolecular and intramolecular motion of the out-of-phase Raman mode is significant to its odd spectral behavior. It is also observed that the *a*-axis of β-GA increasing with cooling, and a relationship between this and the Raman mode can be made, tying the strucural nature of the crystal with the vibrations that it exhibits.

7.5 References

(1) Gholson, R. K.; Sanders, D. C.; Henderson, L. M., Glutaric acid: A product of tryptophan metabolism. *Biochemical and Biophysical Research Communications* **1959,** 1, (2), 98-100.

(2) Neuberger, A.; Sanger, F., The metabolism of lysine. *Biochemical Journal* **1944,** 38, (1), 119-125.

(3) Jia, P.; Bo, C.; Hu, L.; Zhang, M.; Zhou, Y., Synthesis of a novel polyester plasticizer based on glyceryl monooleate and its application in poly(vinyl chloride). *Journal of Vinyl and Additive Technology* **2015,** 22, (4), 514-519.

(4) Xhanari, K.; Finšgar, M., Organic corrosion inhibitors for aluminum and its alloys in chloride and alkaline solutions: A review. *Arabian Journal of Chemistry* **2016**.

(5) Wyatt Victor, T., Effects of swelling on the viscoelastic properties of polyester films made from glycerol and glutaric acid. *Journal of Applied Polymer Science* **2012,** 126, (5), 1784-1793.

(6) Espeau, P.; Négrier, P.; Corvis, Y., Crystallographic and Pressure–Temperature State Diagram Approach for the Phase Behavior and Polymorphism Study of Glutaric Acid. *Crystal Growth & Design* **2013,** 13, (2), 723-730.

(7) Morrison, J. D.; Robertson, J. M., 212. The crystal and molecular structure of certain dicarboxylic acids. Part VII. [small beta]-Glutaric acid. *Journal of the Chemical Society (Resumed)* **1949**, (0), 1001-1008.

(8) Yeung, M. C.; Ling, T. Y.; Chan, C. K., Effects of the Polymorphic Transformation of Glutaric Acid Particles on Their Deliquescence and Hygroscopic Properties. *The Journal of Physical Chemistry A* **2010,** 114, (2), 898-903.

(9) Jorunn, G.; Emil, J. S., A Raman Study of Crystalline Glutaric Acid. *Physica Scripta* **1984,** 29, (6), 556.

(10) Dovesi, R.; Erba, A.; Orlando, R.; Zicovich-Wilson, C. M.; Civalleri, B.; Maschio, L.; Rérat, M.; Casassa, S.; Baima, J.; Salustro, S.; Kirtman, B., Quantum-mechanical condensed matter simulations with CRYSTAL. *Wiley Interdisciplinary Reviews: Computational Molecular Science* 0, (0), e1360.

(11) R. Dovesi, V. R. S., C. Roetti, R. Orlando, C. M. Zicovich-Wilson, F. Pascale, B. Civalleri, K. Doll, N. M. Harrison, I. J. Bush, P. D'Arco, M. Llunell, M. Causà, Y. Noël, L. Maschio, A. Erba, M. Rerat and S. Casassa, *CRYSTAL17 User's Manual*. ed.; University of Torino, Torino, 2017.

(12) Perdew, J. P.; Burke, K.; Ernzerhof, M., Generalized gradient approximation made simple. *Phys. Rev. Lett.* **1996,** 77, (18), 3865-3868.

(13) Weigend, F.; Ahlrichs, R., Balanced basis sets of split valence, triple zeta valence and quadruple zeta valence quality for H to Rn: Design and assessment of accuracy. *Physical Chemistry Chemical Physics* **2005,** 7, (18), 3297-3305.

(14) Grimme, S.; Antony, J.; Ehrlich, S.; Krieg, H., A consistent and accurate ab initio parametrization of density functional dispersion correction (DFT-D) for the 94 elements H-Pu. *J Chem Phys* **2010,** 132, (15), 154104.

(15) Grimme, S.; Ehrlich, S.; Goerigk, L., *Effect of the Damping Function in Dispersion Corrected Density Functional Theory*. ed.; 2011; Vol. 32, p 1456-65.

(16) Bhattacharya, S.; Saraswatula, V. G.; Saha, B. K., Thermal Expansion in Alkane Diacids—Another Property Showing Alternation in an Odd–Even Series. *Crystal Growth & Design* **2013,** 13, (8), 3651-3656.

(17) Noel, Y.; Zicovich-Wilson, C. M.; Civalleri, B.; D'Arco, P.; Dovesi, R., Polarization properties of ZnO and BeO: An *ab-initio* study through the Berry phase and Wannier functions approaches. *Physical Review B* **2001,** 65, (1), 014111.

(18) Maschio, L.; Kirtman, B.; Rerat, M.; Orlando, R.; Dovesi, R., Ab initio analytical Raman intensities for periodic systems through a coupled perturbed Hartree-Fock/Kohn-Sham method in an atomic orbital basis. I. Theory. *J. Chem. Phys.* **2013,** 139, (16), 164101/1-164101/13.

(19) Maschio, L.; Kirtman, B.; Rerat, M.; Orlando, R.; Dovesi, R., Ab initio analytical Raman intensities for periodic systems through a coupled perturbed Hartree-Fock/Kohn-Sham method in an atomic orbital basis. II. Validation and comparison with experiments. *J. Chem. Phys.* **2013,** 139, (16), 164102/1-164102/9.

(20) Anderson, D. G., Iterative Procedures for Nonlinear Integral Equations. *Journal of the American Chemical Society* **1965,** 12, (4), 547-560.

CHAPTER 8: Distinguishing Quinacridone Pigments *via* Terahertz Spectroscopy: Absorption Experiments and Solid-State Density Functional Theory

The following material is published in *Journal of Physical Chemistry A* (Squires, A. D.; Lewis, R. A.; Zaczek, A. J.; Korter, T. M., *J. Phys. Chem. A* **2017,** 121, (18), 3423-3429.)

Contribution to the work: All geometry optimizations and frequency simulations, allowing for comparison to the experimental results. Also the creation of figures 1, 2, 3, 4, and Table 1, as well as all discussions relating to the computational aspects of the work and descriptions of the type of vibrational modes observed.

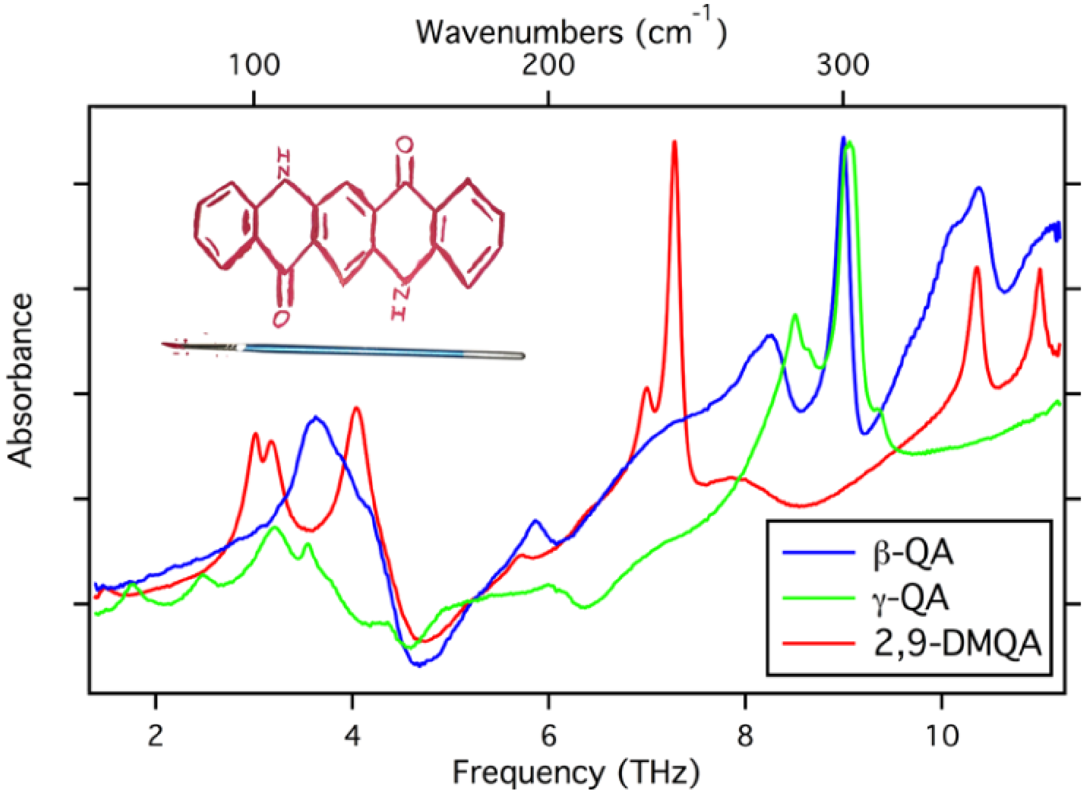

Abstract

Through a combined experimental and theoretical approach, the fundamental vibrational modes of three quinacridones pigments that fall in the terahertz spectral range (1–10THz, ~30–300cm^{-1}) are investigated. In each spectrum, the terahertz resonances correspond to wagging, rocking, or twisting of the quinacridone rings, yielding similar yet clearly distinct patterns. The terahertz measurements readily differentiate β-quinacridone, γ-quinacridone, and 2,9-dimethylquinacridone solids, a task that has been challenging for other characterization techniques. Since quinacridones are the basis of widely-used synthetic pigments of relatively recent origin, our findings offer promising applications in the rapid, non-contact, and non-destructive identification and dating of modern art.

8.1 Introduction

Quinacridone (QA), **Figure 8-1**, discovered in 1935, has now become the most important pigment for red-violet shades, and is widely used in coatings, dyes, plastics, and printing inks, being light-fast, heat-resistant, and weather-resistant.[1,2] Four crystalline phases are known: α^I, α^{II}, β, and γ.[3] Since the α phases are thermodynamically unstable and not light-fast these do not find commercial application. On the other hand, the β and γ phases are rather stable and do not interconvert post-production, except in the presence of high temperatures and strong solvents such as concentrated NaOH.[3] Furthermore, modifying the base structure, typically with Cl or CH_3, broadens the range of shades available. An important example of this is 2,9-dimethylquinacridone (2,9-DMQA; **Figure 8-2**).

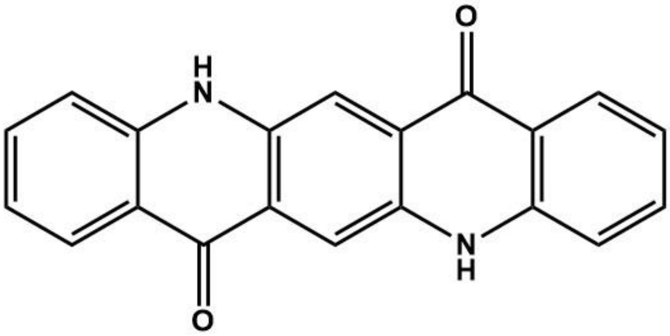

Figure 8-1. Quinacridone (QA)

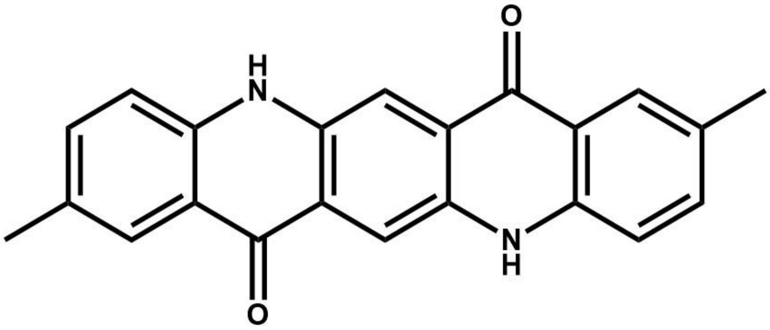

Figure 8-2. 2,9-dimethylquinacridone (2,9-DMQA)

At least ten variations of ‘quinacridone’ are commercially produced, including Pigment Orange (PO48, PO49), Pigment Red (PR122, PR192, PR202, PR206, PR207, PR209), and Pigment Violet (PV19, PV42).[4,5] We focus on three pigments in this study, namely PR122 and two variants of PV19.

Confusingly, there is considerable discrepancy in the literature and among art suppliers in how different ‘quinacridones’ are described. To illustrate the variation in notation, let us begin with PR122. The label ‘PR’ stands for ‘Pigment Red’ (as indicated above). Accordingly, de Courlon *et al*.[6] describe PR122 as ‘quinacridone red’. Gottshaller *et al*.[7] likewise in one place (page 82) call PR122 ‘quinacridone red’ but in another place (page 88) call it ‘quinacridone magenta’. Lomax[8] calls PR122 ‘magenta yellow’ whereas Paulus *et al*. identify the color as ‘more violet than gamma quinacridone’.[3] In view of this confusion in descriptive nomenclature, we will refer to this pigment simply as ‘PR122’. Now we turn to PV19. The difficulty here is that the label PV19 corresponds to pure quinacridone, but does not specify the crystalline phase. The β phase has a ‘reddish violet’ color[3] and is called by art suppliers, such as Schmincke,[9] ‘quinacridone violet’. We will thus refer to this pigment as ‘PV19-Violet’. On the other hand, the γ phase is ‘red’[3] and called by art suppliers, such as Langridge,[10] ‘quinacridone red’. We will refer to this pigment as ‘PV19-Red’.

Quinacridone pigments are becoming increasingly important in works of modern art. For instance, the Italian painter Lucio Fontana is likely to have used quinacridone in the *Pietre* series (1951–1958).[7] Likewise, the Australian painter Michael Johnson employed quinacridone in the fragile matt surface of the abstract work *Night* (1968).[6] The identification of quinacridone pigments in artworks is thus of practical and contemporary interest.

In analyzing quinacridone pigments in a painting, the conventional tools of infrared or X-ray spectroscopy are of limited use. While near-infrared and mid-infrared spectroscopies may distinguish between different quinacridones, such photons do not penetrate far into the paint. Furthermore, while X-ray absorption and fluorescence are sensitive to average mass number and to particular atoms, respectively,[11] they cannot distinguish different polymorphs. Although X-ray diffraction (XRD) can distinguish these, it is generally impractical for examining paintings. As Lomax concludes, "X-ray powder diffraction, therefore, is of limited utility in the identification of synthetic organic pigments in paints".[8] In fact, quinacridone is given as an exemplar in which the Rietveld refinement of the powder XRD data leads to a completely wrong structure.[12] Thus there is currently a need for a better method to investigate works of art and other cultural heritage items in determining the precise pigmentation.

Recently, terahertz techniques[13,14] have begun to be applied to the analysis of art work.[15–17] Both conventional and panel paintings have been studied in this way.[18,19] Artists' materials are now being examined in greater detail.[20] These materials include pigments, such as seven red mineral pigments used in ancient Chinese artworks,[21] and, most recently, quinacridone.[22] However, the studies to date have been largely phenomenological, simply presenting 'signatures' of various materials without fundamental understanding. Here we add powder x-ray diffraction (PXRD) analysis and solid-state density functional theory (ss-DFT) to terahertz spectroscopy to obtain a full understanding of the fundamental modes of three particular quinacridones: PV19-Violet, which we identify with β-QA; PV19-Red, which we identify with γ-QA; and PR122, which we identify with 2,9-DMQA.

The coupling of experimental terahertz spectroscopy with ss-DFT in recent years has proven to be a powerful combination, giving insight into many physical systems. For example, this approach has been applied fruitfully to a range of problems,[23,24] including crystalline pharmaceuticals,[25] amino acid crystals,[26] explosives,[27,28] and even the collective librations of water molecules.[29]

8.2 Methods

8.2.1 Experimental

Three commercial pigment powders were examined in this study. PV19-Violet, sold under the name ‘Quinacridone Violet’, was obtained from Schmincke.[9] PV19-Red, sold under the name ‘Quinacridone Red Pigment (Pigment Violet 19)’ was obtained from Langridge.[10] PR122, sold under the name ‘Quinacridone Magenta Pigment (Pigment Red 122)’, was also obtained from Langridge. (Additional PR122 pigment obtained from the art supplier Old Holland[30] was found to have an identical terahertz spectrum to the Langridge PR122).

A commercial beeswax medium (R & F Handmade Paints[31]) was used to bind the pigment powder into a paint. Our previous work has shown white beeswax transmits well in the terahertz spectral region.[22] White beeswax is decolorized by mechanical filtration, not chemical bleaching. This is important as chemicals used in bleaching other wax mediums react with some pigments. The melting point of 62–66˚ C is well below the temperatures required to cause phase changes in quinacridone. Thus, we are confident that the pigment properties are not changed by the thermal or chemical processes we employ in combining with white beeswax. Samples were made by mixing 0.7 g of melted beeswax with 0.07 g of paint pigment. This ratio (10:1) generates strong absorption features in the terahertz spectrum without sacrificing cut-off frequency. The molten mixture was cooled on perspex before being rolled to approximately 1 mm thickness.

To search for spectral features below 1 THz, two terahertz time-domain spectrometers were used, an Advantest TAS7400TS and a Z-omega 2.5. These investigations confirmed that the lowest-frequency modes are ∼1.5 THz. (Further details are given in our previous work.[22]) These two spectrometers are limited to about 5 THz. To extend the spectral range to higher frequencies, we have now taken measurements on a Bomem DA3.26 Fourier-transform infrared spectrometer. All the measurements reported here are from this instrument. In all measurements a spectral range of 1–10 THz (34–334 cm^{-1}) at unapodized resolution of 0.03 THz (1 cm^{-1}) was used. A liquid-helium–cooled Si bolometer was employed as the detector.

8.2.2 Computational

All ss-DFT simulations were performed using a developmental version of the CRYSTAL14[32] software package. Structural optimizations were initiated with solid-state parameters based on the previously published x-ray data.[3,33] The unit cell dimensions and atomic positions were allowed to fully relax within their respective space group symmetries. The Perdew-Burke-Ernzerhof (PBE)[34] exchange correlation functional and Ahlrich's VTZ basis set was used with polarization functions[35] added to all atoms. Truncation tolerances within the software used to describe the Coulomb and Hartree-Fock exchange integral series (keyword TOLINTEG) were set to 10^{-10}, 10^{-10}, 10^{-10}, 10^{-10}, and 10^{-20} hartree for all calculations. The calculations were augmented with Grimme's DFT-D3 correction[36,37] to better account for intermolecular London dispersion forces. An energy convergence criterion of $\Delta E < 10^{-8}$ hartree was used in all geometry optimizations. Frequency analyses were performed on the final optimized structures to determine the vibrational frequencies and IR intensities (via the Berry phase method[38]) of the normal modes in these solids. For frequency simulations, the energy convergence was set to a more stringent $\Delta E < 10^{-10}$ hartree threshold.

8.3 Results and Discussion

8.3.1 Structural Analysis

Results of the structural calculation appear in **Table 8-1** where they are compared to published single-crystal XRD data. The unit cells for the calculated structures of *β*-QA, *γ*-QA, and 2,9-DMQA are depicted in **Figures 8-3, 8-4,** and **8-5**, respectively. As shown in **Table 8-1**, the simulations of the solid-state structures match very well with the earlier experiments, but reveal a consistent underestimation of the unit cell volume in the quinacridone solids, as compared to the reported crystallographic data. This can be attributed to the ss-DFT calculations representing 0 K structures since there is no inclusion of temperature effects, while the previously-reported experimental structures were obtained at room temperature for the *β*- and *γ*- polymorphs and 125 K for 2,9-DMQA.

The approximately 3% volume contraction is not unusual for organic crystals over this temperature range, with a smaller contraction observed in 2,9-DMQA due to its colder experimental conditions.

Table 8-1. Comparison of the calculated and measured crystallographic unit cells for quinacridone solids

	β-QA			γ-QA			2,9-DMQA		
quantity	Calc.	Exp.[3]	Error (%)	Calc.	Exp.[3]	Error (%)	Calc.	Exp.[33]	Error (%)
$a/\text{Å}$	5.67	5.69	0.37	13.50	13.70	1.460	3.901	3.87	0.93
$b/\text{Å}$	3.92	3.98	1.28	3.84	3.88	1.159	6.304	6.37	1.07
$c/\text{Å}$	29.69	30.02	1.01	13.27	13.40	0.9701	15.59	15.78	1.20
$V/\text{Å}$	657.25	674.50	2.55	679.81	700.63	2.969	377.0	381.5	1.18
$\alpha/^\circ$	90	90	–	90	90	–	94.61	93.94	0.71
$\beta/^\circ$	95.84	96.76	0.95	98.54	100.44	1.853	91.01	91.51	0.55
$\gamma/^\circ$	90	90	–	90	90	–	99.91	100.00	0.09

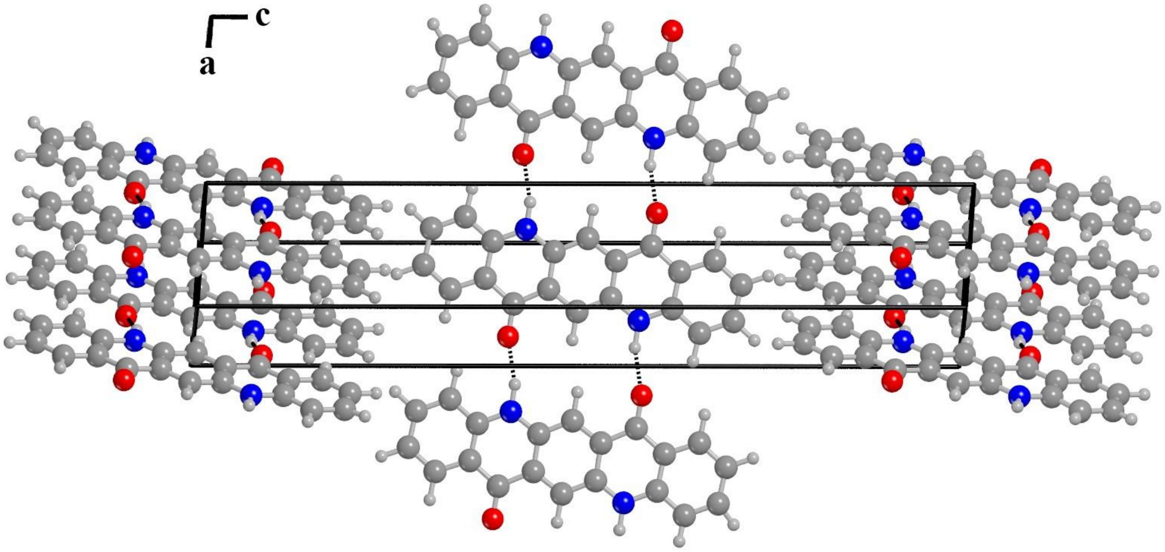

Figure 8-3. Crystallographic unit cell of the calculated *β*-QA structure

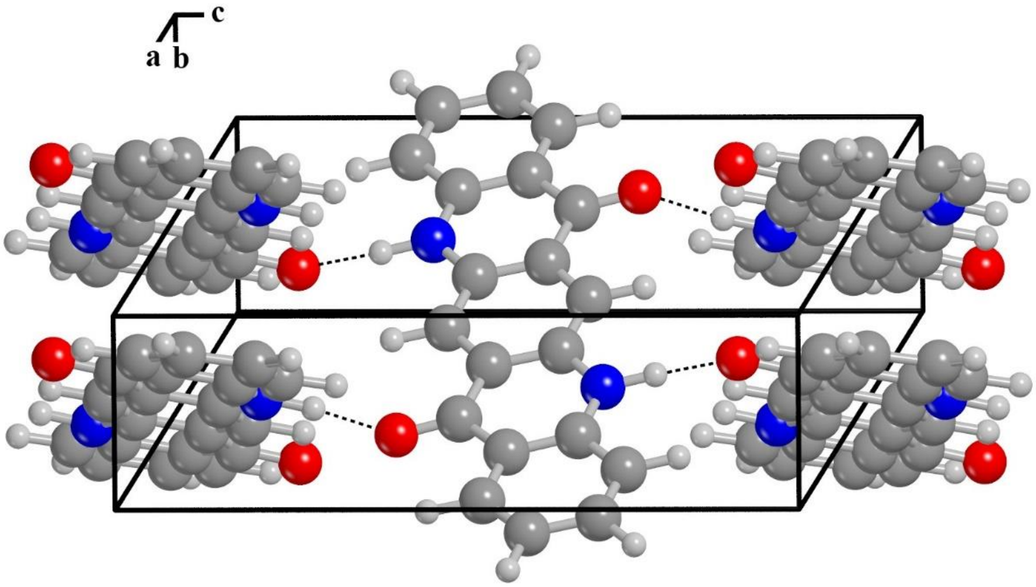

Figure 8-4. Crystallographic unit cell of the calculated γ-QA structure

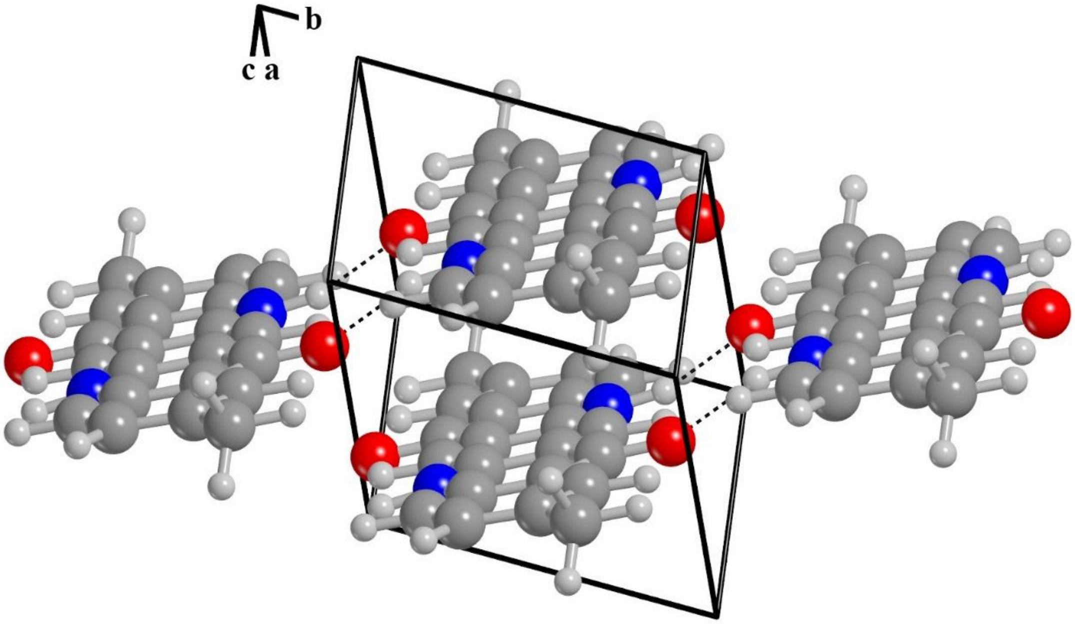

Figure 8-5. Crystallographic unit cell of the calculated 2,9-DMQA structure

8.3.2 PXRD Comparison

PXRD measurements were undertaken to confirm sample purity and identity. Previous authors have presented PXRD graphs for quinacridones but without giving numerical data.[3,39] We have digitized these previously reported spectra to compare with ours. In addition, we have compared our PXRD spectra with the 'strong', 'medium', and 'weak' reflections tabulated by Smith.[40] Finally, we have calculated the diffraction patterns from our calculated structures, which we present now with our experimental PXRD data.

PXRD data is not unambiguous, as has been pointed out by Buchsbaum and Schmidt.[12] Citing β-QA and γ-QA PXRD as examples, they demonstrated that a reasonable Reitveld refinement may lead to a *completely wrong* crystal structure (their emphasis). Thus caution is required in interpreting PXRD data.

Very good agreement is found between our PXRD data for the PV19-Red pigment and our calculations for γ-QA (**Figure 8-6**). Moreover, all the lines tabulated previously are reproduced.[40] We also see some additional smaller features that appear in the later reports.[3,39] On this basis we are confident that the pigment we label PV19-Red comprises γ-QA.

Quite good agreement is found between our PXRD data for PV19-Violet pigment and our calculation for β-QA (**Figure 8-7**). We observe the features previously reported.[3,39,40] We also detect lines at about 12° (which may be an unresolved splitting) and 25° that are not evident in the other reported diffraction patterns[3,39] or our calculation. These lines may indicate minor amounts of an additional phase or phases.

For PR122 we also obtain good agreement between our data, our calculations for 2,9DMQA and the earlier tabulation of lines[40] (**Figure 8-8**). On this basis we are confident to identify our PR122 pigment with the chemically-engineered variant 2,9-DMQA.

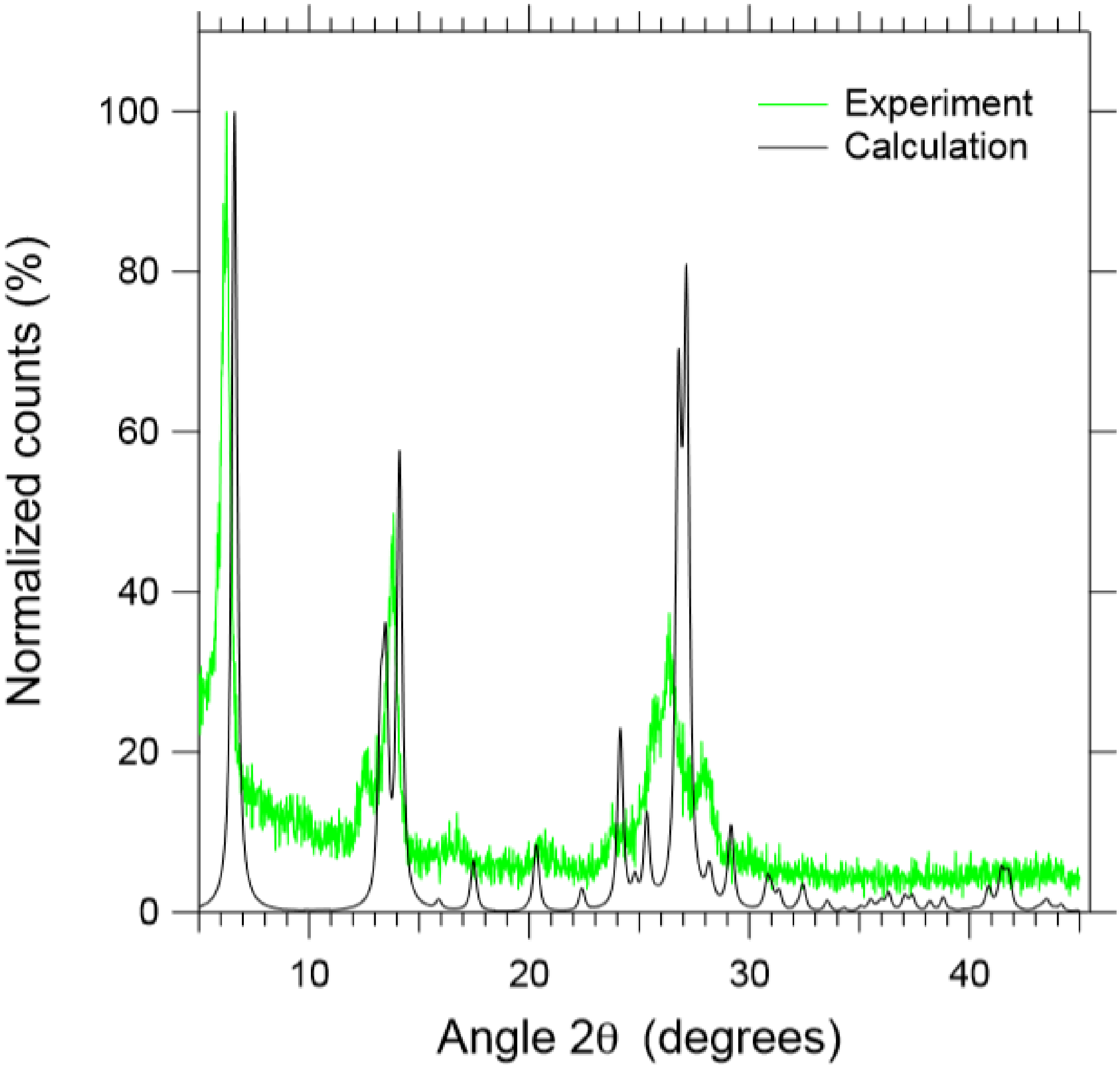

Figure 8-6. Experimental PXRD of PV19-Red pigment and comparison with that of calculated *γ*-QA.

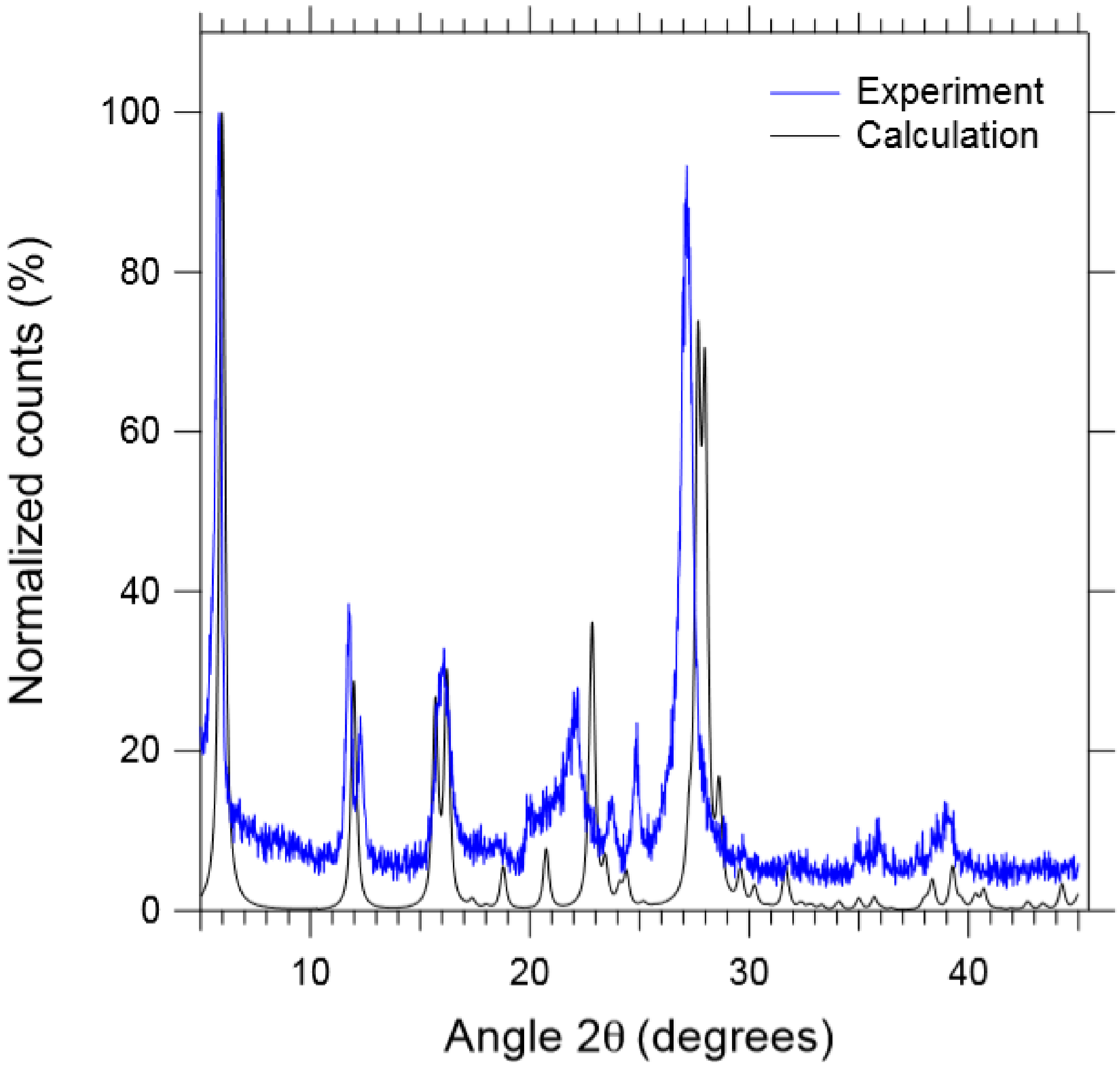

Figure 8-7. Experimental PXRD of PV19-Violet pigment and comparison with that of calculated *β*-QA.

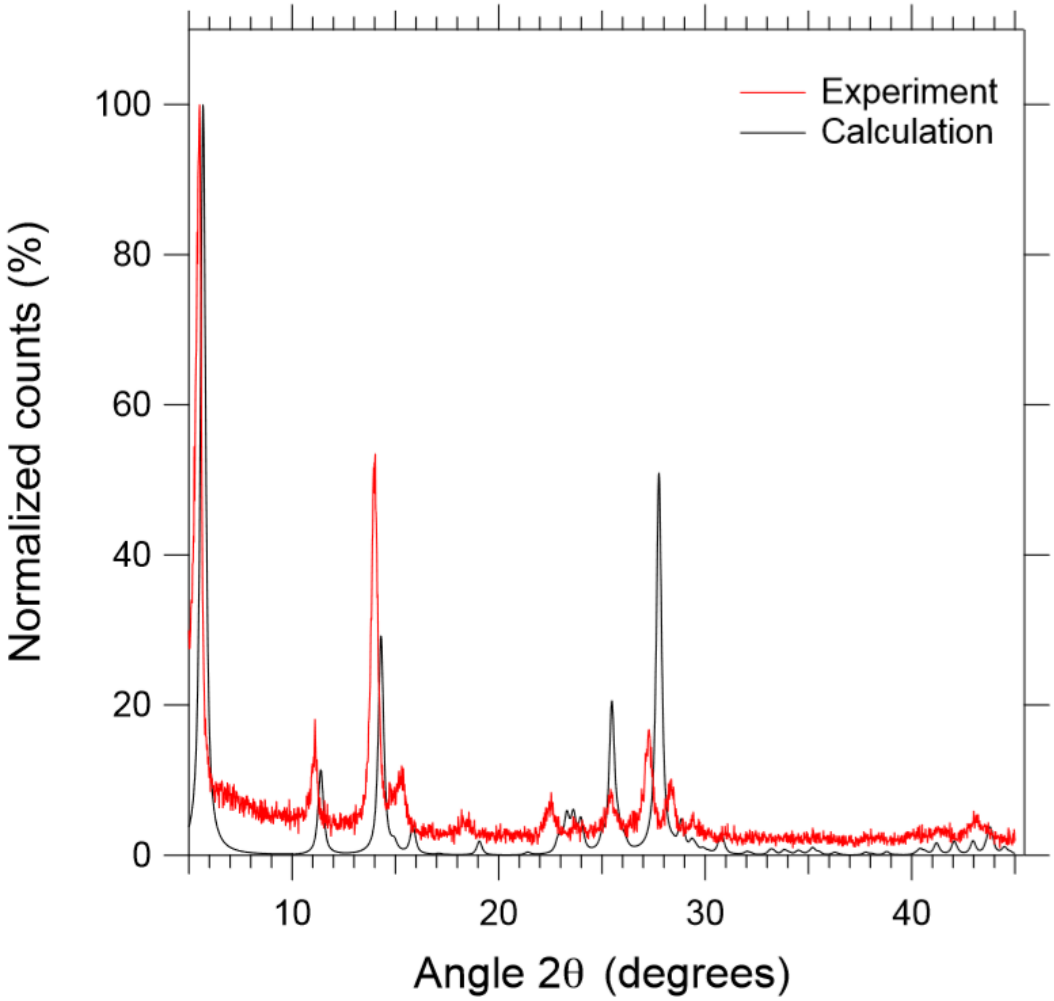

Figure 8-8. Experimental PXRD of PR122 pigment and calculation for 2,9-DMQA

8.3.3 Terahertz spectroscopy

The experimental terahertz spectra are now presented and compared with the calculations. The calculations are presented as line spectra. In addition, for ease of comparison, the theoretical spectra have been convolved with Lorentzian line shapes with full-width half-maxima (FWHM) of 5 cm^{-1} and these convolved spectra are also presented.

The PV19-Red pigment experimental spectrum shows very good agreement with the simulation for γ-QA. The main feature at around 9 THz and three very minor satellites are all evident in both experiment and simulation (**Figure 8-9**). Likewise, the complex of half a dozen lines around 3 THz appears in both experiment and simulation. The only discrepancy is that a strong absorption predicted at about 4.5 THz is not evident in the experiment; the reason for this is not clear, but may be related to an instrumental artefact, as it appears in all of the terahertz spectra.

The PV19-Violet pigment experimental spectrum shows the features predicted by the β-QA simulation, namely, a strong absorption around 9 THz and a series of modes around 4 THz (**Figure 8-10**). However, the experimental spectrum shows additional absorptions (notably at around 8.5 THz and 10.5 THz) not evident in the simulation. These additional absorption features we attribute to an unknown phase (or phases). This assessment is consistent with our PXRD investigation of this pigment.

The PR122 experimental and calculated spectra are in very good agreement (**Figure 8-11**). There is a pair of modes between 10 and 11 THz, a second pair at around 7 THz, and a group of three around 3.5 THz.

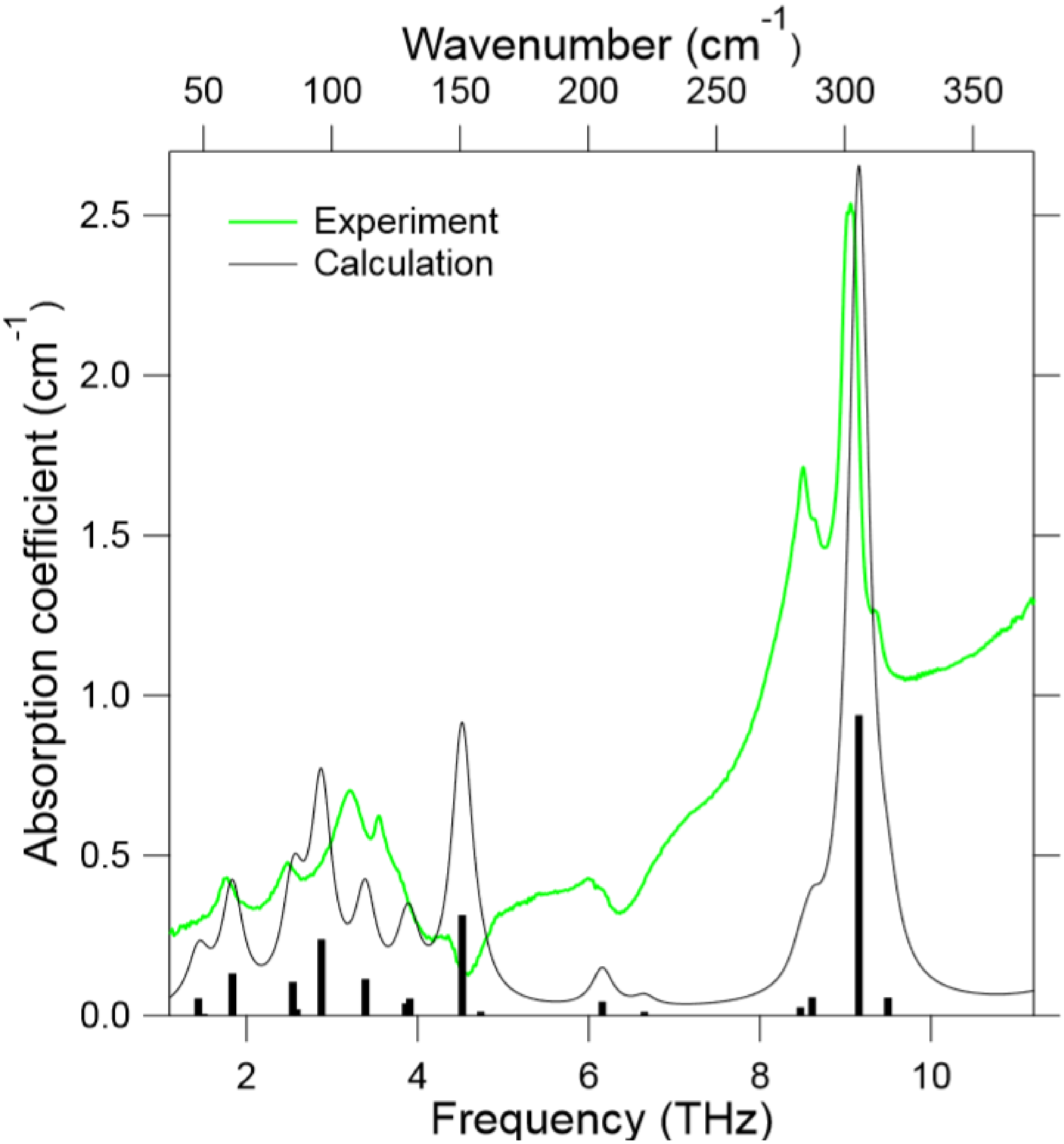

Figure 8-9. Experimental terahertz spectrum of PV19-Red pigment compared with the calculated spectrum for *γ*-QA.

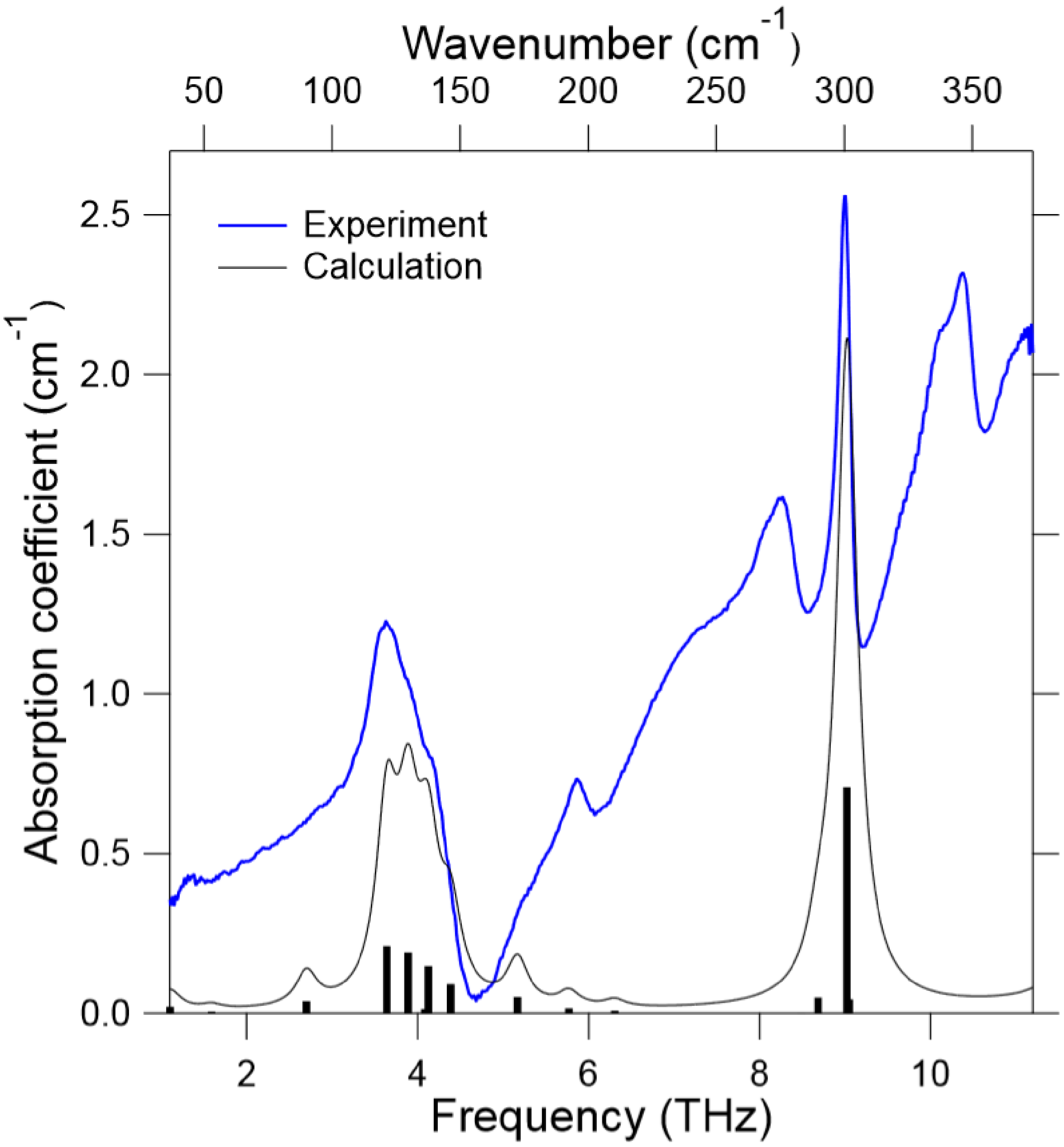

Figure 8-10. Experimental terahertz spectrum of PV19-Violet pigment compared with the calculated spectrum for *β*-QA.

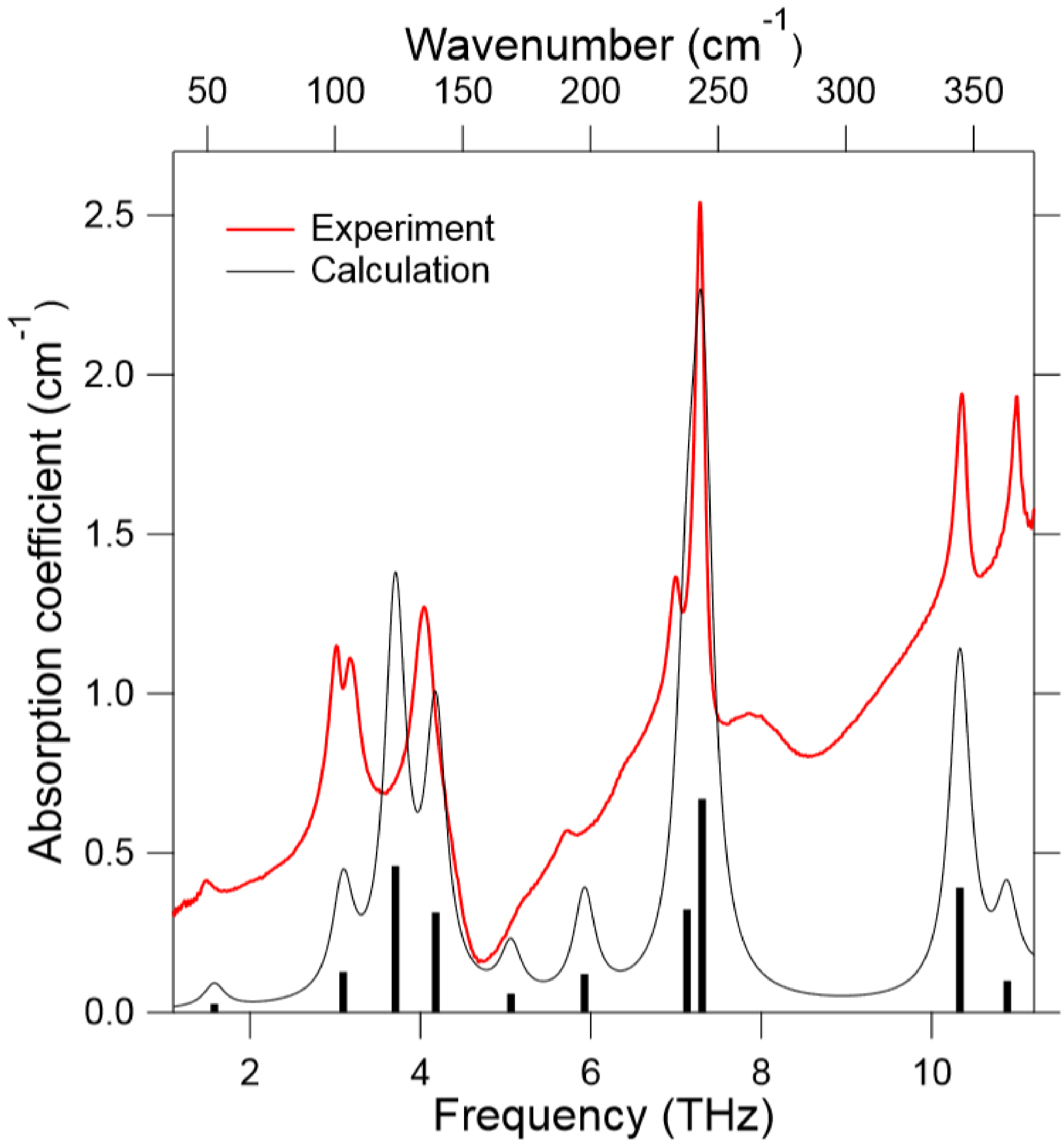

Figure 8-11. Experimental terahertz spectrum of PR122 pigment compared with the calculated spectrum for 2,9-DMQA.

In all of the quinacridone solids, similar vibration types contribute to the observed THz spectra. These vibrations all correspond to intramolecular motions with the majority composed of wagging, rocking, and twisting of the quinacridone rings. The most intense THz spectral feature in all three samples is assigned to an in-plane rocking vibration of the carbonyl oxygens. The intermolecular vibrations (e.g. translations) of the molecules within these solids are IR-inactive and therefore play no role in the THz absorption profile.

8.4 Conclusions

We have shown, by experiment and simulation, that the characteristic vibrational modes of β-quinacridone, γ-quinacridone, and 2, 9-dimethylquinacridone all fall in the terahertz spectral range and all have similar origins in fundamental wagging, twisting, and rocking motions. Furthermore, in spite of these similarities, we have demonstrated that the terahertz spectra of three quinacridones differ sufficiently to unambiguously distinguish the three quinacridones. These findings invite the application of terahertz spectroscopy in the dating and authentification of works of art.

In particular, we have demonstrated that terahertz spectroscopy identifies characteristic 'fingerprints' of three commercial quinacridone pigments. This capability of terahertz frequency photons gives advantages over visible, infrared and x-ray electromagnetic radiation in examining artwork. Of course, most art is produced with the aim that it is to be viewed by the human eye in the visible spectral region. Yet many different pigments appear to have the same color to the human eye. Terahertz spectroscopy is able to distinguish these. Secondly, terahertz photons penetrate deeper into material, and so can probe the paint further below the surface than near- or mid-infrared photons. Thirdly, although x-ray absorption and fluorescence are sensitive to average mass number or to particular atoms, respectively, they cannot distinguish different polymorphs, such as *β*and *γ*-quinacridone. Thus, terahertz methods have important advantages over visible, infrared and x-ray methods. Art fraud, for example, might be detected, if a painting claimed to be pre-modern was found to contain synthetic quinacridone pigments.

8.5 Acknowledgement

A.D.S and R.A.L. thank Joseph Horvat for a careful reading of the manuscript, Madeleine Kelly and Paula Dredge for insightful discussions, Nicola Dowse and Jarrod Colla for experimental assistance, and the Australian Research Council and the University of Wollongong Global Challenges Program for funding associated with this research. A.J.Z. and T.M.K. acknowledge the support of a grant from the National Science Foundation (CHE-1301068).

8.6 References

(1) Parikh, M.; Shah, S. S. Preparation of New Pigments of Quinacridone Group and their Pigmentory Properties. *International Journal of ChemTech Research* **2010**, *2*, 1391–1396.

(2) Gao, H.-Z. Theoretical Study on Charge Transport of Quinacridone Polymorphs. *International Journal of Quantum Chemistry* **2012**, *112*, 740–746.

(3) Paulus, E. F.; Leusen, F. J. J.; Schmidt, M. U. Crystal structures of quinacridones. *CrystEngComm* **2007**, *9*, 131–143.

(4) Herbst, W.; Hunger, K. *Industrial Organic Pigments*, 3rd ed.; WILEY-VCH: Tokyo, 2004.

(5) Lomax, S. Q. Phthalocyanine and quinacridone pigments: their history, properties and use. *Studies in Conservation* **2005**, *50*, 19–29.

(6) de Courlon, C.; Ives, S.; Dredge, P. Fields of colour: The conservation of matt, synthetic paintings by Michael Johnson. *AICCM Bulletin* **2015**, *36*, 136–146.

(7) Gottschaller, P.; Khandekar, N.; Lee, L. F.; Kirby, D. P. The evolution of Lucio Fontana's painting materials. *Studies in Conservation* **2012**, *57*, 76–91.

(8) Lomax, S. Q. The application of x-ray powder diffraction for the analysis of synthetic organic pigments. Part 2: artists' paints. *J. Coat. Technol. Res.* **2010**, *7*, 325–330.

(9) http://www.schmincke.de/.

(10) http://langridgecolours.com/.

(11) Dredge, P.; Ives, S.; Howard, D. L.; Spiers, K. M.; Yip, A.; Kenderdine, S. Mapping Henry: Synchrotron-sourced X-ray fluorescence mapping and ultra-high-definition scanning of an early Tudor portrait of Henry VIII. *Applied Physics A* **2015**, *121*, 789–800.

(12) Buchsbaum, C.; Schmidt, M. U. Rietveld refinement of a wrong crystal structure. *Acta Crystallographica Section B* **2007**, *63*, 926–932.

(13) Lewis, R. A. *Terahertz Physics*; Cambridge University Press: Cambridge, 2012.

(14) Lewis, R. A. In *The Encyclopaedia of Spectroscopy and Spectrometry*, 3rd ed.; Lindon, J. C., Tranter, G. E., Koppenaal, D. W., Eds.; Academic Press: Oxford, 2017; Vol. 4; pp 422–426.

(15) Manceau, J.-M.; Nevin, A.; Fotakis, C.; Tzortzakis, S. Terahertz Time Domain Spectroscopy For The Analysis Of Cultural Heritage Related Materials. *Applied Physics B* **2008**, *90*, 365–368.

(16) Jackson, J. B.; Bowen, J.; Walker, G.; Labaune, J.; Mourou, G.; Menu, M.; Fukunaga, K. A Survey of Terahertz Applications in Cultural Heritage Conservation Science. *IEEE Transactions on Terahertz Science and Technology* **2011**, *1*, 220–231.

(17) Fukunaga, K. *THz Technology Applied to Cultural Heritage in Practice*; Springer: Tokyo, 2016.

(18) Abraham, E.; Younus, A.; Delagnes, J. C.; Mounaix, P. Non-Invasive Investigation of

Art Paintings by Terahertz Imaging. *Applied Physics A* **2010**, *100*, 585–590.

(19) Picollo, M.; Fukunaga, K.; Labaune, J. Obtaining noninvasive stratigraphic details of panel paintings using terahertz time domain spectroscopy imaging system. *Journal of Cultural Heritage* **2015**, *16*, 73–80.

(20) Fukunaga, K.; Picollo, M. Terahertz spectroscopy applied to the analysis of artists' materials. *Applied Physics A* **2010**, *100*, 591–597.

(21) Zhang, Z.; Zhang, C.; Yang, Y. THz spectra of seven red mineral pigments used in ancient Chinese artworks. 2016 41st International Conference on Infrared, Millimeter, and Terahertz waves (IRMMW-THz). 2016.

(22) Squires, A. D.; Kelly, M. T.; Lewis, R. A. THz analysis of quinacridone pigments. *International Journal of Infrared, Millimeter and Terahertz Waves* **2016**, 1–1.

(23) Dash, J.; Ray, S.; Nallappan, K.; Kaware, V.; Basutkar, N.; Gonnade, R. G.; Ambade, A. V.; Joshi, K.; Pesala, B. Terahertz Spectroscopy and Solid-State Density Functional Theory Calculations of Cyanobenzaldehyde Isomers. *The Journal of Physical Chemistry A* **2015**, *119*, 7991–7999.

(24) Ruggiero, M. T.; Sibik, J.; Zeitler, J. A.; Korter, T. M. Examination of l-Glutamic Acid Polymorphs by Solid-State Density Functional Theory and Terahertz Spectroscopy. *The Journal of Physical Chemistry A* **2016**, *120*, 7490–7495.

(25) King, M. D.; Buchanan, W. D.; Korter, T. M. Application of London-type dispersion corrections to the solid-state density functional theory simulation of the terahertz spectra of crystalline pharmaceuticals. *Phys. Chem. Chem. Phys.* **2011**, *13*, 4250–4259.

(26) Williams, M. R. C.; Aschaffenburg, D. J.; Ofori-Okai, B. K.; Schmuttenmaer, C. A. Intermolecular Vibrations in Hydrophobic Amino Acid Crystals: Experiments and Calculations. *The Journal of Physical Chemistry B* **2013**, *117*, 10444–10461.

(27) Lepodise, L. M.; Horvat, J.; Lewis, R. A. Terahertz Spectroscopy of 2,4-Dinitrotoluene over a Wide Temperature Range (7–245 K). *The Journal of Physical Chemistry A* **2015**, *119*, 263–270.

(28) Shi, L.; Duan, X.-H.; Zhu, L.-G.; Liu, X.; Pei, C.-H. Directly Insight Into the Inter- and Intramolecular Interactions of CL-20/TNT Energetic Cocrystal through the Theoretical Simulations of THz Spectroscopy. *The Journal of Physical Chemistry A* **2016**, *120*, 1160–1167.

(29) Lepodise, L. M.; Horvat, J.; Lewis, R. A. Collective librations of water molecules in the crystal lattice of rubidium bromide: experiment and simulation. *Phys. Chem. Chem. Phys.* **2013**, *15*, 20252–20261.

(30) http://www.oldholland.com/.

(31) http://www.rfpaints.com/.

(32) Dovesi, R.; Orlando, R.; Erba, A.; Zicovich-Wilson, C. M.; Civalleri, B.; Casassa, S.; Maschio, L.; Ferrabone, M.; De La Pierre, M.; D'Arco, P. et al. CRYSTAL14: A program for the ab initio investigation of crystalline solids. *International Journal of Quantum Chemistry* **2014**, *114*, 1287–1317.

(33) Senju, T.; Sakai, M.; Mizuguchi, J. Cohesion of γ-quinacridone and 2,9dimethylquinacridone in the solid state. *Dyes and Pigments* **2007**, *75*, 449–453.

(34) Perdew, J. P.; Burke, K.; Ernzerhof, M. Generalized gradient approximation made simple. *Physical Review Letters* **1996**, *77*, 3865–3868.

(35) Schäfer, A.; Huber, C.; Ahlrichs, R. Fully optimized contracted Gaussian basis sets of triple zeta valence quality for atoms Li to Kr. *Journal of Chemical Physics* **1994**, *100*, 5829–5835.

(36) Grimme, S.; Antony, J.; Ehrlich, S.; Krieg, H. A consistent and accurate *ab initio* parametrization of density functional dispersion correction (DFT-D) for the 94 elements H–Pu. *Journal of Chemical Physics* **2010**, *132*, 154104–154118.

(37) Grimme, S.; Ehrlich, S.; Goerigk, L. Effect of the damping function in dispersion corrected density functional theory. *Journal of Computational Chemistry* **2011**, *32*, 1456– 1465.

(38) Noel, Y.; Zicovich-Wilson, C. M.; Civalleri, B.; D'Arco, P.; Dovesi, R. Polarization properties of ZnO and BeO: An *ab initio* study through the Berry phase and Wannier functions approaches. *Physical Review B* **2001**, *65*, 014111–1–014111–9.

(39) Panina, N.; Leusen, F. J. J.; Janssen, F. F. B. J.; Verwer, P.; Meekes, H.; Vlieg, E.; Deroover, G. Crystal structure prediction of organic pigments: quinacridone as an example. *Journal of Applied Crystallography* **2007**, *40*, 105–114.

(40) Smith, H. M. *High Performance Pigments*; Weinheim Wiley-VCH, 2002.

CHAPTER 9. Conclusions

The effect of temperature will always be of great significance and impact chemical systems. The culmination of all the research presented in this work has illustrated the importance of using low-frequency vibrational spectroscopy to analyze crystalline lattice vibrations. Combining the complementary techniques of THz and Raman spectroscopies provides a full determination of all the active modes that are present, leading to a more complete understanding into the nature of the systems studied. By obtaining spectra over a range of temperatures, it is possible to see the subtle shifts in the vibrational spectra (**Chapter 7**) or induce and detect polymorph changes (**Chapter 6**). The use of low-frequency spectroscopy in polymorph detection has been very well documented in this work, and experimental results provided a backdrop to further analyze the systems with ss-DFT calculations.

All of the studies utilized ss-DFT which made it possible to discern the molecular motions that correspond to vibrational modes in the low-frequency range. A further analysis of these motions made it possible to determine how specific vibrational modes were affected by temperature. While the energetic analysis of the relative stabilities was significant to the results that were presented, these energies were representative of 0 K structures. By calculating the temperature-dependent energies, it was possible to investigate how the relative stabilities of polymorphs can switch with temperature (**Chapter 4** and **Chapter 6**), revealing an enantiotropic nature. Calculations were also performed along specific vibrational modes in this work, enabling for the construction of potential energy surfaces across specific coordinates tied with isomeric or polymorphic transformations (**Chapter 5** and **Chapter 6**).

While this research provides a more complete picture into the behavior of temperature-dependent crystalline systems, it is still a large area of study that has great potential in future work. Oftentimes temperature effects induce strain on a crystalline system, and an investigation of this strain energy may provide further insight into the nature of temperature-dependent polymorph transformations. Because much of this work deals with transformations, it is also likely that molecular dynamics simulations can be used in tandem with ss-DFT to arrive at more insightful results. Experimentally, spectrometer systems are always being improved upon, and it is likely that as time goes on, methods of obtaining low-frequency spectra will have access to greater bandwidth and resolution, enabling the better detection of less intense modes and allowing for an improved characterization of a sample.

The outcome of this research has focused on the use of low-frequency spectroscopy and modeling through ss-DFT in order to provide information into how crystalline systems behave with temperature. These systems can be used as benchmarks in projects with species that behave in similar ways. Temperature effects all chemical systems in some way, and for that reason it is important to be able to determine and analyze these effects. The results presented in this work are valuable to the future research endeavors in the Korter group and more broadly to the low-frequency spectroscopy and solid-state density functional theory communities as a whole.

APPENDIX A: CHAPTER 4 Supporting Information

CONTENTS:

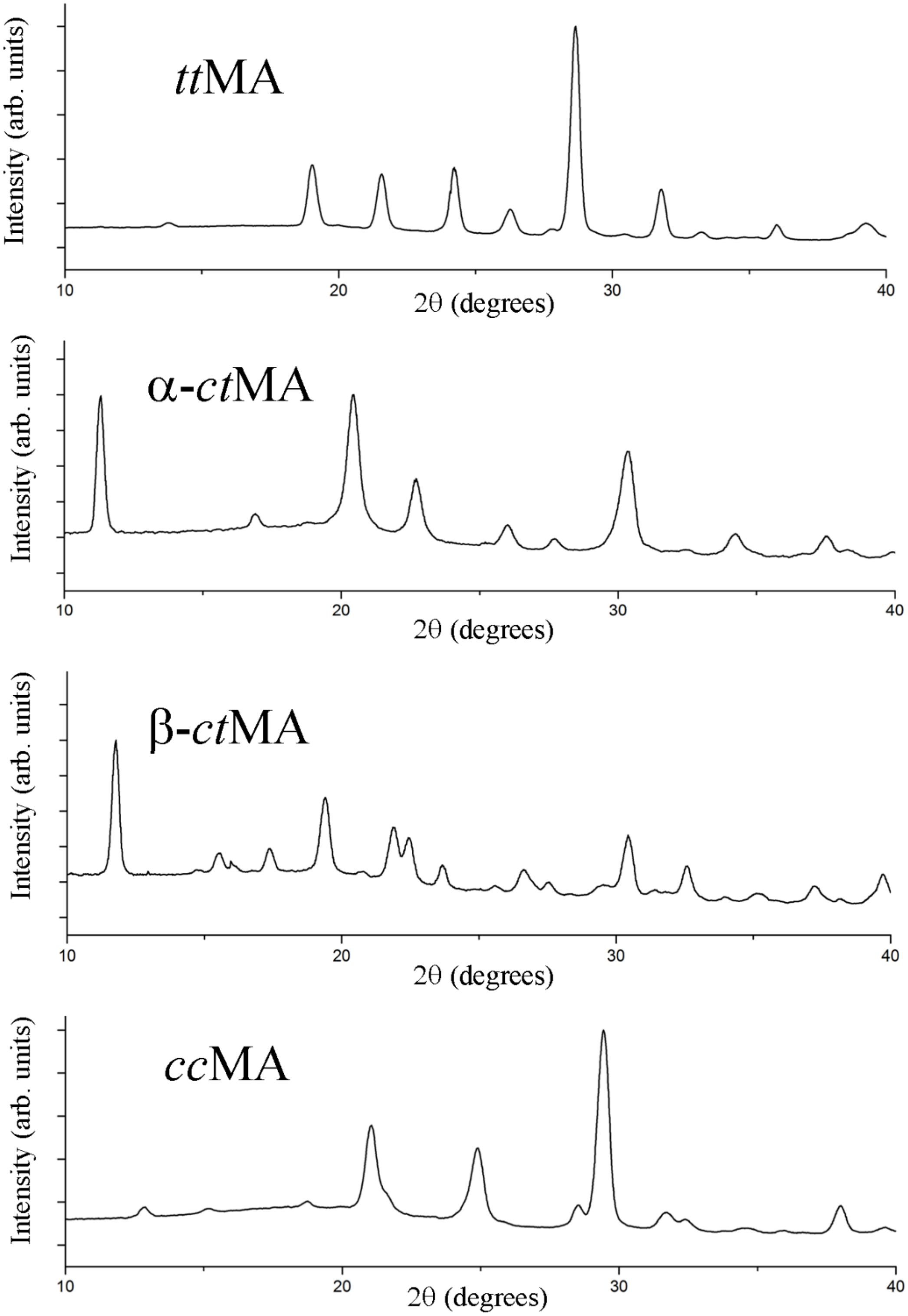

Figure A1. PXRD patterns at 95 K for *tt*MA, α-ctMA, β-ctMA and *cc*MA.

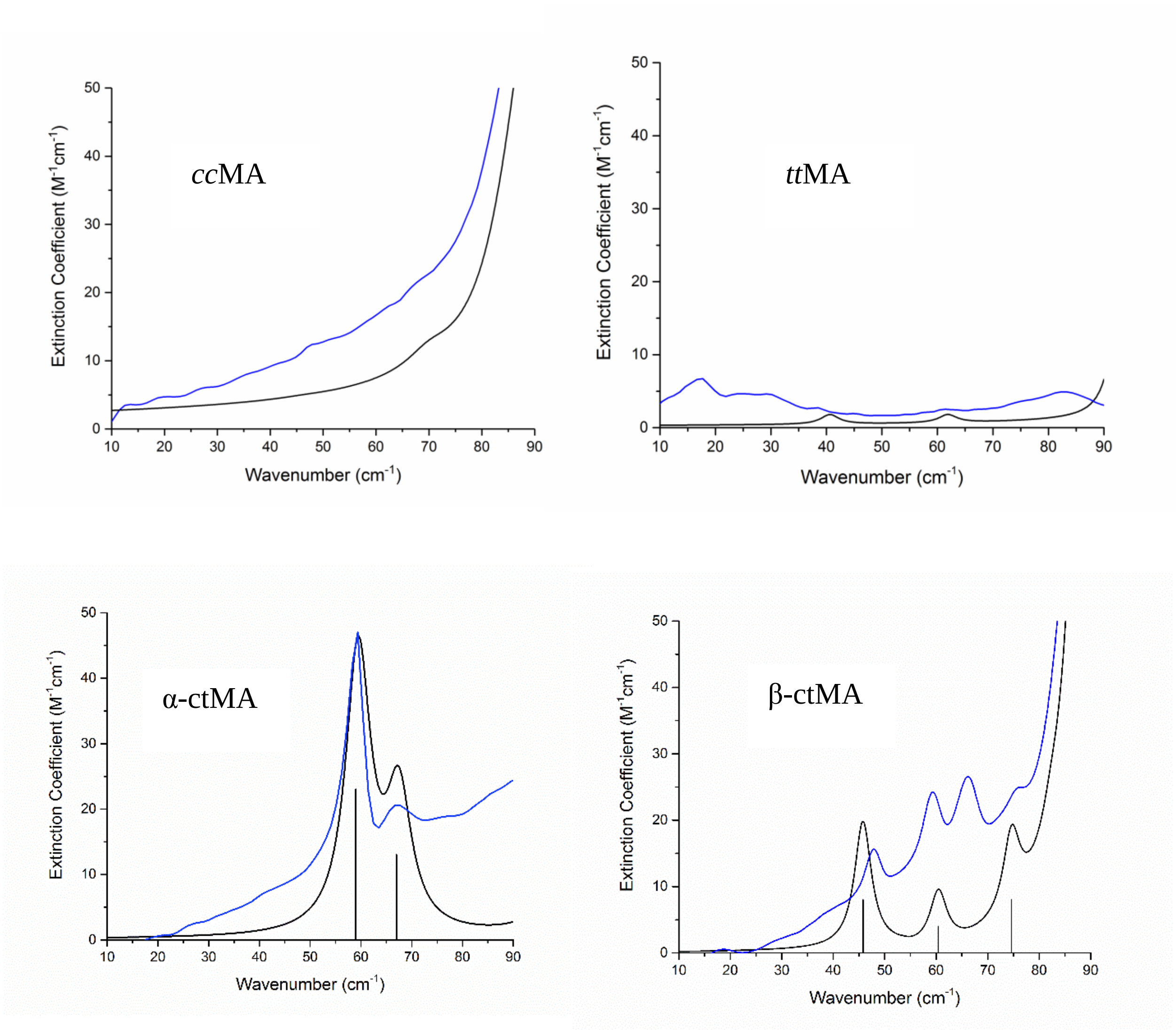

Figure A2. Full experimental (blue) and simulated (black) terahertz spectra for all muconic acid isomer crystals.

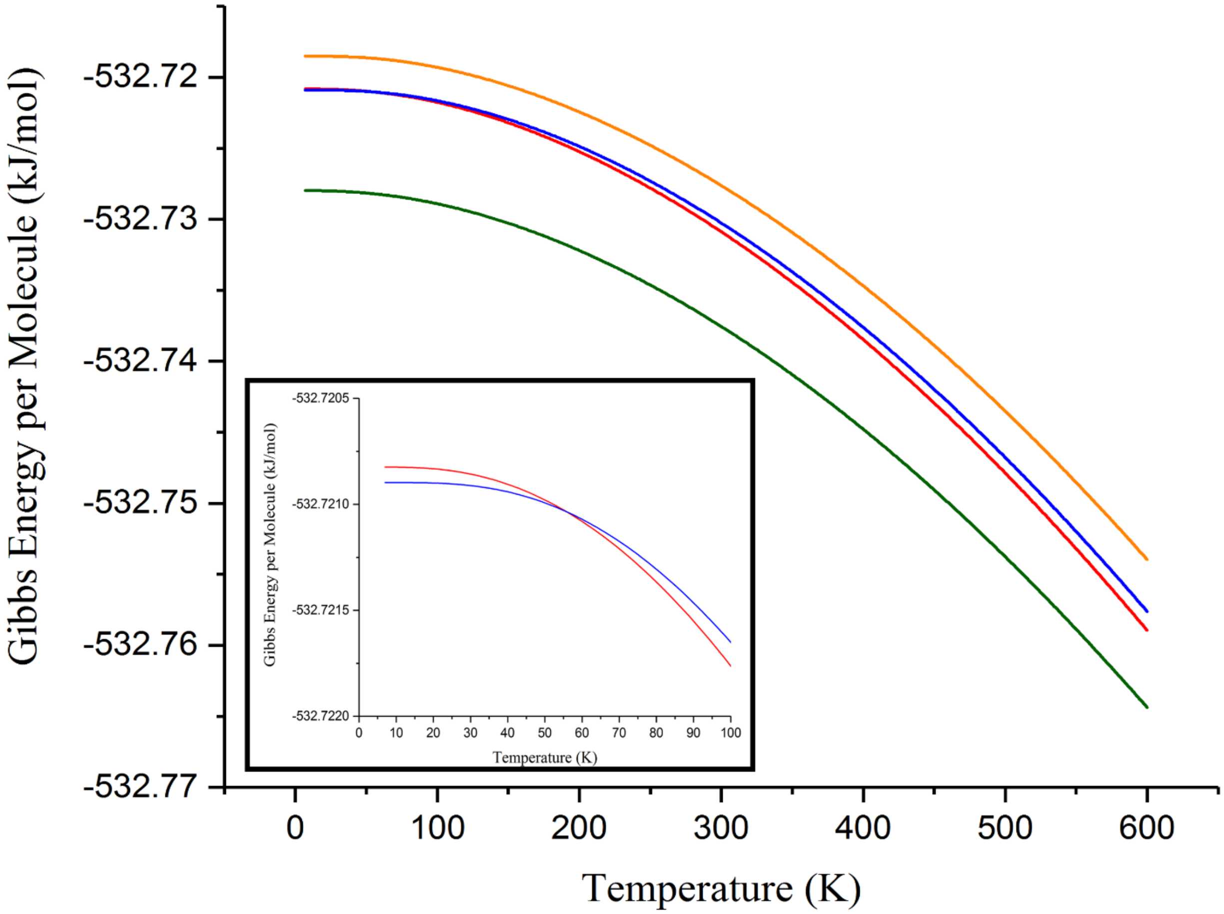

Figure A3. Gibbs energy curves for all muconic acid polymorphs (PBE-D/def2-TZVP) with *tt*MA (green), α-*ct*MA (blue), β-*ct*MA (red) and *cc*MA (yellow). Inset shows the *ct*MA polymorphs crossing point.

Table A1. Bond length and angle analysis for *tt*MA and the corrresponding root-mean-squared deviations (RMSDs). Experimental data is from 95 K SCXRD and calculated is from PBE-D3/def2-TZVP. Hydrogen bond lengths are measured as intermolecular O···O distances.

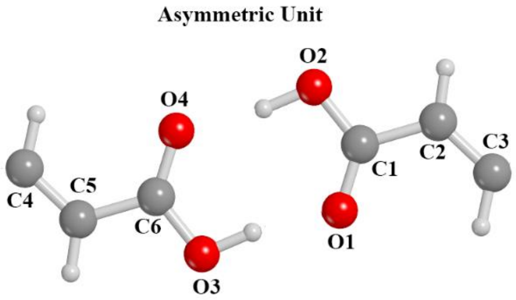

Bond (Å)	Experimental	Calculated
O1-C1	1.316	1.323
O2-C1	1.227	1.248
C1-C2	1.471	1.466
C2-C3	1.336	1.353
C3-C3	1.446	1.437
C4-C5	1.332	1.353
C5-C6	1.472	1.466
C4-C4	1.445	1.438
C6-O3	1.303	1.323
C6-O4	1.238	1.248
	RMSD	**0.014**
H-Bonds		
O1-O2	2.620	2.560
O3-O4	2.620	2.570
	RMSD	**0.055**
Angle (^{0})	**Experimental**	**Calculated**
O1-C1-O2	123.31	123.17
O1-C1-C2	113.38	113.76
O2-C1-C2	123.30	123.06
C1-C2-C3	121.17	121.57
C2-C3-C3	122.88	122.94
C4-C4-C5	123.20	122.75
C4-C5-C6	121.47	121.61
C5-C6-O3	113.81	113.38
C5-C6-O4	122.53	123.29
O3-C6-O4	123.66	123.32
	RMSD	**0.39**

Table A2. Bond length and angle analysis for α-*ct*MA and the corrresponding root-mean-squared deviations (RMSDs). Experimental data is from 95 K SCXRD and calculated is from PBE-D3/def2-TZVP. Hydrogen bond lengths are measured as intermolecular O···O distances.

Bond (Å)	**Experimental**	**Calculated**
O1-C1	1.311	1.324
O2-C1	1.237	1.247
C1-C2	1.469	1.467
C2-C3	1.332	1.352
C3-C4	1.447	1.441
C4-C5	1.346	1.356
C5-C6	1.474	1.469
C6-O3	1.234	1.248
C6-O4	1.298	1.325
	RMSD	**0.014**
H-Bonds		
O1-O3	2.617	2.558
O2-O4	2.635	2.570
	RMSD	**0.062**
Angle (^{0})	**Experimental**	**Calculated**
O1-C1-O2	123.18	123.46
O1-C1-C2	114.21	113.19
O2-C1-C2	122.61	123.35
C1-C2-C3	122.14	121.91
C2-C3-C4	120.88	121.58
C3-C4-C5	128.11	127.31
C4-C5-C6	126.29	126.27
C5-C6-O3	123.09	124.26
C5-C6-O4	113.59	112.98
O3-C6-O4	123.32	122.76
	RMSD	**0.70**

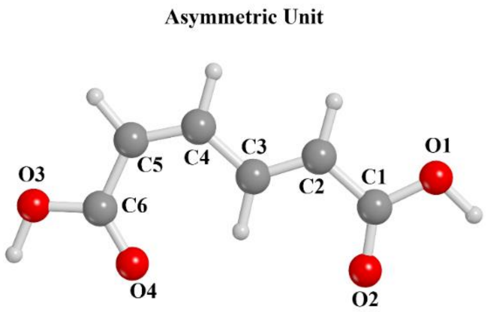

Table A3. Bond length and angle analysis for β-*ct*MA and the corrresponding root-mean-squared deviations (RMSDs). Experimental data is from 95 K SCXRD and calculated is from PBE-D3/def2-TZVP. Hydrogen bond lengths are measured as intermolecular O···O distances.

Bond (Å)	**Experimental**	**Calculated**
C1-C2	1.474	1.465
C2-C3	1.337	1.353
C3-C4	1.456	1.441
C4-C5	1.340	1.355
C5-C6	1.480	1.469
C6-O3	1.237	1.247
C6-O4	1.310	1.324
O1-C1	1.226	1.321
O2-C1	1.325	1.247
	RMSD	**0.042**
H-Bonds		
O1-O2	2.644	2.589
O3-O4	2.635	2.566
	RMSD	**0.062**
Angle (^{0})	**Experimental**	**Calculated**
O1-C1-O2	122.32	122.13
O1-C1-C2	122.32	121.67
O2-C1-C2	115.36	116.20
C1-C2-C3	124.76	124.31
C2-C3-C4	120.44	120.55
C3-C4-C5	128.31	127.60
C4-C5-C6	126.12	126.49
C5-C6-O3	124.23	124.62
C5-C6-O4	112.73	112.38
O3-C6-O4	123.04	123.00
	RMSD	**0.48**

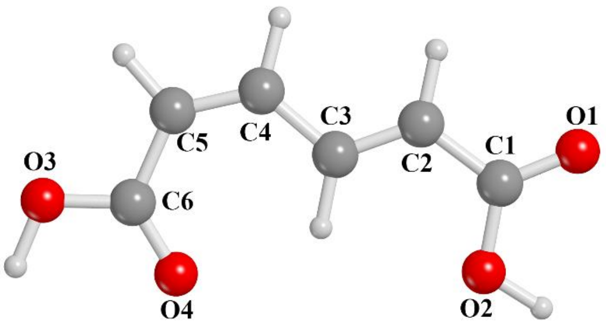

Asymmetric Unit

Table A4. Bond length and angle analysis for *cc*MA and the corrresponding root-mean-squared deviations (RMSDs). Experimental data is from 95 K SCXRD and calculated is from PBE-D3/def2-TZVP. Hydrogen bond lengths are measured as intermolecular O···O distances.

Bond (Å)	**Experimental**	**Calculated**
O1-C1	1.226	1.248
O2-C1	1.319	1.326
C1-C2	1.475	1.468
C2-C3	1.343	1.356
C3-C3	1.446	1.441
	RMSD	**0.012**
H-Bonds		
O1-O2	2.637	2.580
	RMSD	**0.057**
Angle (^{0})	**Experimental**	**Calculated**
O1-C1-O2	122.87	122.86
O1-C1-C2	125.39	125.16
O2-C1-C2	111.74	111.98
C1-C2-C3	127.27	127.77
C2-C3-C3	126.27	126.16
	RMSD	**0.60**

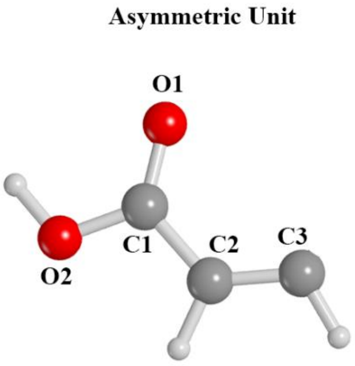

Table A5. Solid-state DFT (PBE-D3/def2-TZVP) simulated IR-active vibrational frequencies (cm^{-1}) with corresponding intensities (km/mol) for *tt*MA.

Frequency	Intensity
40.623	0.19
61.876	0.16
92.268	1.50
97.974	1.51
107.787	5.49
123.477	10.33
128.649	0.27
188.266	147.37
204.841	32.62
263.726	1.38
268.434	1.98
417.135	374.93
421.717	295.86
550.194	103.70
555.965	106.56
674.904	6.36
685.844	10.77
714.304	209.78
718.168	22.62
863.885	76.16
868.996	40.49
954.519	14.31
957.334	19.44
1022.025	697.74
1030.834	76.90
1030.966	26.47
1037.606	53.08
1180.860	153.01
1181.921	166.30
1262.881	331.78
1283.008	4806.52
1297.000	1034.18
1312.599	262.32
1450.870	42.66
1453.125	16.36
1593.621	1979.79
1597.285	1614.48
1638.571	1845.13
1645.865	290.15
2588.201	22963.05
2633.271	1908.97
3106.832	48.24
3108.684	63.41
3136.544	21.16
3145.491	21.22

Table A6. Solid-state DFT (PBE-D3/def2-TZVP) simulated IR-active vibrational frequencies (cm^{-1}) with corresponding intensities (km/mol) for α-*ct*MA.

Frequency	Intensity	Frequency	Intensity
50.079	0.02	1110.539	0.46
59.516	28.37	1111.988	261.04
67.800	13.43	1193.812	145.13
101.628	17.32	1196.388	12.18
120.884	0.21	1229.119	21.86
134.371	8.28	1233.549	2693.67
153.636	3.92	1240.572	143.68
158.823	0.07	1248.710	3293.91
186.492	0.28	1264.896	2006.20
191.253	0.09	1283.515	30.19
201.688	3.93	1316.171	4168.73
227.513	1.66	1342.486	2.95
271.145	1.64	1407.556	170.05
292.288	326.82	1419.650	113.79
338.869	0.21	1440.900	133.00
361.602	479.98	1457.371	20.39
378.788	1.21	1471.433	0.33
382.271	118.12	1476.994	24.43
440.999	368.52	1578.507	693.75
514.026	77.48	1591.795	1851.35
538.988	148.03	1598.961	42.66
590.208	21.40	1605.273	0.21
591.837	58.66	1616.018	3870.49
662.995	52.60	1631.975	124.48
680.179	0.74	1646.133	245.18
700.343	52.15	1657.454	1922.21
744.544	191.19	2475.212	42.74
748.390	9.04	2475.912	4.87
754.332	236.97	2574.530	27193.44
835.531	166.23	2671.919	15508.43
900.070	240.90	3088.822	37.67
911.674	9.19	3089.238	0.34
911.814	1.85	3131.813	0.25
974.309	3.96	3132.342	0.15
976.407	16.77	3141.294	99.42
982.463	216.54	3141.707	9.39
997.191	96.52	3156.694	129.87
1017.023	596.58	3157.201	14.52
1058.129	491.39		

Table A7. Solid-state DFT (PBE-D3/def2-TZVP) simulated IR-active vibrational frequencies (cm^{-1}) with corresponding intensities (km/mol) for β-*ct*MA.

Frequency	Intensity	Frequency	Intensity	Frequency	Intensity
45.760	1.37	760.955	42.60	1615.903	2497.36
60.429	0.59	835.653	281.62	1628.701	242.13
74.639	0.86	839.162	1.20	1643.826	4445.47
82.260	0.20	907.994	75.10	1650.755	1038.82
90.083	0.40	908.116	11.60	1655.679	41.09
91.977	42.70	914.502	55.50	2611.445	13760.97
96.979	6.63	915.031	0.04	2621.523	7139.21
109.025	0.38	951.668	205.29	2699.624	8398.28
115.781	0.52	967.022	19.83	2795.733	7791.42
121.497	12.53	980.737	0.32	3070.416	0.34
133.168	0.47	981.095	238.85	3070.537	31.01
138.586	71.26	994.141	675.25	3102.568	85.13
144.601	17.98	1010.732	4.60	3103.197	325.90
178.224	21.30	1018.382	518.28	3140.007	35.85
182.265	5.53	1023.901	4.89	3140.137	156.37
187.054	91.11	1050.607	114.52	3163.981	5.37
193.357	45.45	1053.119	4.88	3167.697	5.47
195.008	16.74	1109.375	19.90	3140.137	156.37
199.907	26.49	1112.476	19.39	3163.981	5.37
265.067	31.37	1221.179	291.81	3167.697	5.47
269.262	167.82	1223.130	536.66		
341.393	94.20	1240.708	773.31		
349.977	5.49	1245.920	54.82		
373.825	10.94	1250.364	5672.68		
376.183	14.69	1266.483	676.10		
426.615	399.63	1283.669	252.33		
427.797	90.09	1294.318	148.20		
530.779	85.26	1305.769	73.58		
536.945	16.23	1314.570	1713.36		
591.265	22.70	1403.100	20.98		
596.567	13.49	1405.207	849.06		
663.287	83.47	1428.779	334.34		
668.431	7.95	1441.458	524.22		
690.796	47.54	1446.351	91.46		
691.852	295.04	1468.070	1.08		
740.219	13.05	1543.102	877.68		
742.961	75.30	1592.046	197.51		
758.764	161.98	1600.428	1515.91		

Table A8. Solid-state DFT (PBE-D3/def2-TZVP) simulated IR-active vibrational frequencies (cm^{-1}) with corresponding intensities (km/mol) for *cc*MA.

Frequency	Intensity
46.228	0.04
53.399	0.00
69.865	0.79
85.579	0.89
93.675	18.74
115.525	4.11
121.379	1.36
185.846	152.42
193.610	10.21
281.083	0.81
284.686	0.01
406.138	28.94
409.337	400.90
559.368	66.08
561.968	34.01
630.151	6.14
639.628	44.10
714.013	393.82
716.694	8.94
830.712	271.53
837.019	1.83
925.598	0.52
929.411	2.21
1004.034	522.87
1004.342	37.13
1028.936	4.39
1030.012	22.71
1186.116	519.71
1204.831	1.56
1240.533	4200.09
1253.582	152.20
1348.453	708.87
1361.254	163.63
1439.626	37.42
1443.820	35.98
1582.100	1971.98
1584.960	232.45
1640.482	1957.57
1649.737	410.30
2669.373	20506.71
2676.879	423.11
3146.880	14.17
3148.960	0.25
3156.193	3.79
3157.600	44.63

Table A9. Calculated (PBE-D3/def2-TZVP) Gibbs energies (per molecule) of all muconic acid polymorphs at 0K and 298K (kJ/mol).

Temperature (K)	*cc*MA	α-*ct*MA	β-*ct*MA	*tt*MA
0	-532.718519	-532.720824	-532.720897	-532.727972
298	-532.727505	-532.730744	-532.730134	-532.737425

Adam Zaczek

Department of Chemistry
Syracuse University
1-014 Center for Science and Technology
Syracuse, NY. 13244-4100

Education

State University of New York at Geneseo- Geneseo, NY

- Bachelor of Science, Chemistry (Biology Minor), 2014

Syracuse University: College of Arts and Sciences- Syracuse, NY

- Master of Philosophy, Chemistry, 2016
- Ph.D., Chemistry, August 2018
- Advisor: Timothy M. Korter

Research Experience

Research Assistant – Syracuse University, Syracuse New York, USA.

Supervisor Prof. Timothy M. Korter

Investigation of the atomic-level origins of the solid-state properties that exist in a variety of small organic systems. Analysis is done utilizing terahertz time-domain spectroscopy and low-frequency Raman spectroscopy at a range of temperatures (78K-320K), as well as powder and single-crystal X-ray diffraction methods. Experimental results are coupled with solid-state density functional theory calculations to achieve a complete understanding of the chemical phenomena. Impacts of this research range from insight into the energetic stabilities of isomers and polymorphs, non-destructive fingerprinting of samples, and the determination and characterization of the vibrational modes responsible for crystalline transformations.

Skills developed include:

- Extensive use of terahertz time-domain spectroscopy, Raman spectroscopy, and X-ray diffraction coupled experimental results to solid-state density functional theory simulations
- Applied these methods to diverse chemical systems:
    - Organic pigments
    - Thermosalient materials
    - Dicarboxylic acids
    - Pharmaceutical agents

Teaching Experience

2018-X-ray Teaching Assistant, Syracuse University, Syracuse, New York, USA

Responsible for maintenance and upkeep of the powder and single-crystal X-ray diffractometers at Syracuse University and managing the user schedule. Also in charge of training new users on how to properly use the diffractometers and solve crystal structures. Maintaining an open means of communication with users and addressing any issues. Often tasked with mounting crystals for inexperienced users and groups unfamiliar with the X-ray equipment as well as solving crystal structures for users who require assistance with challenging crystals

2015-2017-Teaching Assistant, Syracuse University, Syracuse, New York, USA

Taught General Chemistry Laboratory I and II. Assisted in supervising and teaching laboratory experiments to undergraduate students. Responsibilities included pre-laboratory instruction, experimental set-up and break-down, post-laboratory assistance (office hours), and grading of scientific reports

LABORATORY SKILLS

- Infrared Spectroscopies (FTIR, THz)

-Single-Crystal and Powder X-ray Diffraction

- Continuous-Wave Diode Lasers

-Raman Spectroscopy

Training/Workshops

- 252nd ACS National Meeting & Exposition, Philadelphia, PA. August 21-25, 2016
- *Ab inito* Modeling in Solid State Chemistry, Turin Italy. September 4-9, 2016
- Intro to Single Crystal X-ray Diffraction Applications Training, Madison Wisconsin, October 10-12, 2016
- The Minnesota Workshop on *Ab initio* Modeling in Solid State Chemistry with CRYSTAL, Minneapolis, July 9-14, 2017
- Bruker APEX II Duo Service Training, August 8-10, 2017

Presentations

Zaczek, A.; Korter, T. Cis-Trans Isomerization Mechanisms of Muconic Acid, 252nd ACS National Meeting & Exposition, Philadelphia, PA. August 24, 2016. (poster)

Selected for Sci-Mix Presentaion on August 22.

Zaczek, Adam; Korter, Timothy M., Characterization of Crystalline Muconic Acid Polymorphs, IRMMW-THz 2017, August 27-September 1, 2017, Cancun Mexico

Publications

7. A.D. Squires, **Adam J. Zaczek**, R.A. Lewis, and Timothy M. Korter, Determining the Mechanisms of Vibrational Modes of Quinacridones via Temperature-Resolved Terahertz Spectroscopy: Absorption Experiments and Solid-State Density Functional Theory (**in preparation)**

6. **Adam J. Zaczek**, Luca Catalano, Timothy M. Korter, Pance Naumov, Lattice Vibrations and Polymorph Transformation Mechanisms in Thermosalient 1,2,4,5-Tetrabromobenzene Crystals (**in preparation**)

5. Aytekin, Y. S.; Köktürk, M.; **Zaczek, A**.; Korter, T. M.; Heilweil, E. J.; Esenturk, O., Optical properties of Meloxicam in the far-infrared spectral region. Chemical Physics 2018. (**article in press**)

4. Michael T. Ruggiero, Joshua J. Sutton, Sara J. Fraser-Miller, **Adam J. Zaczek**, Timothy M. Korter, Keith C. Gordon, and J. Axel Zeitler, Revisiting the Thermodynamic Stability of Indomethacin Polymorphs with Low-Frequency Vibrational Spectroscopy and Quantum Mechanical Simulations. ed.; 2018 (**in review**)

3. Qi Li, **Adam J. Zaczek**, Timothy M. Korter, J. Axel Zeitler, Michael T. Ruggiero, Quantum Mechanical Interpretation of the Ultra-Low Energy Methyl-Rotation Dynamics in Porous Metal-Organic Frameworks Probed by Low -Frequency Vibrational Spectroscopy and ab initio Simulations, ChemComm 2018, 54, (45), 5776-5779

2. **Zaczek, A. J**.; Korter, T. M., Polymorphism in cis-trans Muconic Acid Crystals and the Role of C-H···O Hydrogen Bonds. Cryst. Growth Des. 2017, 17, (8), 4458-4466.

1. Squires, A. D.; Lewis, R. A.; **Zaczek, A. J**.; Korter, T. M., Distinguishing Quinacridone Pigments via Terahertz Spectroscopy: Absorption Experiments and Solid-State Density Functional Theory Simulations. J. Phys. Chem. A 2017, 121, (18), 3423-3429